Investigating the Fundamentals of Liquid-Fuelled Pulse Detonation Engines

Thesis submitted for the
Degree of Doctor of Philosophy
of Cardiff University

by
Ashish Majithia
(MEng)

May 2011

ProQuest LLC
789 East Eisenhower Parkway
P.O. Box 1346
Ann Arbor, MI 48106-1346

Abstract

This thesis is concerned with the applicability of liquid fuels to Pulse Detonation Engines, specifically those fuels already in use by the aviation industry such as aviation kerosene. Pulse Detonation Engines provide the possibility of a step change in the efficiency of aviation propulsion systems through the increased thermodynamic efficiency of detonations over deflagrations. Although much research has been conducted in the past decade and more on Pulse Detonation Engines, a bespoke flight ready engine is yet to be tested.

During the course of this study, the potential for reflected shocks to provide detonable liquid fuel-air mixes and initiate detonation was investigated. This was achieved through the design and build of a new shock tube facility housed at Cardiff University's Gas Turbine Research Facility (GTRC). The shock tube enabled investigation of gaseous fuels of relevance to the study of kerosene, and the investigation of the affect of different reflecting faces on combustion initiation. In addition, the mixing process of a real prototype Pulse Detonation Engine has been studied by numerical simulation; and the processes by which liquid droplets undergo breakup in steady and pulsed flows have been studied experimentally.

The shock tube test programme has shown that detonation initiation is achievable for gaseous fuel-air mixtures with a reflected shock. Also demonstrated is the fact that the presence of a shaped reflecting face enhances combustion initiation significantly. Combustion initiation has been demonstrated for a liquid kerosene-air mixture with a flat reflecting face, suggesting that the presence of a shaped reflecting face will lead to detonation. In addition, the numerical simulation programme has evaluated the fuel-air mixing characteristics of the prototype Pulse Detonation Engine and made recommendations for improvements. The droplet breakup study has demonstrated that a liquid fuel-air mixture suitable for detonation propagation is achievable in the shock tube.

Acknowledgements

Firstly I would like to thank my supervisors Professor Phil Bowen and Professor Tim O'Doherty without whose help, support and expertise this work would not have been possible.

I would also like to thank the staff of the GTRC and School of Engineering who have helped me along the way: Steve Morris and Terry Treherne for their help and support in getting the shock tube up and running; Dr. Andrew Crayford for his in-depth knowledge on combustion process; Dr. Peter Kay for his help and insight into sprays and laser diagnostics and Paul Malpas, Alan Griffiths, Steve Mead and Malcolm Seabourne for their technical support and know-how. Also thank you to Kate Osbaldeston, Liesa Nottle and the staff in the Research office for all their help over the past few years.

I would like to give a special mention to Gwyn Oakley (Aber Shock and Detonation Research Ltd) for opening the doors on the black arts that are detonation and shock tube research.

Finally, a big thank you to my friends and family who have supported me throughout this process and kept me going through the tough times and helped me enjoy the good times.

DECLARATION

This work has not previously been accepted in substance for any degree and is not concurrently submitted in candidature for any degree.

Signed ..... (candidate) Date 31/5/2011

STATEMENT 1

This thesis is being submitted in partial fulfilment of the requirements for the degree of Doctor of Philosophy

Signed ..... (candidate) Date 31/5/2011

STATEMENT 2

This thesis is the result of my own independent work/investigation, except where otherwise stated.

Other sources are acknowledged by explicit references.

Signed ..... (candidate) Date 31/5/2011

STATEMENT 3

I hereby give consent for my thesis, if accepted, to be available for photocopying and for inter-library loan, and for the title and summary to be made available to outside organisations.

Signed ..... (candidate) Date 31/5/2011

Nomenclature

Roman Characters

Symbol	Definition	Unit
A	Constant	
a	Speed of Sound	ms^{-1}
D	Characteristic Length	m
d_0	Orifice Size	m
e	Internal Energy	J
g	Acceleration due to Gravity	ms^{-1}
M	Mach Number	
MW	Molecular Weight	$kg\ mol^{-1}$
$\dot{m}$	Mass Flow Rate	kgs^{-1}
m_d	Mass	kg
P	Pressure	Pa
R	Gas Constant	$J\ kg^{-1}K^{-1}$
R_0	Universal Gas Constant	$J\ K^{-1}\ mol^{-1}$
T	Temperature	K
u	Gas Velocity	ms^{-1}
V	Volume	m^3
v	Shock Velocity	ms^{-1}
w	Wave velocity	ms^{-1}

Greek Characters

Symbol	Definition	Unit
γ	Ratio of Specific Heats	
μ	Viscosity	Nsm^{-2}
ρ	Density	kgm^{-3}
σ	Surface Tension	kgs^{-2}

Acronyms

Symbol	Definition
BPR	Bypass Ratio
C-J	Chapman-Jouget
CAD	Computer Aided Design
CFD	Computational Fluid Dynamics
DAQ	Data Acquisition System
DDM	Double Diaphragm Method
DDT	Deflagration to Detonation Transition
FAM	Fuel Air Mixture
HBR	High Bypass Ratio
LBR	Low Bypass Ratio
PDE	Pulse Detonation Engine
We	Weber Number
ZND	Zel'dovich, von Neumann, Doring

Table of Contents

Index of Figures

Index of Tables

Chapter One

Introduction

1.1 Aerospace Propulsion

1.1.1 History and Current Technologies

The flight of the first jet propelled aircraft, the de Havilland Comet in 1952, heralded a new dawn in transportation. Jet Engines (more correctly known as Gas Turbines) allowed aircraft to fly at speeds of 500-600 mph, cutting transport times by almost 50% compared to their piston-engine contemporaries [1]. They have enabled the growth of the airline industry to 4.882 billion passengers in 2008 [2]. Although the basic gas turbine design has remained largely unchanged to that of the original mid-20th Century, much research effort has gone into making engines lighter, more powerful, more reliable and more efficient – the new Rolls-Royce Trent 900, which powers the Airbus A380, produces 70-80,000lbf (310-360kN) of thrust with a weight of 14,190lb (6,450kg) [3]. Recently, the pace of improvement of gas turbines has plateaued, leading engine manufactures to investigate new technologies to make a step change in efficiency.

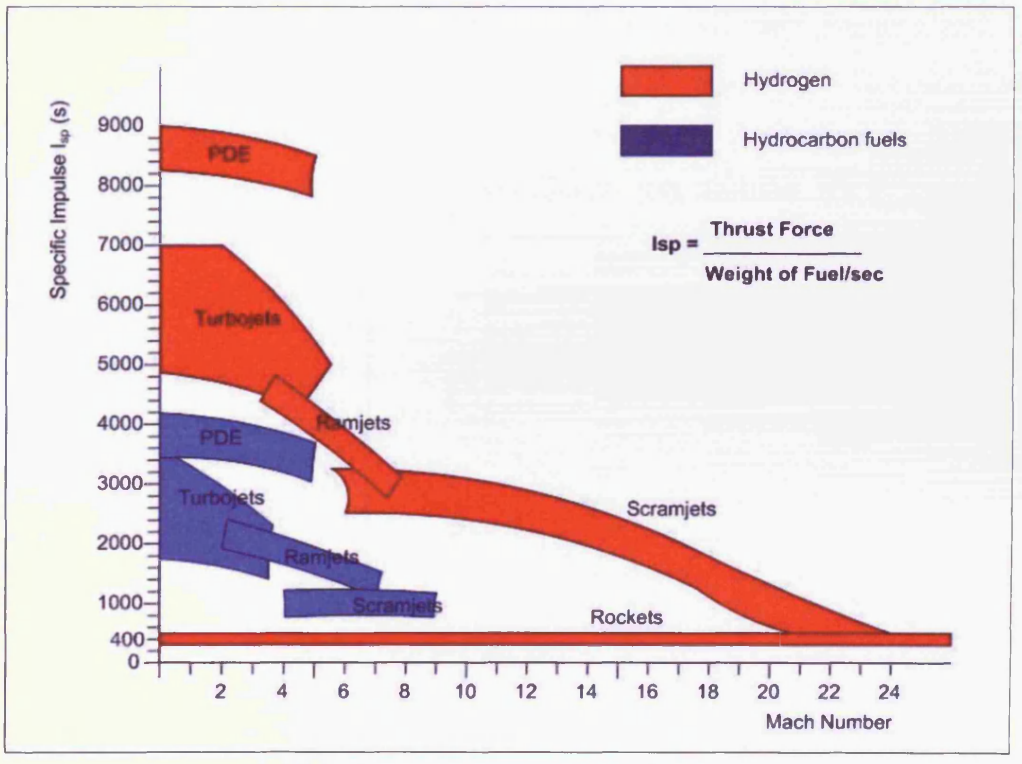

Figure 1.1: Comparison of Aerospace Propulsion Technologies [4]

As shown by Figure 1.1, different air-breathing propulsion technologies have been developed for higher speed flight that provide a better solution than gas turbines. At the current time the gas

turbine remains the most efficient for subsonic and low supersonic flight, however the current research and development effort into Pulse Detonation Engines (PDEs) aims to change this fact.

1.1.2 Gas Turbine Operation

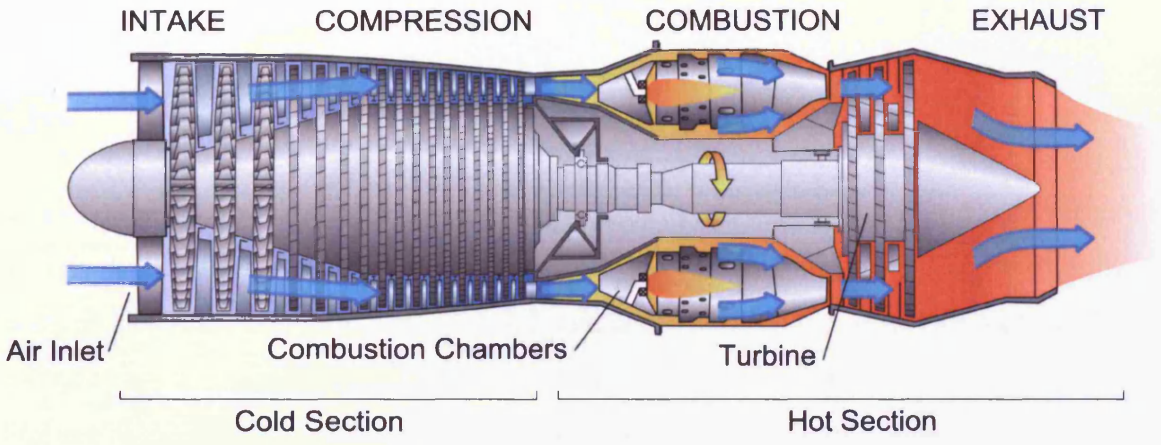

Figure 1.2: Gas Turbine Engine Schematic [5]

Gas Turbines are steady engines that operate on the Brayton Thermodynamic Cycle. Figure 1.2 shows a schematic of a Gas Turbine and Figure 1.3 shows the Brayton Cycle on a Pressure/Volume Diagram. Moving through the engine from the front, the main components of a gas turbine are: Intake, Compressor, Combustion Chamber(s), Turbine, and Exhaust Nozzle.

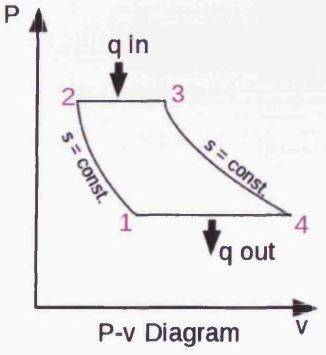

Figure 1.3: Ideal Brayton Cycle

The compressor (and to some extent the intake on an aerospace gas turbine) compress the inlet air (point 1 to point 2 in Figure 1.3) delivering high-pressure, high-temperature air to the

combustion chamber(s). In the combustion chamber, fuel is added and combustion occurs adding energy to the system (points 2-3). The hot combustion products then pass through the turbine, which is connected to and drives the compressor (points 3-4). The nozzle then delivers the combustion products to the atmosphere. The cycle is completed (points 4-1) by the expelling of the hot gas to the atmosphere where it mixes and loses energy, and the ingestion of fresh, cool air at inlet of the engine. Thrust is provided by the momentum of the expelled combustion products.

1.1.3 Gas Turbine Variants

There are three main variants of the jet engine for the aerospace sector: turbojet, turbofan and turboshaft. In a turbojet, the thrust is provided by the momentum of the expelled combustion products as described above in Section 1.1.2, and is the basis of the other two variants. Turbojets have limited applications in the modern aerospace sector due to their relative inefficiency, mainly finding use in the military sector where performance takes priority over efficiency.

Turbofans can be further categorised to High-Bypass-Ratio (HBR) and Low-Bypass-Ratio (LBR). Turbofans have a fan ahead of the main compressor, which is driven by an additional turbine stage. The fan increases the velocity of the air drawn into the engine. Part of this air then passes through the core of the engine (as described in Section 1.1.2 and shown in Figure 1.2) to provide air for combustion. The rest of the air (the bypass air) passes through the engine. Thrust is provided, in the main, by the increase in momentum of the bypass air. The Bypass Ratio (BPR) is the ratio of the mass flow rate of the air "bypassing" the core to that of the air entering the core. HBR Turbofans are the most common engine for transport aircraft, examples include the Pratt & Whitney JT9D (which powers the Boeing 747, BPR=5.0 [6]), the Rolls-Royce Trent 900 (Airbus A380, BPR=8.5-8.7 [3]), and the General Electric GE90 (Boeing 777, BPR=7.1 [7]). LBR turbofans are common on many military aircraft and include the EJ200 (Eurofigher Typhoon, BPR=0.4), and the Rolls Royce Pegasus (BAe Harrier, BPR=1.2).

Turboshaft engines contain extra turbine stages that convert the kinetic energy of the exhaust into shaft power that can then be used to drive either a propeller (Turbo-prop engine) or a rotor (for example in helicopters).

1.2 Pulse Detonation Engines

1.2.1 History and Development

The use of detonations for power generation was an idea that first began being explored in the mid 20th Century by companies such as Rolls Royce [8, 9]. They patented an engine design that involved a detonation wave continuously rotating around an annular chamber, the so-called Continuous-Detonation-Wave-Engine (CDWE). Research into detonation for power generation then cooled off until the mid 1990's, when Bussing revisited the area with Adroit Systems, a high-tech research company [10]. He (and his research group) worked on a multi-tube system with a rotating valve to isolate the constant flow of the inlet from the intermittent operation of the tubes. Their work sparked a great deal of interest in the USA with General Electric (GE) and Pratt & Whitney (P&W) starting development programmes (in fact P&W bought the PDE group from Adroit in 2001), the Department of Defence (DoD) investing in much public (and presumably in-house) research, and many academic institutions beginning research programmes. Around the world, research programmes started in countries as far afield as France, Russia, Japan and China.

Figure 1.4: AFRL's PDE Powered Long-EZ Aircraft over the Mohave Dessert [11]

1.2.2 Cycle and Operation

Current combustion systems operate on a constant pressure cycle, which has a theoretical thermodynamic efficiency of 30%. A constant volume combustion cycle has a thermodynamic efficiency of 40%, while detonation has a thermodynamic efficiency of 42% [12]. This potential increase in thermodynamic efficiency is one of the main drivers behind the current research into PDEs. The other main attraction of PDEs is the fact that they can potentially operate with no turbomachinery and very few other moving parts such as valves. This makes them potentially cheap to manufacture and run with increased reliability.

Unlike the engine technologies that it is expected to replace, the Pulse Detonation Engine Cycle is unsteady. It shares more with the internal combustion engine cycle than with current aerospace propulsion technologies, and the only PDE engine to have been used on an aircraft to date (to the author's knowledge) was an internal combustion engine modified for detonation (Figure 1.4) [13]. The cycle (Figure 1.5) can be broken down into the following stages:

Figure 1.5: PDE Engine Cycle [14]

1. Fill – with air and fuel
2. Initiation – directly through a strong spark, through DDT or another novel method
3. Combustion – the detonation wave propagates along the combustion chamber
4. Propagation – the high-pressure combustion products fill the chamber.
5. Exhaust/Purge – the exit of the combustion products draws in fresh air.

Due to the unsteady nature of the cycle, it is necessary for an engine to have several combustion chambers in order to provide a consistent thrust.

1.2.3 Integration into aircraft

When compared to other current aerospace engine designs (Fig 1.1), it can be seen that the usable flight envelope of PDEs goes from static to around Mach 4, wider than any other air-breathing technology. This makes it an attractive alternative to combined engines such as those used on the SR-71 Blackbird for high-speed flight [15]. PDEs have also been investigated for orbital applications with an on-board oxidiser [16]. This leads to the possibility of PDEs being used in launch vehicles, with atmospheric air used as the oxidiser before switching to the on-board oxidiser when necessary.

Although the above may not seem relevant to the current aerospace industry which is dominated by subsonic transport aircraft, PDEs can either be used instead of, or as a modification to the gas turbine engine. The first design, which would be more suited to military-type applications, would be to replace the gas turbine engine entirely with a multi-tube PDE. Similar to a turbojet, the engine would provide thrust through the momentum of the exhaust products. There would be no need for any turbomachinery, significantly improving the weight, cost and life of the engine.

The second method would be to uses pulse detonation combustors in addition to, or as a partial replacement for gas turbines, potentially more suitable for the civil aerospace industry. The combustors could be mounted in the bypass section of a HBR turbofan, providing additional momentum to the bypass air supplementing the effect of the fan, or pulse detonation combustors could be used to replace the standard combustion chambers and some of the turbomachinery. This method would allow the advantages of detonations and HBR turbofans to be utilised.

1.2.4 Technological Issues

With all the research and development undertaken over the past two decades, two favoured methods have emerged for initiation of detonations: the predetonator and Deflagration-to-Detonation Transition (DDT).

The predetonator concept involves igniting a small charge of highly reactive fuel-air mix, for example hydrogen-oxygen, so that it detonates. This detonation then transfers into the main detonation chamber where the less reactive main fuel-air mix detonates, providing thrust. This method suffers from the fact that at least two fuels need to be used and potentially two oxidisers. For an aircraft, carrying gaseous fuels and/or oxidisers is problematic as to the low energy density of gases has volumetric and structural implications. Also, carrying additional oxidisers is detrimental to the overall propulsive efficiency of the aircraft as measured by Specific Thrust (I_{sp}) (Figure 1.1), so is avoided.

DDT involves initiating a deflagration (normal slow combustion) in the main combustion chamber. The flame then accelerates due to turbulence provided by obstacles placed in the chamber – orifice plate or, more usually, a spiral. This method is not ideal as the obstacles in the flow disrupt the filling and purging process and reduce the momentum of the combustion products (which provide the thrust) by introducing a drag force.

As alluded to above, aircraft operate on liquid fuels due to the difficulties of carrying gaseous fuels. The current fuel of choice for the aviation industry, both civil and military, is the hydrocarbon blend kerosene. Kerosene contains longer chain hydrocarbons than gasoline (typically 6-16 carbon atoms compared to 4-12) and is less reactive, which makes it safer to transport. So that the liquid fuel is able to react efficiently with the gaseous air oxidiser, the fuel is sprayed into the airflow. The spray increases the surface area of the fuel for improved combustion and evaporation. Current spray technologies are not able to generate sprays suitable for use in detonations for reasons discussed in Chapter 2.

These combustion related problems – detonation initiation, fuel preparation and fuel-air mixing – are the motivation behind this thesis entitled "***Investigating the Fundamentals of Liquid-Fuelled Pulse Detonation Engines***".

1.3 Aims and Objectives

1.3.1 Aim of Thesis

The aim of this thesis is to explore mechanisms inhibiting practical operation of liquid-fuelled Pulse Detonation Engines (PDEs) and to appraise the effectiveness of innovative solutions.

1.3.2 Objectives

- Investigate the current knowledge in detonations, explore the current state of PDE technology and investigate technological obstacles to a practical PDE.
- Design, commission and characterise an experimental facility suitable for conducting studies into gaseous and liquid fuelled detonation initiation though shock focussing.
- Experimentally investigate Shock-Wave initiation of detonations in gaseous fuel/air mixtures through shock focussing to provide a benchmark for liquid-fuelled systems.
- Simulate the problem of fuel/air mixing for an industrial PDE prototype and propose improvements as a precursor to liquid fuel mixing studies.
- Analyse the phenomenon of droplet breakup to benefit the experimental study into Shock-Wave initiation of detonations in liquid fuel/air mixtures.
- Experimentally investigate Shock-Wave initiation of detonations in liquid fuel/air mixtures.

1.4 Structure of Thesis

Chapter One is a general introduction to this thesis.

Chapter Two provides a phenomenological description of detonation including: an introduction to the models of detonation, the structure of the detonation front, the effects of confinement, initiation modes including deflagration-to-detonation transition and information regarding detonation with liquid fuels. The chapter concludes with an introduction to pulse detonation

engines, their operational cycle and some of their issues. This explains the focus behind the rest of the work in this thesis.

Chapter Three introduces the theory behind shock waves and presents the design considerations required for design of a shock tube. The Chapter describes the bespoke shock tube designed, built and commissioned to study detonation initiation in gaseous and liquid fuels in subsequent Chapters.

Chapter Four utilises the shock tube designed and built in Chapter Three to study its operation in non-reactive flows. This work is then used in subsequent Chapters to identify and quantify the phenomena associated with combustion in gaseous and liquid fuels. The Chapter presents empirical relationships that describe the non-ideal operation of the shock tube more accurately than the ideal theory presented in Chapter Three.

Chapter Five presents the first combustion results obtained with the shock tube designed in Chapter Three. It utilises the results from Chapter Four to identify and quantify combustion events. The Chapter describes the results obtained from stoichiometric mixtures of propane-air and hydrogen-air. Propane is used as a comparator to kerosene to investigate the detonation potential of liquid kerosene without the associated problems of mixing and droplet breakup. Hydrogen is used due to its detonability and to benchmark the shock tube against other design variants.

Chapter Six describes the studies undertaken on single-droplet breakup phenomenon to aid the liquid fuel detonation studies in Chapter Seven. The Chapter begins by describing the previous work undertaken on droplet breakup in constant and pulsed/shocked flows. It presents high-speed, high quality videographic images of the breakup process, and moves on to quantify the post-breakup spray in both constant and pulsed flows.

Chapter Seven builds on Chapters Three, Four, Five and Six by studying the detonation initiation of liquid kerosene spray in the shock tube. It presents the results of the experiments undertaken and presents possible reasons for the results obtained. It suggests improvements to the shock tube which would improve the quality of data obtained.

Chapter Eight presents the results of numerical simulation of an air-fuel mixing valve from a prototype liquid fuelled pulse detonation engine. The study evaluates previous simulations undertaken to aid design of the valve and builds on this work by addition of a gaseous fuel to better understand the mixing characteristics of several different versions of the valve. It concludes by making recommendations on how the design of the valve could be improved.

Chapter Nine draws together the conclusions from each of the previous Chapters and suggests areas for further study.

Chapter Two

Detonations and Pulse Detonation Engines

2.1 Introduction

This Chapter discusses detonations and Pulse Detonation Engines (PDEs) leading to a justification of the work programme. The first part of the chapter will introduce detonations and the development of their understanding since the beginning of the 20th Century. It will give a phenomenological description of detonation and outline the most utilised theories then go on to discuss detonation initiation and detonation of liquid fuels, as well as outlining issues with detonation confinement and the structure of the detonation front. The second part of this chapter discusses technical problems associated with PDEs. After a brief discussion on some system-level problems, the main problems associated with combustion, detonation initiation, fuel-air mixing and liquid fuel preparation are discussed. This leads onto a justification for the rest of the work in this thesis.

2.2 Detonations

Detonation is a form of combustion that differs from deflagration, which is the more common form of combustion. In detonation, the detonation front consists of a shock wave and a reaction zone coupled together. The shock front raises the temperature and pressure of the reactants to a point where they react in the reacting zone. The energy produced by the reacting zone enables the shock front to propagate. Table 2.1 shows the change in properties across a detonation front compared to a deflagration front.

Table 2.1: Comparison of Detonation and Deflagration [17]

Deflagration	**Detonation**
Velocity Increases	Velocity Decreases
Pressure Decreases Slightly	Pressure Increases (due to shock wave)
Temperature Increases	Temperature Increases (more than for deflagration)
Density Decreases	Density Increases

2.2.1 The Chapman-Jouget Model

The Chapman-Jouguet Model (C-J Model) is the simplest model that represents detonations. It was proposed independently by Chapman [18] and Jouget [19]. The model is not physically accurate, however it predicts the detonation velocity well and in the absence of a simple, 3D model, it is still widely used to estimate the properties of a detonation. However, its predictions of pressure and density are 10-15% higher than those seen by experiment [20].

The C-J model assumes a planar shock front followed by a heat addition zone behind the shock. It does not take into account the amount of time taken to release energy in the chemical reaction following the shock; it assumes that all the energy is added instantaneously.

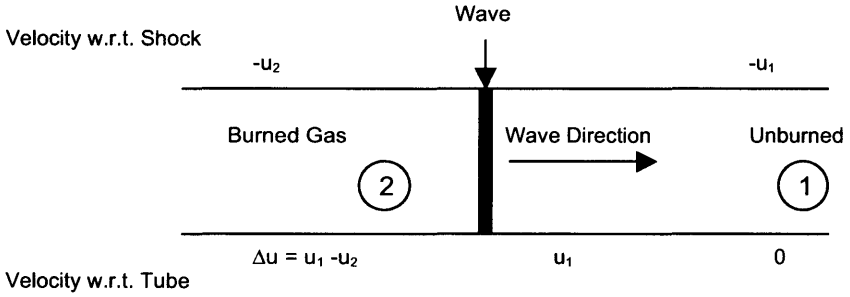

Figure 2.1: Propagation of a Detonation Wave

The velocity of the burned gas, Δu, is given by:

$$\Delta u = u_1 - u_2$$

$$\Delta u = \left(\left[\frac{1}{\rho_1} - \frac{1}{\rho_2} \right] * [P_2 - P_1] \right)^{\frac{1}{2}} \qquad \text{Equation 2.1}$$

The C-J model uses the Rankine – Hugoniot equation as its basis. The Rankine – Hugoniot equation is an equation which describes a disturbance propagating in a flow, such as a shock wave, but can also be used to describe combustion and its two forms (i.e. deflagration and detonation).

The Rankine – Hugoniot Equation is:

$$e_2 - e_1 = \frac{1}{2}(P_2 - P_1)*\left[\frac{1}{\rho_1} - \frac{1}{\rho_2}\right] \qquad \text{Equation 2.2}$$

The Rankine – Hugoniot Curve is the plot of P_2 vs. $\frac{1}{\rho_2}$ for set values of $(e_2\text{-}e_1)$, P_1 and ρ_1. The values of P_1 and ρ_1 (the upstream conditions) are plotted on the curve as Point A. If no energy is released (i.e. $e_2\text{-}e_1 = 0$), then the curve will pass through A. This is the curve for a shock wave. For a system where energy is added, the curve is displaced in the positive y direction, with the amount of displacement proportional to the amount of energy added to the system.

On the graph, the region where $\frac{1}{\rho_2} > \frac{1}{\rho_1}$ and $P_2 < P_1$ represents Deflagrations (Regions IV and V), $\frac{1}{\rho_2} > \frac{1}{\rho_1}$ and $P_2 > P_1$ represents non-physical solutions (Region III), and $\frac{1}{\rho_2} < \frac{1}{\rho_1}$ and $P_2 > P_1$ represents Detonations (I and II).

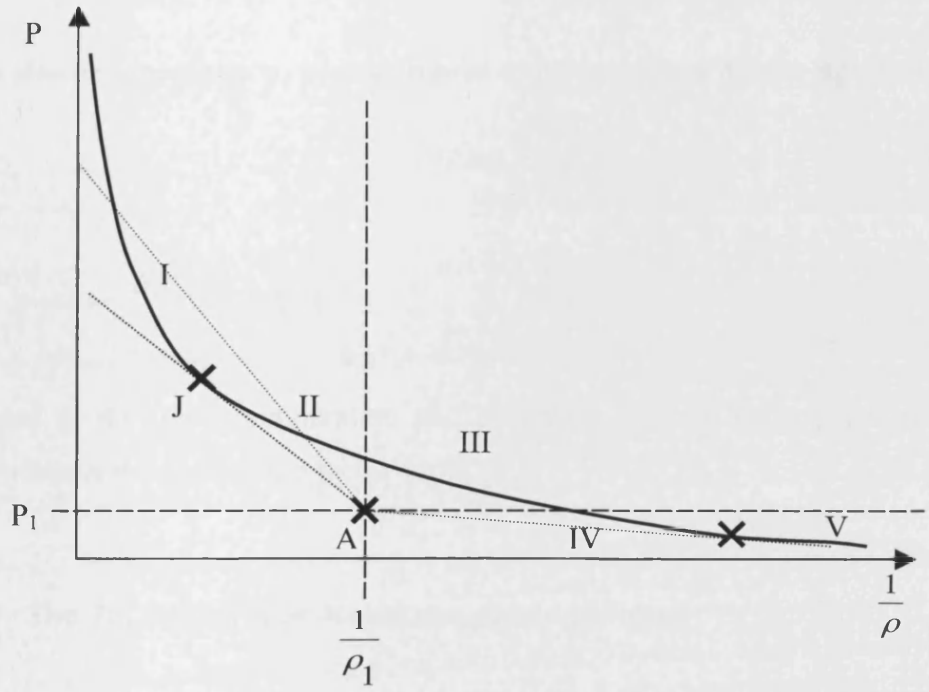

Figure 2.2: Rankine – Hugoniot Equation for C-J Model

Point J is the only stable solution for detonations. This point is the tangent to the Rankine – Hugoniot Curve that passes through A. All other rays that come from A intersect the curve twice, suggesting that there are two possible solutions. For the possible solutions below J (Region II), the entropy is lower than the corresponding solution above J. During combustion, the products will tend to the state with the highest entropy. This means that solutions in Region II are thermodynamically improbable. For points above J (Region I), the speed of sound is greater than the speed of the detonation wave. This means that any disturbances will travel faster than the detonation wave and catch it up causing P_2 and ρ_1 to decrease, moving the solution to J. Therefore, points in Region I are possible, but not stable. All detonations in this zone will tend towards Point J.

At J, u_1 is at its minimum, and it can be shown that it is equal to the sum of the speed of sound in the products and the speed of the burned gases w.r.t. the tube, i.e.:

$$u_1 = a_2 + \Delta u \qquad \text{Equation 2.3}$$

This is the Chapman-Jouguet hypothesis.

It can also be shown that u_1 is proportional to the inverse of the average molecular weight:

$$u_1 = \mu\sqrt{\frac{\gamma_2 R_0 T_2}{MW_2}} \qquad \text{Equation 2.4}$$

where: $$\mu = \left(\frac{1}{\rho_1}\right) * \left(\frac{1}{\rho_2}\right)$$

Changes to the initial temperature and pressure do not affect u_1, it is the average molecular weight that is the controlling factor for u_1 [17].

2.2.2 The Zel'dovich, von Neumann, Doring Model

As already stated, the main flaw with the C-J model is how it deals with energy release. The Zel'dovich [21], von Neumann [22], Doring [23] (ZND) model is an addition to the C-J model which does not assume that energy release happens instantly after the shock, but after a slight delay and at a finite rate. This delay is equivalent to the chemical induction time, i.e. the time

taken for enough radicals to form to initiate the reaction, and then the reaction proceeds at a finite reaction rate. All energy is added before the sonic plane, which is the plane behind the shock whose velocity is sonic w.r.t. the detonation front.

This model also uses Rankine – Hugoniot curves in a similar way to the C-J model. The shock is a region of high temperature and pressure corresponding to the shock travelling in a non-reactive gas. The high temperature and pressure causes the reaction to start and it continues in the reaction zone until all the reactants are exhausted. Each part of the reaction zone will have its own Rankine – Hugoniot curve, so the whole reaction will be represented by an infinite number of Rankine – Hugoniot curves.

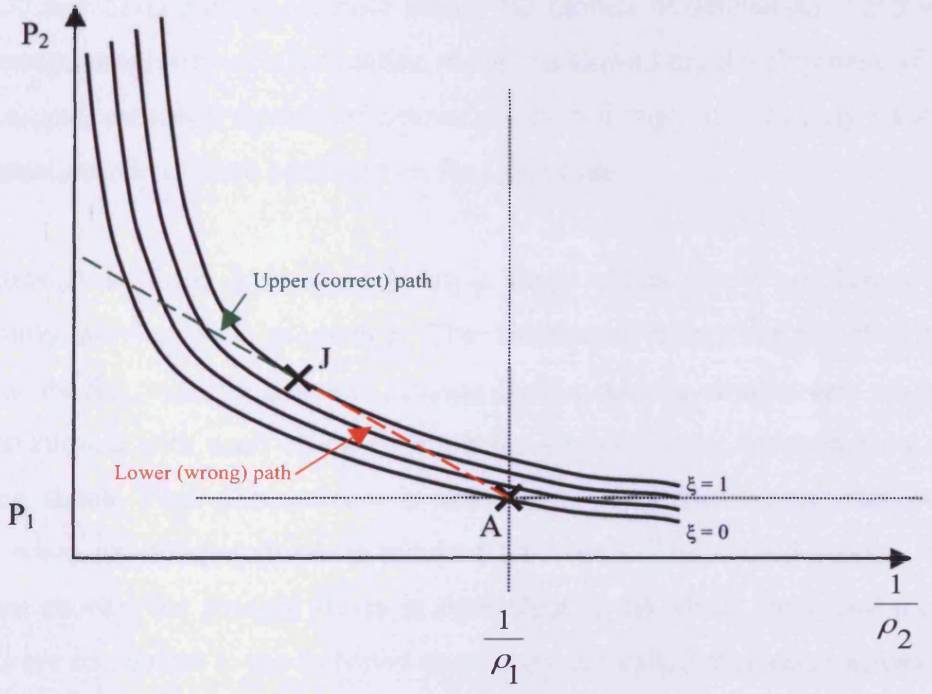

Figure 2.3: Rankine – Hugoniot Equation for ZND Model

$\xi = 0$ is the plane of unreacted gas (i.e. just downstream of the initial shock)
$\xi = 1$ is the plane of complete reaction (i.e. the sonic plane)

Using the tangent to $\xi = 1$ that passes through A (the initial conditions), it can be seen that there are two possible paths between $\xi = 0$ and $\xi = 1$. $\xi = 0$ represents the position just after the leading shock which has higher pressure and density than the sonic plane. This corresponds to the upper path from $\xi = 0$ to $\xi = 1$. The lower path starts off with the conditions equal to those upstream of

the shock (i.e. the conditions before and after the shock are the same), so this solution is not physically correct.

Therefore, when a detonation shock passes through a reactive gas, pressure and density initially increase as they would for a shock passing through an unreactive gas, then they decrease in the reaction zone as the reaction proceeds, while at the same time the temperature increases due to the energy released in the reaction.

2.2.3 Detonation Front Structure

The C-J and ZND models are both steady 1D models of detonation. Their success in predicting the average properties of a detonation wave has slowed the development of full theoretical three dimensional, unsteady models of detonation even though the unsteady three-dimensional nature of detonation waves have been known for some time.

The detonation front, instead of being a single shock wave, consists of many shock waves constantly moving and interacting. The detonation front consists of alternating curved and straight shocks, with "backward" running shocks running downstream of the front. The curved shocks interact with each other, forming the straight shock between them and the backwards-running shock. This phenomenon is similar to "Mach Reflection" that occur in non-reactive flows when an oblique shock is incident on a wall. The curved shocks are equivalent to the incident shocks, the straight shock is equivalent to the Mach Stem, and the backwards-running shocks are equivalent to the reflected shocks and are called transverse waves.

Figure 2.4: The Nature of the Detonation Front [20]

Figure 2.4 shows blast waves from a series of exploding wires. The structure of the interaction of the different blast waves produces a structure similar to that in the detonation front, with incident waves, Mach stems and transverse waves.

The separate blast waves can be seen in the first two pictures. In the third picture, the waves are beginning to overlap each other and interact. In the forth picture, the "wave front" consists of parts of the original blast waves, and normal shocks between them. Waves can also be seen coming from the intersection of the original blast waves and normal shocks, running "backwards".

Fluid that passes through the incident shocks will also pass through the reflected shock, while fluid that passes through the Mach stem will not pass through either of the other shocks. The slipstream defines the boundary between the fluid that has passed through the incident/reflected shocks and the Mach stem.

The point of interaction of the three shocks is known as the triple point. It is the projection of this point, i.e. the slipstream sheet, which produces the famous "fish-scale" patterns that have been seen on sooted plates, and that gives rise to the "cell size" measure of detonability that is also widely used. As the detonation proceeds, the triple points move so that the Mach stem becomes longer and the incident shock becomes smaller. At a certain point, two triple points, and therefore transverse waves, will collide. This re-energises both of the transverse waves and reverses their direction. Now what was the incident shock becomes the Mach stem, and vice versa.

The collision of the transverse waves leaves a high-pressure region behind the new Mach stem and the waves propagate towards the new (weaker) incident shocks. The figure below shows the cell structure with the movement of the shock waves and regions of burning superimposed.

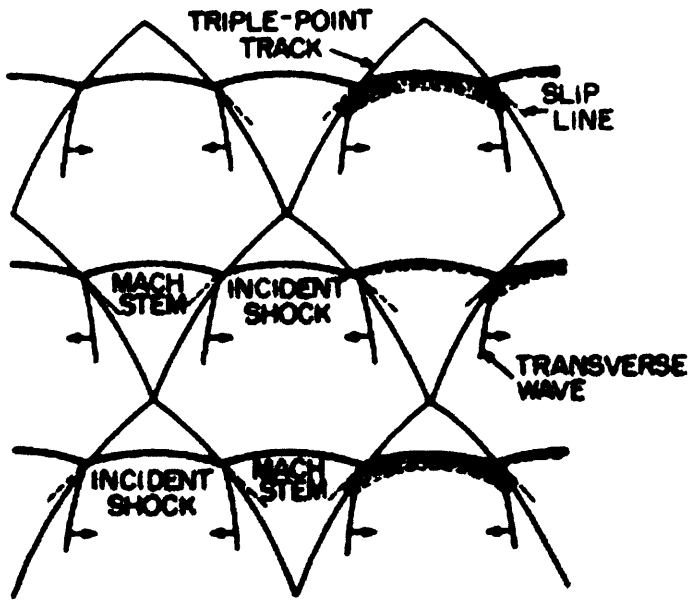

Figure 2.5: Schematic of the Detonation Front [20]

Thus, the detonation front is a transient structure. It is continuously decaying and being re-energised by collisions of the transverse waves.

2.2.4 Detonations and Confinement

The majority of detonation research has been carried out in confined volumes due to the inherent risks of unconfined detonations. The confinement geometry has a significant effect on the structure of the detonation, and in fact whether a detonation occurs at all.

In general, to obtain a stable detonation, the width of the confining geometry must be greater than the cell size of the mixture being detonated to allow a stable detonation to form. Therefore, the cell size is a lower limit on the size of a geometry that can support a detonation in the said mixture.

Changes in the confinement of a detonation are important for Pulse Detonation Engines, especially those designed with a predetonator. The detonation must be able to transit from the smaller predetonator to the larger main tube without failing.

Several authors have reported that to transit a detonation from a circular tube to an unconfined volume, the diameter of a circular tube must be at least 13 times the cell width for the mixture concerned while for a planar channel, the ratio must be at least 10 [24].

When moving from a smaller confined volume to a larger confined volume, the picture is not quite so clear. When considering circular tube, the diameters of the smaller and larger tubes and the ratio between them are all important. This is due to the fact that the detonation is maintained by the interaction of the triple points and the wall. When the triple point encounters a wall, it is reflected and reenergised in a similar way to when it encounters another triple point (Section 2.2.3). Therefore, when the detonation front moves into a larger volume, the end triple point now has further to go before it is reenergised. This weakens the detonation at this point. Also, as the triple point next to it has not been reenergised as it normally would, this part of the detonation also becomes slightly weaker. This continues all along the detonation front. Therefore, for the detonation to transmit successfully from one tube to another, the detonation must have sufficient energy to overcome change in radius. This loss of energy also explains why the detonation front curves when it goes from a smaller volume into a larger one – the drop in energy means that section of the detonation front is travelling more slowly than the main detonation.

The use of a gradual change in diameter from the smaller tube to the larger one has been shown to aid the transmission of the detonation [25]. This gradual change in the confinement geometry allows the end triple points to re-energise. It has been shown that the more gradual the change in geometry, the more likely the detonation will successfully transmit into the larger cone [26].

2.2.5 Detonation Limits

Detonations, in a similar way to flammability limits in deflagrations, have lean and rich boundaries past which the detonations will not propagate. In general, detonation limits are narrower than flammability limits. However there are so many factors that influence the limits that it is difficult to define general limits. Some of the factors that have been found experimentally to affect the detonation limit include, but aren't limited to: initial temperature, pressure and density; confinement; initiation and chemical composition (e.g. equivalence ratio). Different measurement techniques can also give different results [27]. A further complication is that a weak ignition source can initiate a detonation via DDT in a sufficiently long tube.

2.2.6 Blast (Strong Shock/Direct) Initiation

Direct initiation of detonations can only occur when a strong shock is generated by a strong source (e.g.: a solid explosive; exploding wire) and this shock has a certain strength and duration. When a detonation is initiated in this way, the initial shock and detonation shock combine to form a single shock which travels at approximately the detonation velocity.

When high explosives are ignited in a reactive mixture, it is possible that the detonation starts in the way stated above. However, it is also possible that a small piece of unburnt high explosive is propelled into the reactive mixture which then ignites due to the elevated temperature and pressure in the reactants (from combustion and the shock wave), and detonation then starts from this point, not the main ignition.

2.2.7 Deflagration to Detonation Transition (DDT)

If an explosive mixture is ignited in an open tube, a deflagration will propagate along the length of the tube. The wave may accelerate slightly, but it is unlikely that it will form a detonation within a reasonable distance.

If the same mixture is ignited in the same manner at the closed end of a tube with one end open and one end closed, the explosion will start off as a deflagration and then accelerate into a detonation wave.

In a deflagration, the density of the products is significantly less than the reactants. As the products expand, a compression wave travels at the speed of sound through the reactants, raising their temperature. As the new (now hotter) reactants react and expand, another compression wave is generated which travels slightly faster than the previous one due to the increase in temperature (and therefore Mach number) of the reactants. All of the waves tend to catch up to the first one and coalesce forming a shock wave. The increase in temperature also causes the combustion wave (flame) to accelerate. This causes the reactants to accelerate to a point where they become turbulent. This further accelerates the reactants to a point where the shock is strong enough to ignite the reactants that pass through it. The reaction zone behind the shock continues to send out

compression waves which sustain the detonation. This is known as Deflagration to Detonation Transition (DDT).

The DDT length is the distance that is required for the deflagration to undergo transition into a detonation, or in other words, the distance that the shock is formed from the ignition source. The DDT length can be affected by many factors including, but not limited to: overall chemical composition (e.g. equivalence ratio); tube characteristics (such as surface roughness); ignition characteristics (intensity and duration of energy deposited) and initial pressure, temperature and density.

2.2.8 Detonations and Liquid Fuels

The majority of research work into detonations has been carried out in a single phase – i.e. with a gaseous fuel and gaseous oxidiser. This is due to the difficulties in obtaining a homogeneous mixture of liquid fuel and gaseous oxidiser required when attempting to study the fundamentals of detonation. As mentioned in Section 1.2.4, PDEs designed for use in aircraft require liquid fuels, specifically the use of those already in use by the aviation industry is desirable. This has lead to an increase in the research on liquid fuelled detonations recently. However, the importance of liquid fuel detonations had been recognised before the current renewed interest in PDEs, as demonstrated by the review paper by Dabora from 1979 [28].

Early work on two-phase (heterogeneous) detonations used droplet sizes of the order of 1mm. They found that the velocity of the detonation wave was less than the C-J velocity, and it was found that the smaller the droplet size, the smaller the velocity deficit [29]. Cramer [30] suggested that mechanical shattering of droplets was required to produce enough sub 10μm droplets and fuel vapour to sustain detonation. Thus, it was realised that liquid detonations are more complex than a shock wave followed by heterogeneous burning as was first thought, and that factors such as droplet breakup, droplet size and the presence of fuel vapour were also important [31].

A theoretical analysis by Borisov et al [32] concluded that for droplets larger than 10μm evaporation and burning alone could not sustain detonation, i.e. for droplets larger than 10μm, droplet breakup must occur to sustain detonation. Therefore for droplets larger than 10μm, a

velocity deficit compared to ideal C-J velocity will be present. This appears to be the basis of the currently held goal of 10μm fuel droplet size in PDEs.

Bowen et al [33] found that for droplets of 2μm, the process of transition to detonation was similar to that for gaseous detonations. They also found that the detonation velocity increased with increasing tube diameter, implying energy losses to the wall were important. However, Bull et al [34] found that there was a velocity deficit for unconfined liquid detonations even with small droplets. They also found that high-vapour-pressure fuels are much easier to detonate than low-vapour-pressure fuels. This suggests that some fuel vapour must be present for a liquid fuel to detonate.

Work done by Brophy et al [35] shows that PDEs can operate using JP-10 with both O_2 and air. For JP-10/O_2, detonation was observed with a droplet size of 10μm. However, for JP-10/air, the required droplet size fell to 3μm and the fuel vapour content had to be 70% for detonation to occur. The corresponding inlet temperature was 375K. At 425K JP-10 is fully vaporised.

Austin and Shepherd [36] conducted single shot experiments with JP-10 vapour to find average cell widths using exploding wire initiation. They varied several parameters including nitrogen dilution and initial pressure. They found that the cell size increased with increasing dilution and with decreasing pressure. They also found that the cell widths of JP-10 vapour and air were similar to propane and air at about 60mm. This suggests that propane can be used to test PDE designs. They also investigated the affects of thermally cracking JP-10 with both O_2 and air. They found that for cracking with O_2, the cell size reduced by about half, while with air the cell size remained almost constant.

Ciccarelli and Card [37] also conducted experiments with JP-10 vapour, but they investigated the effect of initial temperature and fuel fraction. They used a standard automobile spark to initiate a deflagration then used orifice plates to accelerate the flame. They initially found that detonation did not occur at a pressure of 1 atm for any temperature tested. This could be due to the initiation method as Austin and Shepherd [36] managed to get a detonation at 1 atm, and the cell size they measured was smaller than the tube sized used by Ciccarelli and Card [37] (60 mm cell size compared to 10 cm inner-diameter tube). They found that for temperatures above 528 K, autoignition occurred, providing an upper limit for the initial temperature.

Their main conclusion is that the rich limit for detonation is unchanged over the temperature range tested (373 K – 528 K). The lean limit rose from 1.1% JP-10 for 373 K to 1.25% for 528 K (the stoichiometric mixture is equivalent to 1.5 % JP-10). They state that the cell size is constant, within experimental error, with changing temperature. Their other main conclusion is that at 2 atm and 528K, the cell size for JP-10/air is similar to that of propane/air.

2.3 Pulse Detonation Engines

As discussed in Chapter I, the development effort for PDEs has been high over the past 10-15 years. Despite this, as far as the author is aware, there are currently no flight-ready PDEs with the only PDE flown being a modified internal combustion engine [13]. This suggests that although much progress has been made towards a flight-ready PDE, much is left to do. From the vast number of journal articles and conference proceedings as well as the many Patents obtained, several main areas of research interest appear prevalent. These main areas appear to be detonation initiation, noise, vibration and fatigue, liquid fuel preparation, valves, nozzles, system integration, engine and total system efficiency and fuel-air mixing.

2.3.1 System-Level and Combustion-Level Technical Issues

It is possible to split the main research problems into two groups: system level problems and combustion level problems. Those that fall into the system level group include: noise, vibration, fatigue, valves, nozzles, system integration, and engine and total system efficiency. Those that fall into the combustion level group include fuel-air mixing, liquid fuel preparation and detonation initiation.

2.3.2 System-Level Technical Issues

As the categorisation above suggests, these problems have less to do with combustion and its directly associated processes, and more to do with the overall engine – the engine's performance and integration into the aircraft. Although providing solutions to these problems is very important to allow a PDE-powered aircraft to fly, focus on these problems appear somewhat redundant if the combustion process is not operating correctly.

However, these problems do in fact provide an input into the combustion level problems. For example, the development of tools to calculate the system efficiency of a PDE allows comparisons of a particular design against current technologies, enabling developers to understand the amount of development still required. Alternatively, the tool can be used in a reverse fashion to find the performance required from the combustion system to match the performance of current technologies. Additionally, system integration requirements in terms of size (engine length) have forced engineers to come up with innovative ways of reducing DDT lengths.

The unsteady nature of PDEs, coupled to the high pressure and temperatures obtained during detonation are likely to cause significant problems for engineers. Detonation chamber materials will likely require specialist materials to cope with the demands placed on them. However, it has been found that the load experienced by the containing walls can vary considerably (between 0.5 and 4 times the dynamics pressure experienced) depending on the acoustic properties of the chamber [38]. Additionally, the other sub-systems in the engine (such as the fuel subsystem, electronics, valves and turbomachinery) will need to be robust enough to withstand the vibrations caused by the engine and the rest of the aircraft (wings, main body) will need to be isolated from the vibrations as this will impose additional strength requirements on these parts of the aircraft, and for passenger transport aircraft will likely cause discomfort to the passengers.

2.3.3 Liquid Fuels in PDEs

As discussed in Section 2.2.8, a liquid fuel-air mixture with large droplets leads to a decrease in the velocity of the detonation front compared to the vapour fuel-air case. For a PDE, this will lead to a decrease in the thrust generated. In order to eliminate this velocity deficit, the liquid fuel droplet sizes need to be in the region of 3-10μm for kerosene-based fuels [35].

Although the reliable use of a liquid fuel has been demonstrated in a prototype PDE [39], the fuel used was heptane which is much more volatile and reactive then kerosene, thus easier to detonate. The difficulty of detonating liquid kerosene has led to studies investigating the possibility of breaking down the fuel in the engine. This process would produce smaller hydrocarbon chains which are then easier to detonate, and can be achieved either chemically or thermally.

Although it has been shown experimentally that kerosene can be degraded thermally to a more detonable mixture, the temperature required (over 600°C, although better results were obtained at 1000°C) and the long residence time required (30 seconds) [40] suggests it would be difficult to apply this to a practical system, as proved to be the case [41]. However, work continues as synthetically generated blends have shown that the detonation cell size may reduce by as much as 50% [36].

Work is continuing on improving the detonability of kerosene by increasing the surface area or altering the chemistry of the fuel to inject the fuel directly into the detonation chamber. However, one well known research group is following internal combustion engine design by using a carburettor type device to mix the fuel and air before it enters the detonation chamber [11].

2.3.4 Detonation Initiation in PDEs

As outlined in Section 1.2.4, two main initiation methods have emerged for pulse detonation engines – pre-detonators and DDT, and, as is to be expected, both methods have advantages and disadvantages.

With a pre-detonator system, a detonation is not originally initiated in the main combustion chamber, but in a smaller, ancillary chamber, the pre-detonator, which feeds into the main chamber. The pre-detonator contains a highly reactive fuel mix, such as the main fuel and oxygen, or air and a reactive gaseous fuel such as hydrogen [42]. The detonation is initiated in the tube, usually directly as opposed to via DDT (Sections 2.2.6 and 2.2.7), and the detonation moves out from the pre-detonator into the main detonation chamber. The transition between the pre-detonator and the main detonation chamber is very important (as mentioned in Section 2.2.4), as poor design may cause the detonation to fail during this transition. As also previously mentioned in Section 1.2.4, the need to carry an additional gaseous fuel for the pre-detonator system causes difficulties in aerospace applications due to the volume and structural strength required.

For systems initiated via DDT, no additional chamber is required – the detonation begins as a deflagration then the flame is accelerated to detonation through the use of turbulence. Although several unusual turbulence generation devices have been proposed [42], the two most prevalent

devices are orifice plates, and the so-called Schelkin Spiral (actually a helix). Although DDT initiation removes the problems with fuels and additional oxygen of pre-detonators, the method has its own problems. The presence of the turbulence generating device, which is vital for the method to work, causes drag in the flow, reducing the velocity of the detonation front and the combustion products – resulting in a reduction in thrust [43]. Additionally, the force experienced by the turbulence generators from the detonation process can result in the failure of the device – as

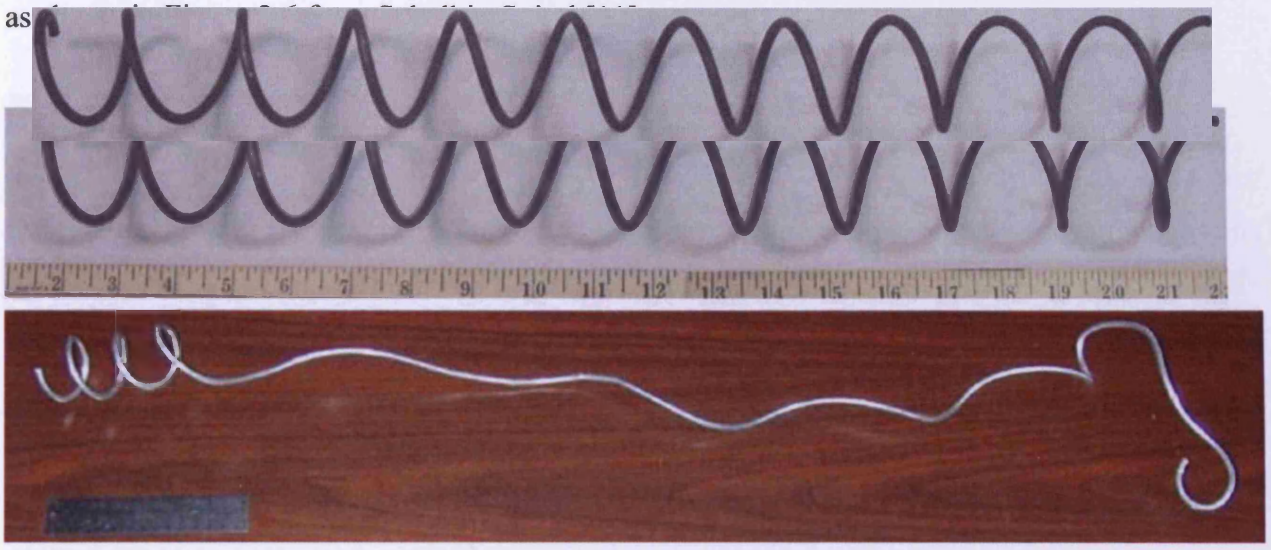

Figure 2.6: Damage Caused to a Shelkin Spiral [11]

The inherent problems with these two methods has led to the investigation of many novel initiation methods including shaped detonation tubes which promote DDT without turbulence generating inserts [44], the use of interacting shock waves/ supersonic streams of reactants [45-47] and, for multi-tube PDE, the use of one detonation tube to initiate detonation in another. Considering the aim of this thesis to Investigate Liquid-Fuelled PDEs and Section 2.3.3, the concepts behind this final method are discussed further here.

The design reviewed [48] describes a device where the combustion products of one detonation chamber are directly into a second combustion chamber by a rotating valve at the exit of the chambers. The second chamber has been filled with fresh reactants, and the interaction of the reactants from the second chamber and the hot combustion products from the first chamber causes a detonation to form.

Extending this idea, instead of transmitting the combustion products between chambers, it may be possible transmit the detonation shock wave between the two chambers. This would potentially remove the need for initiation and the associated problems when the PDE is running.

Transmission of a detonation would be tricky for the geometric and mixing reasons described above. It would be much easier to design a system where the detonation "failed" in the transmission tube between the two chambers. This would leave a shock wave travelling into the second chamber. Using the design detailed above, the shock wave would then travel "upstream" relative to the engine until it reached the end wall of the detonation chamber where it would be reflected, potentially causing a detonation to form.

2.3.5 Fuel-Air Mixing in PDEs

Detonations, similar to deflagrations, are sensitive to the concentration of the fuel-air mix through which they propagate. It has been shown that a detonation moving through a fuel-air mix is affected by changes in fuel concentration both normal and parallel to the direction of propagation. In the case of concentration gradients parallel to the direction of travel, for hydrogen-air mixtures it has been shown that the for a detonation to move through a concentration gradient, the gradient must be relatively gentle. For sharp gradients, the likelihood of the detonation failing is high [49].

For gradients normal to the direction of propagation, experiments with hydrogen-oxygen mixtures have been conducted [50]. These experiments have shown that a concentration gradient will reduce the velocity of the detonation, delay DDT initiation of the detonation and cause curvature of the detonation front.

This problem has been demonstrated in practice by the difficulty of obtaining a fuel air mix suitable for detonation in a prototype PDE engine [51].

2.4 Justification of the Work Programme

From the published work reviewed, liquid fuel preparation, fuel-air mixing and detonation initiation are three major contributing factors to the delay in producing a flight-ready PDE. As mentioned in Section 2.3.4, a possible method of initiating detonations in a multi-tube PDE is to use the detonation wave from one detonation tube to initiate the detonation in another. It is possible to design the engine so that the detonation wave is made to fail during the transition from the first tube to the second to form a shock wave. If the shock wave was introduced at the

end of the detonation chamber, it could be used to prepare a fuel-air mix for detonation propagation by breaking up larger fuel droplets.

In order to test this hypothesis experimentally, a new experimental facility is required, in the shape of a shock tube, that will allow investigation of detonation initiation through reflected shock waves. The facility should be able to support detonations of liquid kerosene and gaseous fuels such as propane that can be used to commission the new facility and allow comparison to other published work. A work programme is also required to investigate the breakup of liquids in pulsed flows to assess the ability of shocks to prepare liquid fuels for detonation. Finally, an investigation into mixing processes is required to confirm the ability to for a homogeneous fuel-air mixture within the confinements of a PDE.

2.5 Summary

This Chapter has introduced detonations and Pulse Detonation Engines. It has discussed the two most common detonation models – the Chapman-Jouget Model and the ZND Model. The assumptions of the two models have been discussed with their success in predicting the detonation phenomenon. The use of the Rankine-Hugnoit Equation for detonation modelling has also been introduced.

The three-dimensional, unsteady nature of the detonation front has been presented; the triple-point has been defined in terms of detonation front structure, along with the other transient shocks that constitute the detonation front. The discussion of the detonation front structure has lead onto a discussion on the affects of confinement on detonation, the minimum cross sectional area required to support detonation and how the detonation reacts when the confinement is altered, specifically when the cross sectional area is increased.

After a brief discussion on detonation propagation limits, the initiation of detonation have been presented in terms of the two initiation mechanisms, direct initiation and deflagration-to-detonation transition. A detailed phenomenological description is presented for DDT. The section concludes by introducing the problems associated with detonating liquid fuels in air and the losses associated with large fuel droplets. It presents a criterion for the propagation of a

detonation in a liquid fuel-air mix where the detonation propagation velocity is the same as it is for the vapour case.

The second part of the chapter discusses pulse detonation engines and introduces two different categorisations to the technical problems present – system level and combustion level. System level problems have been defined as those technical issues which are overtly to do with the performance of the propulsion system and its integration into the airframe. Combustion level problems have been defined as those technical issues that directly affect the combustion process.

The combustion-level problems discussed were detonation initiation, fuel-air mixing, and preparation of the liquid fuel so that it can support detonation propagation. The criterion for detonation propagation in liquid kerosene has been reiterated, and some novel methods for improving the detonation properties of liquid kerosene have been discussed.

The two main methods of detonation initiation in PDEs – the use of a predetonator or DDT – have been presented. The practical difficulties associated with both methods have been highlighted. An alternate method of detonation initiation, based on previously published work, has been presented.

The importance of fuel-air mixing has been highlighted by presentation of experimental studies demonstrating the sensitivity of detonations to changes in fuel-air mixture concentration. Concentration gradients both normal and parallel to the direction of propagation of the detonation front have been shown to be detrimental to the detonation.

The chapter concluded with a practical justification for the work programme chosen.

Chapter Three

Shock Wave Theory and Shock Tube Design

3.1 Introduction

This Chapter builds on the justification of the work programme given in Chapter Two by introducing the phenomenon of shock waves and their practical application in a shock tube. The idealised theory associated with shocks in a shock tube, as well as the theory behind generating the shocks is presented. This theory is used during the design of the new bespoke Shock Tube, which is then used in Chapters Four, Five and Seven to fulfil the aims of this thesis to investigate the future use of kerosene based fuels in flight operational PDEs.

3.2 The Simple Shock Tube

A shock tube is a device which produces a planar shock wave by the almost instantaneous release of high-pressure gas into lower pressure gas. The high and low-pressure sections are separated by a diaphragm, which is burst to "fire " the shock tube and produce the shock wave (Figure 3.1). After the diaphragm is burst, a shock wave travels into the low-pressure section with velocity v_1 suddenly increasing the pressure, and a rarefaction (or expansion) wave travels into the high-pressure section, gently decreasing the pressure, as shown in Figure 3.2.

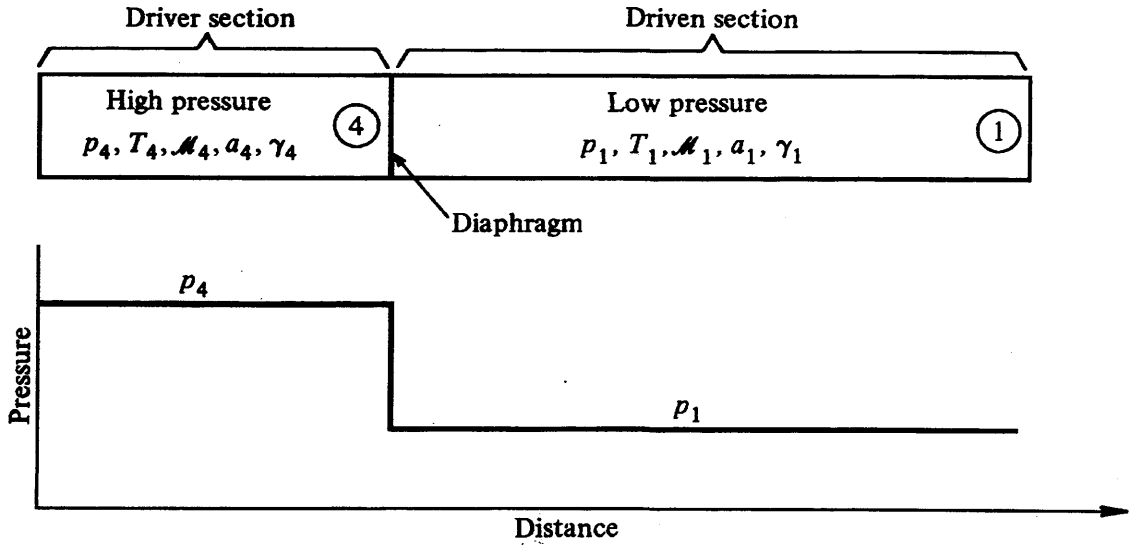

Figure 3.1: Shock Tube Pressure Initial Condition [52]

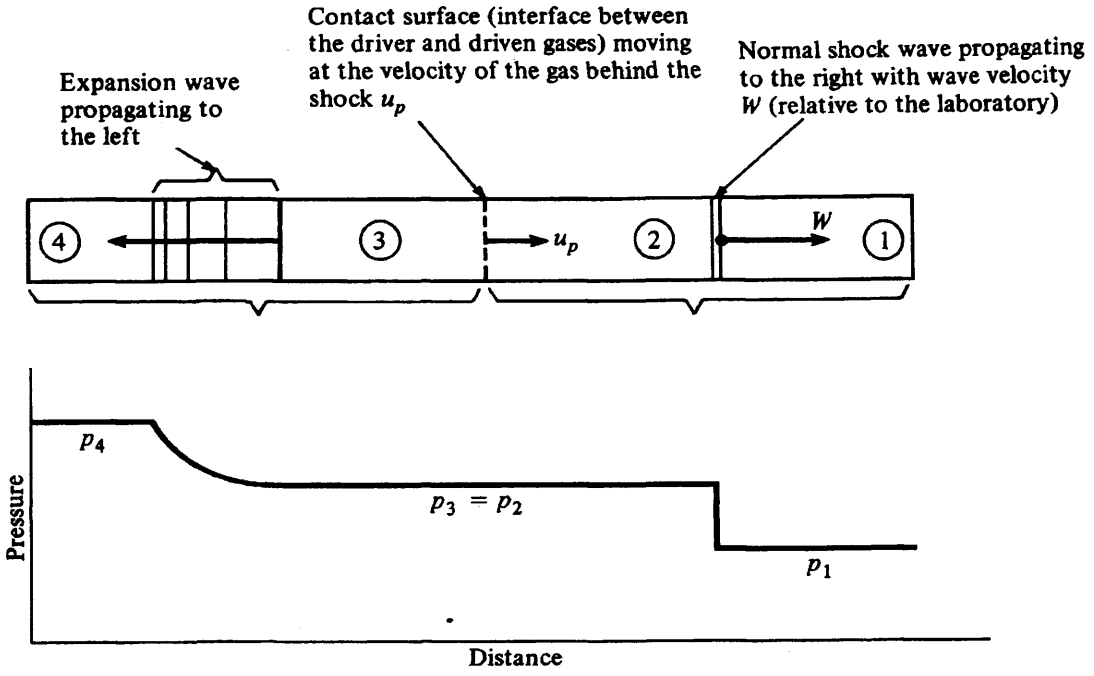

Figure 3.2: Shock Tube Pressure Operational Condition [52]

Region 1 in Figure 3.1, Figure 3.2 and subsequent discussions in this thesis is the low-pressure region which has not been affected by the shock wave. The conditions in this region are detonated by the subscript 1 – e.g. pressure = P_1. Region 2, denoted by the subscript 2, is the region of gas from the low-pressure section which has experienced the shock wave. Region 3, denoted by the subscript 3, contains the gas from the original high-pressure section which has been expanded to the post-shock pressure by the rarefaction wave, and Region 4, denoted by the subscript 4, contains gas at the original elevated pressure. Regions 2 and 3 are separated by the Contact Surface, which is the interface between the gas from the driver section and the gas from the driven section. The pressure and gas velocity are constant across the contact surface.

If the shock tube is closed, the shock wave generated will reflect from the end wall. The reflected shock wave, which travels with velocity v_5, is of the precise strength to reduce the gas velocity in Region 2 to zero – necessary due to the zero velocity boundary condition caused by the reflecting end wall. This is depicted in Figure 3.3 and Figure 3.4, where Region 5, denoted by the subscript 5, is the zero-velocity region between the reflected shock wave and reflecting end wall.

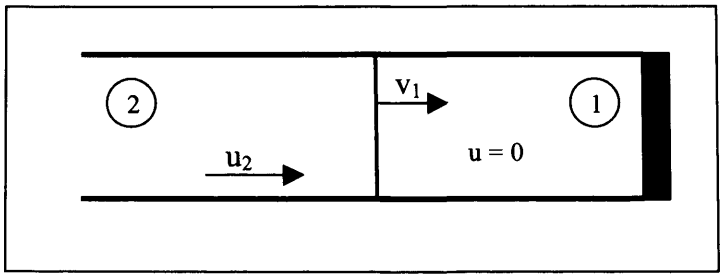

Fig 3.3: Shock Tube Incident Shock Wave

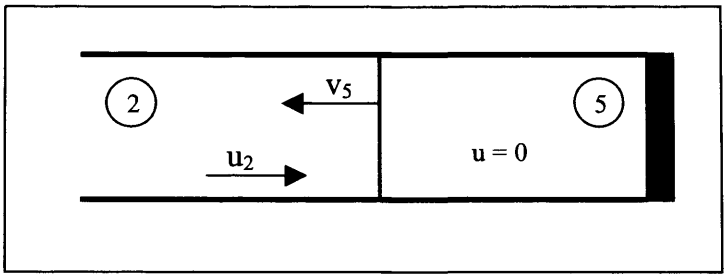

Fig 3.4: Shock Tube Reflected Shock Wave

3.3 Ideal Shock Waves

A shock wave is a disturbance caused by an object or by fluid moving at a speed faster than the speed of sound in the local medium. For example, take the case of a sphere travelling in air. If the sphere is travelling slower than the speed of sound – i.e. the flow is subsonic, the air is "warned" about the presence of the sphere by disturbances travelling upstream of the sphere. These disturbances, which travel at the speed of sound, prepare the flow before the arrival of the sphere and change the upstream flow properties. If the sphere is travelling faster than the speed of sound – i.e. the flow is supersonic, the air is not warned about the presence of the sphere. This leads to very rapid, almost instantaneous, changes in flow properties when the sphere does arrive. This very thin, non-isentropic region where these flow property changes take place is called a Shock Wave. The shock wave increases the downstream pressure, temperature and density of the flow, but reduces its velocity.

3.3.1 Ideal Shock Wave Theory

Although the shock waves created in shock tubes are unsteady – i.e. the flow properties depend on time as well as position – the steady shock wave theory is still applicable.

The speed of sound in a gas depends only on the gas and the temperature of the gas and is given by Equation 3.1. The Mach number of a Flow is the ratio of the local particle velocity to the local speed of sound as shown in Equation 3.2. For a Steady Normal Shock, it can be shown that the post shock Mach Number, M_2, and the pressure ratio across the shock depend only on the upstream Mach Number M_1 and the gas composition as shown in Equation 3.3 and Equation 3.4.

Equation 3.1

$$M = \frac{u}{a} \qquad \text{Equation 3.2}$$

$$\frac{p_2}{p_1} = \frac{2\gamma M_1^{\,2} - (\gamma - 1)}{\gamma + 1} \qquad \text{Equation 3.3}$$

$$M_2^{\,2} = \frac{(\gamma - 1)M_1^{\,2} + 2}{2\gamma M_1^{\,2} - (\gamma - 1)} \qquad \text{Equation 3.4}$$

Equations 3.3-3.4 are derived assuming an ideal gas. Rigorous derivations can be found in Anderson [52] and Gaydon & Hurle [53] and so are not reproduced here. For ease of use, the above equations are published in tabular form, the most common being for air at standard atmospheric conditions and are commonly referred to as the "Normal Shock Tables".

For the reflected shock, relationships can be derived for the pressure and ratio in terms of the incident Mach number M_1, and for the ratio of reflected wave speed to incident shock wave speed in terms of the pressure ratio $\frac{p_1}{p_2}$. Equations 3.5-3.6 are reproduced from Gaydon and Hurle [53]. Kinney and Graham [54] publish similar equations for Pressure and Temperature ratios for blast waves in air, but, in the author's opinion, they are more cumbersome to use. They do however derive an equation for the Reflected Shock Wave Mach Number, which in the notation used here is given by Equation 3.7.

$$\frac{p_5}{p_1} = \left[\frac{2\gamma M_1^{\,2} - (\gamma - 1)}{\gamma + 1}\right]\left[\frac{(3\gamma - 1)M_1^{\,2} - 2(\gamma - 1)}{(\gamma + 1)M_1^{\,2} + 2}\right] \qquad \text{Equation 3.5}$$

$$\frac{v_5}{v_1} = \frac{2 + \left(\frac{2}{\gamma - 1}\right)\left(\frac{p_1}{p_2}\right)}{\frac{\gamma + 1}{\gamma - 1} - \frac{p_1}{p_2}} \qquad \text{Equation 3.6}$$

$$M_5^2 = \frac{2\gamma M_1^2 - (\gamma - 1)}{(\gamma - 1)M_1^2 + 2}$$ Equation 3.7

3.3.2 Driver Pressure Ratios

The strength of the shock wave formed when the high pressure section is released can be shown to be a function of the ratios of the pressure and sound speed of the driven and driver sections [52, 53]. Equation 3.8 can be derived using slightly different methods and presented in slightly different but equivalent ways. The version that the author found most useful to this discussion was that presented by Anderson [52]:

$$\frac{p_4}{p_1} = \frac{p_2}{p_1}\left\{1 - \frac{(\gamma_4 - 1)\left(\frac{a_1}{a_4}\right)\left(\frac{p_2}{p_1} - 1\right)}{\sqrt{2\gamma_1\left(2\gamma_1 + (\gamma_1 + 1)\left(\frac{p_2}{p_1} - 1\right)\right)}}\right\}^{-\frac{2\gamma_4}{\gamma_4 - 1}}$$ Equation 3.8

This shows that the required driver/ driven section pressure ratio (hereafter referred to as the driver pressure ratio) is dependent upon the shock pressure ratio, i.e. the shock strength, and the ratio of sound speeds of the two sections.

By examining Equation 3.8 two important conclusions can be drawn. First, a stronger shock requires a higher driver pressure ratio. Second, increasing the speed of sound in the driver section compared to the driven section will reduce the required driver pressure ratio. An increase in the speed of sound of the driver section can be achieved in two ways: either by increasing the temperature of the driver section compared to the driven section and therefore increasing T in Equation 3.1 above, or by using a gas with a lower molecular weight, usually Helium or Hydrogen in order to increase R in Equation 3.1.

3.4 Shock Tube Design

The shock tube was commissioned to look at liquid fuel detonation as described in Chapter Two, and more specifically the detonation of aviation kerosene. The cell size of JP-10 jet fuel vapour (a military grade of aviation kerosene) in air has been found to be equivalent to that of propane in air i.e. around 50-60mm [36, 55]. Therefore, to allow detonation to occur, it is important that the diameter of the shock tube is greater than this figure to allow sufficient detonation cells to form [20]. Austin and Sheppard [36] conducted detonation experiments with JP-10 in a 280 mm shock tube, while the work of Ciccarelli and Card [37] was conducted in a shock tube with an internal diameter of 100 mm. A shock tube of 280 mm diameter would not be representative of potential PDE engines, as the size would prohibit a multi-tube design. However, a detonation chamber internal diameter of 100 mm is more likely to translate to a multi-tube PDE, as shown by the PDE prototype engine obtained be Cardiff University (as discussed further in Chapter Eight. Therefore, the diameter of the shock tube was set at the nominal figure of 100 mm.

The maximum operating pressure of the shock tube was designed as a compromise taking into account the static pressures required in the driver section, the dynamic pressure peaks caused by detonation and the maximum working pressures of available off-the-shelf components.

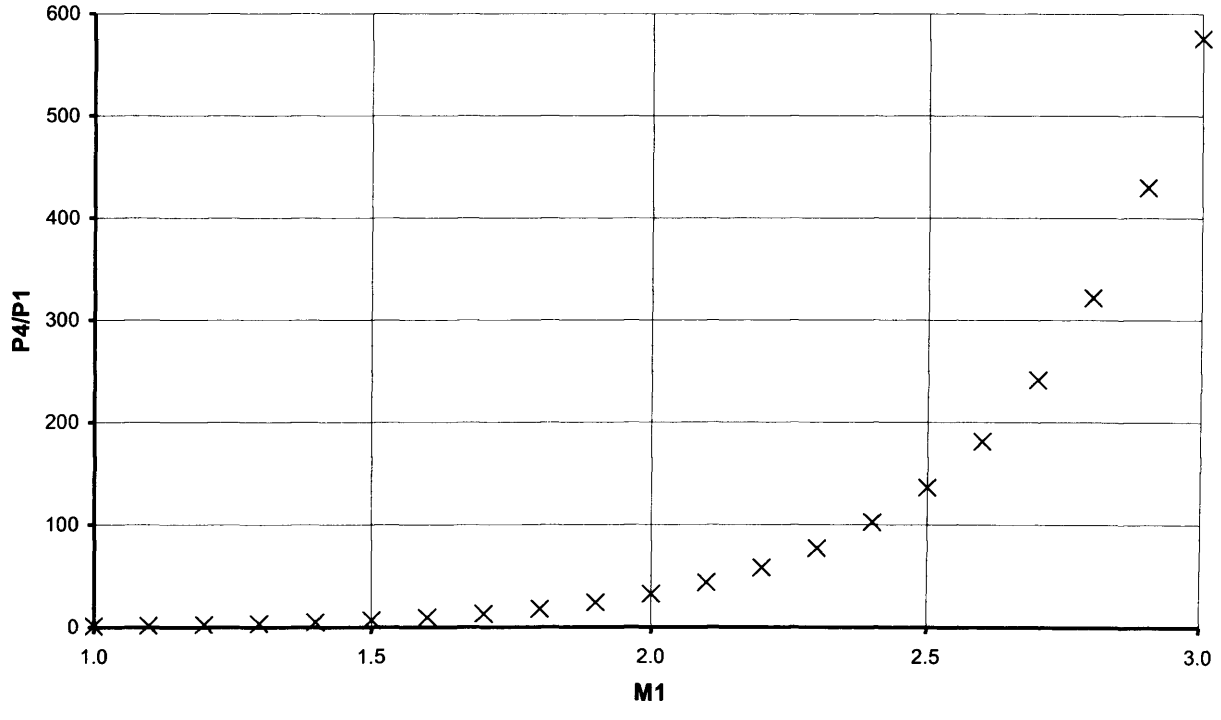

Figure 3.6: Theoretical Driver Pressure Ratio vs. Shock Mach number

As shown in Equation 3.8, the higher the driver section pressure ratio, the stronger the shock wave generated. Therefore, it is desirable to have the maximum possible driver pressure to give the strongest shock. However, the shape of the curve in Figure 3.6 (plotted using Equation 3.8 for a N_2 driver section and air driven section) shows that there is a diminishing rate of return with higher driver pressures. For example, $P_4/P_1 = 43$ would give a shock of $M_1=2.2$, $P_4/P_1 = 103$ gives $M_1=2.4$, while $P_4/P_1 = 183$ gives $M_1=2.6$.

The shock tube was manufactured in stainless steel for its strength and corrosion properties, specifically "marine" grade 316. The corrosion resistance of this grade of stainless steel would allow potentially corrosive fuels (e.g. hydrogen) to be used without the potential of weakening the shock tube or affecting its internal surface finish. After considering different classes of stainless steel pipes and flanges, ASME Schedule 80 was chosen for the pipe, and ANSI Class 600 for the flanges. At room temperature, ASME Schedule 80 pipe has a maximum working pressure of 173 Bar, and ANSI Class 600 flanges have a maximum working pressure of 100 Bar. This sets the maximum working pressure for the shock tube at 100 Bar, giving a maximum shock of $M_1=2.35$ at a test pressure of 1 bar. In order to comply with insurance conditions, the completed shock tube was pressure tested to 150 bar, giving it a certified working pressure of 100 Bar.

The shock tube (Figure 3.7) was designed in three different sections – a high-pressure driver section, a low-pressure "run-up" section, and a test section (which together are called the driven section). The shock tube used by Ciccarelli and Card [37] had a length of 6.2 m, however, this was of a different configuration and had no driver section. Dean et al [56] use reflected shocks in their work, but their shock tube has no driver section. Instead it uses a "high pressure valve with forced start" for the driver section, with a driven section length of 5.5 m. From these two designs, and as the Schedule 80 pipe was only available in 6m lengths, the driven section of the shock tube was set at a length of 6m – 5m for the run-up section and 1m for the test section. The shock tube used by Aberystwyth University Physics Department [57] for autoignition work had a diameter of 64mm, a driver length of 3m and a driven length of 3.75m. The ratio of driven section length to driver section length is 1.25 – which if applied to the 6m driven section length already chosen gives a driver length of 4.8m. For simplicity, the driver section length was chosen as 5m based on the above argument.

Flanges were welded onto the end of each of the sections to enable the sections to be bolted together and a blank flange was bolted to each end of the 11 m shock tube. In order to seal the joints, o-rings seals were used as gaskets are known to be prone to leakage when a dynamic internal pressure is applied. A double o-ring arrangement was used which consists of an o-ring and groove on each flange. The o-rings had different diameters so that when the flanges were bolted together, the o-rings sealed on the opposing flange face and not on each other.

Port holders were placed onto the shock tube at several locations to allow entry and exit of gas and use of pressure sensors to characterise the shock and combustion inside the tube. The ports were designed to be interchangeable so that the layout could be modified for future experiments. Two port holders were placed on the driver and run-up sections (in-line), and four on the test section (three in-line and one at right angles).

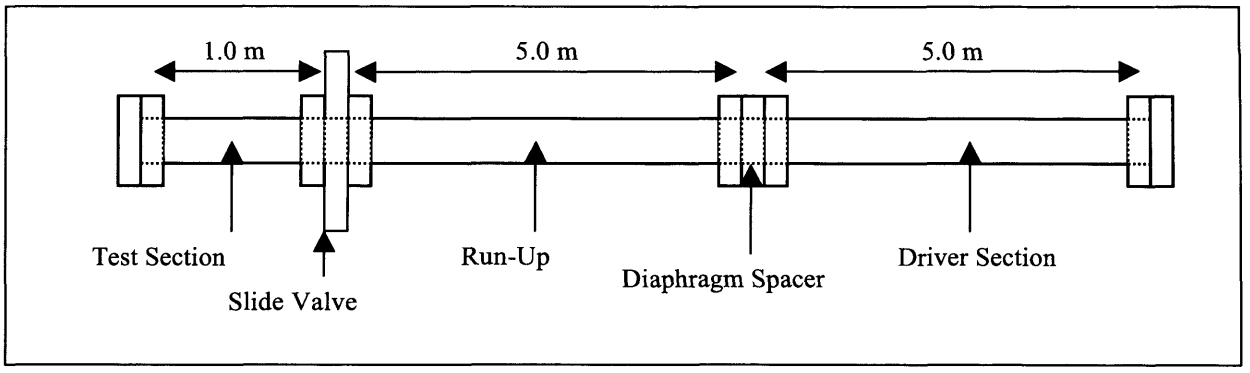

Figure 3.7: Shock Tube Schematic

3.4.1 Isolation of Test Section

To avoid diffusion of the Fuel-Air-Mixture (FAM) from the test section into the run-up section, a method is required to isolate the two from each other whilst maintaining the internal continuity of the tube. If the FAM diffuses from the test section into the run-up section, or air diffuses from the run-up section into the test section, the fuel concentration will not be exactly as mixed. If the FAM diffuses all the way up the test section, causing the entire run-up section to be a lean FAM, there is the possibility of a galloping detonation forming which could cause high dynamic pressures [58]. Three possible solutions were considered: an off-the-shelf ball valve; a bespoke sliding valve or a diaphragm.

At first glance, an off-the-self ball valve appeared the easiest option. The internal diameter of the valve could be specified so that the internal diameter of the shock tube remained constant. However the cost of such a valve is prohibitively expensive.

The use of a diaphragm was also a relatively easy option. The diaphragm would need to hold the pressure differential between the test section and run-up section, which would be limited to the absolute pressure used in the test section. The diaphragm would be burst by the generated shock wave as it hits the diaphragm. This was an inexpensive way of keeping the two gases apart. However, fitting a fresh diaphragm between the two sections for every test meant that the shock tube would have to be split at this point for every test, and therefore the two sections would need to be realigned correctly for every test, which would be extremely difficult given the blockage caused by the diaphragm. Also, the presence of the diaphragm would have interfered with the Shock wave by introducing obstacles into the flow altering the Shock Wave, and probably causing shock reflections off the diaphragm. Therefore, this was not considered a suitable solution.

The third option involved designing a sliding valve. This idea had been employed previously in a shock tube at Aberystwyth University Physics Department [59]. No detailed design was available, but the principle of the design was that a slider would float between two thick plates on o-rings. The slider would have a hole in it, which would be aligned with the internal bore of the Shock Tube to "open" the valve, and moved out of alignment to "close" the valve. When the valve was closed, the o-rings would seal on a solid portion of the slider, so that gas could not travel/diffuse between the two sections.

The Slide Valve was seen as the best solution taking into account cost, ease of use and maintaining experimental reliability and repeatability.

The two stainless steel "thick" plates were 12mm thick. This thickness was chosen as it appeared to be the best compromise. Any thicker and the plates became unnecessarily expensive, any thinner and the plates would likely bow when machined. The "slider" was made from 3mm thick stainless steel sheet (Figure 3.8a). This thickness was the minimum that would be able to take the forces required to open and close the valve without buckling.

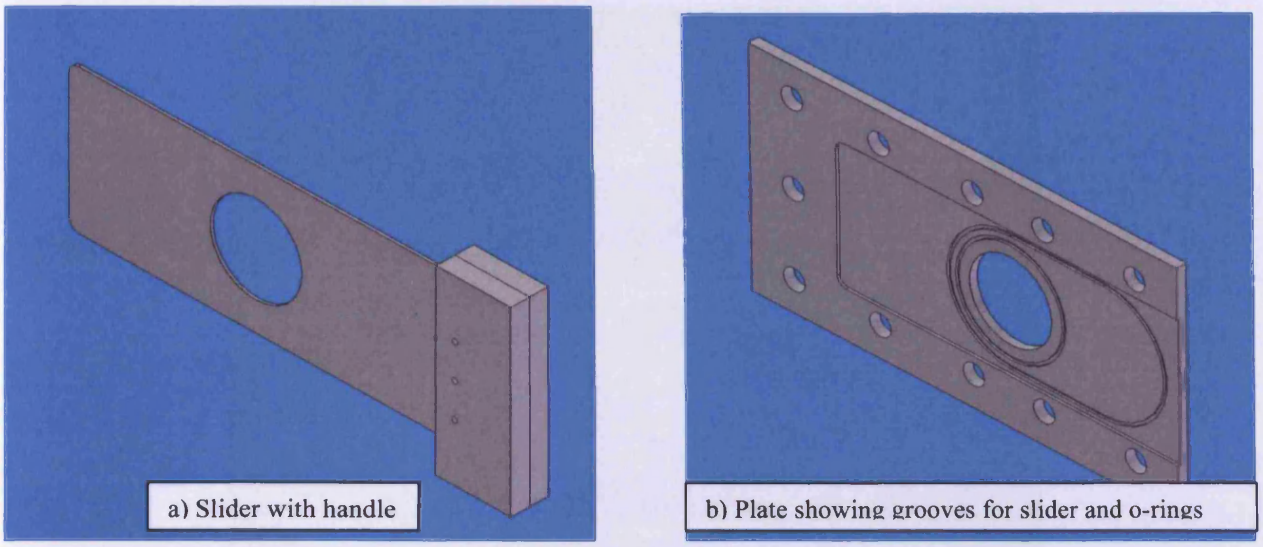

Figure 3.8: Side Valve Components

To seal between the slider and the valve plates two o-rings were used on each side. The first o-ring sealed immediately around the hole in the slider and valve plate, with the second sealing around the hole in the slider in both the open and closed positions as shown in Figure 3.8. This meant that as well as the two sections being isolated from each other, the valve isolated the gas inside the shock tube from the atmosphere during operation of the slide valve, making the shock tube suitable for use with more hazardous materials.

To accommodate the slider in the valve plates, a groove was machined into one of the plates (Figure 3.8b). In the initial design, grooves were cut into both of the plates so that the slider was exactly in the middle of the valve. However, it was realised that this would result in unnecessary set-up and machine time, therefore, cost, so the design was revised. The groove was specified so that it was 0.2mm wider than the slider to give enough clearance for the slider to move freely, while not exposing too much of the o-rings. O-rings with a cross sectional area of 3mm were used, however the grooves were made deeper than recommended by the British Standard at 2.8mm. This reduced the compression on the o-rings, so that it would be enough to seal but not so much that the slider was clamped into position by drag from the o-rings. In order to reduce friction on the o-rings during sliding further, they were lightly greased with a silicon-based lubricant and the slider was electro-polished by MPE Limited, Hirwaun. This process is the opposite of electro-plating and provides a very smooth "mirror" finish. The completed valve is shown in Figure 3.9, attached to the shock tube, with the slider "closed" so the test section and run-up section are isolated from each other.

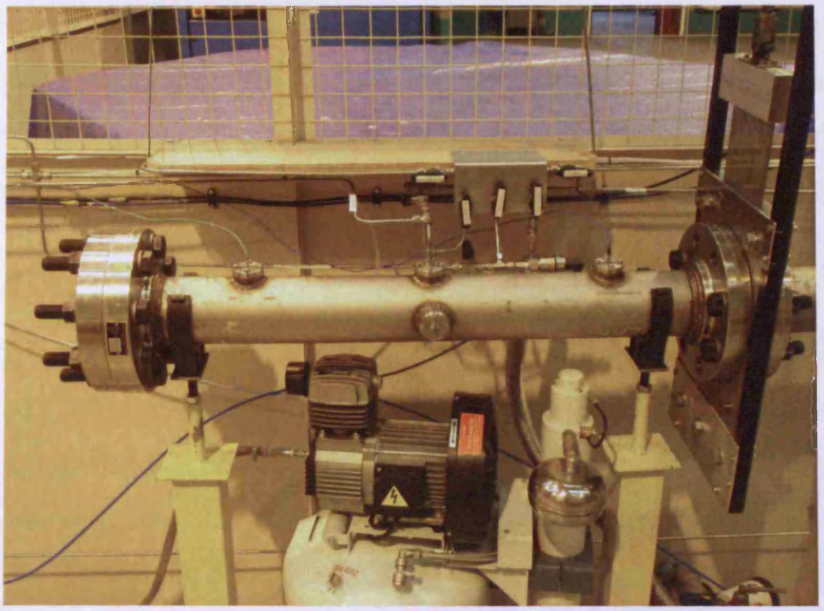

Figure 3.9: Shock Tube Test Section showing Sliding Valve on the right hand side

A simple aluminium handle was made for the slider, which was then modified to accommodate the pneumatic operating system. This system consisted of a pneumatic piston, attached to a frame which was bolted to the slide valve. Both sides of the piston were attached to a low-pressure compressor, so that the valve could be opened and closed remotely.

3.4.2 Producing Reliable Shock Waves

In order to produce repeatable shocks, it is advisable to have a controlled method of releasing the driver pressure. Although through experiment the diaphragm bursting pressures were found to be consistent (Section 3.4.6), there is still some natural variation (up to 7%). To overcome this, the driver pressure should be below the burst pressure of the diaphragm(s) with an added margin of safety, and an artificial method of bursting the diaphragm(s) should be employed.

Two methods were considered. The first involved using a mechanical plunger to burst the diaphragm. A mechanism would need to be designed, probably being spring loaded so that it could be reset easily, which could be set before each test. The shock tube would be filled to the desired pressures and then the device would be "fired", releasing the plunger to burst the diaphragm. The mechanism would need to withstand the pressures in the shock tube, although the inherent dynamic forces present in a shock tube would be more difficult to design for. There would be several sealing surfaces present, including moving ones (e.g. o-ring seals on the

plunger), all of which are additional potential leak points. The mechanism would need to be tested to ensure that it was capable of bursting the required diaphragm thicknesses reliably, and to be designed so that it could be operated remotely to help improve the safety of the operator. This could be done via the use of a solenoid valve, which could then be linked into the DAQ system.

The second would involve the use of two diaphragms, with a spacer gap between – the Double Diaphragm Method (DDM) (Figure 3.10). The spacer would be filled to pressure between that of the driver section and the driven section (intermediate pressure). The diaphragms either side would be strong enough to withstand the intermediate pressure differential, but not the full pressure differential. To fire the Shock Tube, the pressure differential would be increased so that one of the diaphragms burst, leading the other to also burst and release the full pressure.

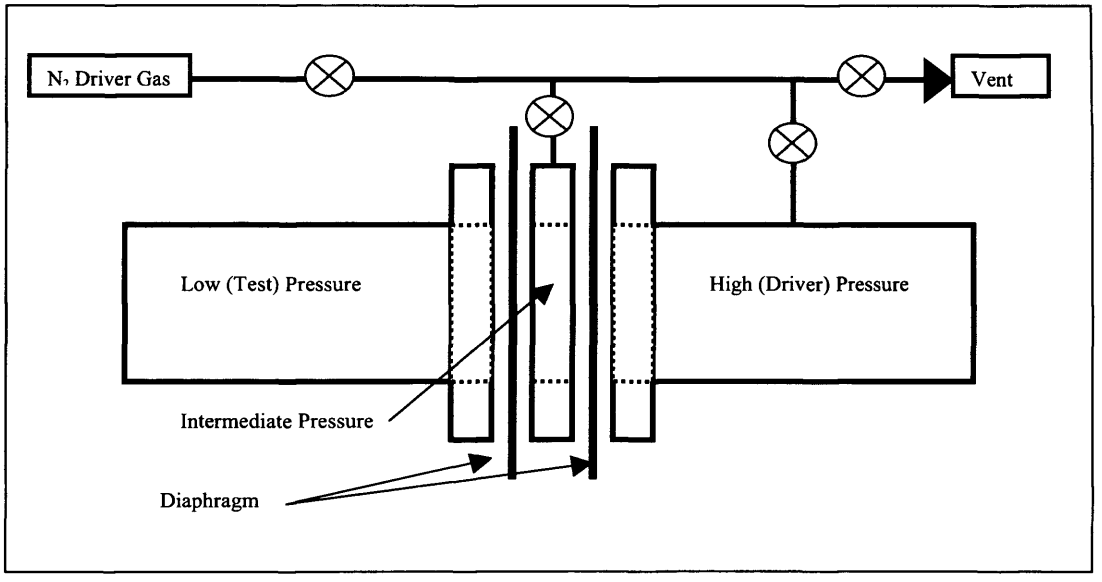

Figure 3.10: Diaphragm Bursting Method

There are two methods to change the pressure differential. The first involves evacuating or venting the intermediate pressure [60] so that the pressure differential between the driver pressure and the intermediate pressure increases, bursting the diaphragms. The second involves equalising the driver pressure and intermediate pressure, thus increasing the pressure differential to the driven section, and bursting the diaphragms. The venting method would mean that some driver gas was being vented off to atmosphere during the run, potentially producing a weaker shock. It would also not be ideal if, in the future, hazardous materials were tested in the shock tube.

The method chosen to control firing of the shock tube was the DDM. This decision was made as it required less design and manufacture of parts, leading to a shorter lead time, and as it was less complicated with less potential failure or leak points. Of the two bursting method for the DDM, the pressure equalisation method was chosen, due to the advantages outlined above.

As discussed the DDM requires a space between the two diaphragms. To make the spacer gap, a blank 4" Class 600lb flange was used. The faces were machined flat, and a centre hole was cut into the flange with a diameter equal to that of the inside of the Shock Tube. O-ring grooves were also cut into the flange faces, so that the faces could seal against the diaphragm material with the use of o-rings.

A remote operating pneumatic valve was used for the DDM so that the shock tube could be fired remotely. The pneumatic valve was connected to the same low-pressure compressor as the sliding valve, and set up in such a way that the shock tube could only be fired when the slide valve was open, reducing the chances of damaging the slider.

3.4.3 Instrumentation and Data Capture

The main parameter which was measured in the shock tube was pressure. However, there were several different "aspects" of pressure that needed to be measured with different ranges, accuracy requirements and characteristic time scales, each requiring its own measurement system.

Firstly, in order to characterise the shock, detonation and combustion waves produced in the shock tube, a method of measuring the dynamic pressure was required. This was done using PCB piezoelectric pressure transducers (model 113B22, shown in Figure 3.11), variations of which have been widely used for this kind of work. These transducers have a maximum pressure range of 340 bar, and a sensitivity of 1mV/psi (0.145mV/kPa) and a resolution of 140Pa (0.001 bar). Two of these transducers were attached to the shock tube via the instrumentation ports described in Section 3.2. In order to power the transducers and log the data, they were connected to a PCB 482A16 signal conditioner.

Figure 3.11: PCB 113B22 Pressure Transducer

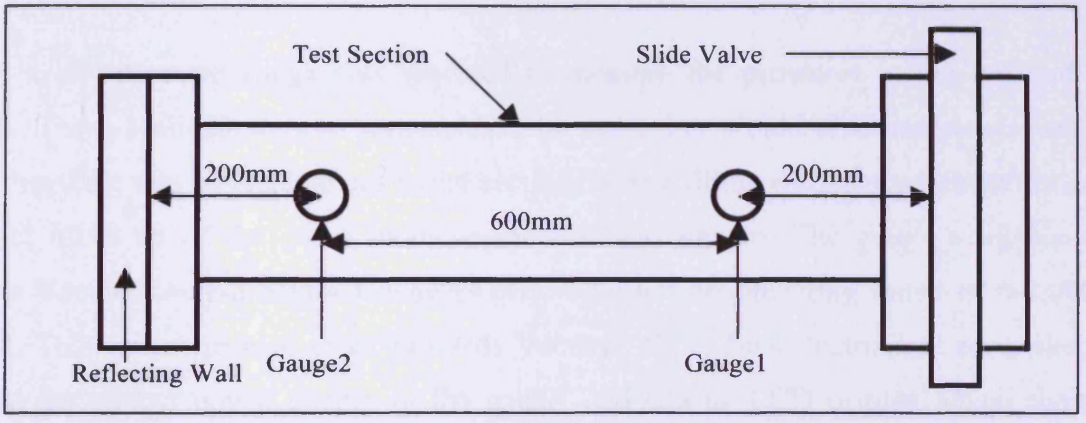

Figure 3.12: Positioning of PCB Pressure Transducers (not to scale)

This signal conditioner provided the correct power, and allowed the signal produced by the transducers to be amplified 1, 10 or 100 times to then be recorded by the DAQ system described below. Unfortunately during the course of experimentation, the signal conditioner failed, so a second, different, signal conditioner was used for the reactive experiments (PCB 482A22) due to availability. This model did not have any amplification, which meant that the noise in the signal from the reactive experiments was much greater than that for the non-reactive experiments. Also, to ensure that the gain difference between the two amplifiers was indeed 10, several non-reactive experiments were carried out using the new signal conditioner to compare the gain to the old signal conditioner. The average gain value came out to be 10.13, so the gain difference was assumed to be 10 to help with ease of calculation.

The signal from the signal conditioner was then read by a National Instruments (NI) PCI-6110 Data Capture Card, via an NI CB-68LP Connector Block. The NI PCI-6110 Data card has a 4-channel, 12 Bit, 5 Million Samples/second/channel analogue input, along with analogue output and digital I/O connectivity. The data was then read and stored by LABVIEW, using a pre-prepared programme available on the NI website [61].

Secondly, to ensure that the driver section was filled to the correct pressure, a static pressure gauge was required on the driver section. Standard 50mm analogue pressure gauges were deemed unsuitable due to the large range of pressures required (5 Bar – 90 Bar) and the reading error inevitably present. Therefore a digital pressure gauge was used, which had a max pressure of 160 Bar, and an error of 0.2% full-scale-deflection. It displayed the pressure to 2 decimal points, and also had an in-built max/min pressure feature, which was useful when determining the diaphragm bursting pressures, as described in Section 3.4.6.

Finally, a low pressure gauge was required to measure the pressures in the test and run-up sections. These sections were at atmospheric pressure, but would also experience vacuum to ensure that there was no residual gas in the sections before filling commenced, therefore ensuring the exact make up of the gases in these sections was known. The gauge available was an Edwards Vacuum Active Strain Gauge (ASG). This has an operating range of 0-2,000 mbar absolute. This was connected to an Edwards Vacuum TIC 3 Head Instrument controller, which provided the correct power supply to the gauge, and had an LCD display which showed the pressure. In order to minimise the affect of any inherent error in the gauge, the same gauge was used for all the low-pressure measurements.

3.4.4 Gaseous Fuel/ Air Mixing

For the gaseous fuel-air combustion experiments, a well mixed mixture was required. The presence of rich or lean pockets of gas would affect the results produced, either causing or quenching the combustion event compared to a fully mixed situation. Due to the design it was not possible to mix directly in the shock tube, so a second vessel was required to act as a pre-mixing chamber. For the hydrogen experimental programme, a completely separate vessel was utilised. This vessel would be filled with sufficient fuel/air mixture to last for 8-10 experiments (or 2-3 days) and left overnight. The filling process was conducted away from the shock tube in a fume cupboard under the guidance of suitably qualified gas handlers. This chamber was required

for two reasons – firstly to minimise the risk of an unexpected hydrogen explosion near the rig, and secondly the Cloud Chamber (as discussed below) was not available at the time of the experiments.

For the propane experiments, a "Cloud Chamber" was available which had been designed and built to produce fully mixed fuel/air mixtures. The cloud chamber was hard wired into position due to the reduced hazard of propane compared to hydrogen and so that mixtures could be prepared easily when required. The chamber was originally designed to produce mono-disperse fuel droplets in air to investigate liquid fuel explosions, but the chamber was easily adapted for gaseous fuel/ air mixtures. The cloud chamber was filled by partial pressures to achieve the required equivalence ratio while fans were running at either end of the chamber to ensure that the fuel/air was fully mixed.

3.4.5 Reflecting Faces

Three different reflecting inserts were manufactured for the reflecting face of the shock tube, a flat face and two concave faces: one conical with a 45° cone angle, and one hemi-spherical. The concave faces are designed to focus the incident shock wave, resulting in easier combustion initiation compared to the flat face.

3.4.6 Diaphragm Characterisation Experiments

Mylar® sheets were used for the diaphragm material. Mylar® is a brand name of DuPont Tejjin Films and is made from the plastic Polyethylene Terephthalate (PET). Several different thickness samples were obtained from the supplier (UK Insulations), and their burst pressures tested. Two thicknesses were chosen from those available– 125μm and 500μm. The burst pressures of these were tested in more detail, the results of which are shown in Table 3.1.

Table 3.1 shows that layering the sheets produces scalable results (i.e. the burst pressure of four 125μm sheets is four times the burst pressure of a 125μm sheet), but increasing the thickness does not (the burst pressure of a 500μm sheet is under three times the burst pressure of a 125μm sheet even though it is four times the thickness). It was found that the average burst pressure for

125μm sheets was 5.25 Bar, and for 500μm sheets was 14.75 Bar. To add a margin of safety, it was decided to assume that the burst pressures were 5 Bar and 14.5 bar respectively.

Table 3.1: Mylar Burst Pressures

Test	125 Micron Sheets	500 Micron Sheets	Total Thickness	Burst Pressure (Bar)	Burst Pressure/ 125 Micron Sheet (Bar)	Burst Pressure/ 500 Micron Sheet (Bar)	Average (Bar)
1	1	0	125	5.26	5.26		
2	1	0	125	5.27	5.27		
3	1	0	125	5.26	5.26		**5.26**
4	2	0	250	10.49	5.25		
5	2	0	250	10.23	5.12		
6	2	0	250	9.99	5.00		
7	2	0	250	10.27	5.14		**5.12**
8	3	0	375	16.11	5.37		
9	3	0	375	16.09	5.36		
10	3	0	375	16.3	5.43		**5.39**
11	4	0	500	22.26	5.57		
12	4	0	500	20.79	5.20		
13	4	0	500	20.89	5.22		**5.33**
14	0	1	500	14.60		14.60	
15	0	1	500	14.74		14.74	
16	0	1	500	14.78		14.78	**14.71**
17	0	2	1000	29.49		14.75	
18	0	2	1000	29.20		14.60	
19	0	2	1000	29.40		14.70	**14.68**
20	1	1	625	20.26			
21	1	1	625	20.25			
22	0	4	2000	59.68		14.92	
23	0	3	1500	44.81		14.94	**14.93**
24	1	1	625	20.06			
25	1	1	625	19.88			

3.5 Summary

This Chapter has introduced shock waves and their practical application in a shock tube. A phenomenological description of shock waves has been presented, and the terms "Steady", "Unsteady", "Normal" and "Oblique" have been defined in this context.

The operation and fluid dynamics of a shock tube has been discussed, with the differences between "Incident" and "Reflected" shock defined. This has led onto the presentation of equations derived from idealised theory that described the generation, propagation and reflection of shock waves in a shock tube.

The design of a shock tube to fulfil some of the objectives of this thesis is then described. The design criteria (some of which have been mentioned previously) are presented and the overall form of the shock tube is presented.

Detail is then given on important bespoke subsystems that have been designed to ensure safe, reliable and repeatable operation of the shock tube. The instrumentation used on the shock tube is detailed and the facilities used to prepare gaseous fuel-air mixtures are discussed. Figure 3.13 shows the completed shock tube, and Figure 3.14 shows the test section and slide valve, with some of the instrumentation highlighted. The Chapter concludes by presenting some commissioning tests that are required for the design of the subsequent experimental programmes in Chapters Four, Five and Seven.

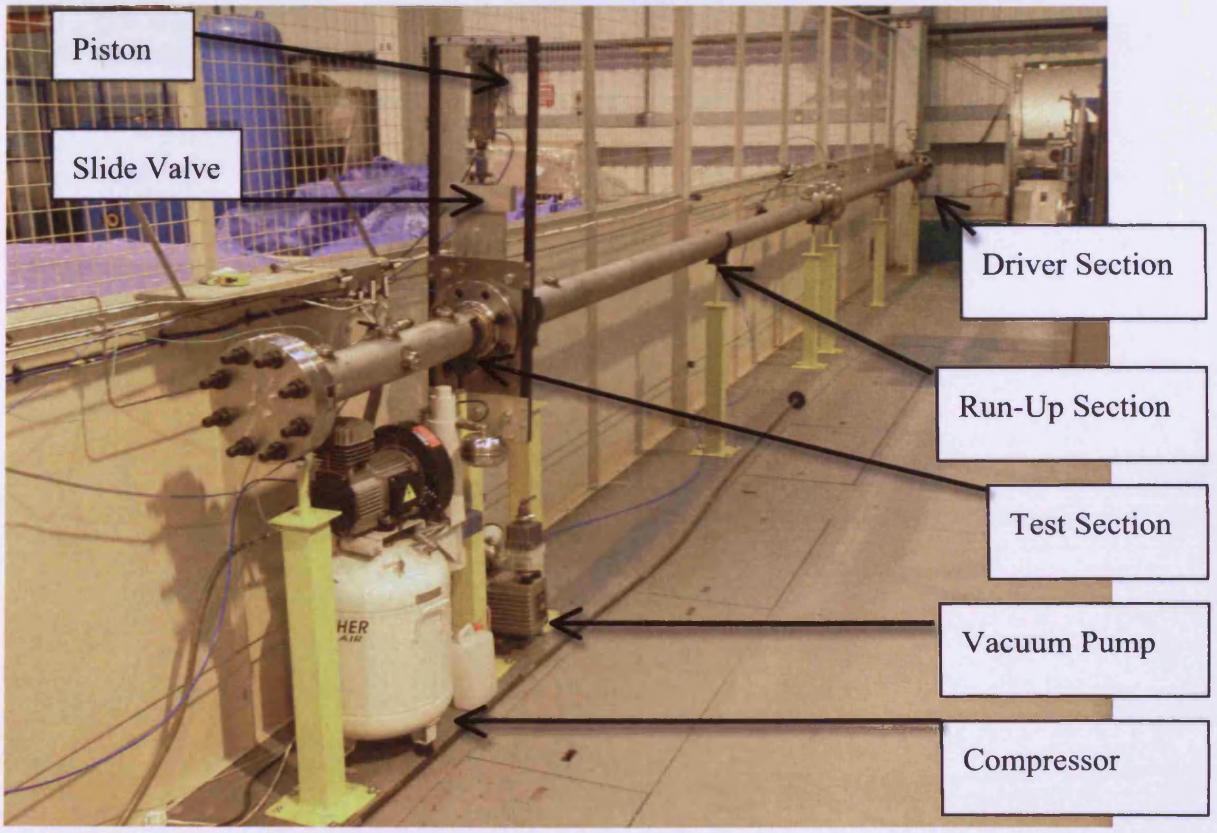

Figure 3.13: 4" Shock Tube

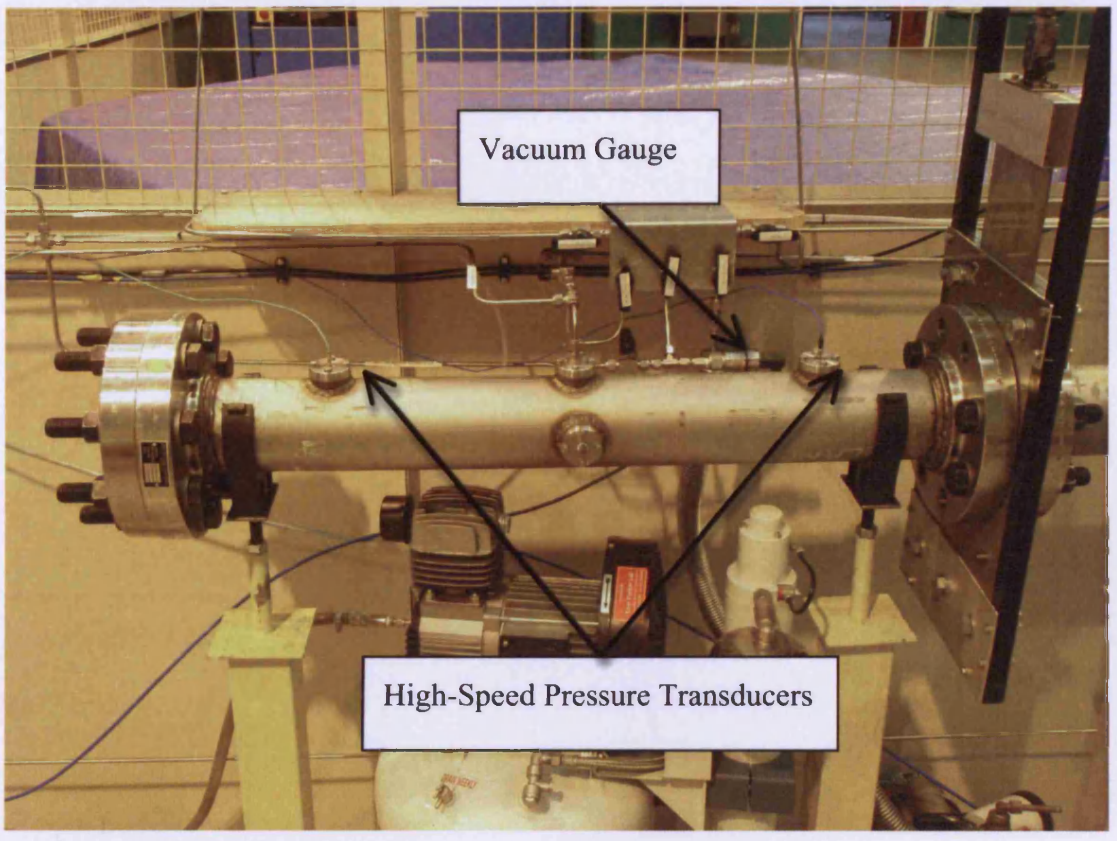

Figure 3.14: Shock Tube Test Section showing Instrumentation

Chapter Four

Non-Reactive Shock Tube Results

4.1 Introduction

This Chapter uses the shock tube described in Chapter Three to provide benchmark results against which the combustion results presented in Chapters Five and Seven can be analysed. Non-reacting experimental data on the propagation and reflection of shock waves is presented and the results are compared to the ideal theory also presented in Chapter Three. New empirical relationships are developed which describe the operation of the shock tube more accurately than ideal theory.

4.2 Experimental Methodology

The experimental procedure utilised for the non-reactive experiments is detailed below. The procedure formed the basis for the reactive experiments conducted in Chapters Five and Seven, with modifications detailed in the appropriate Chapters.

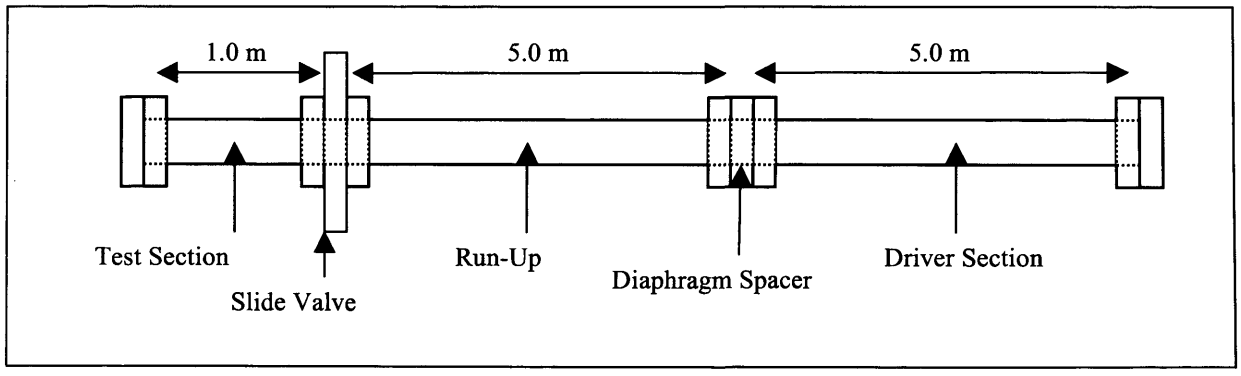

Figure 4.1: Shock Tube Schematic

1. The shock tube was configured as shown in Figure 4.1 with the appropriate reflecting face attached to the end flange and Mylar® diaphragms inserted.
2. The entire shock tube was initially evacuated to below 5 mBar.
3. The driver section and diaphragm spacer were filled with N_2 "driver gas" to the appropriate intermediate pressure, the diaphragm spacer was isolated from the filling line, then filling of the driver section to the final driver pressure was completed.
4. The driven section was filled to the required pressure with bottled compressed air.
5. The vacuum gauge was isolated to protect it from damage, the data acquisition system (DAQ) – as described in Section 3.4.3 – was initialised and the shock tube was fired.

6. The results from the DAQ, which was triggered by the shock wave passing Gauge1, were saved, and the shock tube was vented to atmosphere by manually opening the vent valves.
7. After the shock tube was vented to return it to atmospheric pressure, the Mylar® diaphragms were discarded and the end flange removed. The bursting characteristics of the Mylar® diaphragms led to diaphragm material being deposited along the driven section of the shock tube, so this was carefully removed from the length of the shock tube and reflecting face to prevent interference with subsequent tests.

4.2.1 Experimental Test Matrix

Table 4.1 defines the experiments undertaken. Each of the three reflecting faces was used at all of the conditions except for conditions 6 and 7, where only the concave faces were used.

Table 4.1: Non-Reactive Experimental Test Matrix

Test Number	Test Pressure P1 (BarA)	Driver Pressure P4 (BarA)	Pressure Ratio P4/P1	Mach Number (Calculated)	Number of 125µm diaphragms used	Number of 500µm diaphragms used	Incident Shock Pressure P2 (BarA)	Incident Shock Speed v1 (ms^{-1})	Reflected Shock Pressure P5 (BarA)	Reflected Shock Speed v5 (ms^{-1})
1	1	24	24	1.9	0	2	4.05	659.7	12.63	371.1
2	1	32	32	2.0	2	2	4.50	694.4	15.00	373.9
3	1	43	43	2.1	0	4	4.98	729.1	17.61	377.7
4	1	58	58	2.2	4	4	5.48	763.8	20.45	382.4
5	1	77	77	2.3	2	6	6.01	798.5	23.53	387.8
6	0.5	6.5	13	1.7	2	0	3.21	590.2	8.58	369.4
7	0.5	9	18	1.8	2	0	3.61	624.9	10.49	369.5
8	0.5	12	24	1.9	3	0	4.05	659.7	12.63	371.1
9	0.5	29	58	2.2	2	2	5.48	763.8	20.45	382.4
10	0.5	39	68	2.3	4	2	6.01	798.5	23.53	387.8
11	0.5	52	104	2.4	0	4	6.55	833.3	26.85	393.7
12	0.5	68	136	2.5	4	4	7.13	868.0	30.40	400.2

4.3 Data Processing and Analysis

4.3.1 Data Capture and Post-Processing

As described in Section 3.4.3, the results from the Shock Tube were initially presented in the NI programme LabView. The LabView interface (Figure 4.1) shows the voltages read by the NI PCI-6110 data card plotted against time. The white trace corresponds to Gauge1, and the red trace corresponds to Gauge2 (see Figure 3.15 for transducer positioning). During the initial commissioning experiments, the LabView settings, detailed in Table 4.2, allowed the DAQ to operate reliably therefore they were employed in the main experimental test programme. It should be noted that the maximum data rate that was found to be reliable was 2MHz, despite the maximum data rate of the data capture card being 5MHz. It is thought this is due to a combination of the memory available on the data card and the transfer speeds possible on the computer used.

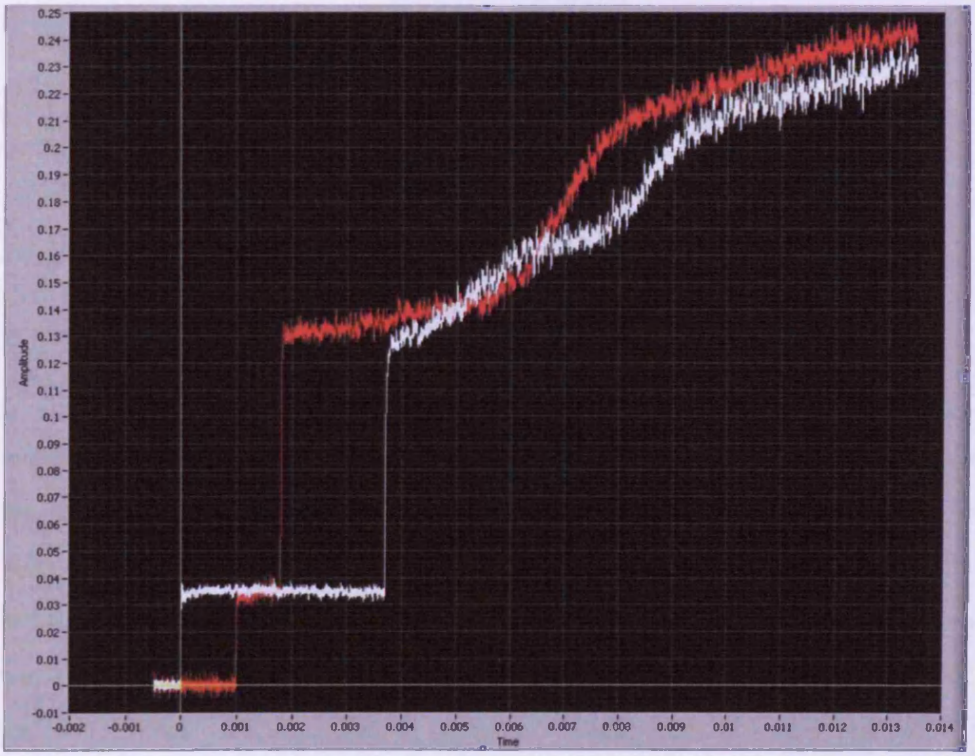

Figure 4.1: Screen Print of LabView (Voltage (V) vs. Time (s))

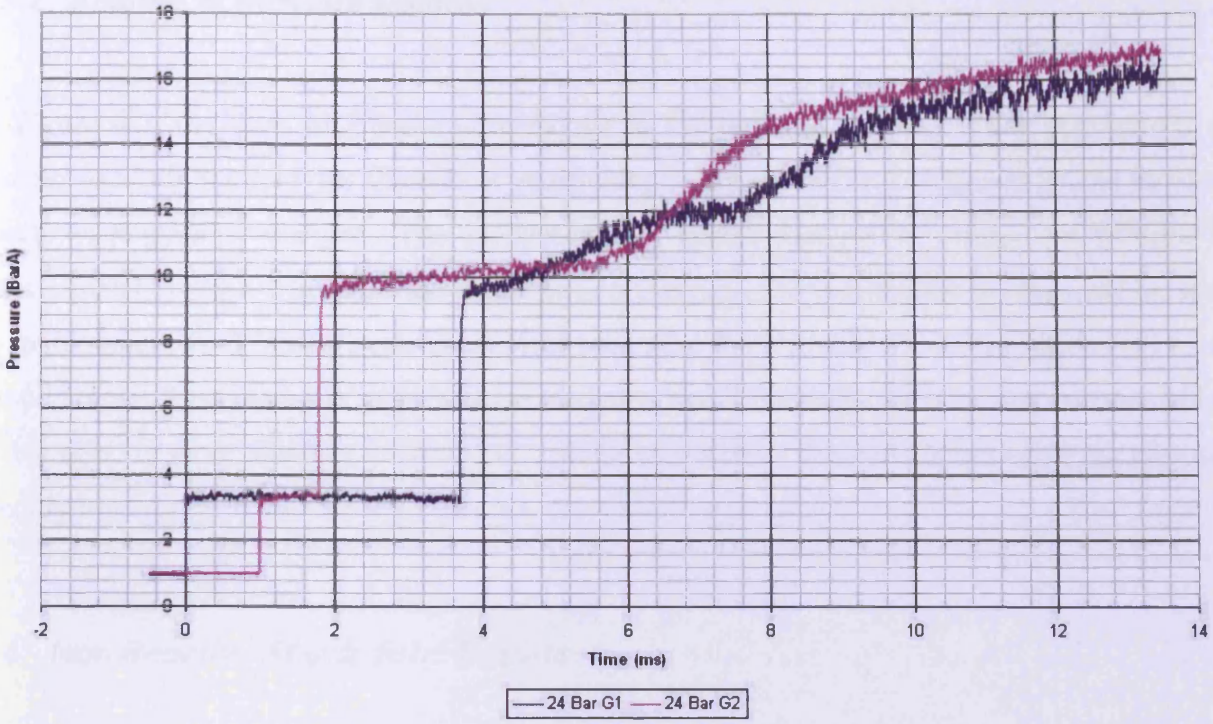

Figure 4.2: Display of Processed Data corresponding to Figure 4.1

Table 4.2: DAQ Options

Samples/Channel	28,000
Sample Rate	2,000,000 Hz
Trigger Level (Signal Conditioner 1)	0.05 Volts
Trigger Level (Signal Conditioner 2)	0.01 Volts
Pre-Trigger Samples	1,000

In order to post-process the data, the results were exported to a ".csv" file which can be read by most modern spreadsheet programmes. The voltages were converted to pressure using the calibration data supplied by PCB with each pressure transducer and corrected to take account of the base static pressure which is not recorded by the transducers. The results for sub-atmospheric test pressures were then normalised to atmospheric pressure to allow the analysis to ignore this variable and concentrate on the driver pressure ratio. An example of the final graph, corresponding to the data shown in Figure 4.1 is shown in Figure 4.2.

4.3.2 Analysis of Pressure Records

In Figure 4.2, the dark blue trace corresponds to Gauge1 and the pink trace corresponds to Gauge2 (see Figure 3.15 for transducer positioning). The system was triggered by the incident shock wave passing Gauge1. The incident shock passed Gauge1 at t=0ms and Gauge2 at approximately t=1ms. The reflected shock passed Gauge2 at approximately t=1.8ms and Gauge1 at approximately t=3.7ms. The pressure rises seen after the reflected shock had past were due to temperature effects on the PCB pressure transducers and the arrival of the contact surface, which is discussed in more detail in Section 5.2.2, along with a more detailed discussion of the pressure records.

4.4 Non Reactive Shock Tube Results

Table 4.3 presents a summary of the experimental results obtained for the non-combustion test programme. For each driver section /driven section pressure ratio (P_4/P_1), the average shock pressure and speed for both the incident and reflected shocks are presented. Preliminary tests showed that there was no clear relationship between the end face and the strength/speed of the reflected shock so, for most conditions, the different faces were used as repeats; the number of experiments conducted at each particular test condition is also shown in the table.

Figure 4.3 and Figure 4.4 show the individual data points for the incident and reflected shocks respectively, along with the averages given in Table 4.3. The incident shock data (Figure 4.3) shows that the scatter of results is very small, and there is a linear relationship between incident shock pressure and incident shock speed.

Figure 4.4 shows that the scatter of repeat data about the mean for the reflected shock is also good, although the spread is greater than is the case for the incident shock.

Table 4.3: Non Reactive Shock Tube Results

Test Number	Test Pressure P1 (BarA)	Pressure Ratio P4/P1	Mach Number (Calculated)	Number of Experiments	Incident Shock Pressure P2 (BarA)	Incident Shock Speed v1 (ms^{-1})	Reflected Shock Pressure P5 (BarA)	Reflected Shock Speed v5 (ms^{-1})
1	1	24	1.9	6	3.38	602.1	10.14	317.2
2	1	32	2.0	3	3.75	635.7	12.35	315.1
3	1	43	2.1	3	4.07	659.2	14.4	313.4
4	1	58	2.2	3	4.37	691	16.87	19.74
5	1	77	2.3	3	4.65	723.7	19.74	310.5
6	0.5	13	1.7	2	2.81	545.6	7.03	311.9
7	0.5	18	1.8	2	3.21	582.9	8.97	317.3
8	0.5	24	1.9	3	3.76	602	10.88	319.4
9	0.5	58	2.2	3	4.48	694.8	16.86	307.9
10	0.5	68	2.3	3	4.87	728.4	19.75	305.6
11	0.5	104	2.4	3	5.26	756.8	22.72	299.1
12	0.5	136	2.5	3	5.64	788.3	26.04	280.3

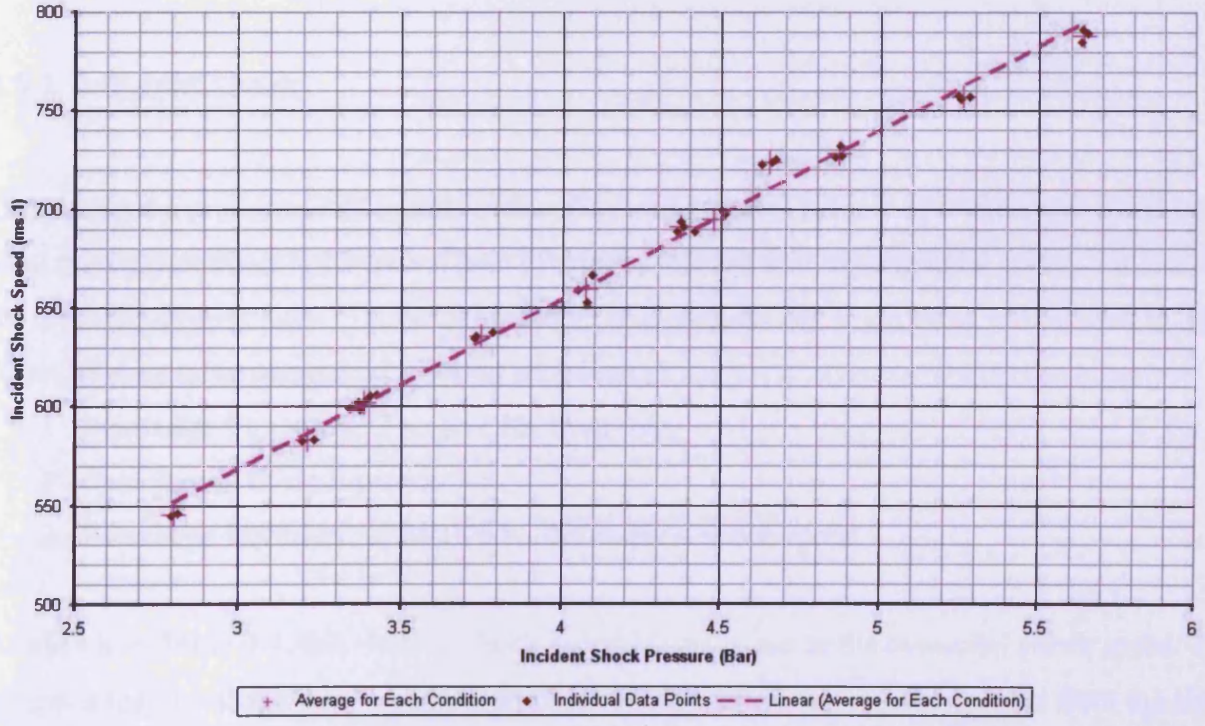

Figure 4.3: Incident Shock Data – Mean and Scatter

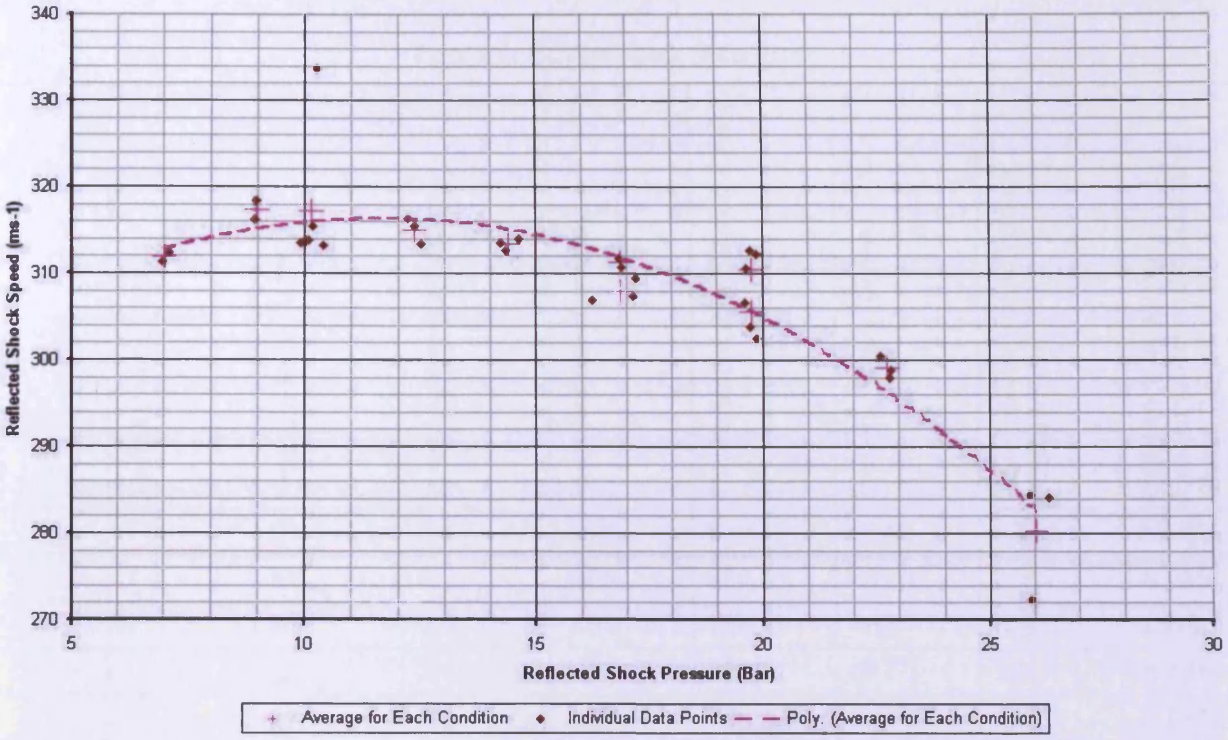

Figure 4.4: Reflected Shock Data – Mean and Scatter

4.5 Analysis of Non-Reactive Shock Tube Data

4.5.1 Incident Shock

Comparing the pressures and speeds obtained by experiment (Table 4.3) to those predicted by the ideal theory described in Chapter Three (Table 4.1) shows that experimental results are less than the theoretical predictions. The actual pressure ratio obtained by experiment can be used to find a "derived" Mach No using the following procedure:

1. Rearrange Equation 3.3 to give M_1 from p_2/p_1
2. Calculate a_1 using Equation 3.1
3. Rearrange Equation 3.2 to give v_1, the incident shock speed

As shown in Table 4.4, this derived shock speed is very close to the measured shock speed. This indicates that the shock can be accurately described by this Mach number derived from the shock pressure ratio (P_2/P_1).

Table 4.4: Incident Shock Speed Error

Test Number	Test Pressure P1 (BarA)	Pressure Ratio P4/P1	Mach Number (Calculated)	Mach Number (Derived)	Theoretical Incident Shock Speed (ms^{-1})	Incident Shock (derived) (ms^{-1})	Experimental Incident Shock Speed (ms^{-1})	**Difference between Experimental and calculated Shock Speed (ms^{-1})**
1	1	24	1.9	1.74	659.7	604.1	602.1	**0.33%**
2	1	32	2	1.83	694.4	635.4	635.7	**-0.05%**
3	1	43	2.1	1.91	729.1	663.1	659.2	**0.59%**
4	1	58	2.2	1.97	763.8	684	691	**-1.02%**
5	1	77	2.3	2.03	798.5	704.8	723.7	**-2.68%**
6	0.5	13	1.7	1.60	590.2	555.5	545.6	**1.78%**
7	0.5	18	1.8	1.70	624.9	590.2	582.9	**1.24%**
8	0.5	58	2.2	2.00	763.8	694.4	694.8	**-0.06%**
9	0.5	68	2.3	2.08	798.5	722.2	728.4	**-0.86%**
10	0.5	104	2.4	2.16	833.3	749.9	756.8	**-0.92%**
11	0.5	136	2.5	2.23	868	774.2	788.3	**-1.82%**

In a practical, non-ideal shock tube, boundary layer effects will cause the shock produced to differ from theory. A boundary layer is formed behind the shock wave due to the gas motion induced by the shock wave, which will have the effect of slowing down the shock wave. This is due to the drag caused by the boundary layer which reduces the driving force for the shock wave. In addition, the boundary layer will speed up the contact surface as the effective cross sectional area that the shocked gas can move through is smaller area. Therefore, the presence of a boundary layer means that the produced shock is slower, with the associated lower pressure ratio, and the run time of the shock tube will be less.

4.5.2 Reflected Shock

The results for the reflected shock are not quite so straightforward to analyse. The first complication is that now there are two theoretical reflected shock cases to compare the experimental results to: first assuming the incident shock wave predicted by theory, second using

the shock wave actually measured during experiment. The second complication is the fact that the experimental data shows that the reflected shock speed reduces with increasing driver pressure ratio (Figure 4.6), even though the experimental reflected shock pressure ratio increase with increasing driver pressure ratio (Figure 4.5) – a phenomenon which is contrary to theory and intuition. A possible reason for this is given below.

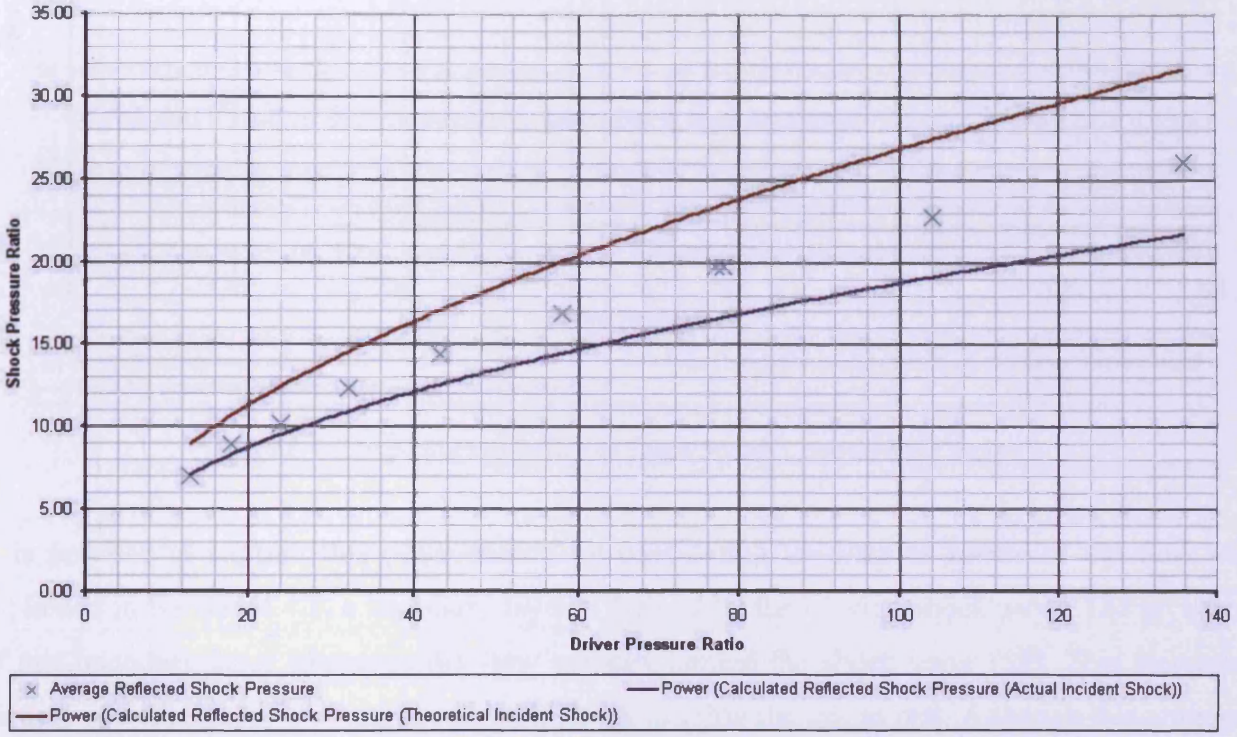

Figure 4.5: Experimental Reflected Shock Pressures Compared to Theory

Comparing the reflected shock to that predicted from the theoretical incident shock wave, the experimental shock pressure and speed are over-predicted, which is as expected given the experimental strength of the incident shock wave is less than predicted by theory, with both the pressure and speed deficits increasing with increasing driver pressure ratio. Comparing the experimental results to those predicted from the actual incident shock wave, the shock pressure ratio is under-predicted, with the absolute difference between the two values increasing with driver pressure ratio, and the shock speed is over-predicted, with the speed deficit increases with increasing driver pressure ratio.

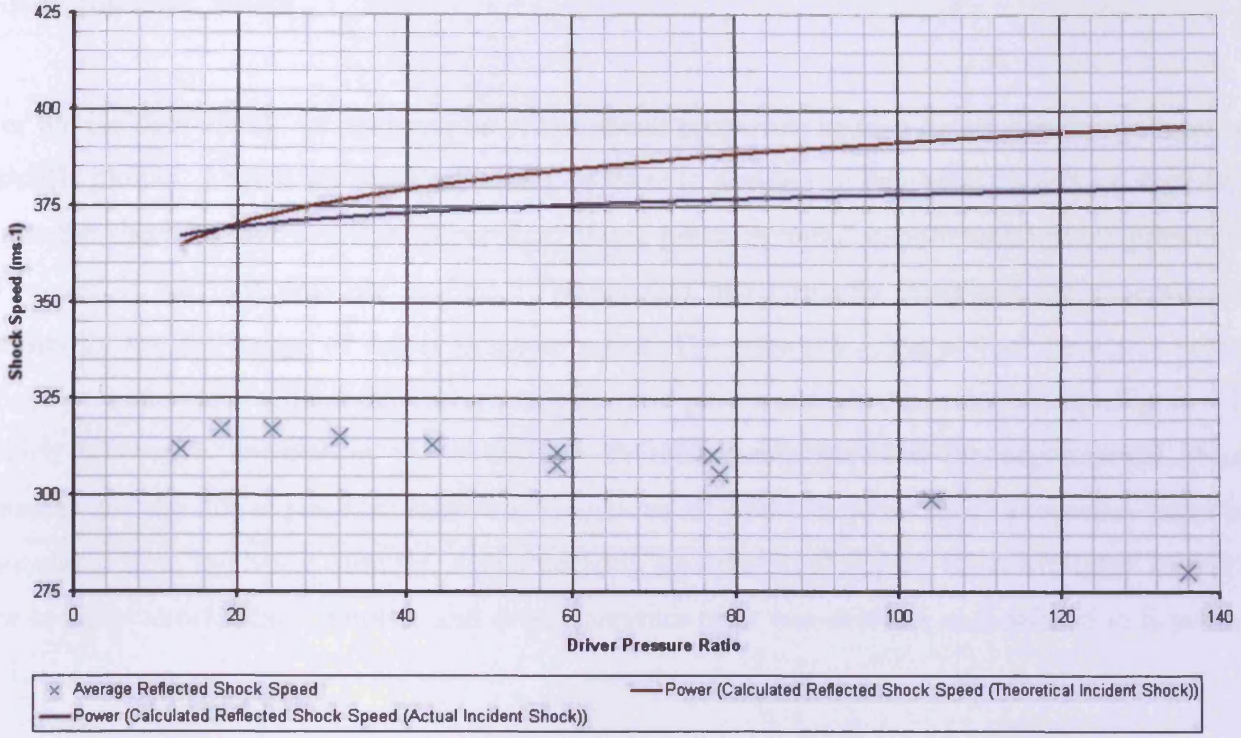

Figure 4.6: Experimental Reflected Shock Speeds Compared to Theory

It is possible to explain this phenomenon by considering the viscous nature of the flow. As explained in Section 4.4.1, a boundary layer is formed by the moving shock wave. The presence of this boundary layer increases the flow velocity behind the shock wave [53]. This increased particle speed requires a stronger reflected shock to bring the gas to rest. Although this stronger shock wave will have a faster shock speed, this speed is with respect to the oncoming flow, not the shock tube (as is being measured). The increased particle velocity behind the incident shock would explain why the reflected shock speed decreases with increasing driver pressure ratio.

4.6 Development of Empirical Relationships

As seen from the data presented above, the actual operation of the shock tube differs from theory due to losses. To allow future users of the shock tube to predict the operation of the shock tube more accurately in order to help experimental design, a series of empirical relationships were sought. From the examination of the data conducted above, relationships are required to characterise the incident shock wave, and the reflected shock pressure ratio and speed as functions of the driver pressure ratio P_4/P_1.

4.6.1 Incident Shock

For the incident shock, several graphs of the shock properties against driver pressure ratio were initially plotted. At first the most promising of these to develop an empirical correlation appeared to be the shock pressure deficit (theoretical shock pressure minus experimental shock pressure). However, it was not possible to find a relationship that correctly described the experimental results for the full range of driver pressure ratios. The natural log/log plot of the experimental shock pressure ratio against the driver pressure ratio gave a straight-line relationship (Figure 4.7) which allowed a correlation to be derived. A relationship between the experimental Mach number and the driver pressure ratio was sought, as all of the incident shock properties could be calculated from the Mach number. Again utilising a natural log/log plot, the relationship between the incident shock Mach number and driver pressure ratio was derived, and defined in Equation 4.1.

$$M_1 = 1.157.(P_4/P_1)^{0.1334} \qquad \text{Equation 4.1}$$

Table 4.5 compares the incident shock properties derived from Equation 4.1 to those obtained by experiment. The low percentage errors (less than 8%) suggest that the correlation adequately describes the incident shock wave for this shock tube from the initial control conditions.

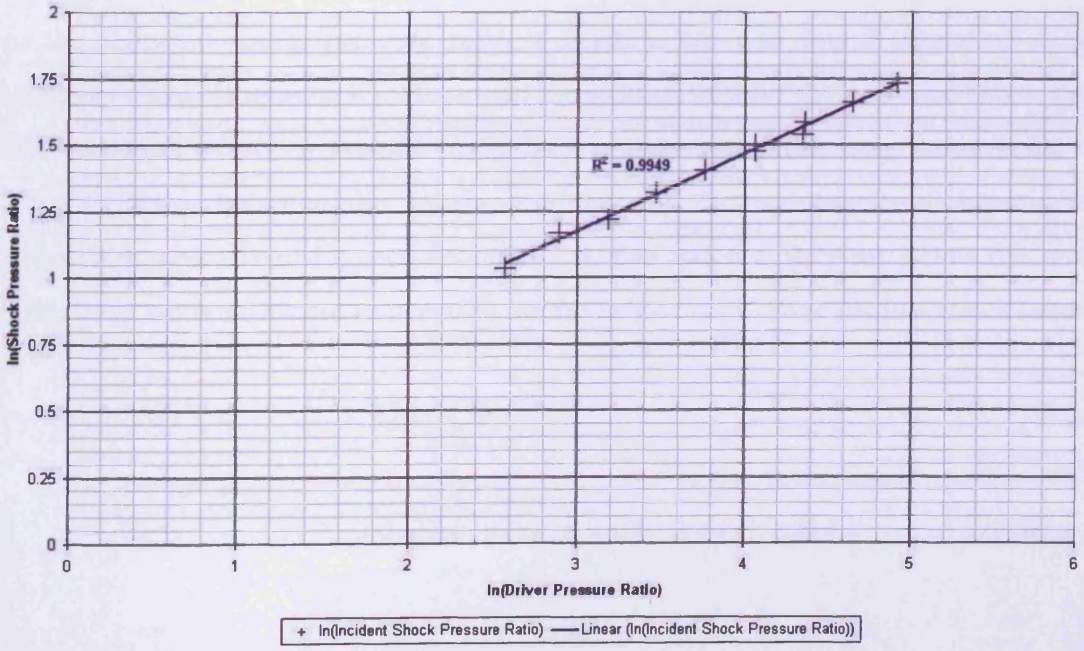

Figure 4.7: log/log Plot of Incident Shock Pressure

Table 4.5: Comparison of Experimental Incident Shock Results to those calculated from Empirical Relationship

Test Number	Test Pressure (BarA)	Driver Pressure Ratio	Mach Number (Derived, from Table 4.4)	Mach Number (Calculated from Equation 4.1)	**Mach Number Error**	Experimental Pressure Ratio (from Table 4.3)	Calculated Pressure Ratio (From Equation 3.3)	**Pressure Ratio Error**	Experimental Shock Speed (ms^{-1}) (from Table 4.3)	Calculated Shock Speed (ms^{-1}) (From Equation 3.4)	**Shock Speed Error (ms^{-1})**
1	1	24	1.74	1.77	**-1.6%**	3.38	3.48	**-2.9%**	602.1	614.5	**-2.1%**
2	1	32	1.83	1.84	**-0.4%**	3.75	3.77	**-0.5%**	635.7	638.8	**-0.5%**
3	1	43	1.91	1.91	**0.0%**	4.07	4.09	**-0.6%**	659.2	663.1	**-0.6%**
4	1	58	1.97	1.99	**-1.0%**	4.37	4.45	**-1.8%**	691.0	690.9	**0.0%**
5	1	77	2.03	2.07	**-1.7%**	4.65	4.81	**-3.4%**	723.7	718.7	**0.7%**
6	0.5	13	1.60	1.63	**-1.8%**	2.81	2.93	**-4.2%**	545.6	565.9	**-3.7%**
7	0.5	18	1.70	1.70	**-0.1%**	3.21	3.21	**0.0%**	582.9	590.2	**-1.3%**
8	0.5	24	1.83	1.77	**3.4%**	3.76	3.48	**7.5%**	602.0	614.5	**-2.1%**
9	0.5	58	2.00	1.99	**0.6%**	4.48	4.45	**0.7%**	694.8	690.9	**0.6%**
10	0.5	68	2.08	2.03	**2.3%**	4.87	4.65	**4.6%**	728.4	704.8	**3.2%**
11	0.5	104	2.16	2.15	**0.5%**	5.26	5.23	**0.7%**	756.8	746.5	**1.4%**
12	0.5	136	2.23	2.23	**0.1%**	5.64	5.63	**0.3%**	788.3	774.2	**1.8%**

4.6.2 Reflected Shock

For the reflected shock pressure ratio, a relationship was found (Equation 4.2) in the same manner as above (Figure 4.X). However, the relationship for the reflected shock speed (Equation 4.3) was found to be represented better by a polynomial expression. As in Table 4.5, Table 4.6 shows the error between the results predicted by the equations and experiment. These are displayed graphically in Figures 4.9 and 4.10. The fact that they are below 6% suggests that the correlations are appropriate to describe the reflected shock wave for this shock tube.

$$P_5 = 1.829\ (P_4/P_1)^{0.5457} \qquad \text{Equation 4.2}$$

$$v_5 = -0.0025\ (P_4/P_1)^2 + 0.091\ (P_4/P_1) + 315.2 \qquad \text{Equation 4.3}$$

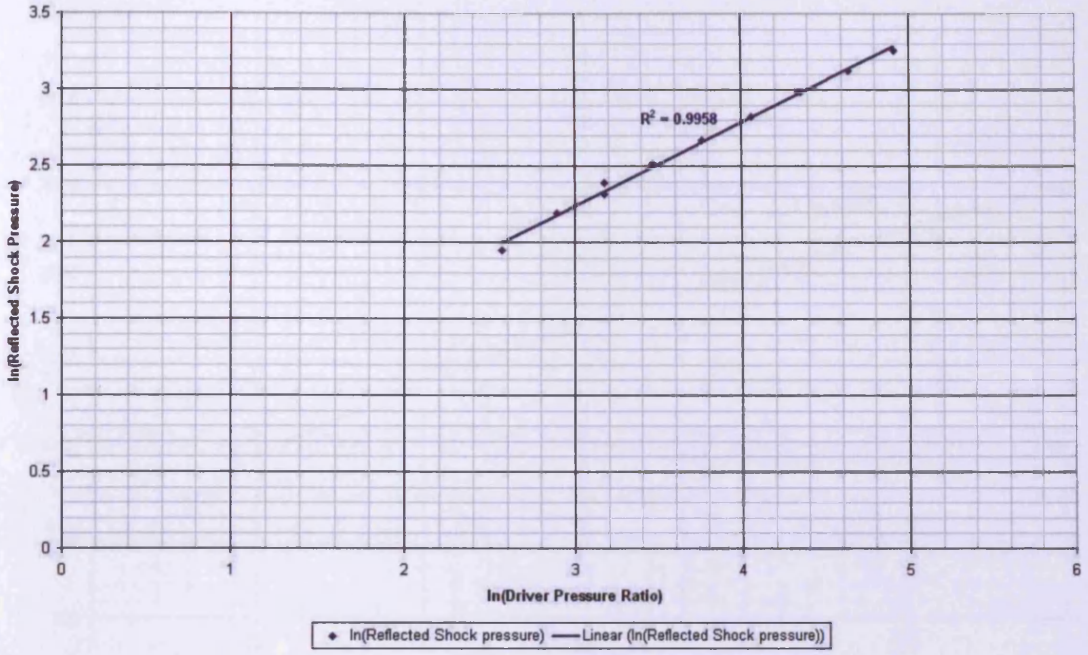

Figure 4.8: log/log Plot of Reflected Shock Pressure

Table 4.6: Comparison of Experimental Reflected Shock Results to those calculated from Empirical Relationship

Test Number	Test Pressure (BarA)	Driver Pressure Ratio	Experimental Reflected Shock Pressure	Calculated Reflected Shock Pressure	**Reflected Shock Pressure Error**	Experimental Reflected Shock Speed (ms^{-1})	Calculated Reflected Shock Speed (ms^{-1})	**Reflected Shock Speed Error (ms^{-1})**
1	1	24	10.14	10.36	**-2.2%**	317.2	315.9	**0.4%**
2	1	32	12.35	12.12	**1.8%**	315.1	315.6	**-0.2%**
3	1	43	14.40	14.24	**1.1%**	313.4	314.5	**-0.4%**
4	1	58	16.87	16.77	**0.6%**	311.3	312.1	**-0.2%**
5	1	77	19.74	19.57	**0.9%**	310.5	307.4	**1.0%**
6	0.5	13	7.03	7.41	**-5.5%**	311.9	316.0	**-1.3%**
7	0.5	18	8.97	8.86	**1.2%**	317.3	316.0	**0.4%**
8	0.5	24	10.88	10.36	**4.8%**	320.7	315.9	**1.5%**
9	0.5	58	16.86	16.77	**0.5%**	307.9	312.1	**-1.3%**
10	0.5	78	19.75	19.71	**0.2%**	305.6	307.1	**-0.5%**
11	0.5	104	22.72	23.06	**-1.5%**	299.1	297.6	**0.5%**
12	0.5	136	26.04	26.70	**-2.5%**	280.3	281.3	**-0.4%**

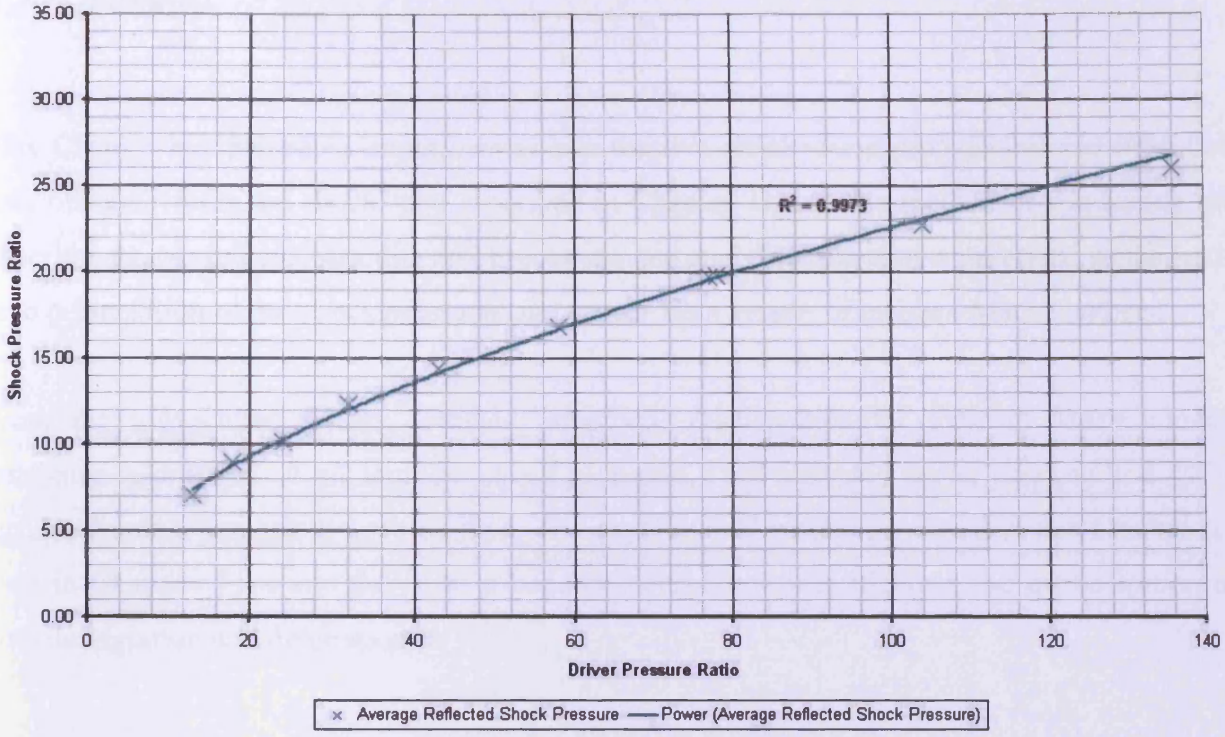

Figure 4.9: Comparison of Reflected Shock Pressure Experiment and Derived Equation

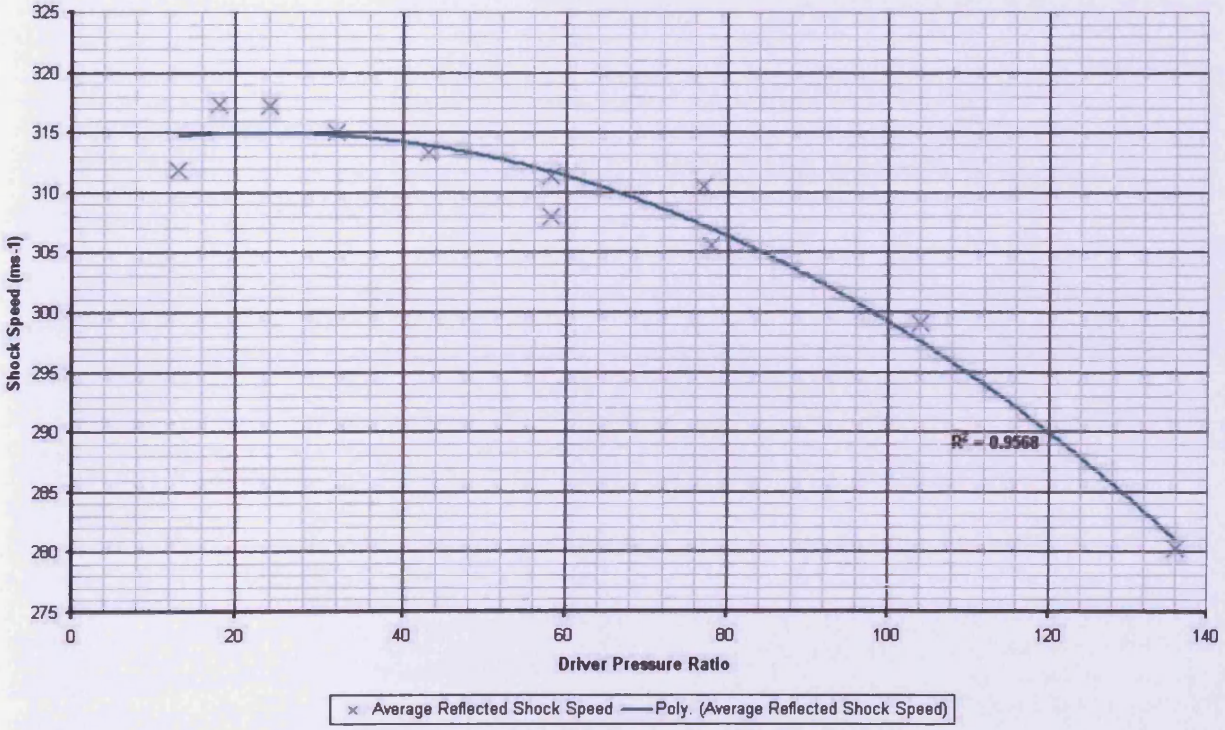

Figure 4.10: Comparison of Reflected Shock Speed Experiment and Derived Equation

4.7 Summary

This Chapter has presented experimental non reactive shock wave propagation and reflection data obtained from the shock tube described in Chapter Three. The method of conducting the experiments, as well as collecting and processing and analysing the data is described which leads onto presentation of the shock pressures and speeds for a variety of incident Mach numbers.

From the low-scatter results obtained, empirical relationships for incident Mach number (enabling calculation of all incident shock properties) and reflected shock pressure and speed against driver pressure ratio are derived. The experimental results presented in this Chapter are used in Chapters Five and Seven as a benchmark to allow identification and quantification of both deflagration and detonation.

Chapter Five

Reflected Shock Initiation for Gaseous Fuels

5.1 Introduction

This Chapter presents the combustion results obtained using the shock tube described in Chapter Three. The results build on the non-reacting results presented in Chapter Four with all the combustion cases compared directly to their non-reacting counterparts. The gaseous fuels used are stoichiometric propane (for its similarity to kerosene vapour in detonation propagation) and stoichiometric hydrogen (due to its readiness to detonate and previous experimental detonation data that allows benchmarking of the shock tube). Three different reflecting faces are used to investigate the effect of shock focusing on combustion initiation. The experiments in this Chapter help build towards to the liquid-fuel combustion experiments conducted in Chapter Seven, and the results are used to aid the analysis of the results in Chapter Seven.

5.2 Experimental Methodology

The method used to conduct combustion initiation experiments was broadly similar to that described in Section 4.1 for the non-reactive experiments. The main difference regarded the filling of the driven section (run-up and test sections). Prior to the tests, the fuel air mixture was prepared as described in Section 5.2.1. After the driver section had been filled (Step 3), the following Steps were substituted for Step 4:

1. The slide valve was closed to isolate the test section from the run-up section.
2. The run-up section was filled with bottled compressed air to the required pressure.
3. The test section was filled with the pre-mixed fuel/air to match the pressure in the run-up section.

A single vacuum gauge was used to measure the pressure in both the run-up and test sections to ensure that the pressure was consistent. To ensure that no contamination occurred between the two sections between fills, the vacuum gauge was connected to the vacuum pump before readings were taken. Once the driven section was filled, the firing procedure continued at Step 5 as described in Section 4.1.

5.2.1 Fuel/Air Preparation

The vessels used for mixing the fuel and air are described in Section 3.4.4. A carefully designed fill procedure was required to ensure that minimal impurities were present in the fuel/air mixture and that the correct ratio of fuel to air is present in the vessel. The following pre-fill procedure was designed to ensure that this occurred:

1. The vessel was vacuumed to 10 mbarA to ensure that a combustible mixture could not be formed in Steps 2-4.
2. The vessel was filled with approximately 200 mbarA of fuel gas. This ensured that the gas in the line prior to filling was 100% fuel gas and not contaminated by air or other gases such as nitrogen.
3. The vessel was filled with bottled oxygen-free nitrogen (OFN) to 2 barA. This rendered the fuel mix safe to release into the atmosphere.
4. The vessel was vacuumed to 10 mbarA to remove the fuel/nitrogen mix.
5. The vessel was filled with bottled air to 1 barA and then vacuumed down to 20 mbar.
6. Step 5 was repeated. This ensured that the residual gas in the vessel that could not be removed from the vessel was of a known composition (air). The error in the composition of the residual gas using this method was 0.04% (i.e. the maximum partial pressure of the impurities was 0.08 barA). The residual pressure of air was noted and the amount of air filled in Step 8 was reduced accordingly.
7. The vessel was filled to the required pressure with fuel gas (adjusting for the residual air pressure already present in the vessel).
8. The vessel was filled to the required pressure with air.

Although this procedure minimised the error in the mixing, a reducible error was still present in the fill process due to the fact that no intrinsically safe vacuum pump was available. Ideally, the test section would have been filled and vacuumed down twice with fuel/air mix, as was done in the fill procedure. The residual pressure in the test section was under 5 mBar for all of the tests, giving a maximum error in the equivalence ratio of 1.0% (i.e. for the worst case $\phi = 0.99$).

5.2.2 Interpreting the Pressure Traces

The pressure traces presented in this Chapter (Figures 5.1-5.30) and in Chapter VIII show the processed results (as described in Section 4.3.1) for the gaseous fuel compared to the non-reacting cases. This direct comparison allows: visualisation of the affect of the addition of fuel compared to the sole air cases (discussed in Section 5.2.3); pressure rise caused by combustion and the effect on the reflected shock wave (both discussed in Sections 5.3 and 5.4). The following points should be noted when studying the pressure traces:

- The dark/light blue traces correspond to Gauge1 – the pressure transducer furthest away from the reflecting wall (see Figure 3.15 for instrumentation positioning).
- The brown/pink traces correspond to Gauge2 – the pressure transducer closest to the reflecting wall.
- The darker colours (dark blue/brown) represent the non-reactive experiments and the lighter colours (light blue/pink) represent the reactive experiments.
- As discussed in Section 4.2, the DAQ system is triggered when the incident shock wave passes Gauge1. This is t=0 on the pressure traces
- As discussed in Section 4.3.1, the results have been normalised to an initial test pressure of 1 BarA (t<0).
- The pressure transducers used are sensitive to temperature rises. The presence of shock waves, both incident and reflected, results in an increase in temperature of the test section gas. This increase in temperature leads to an increase in the pressure recorded by the transducers, which is a contributory factor to the pressure rise seen in the recorded traces after approximately 4ms (Figure 4.1).
- The Contact Surface is the boundary between the driver section gas and driven section gas. As discussed in Chapter III (specifically Section 3.3.4) the arrival of the contact surface leads to a change in pressure of the test section – be it an increase or a decrease. This is an additional contributory factor to the pressure changes seen after approximately 4ms in Figure 4.1
- The run-time for a shock tube has been defined in Section 3.3.4 and calculated for the shock tube in Section 4.7.5. The calculated figure for the conditions shown in Figure 4.1 is 3.3ms, which compares to 3.6-3.8ms seen by experiment for Gauge1. The pressure increase seen by Gauge2 before this time can be put down to the increase in temperature caused by the shocks.

In Figure 5.1, the incident shock passes Gauge1 at t = 0ms and Gauge2 at t = 0.9ms. The reflected shock then passes Gauge2 at t = 1.6ms and Gauge1 at t = 3.6ms.

5.2.3 Experimental Consistency

The results presented in the rest of this chapter show good consistency for the given driver pressure ratios. The combustion and non-reactive experiments were carried out several months apart at different ambient temperatures using different batches of nitrogen driver gas. Figure 5.1 for propane and Figure 5.20 for hydrogen both demonstrate this consistency.

Examining Figure 5.1 in more detail shows that although the pressures after the incident and reflected shocks are very close for propane and air, the arrival time of the reflected shock for propane is slightly later than for air. This can be attributed to the slightly slower speed of sound in the stoichiometric propane/air mixture. This hypothesis can be confirmed by examining Figure 5.18, where the arrival time of the reflected shock is earlier in the mixture than in air due to the increased speed of sound in the hydrogen mix. The fact that the phenomenon is more pronounced in the hydrogen mix is due to the fuel quantities required to produce a stoichiometric mixture (4.2% by volume for propane and 30% by volume for hydrogen).

Careful examination of the pressure traces in both Figure 5.1 and 5.20 shows that the transition between the reflected shock and stagnant zone is not as "sharp" in the mixture cases as in the air cases. It is believed that this is due to a small amount of mixing occurring when the slide valve is opened prior to firing; and buoyancy effects when the two gases mix. Although not conducted during the course of this work, this hypothesis can be confirmed by rotating the test section by 90° so that the pressure transducers are no longer at the top of the test section but at the mid-point, or alternatively a mixture with the same molecular weight (i.e. C_2H_4) as air can be used in the test section.

5.3 Propane Test Programme

Table 5.1 shows the test matrix for the stoichiometric propane combustion programme. The three weaker shocks (M=1.60, M=1.70, M=1.83) were not used for the flat face due to the lack of

combustion at M=2.00. Two additional repeats were carried out at M=2.08 for all three faces to confirm the repeatability seen for the non-reacting test programme.

Table 5.1: Propane Test Matrix

Driver Pressure	Driver Pressure Ratio	Mach Number	Flat Face	Conical Face	Hemispherical Face
6.5	13	1.60		X	X
9	18	1.70		X	X
12	24	1.83		X	X
29	58	2.00	X	X	X
39	78	2.08	X	X	X
52	104	2.16	X	X	X
68	136	2.23	X	X	X

5.3.1 Propane: Flat Face

The Flat Face was the reflecting face thought least likely to give detonation due to the lack of shock focussing compared with the other two reflecting faces and the relative reactivity of propane compared to hydrogen. This proved to be the case with no detonation results identified for any of the conditions in the test matrix for the flat face (Table 5.1) as shown in Figures 5.1-5.4.

Figure 5.1 shows the results for the M=2.0 case, where the agreement between the propane and non-reactive cases over a long time scale indicates that there is no combustion in the time frame that was recorded. The pressure rises seen in Figures 5.2–5.4 (M=2.08, M=2.16, M=2.23 respectively) suggest combustion has occurred. However the pressure rise signifying the combustion event appears after the contact surface has reached the test section. This means that the mixture is likely to be very lean although the exact composition is unknown. Therefore, results from this set of experiments can, at best, be used to be indicative of trends. If combustion occurred before the arrival of the contact surface, than the pressure rises would be greater and the time between the arrival of the reflected shock wave and the combustion event would be reduced. The delay between the arrival of the reflected shock at the pressure transducer and the pressure rise due to combustion, and the relatively low pressure ratio (when compared to the hydrogen tests in Section 5.4) suggest deflagration is occurring and not detonation.

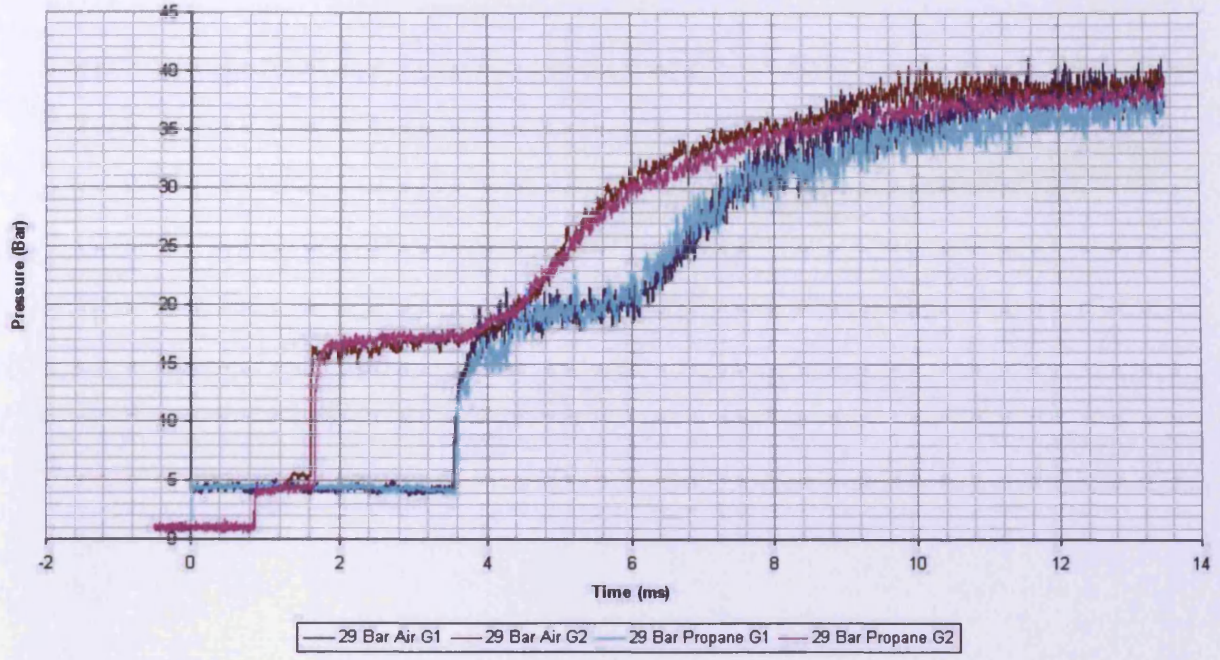

Figure 5.1: Propane Flat Face Results, M=2.00

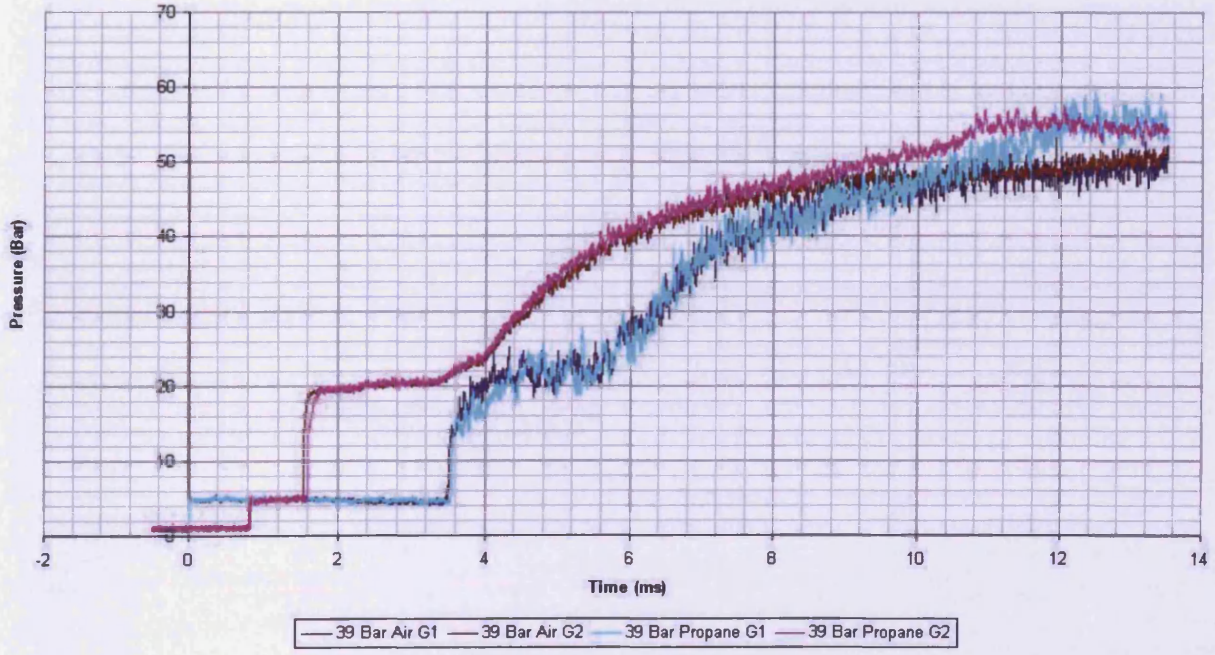

Figure 5.2: Propane Flat Face Results, M=2.08

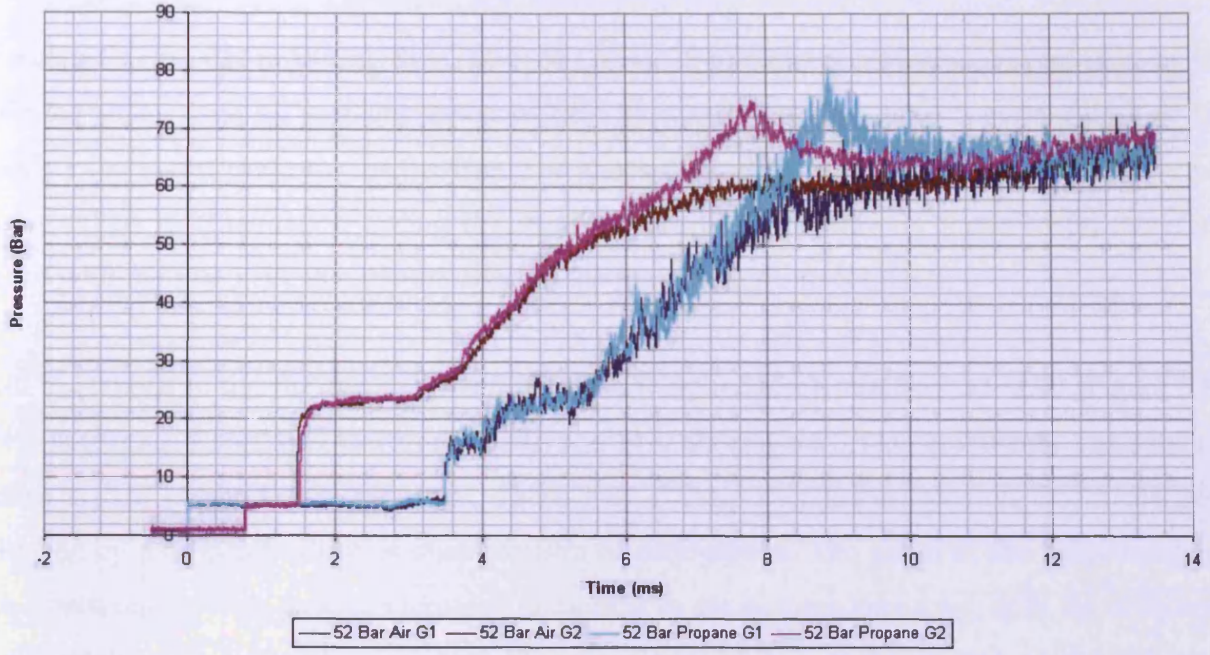

Figure 5.3: Propane Flat Face Results, M=2.16

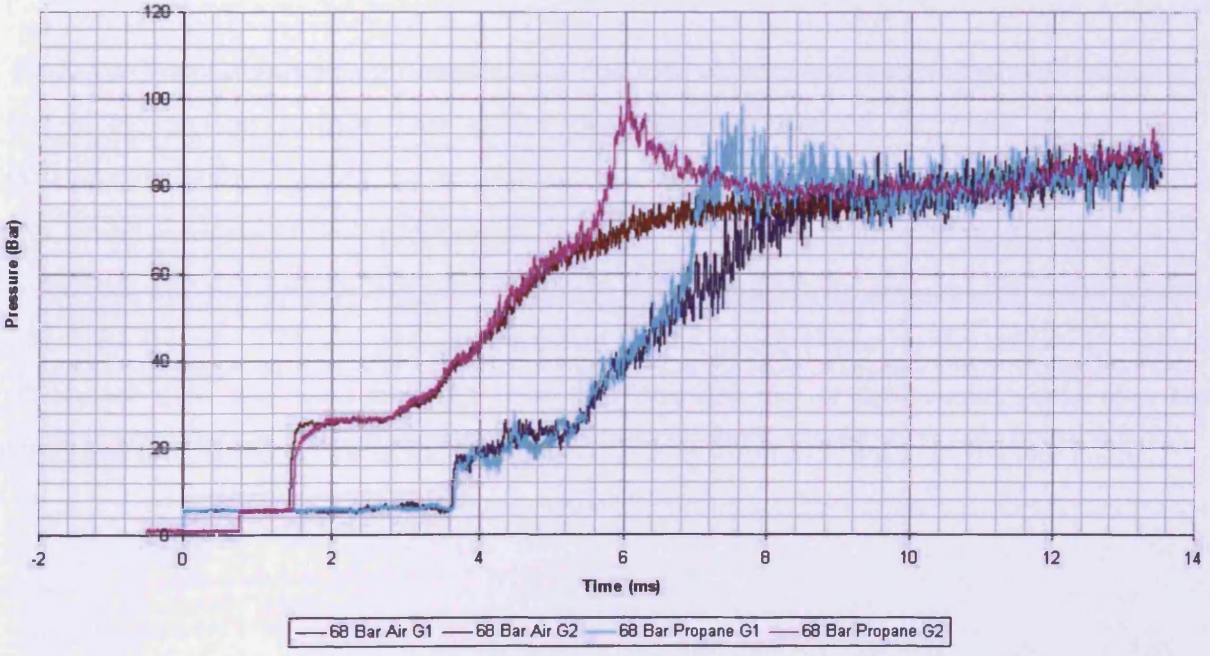

Figure 5.4: Propane Flat Face Results, M=2.23

5.3.2 Propane: Conical Face

In contrast to the flat reflecting face (M=2.08), it was found that combustion was initiated by the reflected shock with an incident shock of M=1.6, which was the lower operating limit of the Shock Tube at test pressures of 0.5 Bar. The shock focussing provided by the conical reflecting face resulted in combustion during the run-time of the shock tube for some cases, therefore, unlike with the Flat Face, the composition of the reactive mixture is known.

Also in contrast to the flat face, it was found that at higher Mach numbers, M=2.00 (Figure 5.8), M=2.08 (Figure 5.9), M=2.16 (Figure 5.10) and M=2.23 (Figure 5.11) combustion was obtained before arrival of the contact surface. There was a sharp increase in pressure up to the peak followed by a drop off which is characteristic of deflagration. The speed of the reflected shock wave between the two gauges increased compared to the non-reacting case, with the difference more notable the higher the incident Mach number. This is probably due to the increased pressure from combustion driving the shock wave in a similar way to the DDT process described in Section 2.2.7. This suggests that given a long enough tube (filled with combustible mixture), these cases would eventually give detonation.

At the lower Mach numbers, combustion was obtained at M=1.6 (Figure 5.5), but it was after the arrival of the contact surface. Due to the low pressures recorded, the noise in the signal is proportionately higher, giving the impression that the pressure peak due to combustion occurs almost simultaneously at both pressure transducers. Using a 50-point moving average, it can be seen that the arrival times of the pressure peaks actually differ by 1ms. At M=1.7 (Figure 5.6) and M=1.83 (Figure 5.7), the pressure recorded by the gauge closest to the reflecting face rose much slower than was seen in other tests (the pressure rise at the second gauge was more consistent with what was seen in the other tests). This is discusses further in Section 5.3.4.

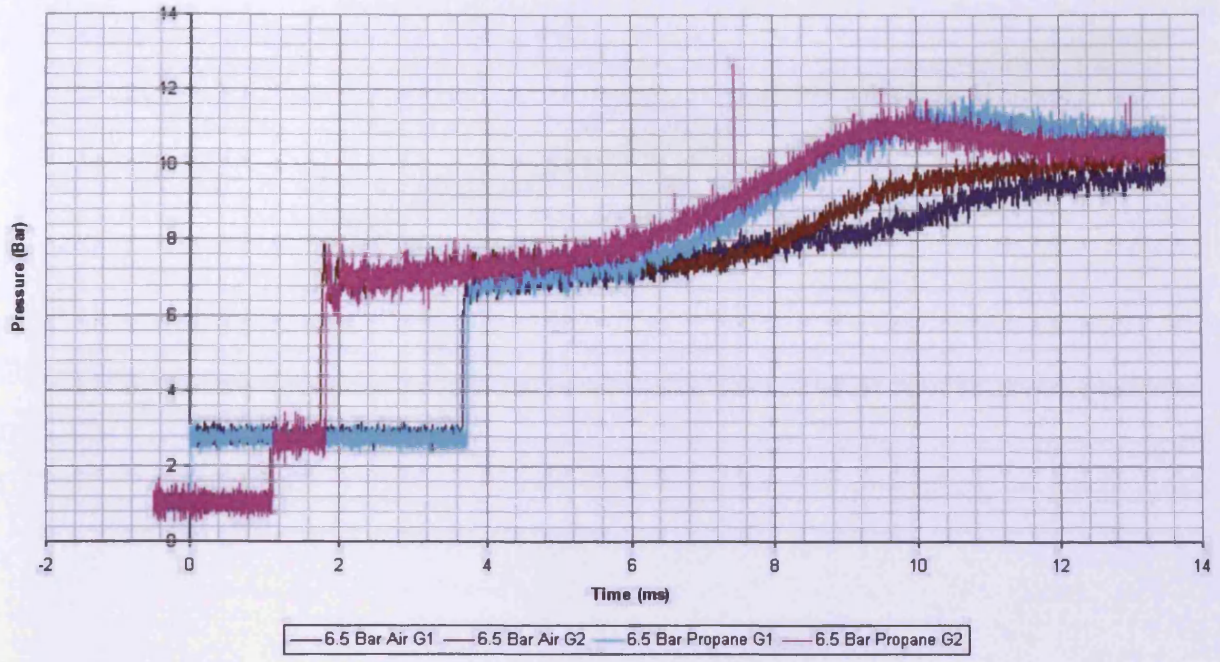

Figure 5.5: Propane Conical Face Results, M=1.60

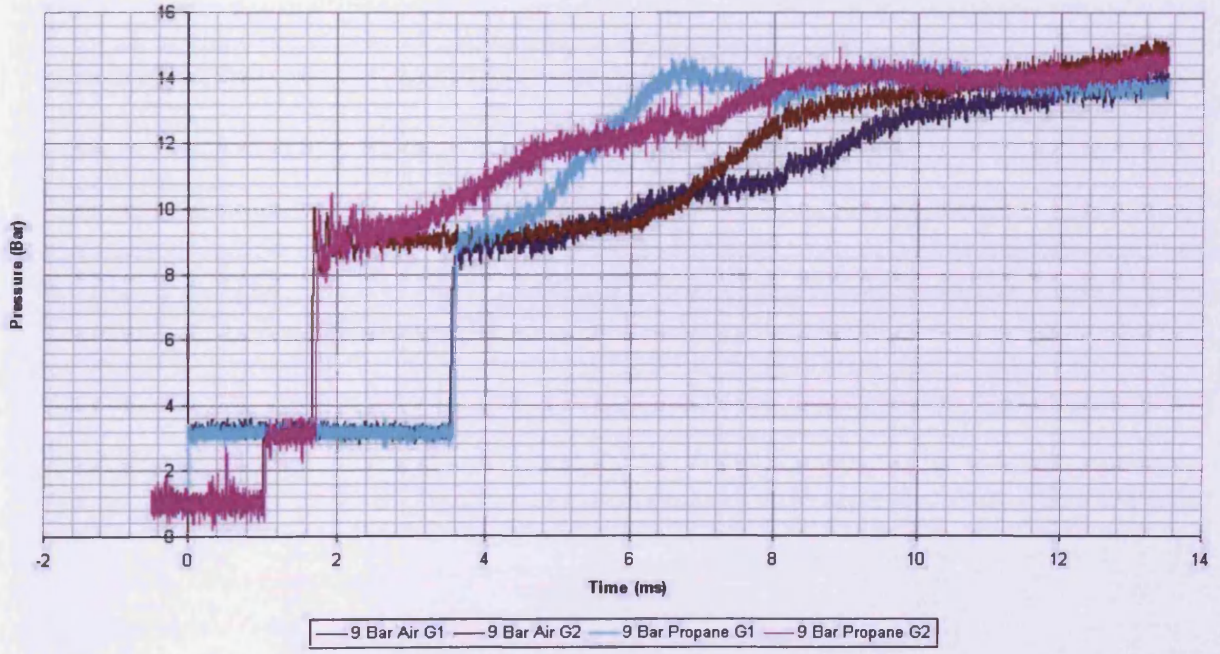

Figure 5.6: Propane Conical Face Results, M=1.70

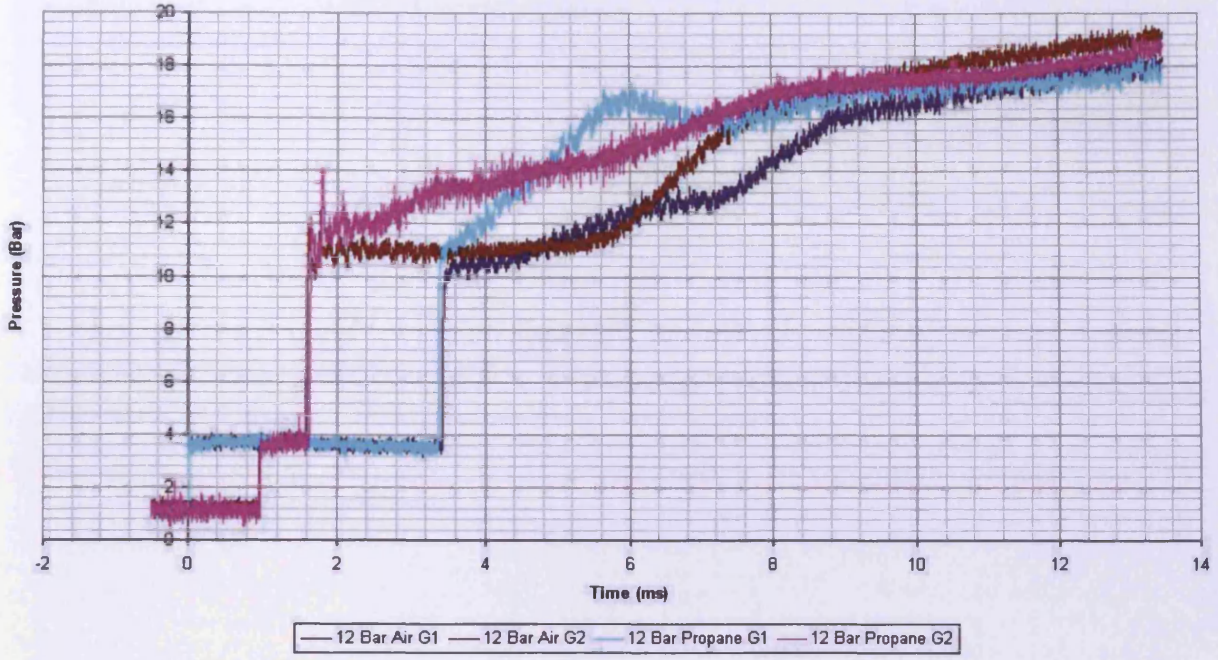

Figure 5.7: Propane Conical Face Results, M=1.83

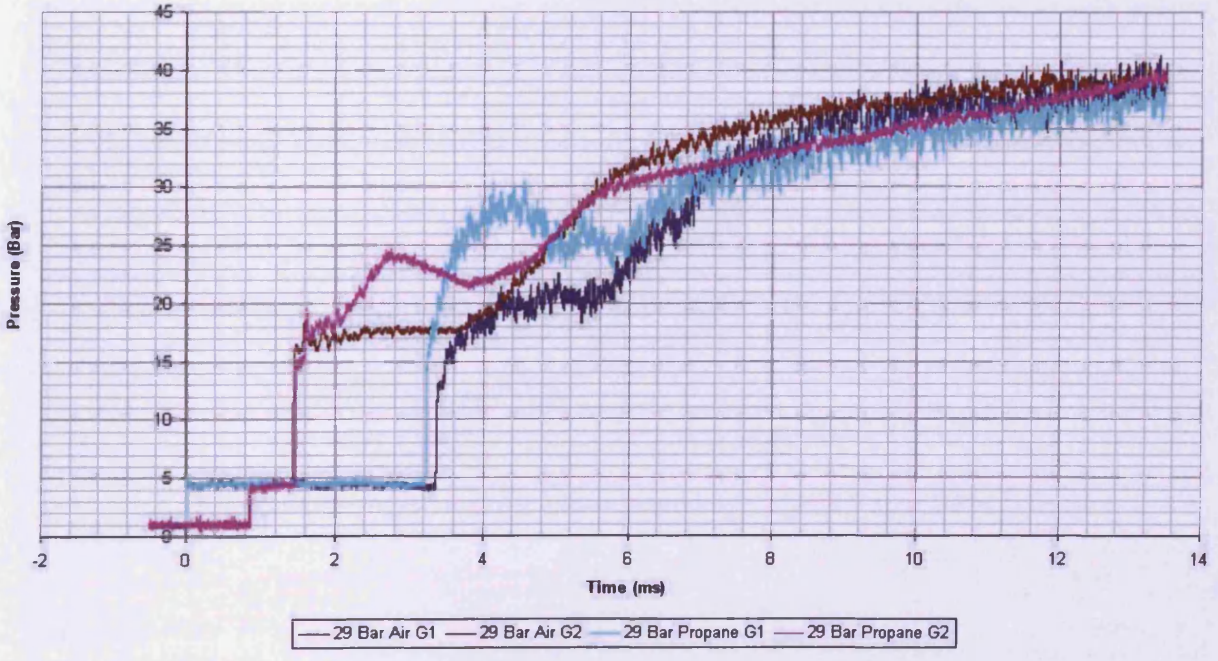

Figure 5.8: Propane Conical Face Results, M=2.00

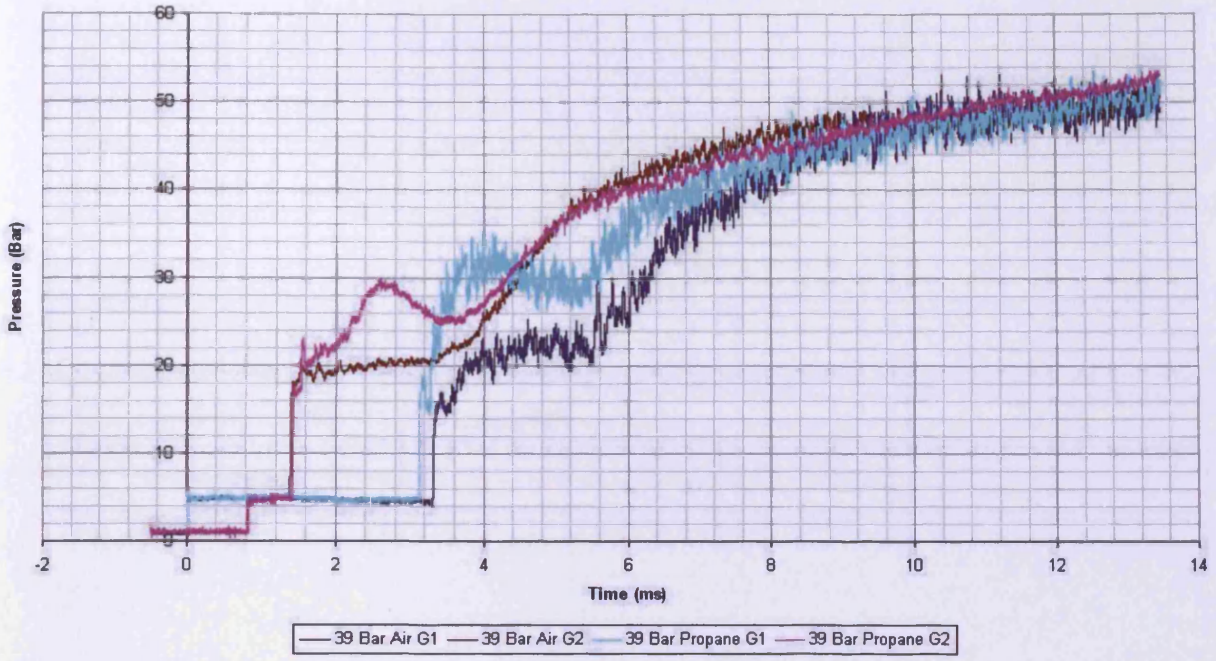

Figure 5.9: Propane Conical Face Results, M=2.08

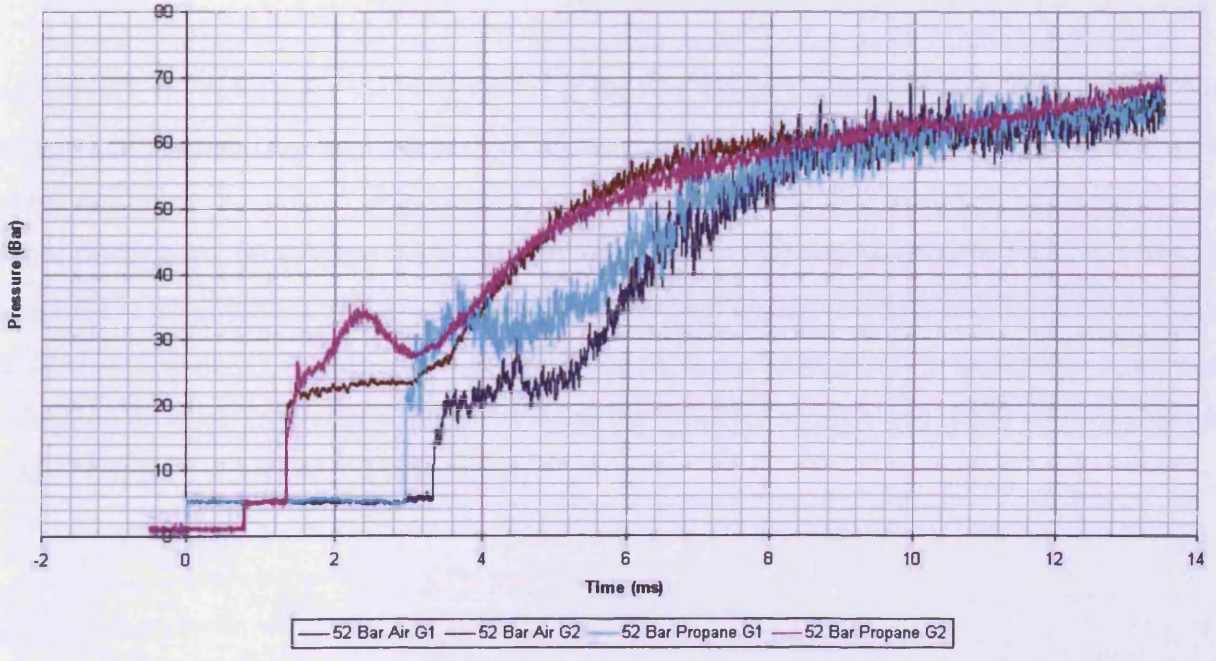

Figure 5.10: Propane Conical Face Results, M=2.16

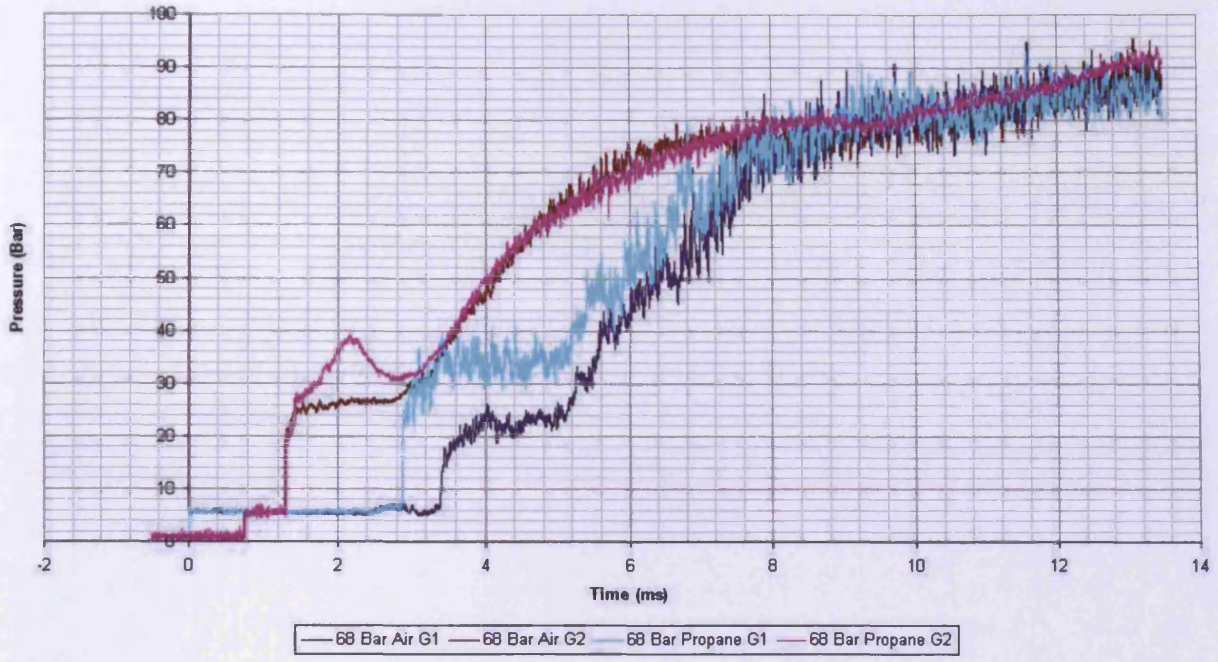

Figure 5.11: Propane Conical Face Results, M=2.23

5.3.3 Propane: Hemispherical Face

Qualitatively, the results for the hemispherical face are broadly similar to that of the conical face. Combustion occurred before the arrival of the contact surface for most of the shock Mach number test cases. At M=1.6 (Figure 5.12) no combustion event was recorded, while for M=1.83 (Figure 5.12), M=2.00 (Figure 5.14), M=2.08 (Figure 5.15), M=2.16 (Figure 5.16) and M=2.23 (Figure 5.17) the pressure traces were consistent the combustion events seen for the conical face. The M=1.7 (Figure 5.13) case shows a slow build-up to the peak pressure and only a small post-combustion drop-off in pressure. An increase in the reflected shock wave speed was observed for the M=2.00, 2.08, 2.16 and 2.23 cases only.

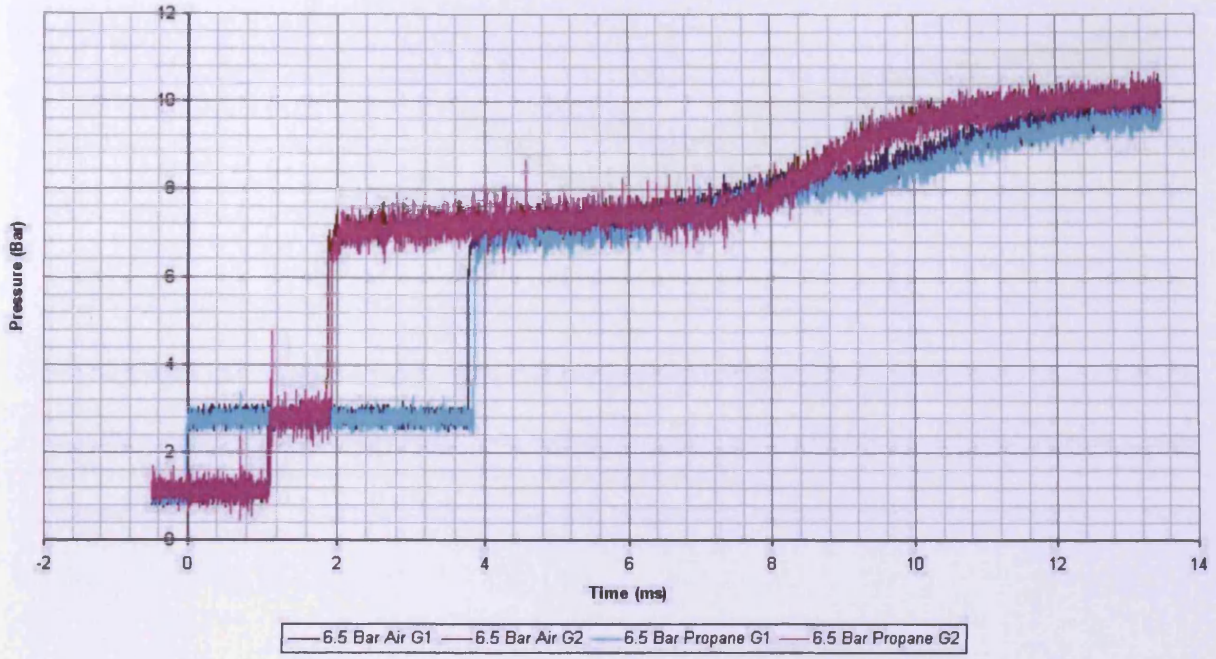

Figure 5.12: Propane Hemispherical Face Results, M=1.60

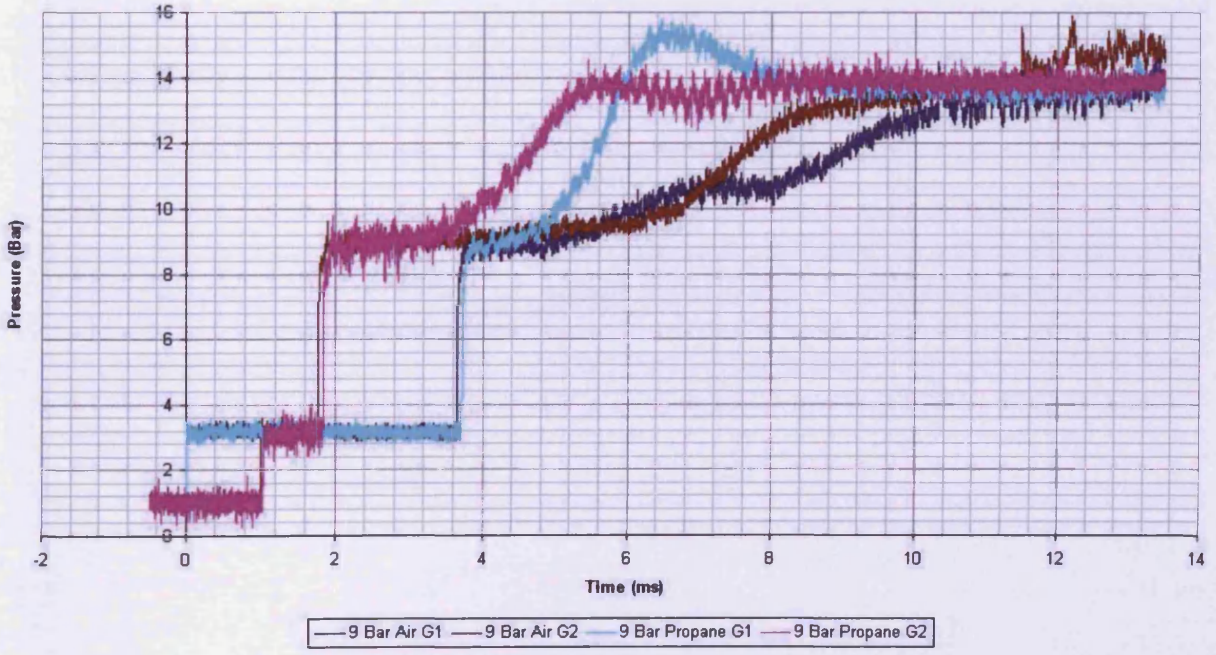

Figure 5.13: Propane Hemispherical Face Results, M=1.70

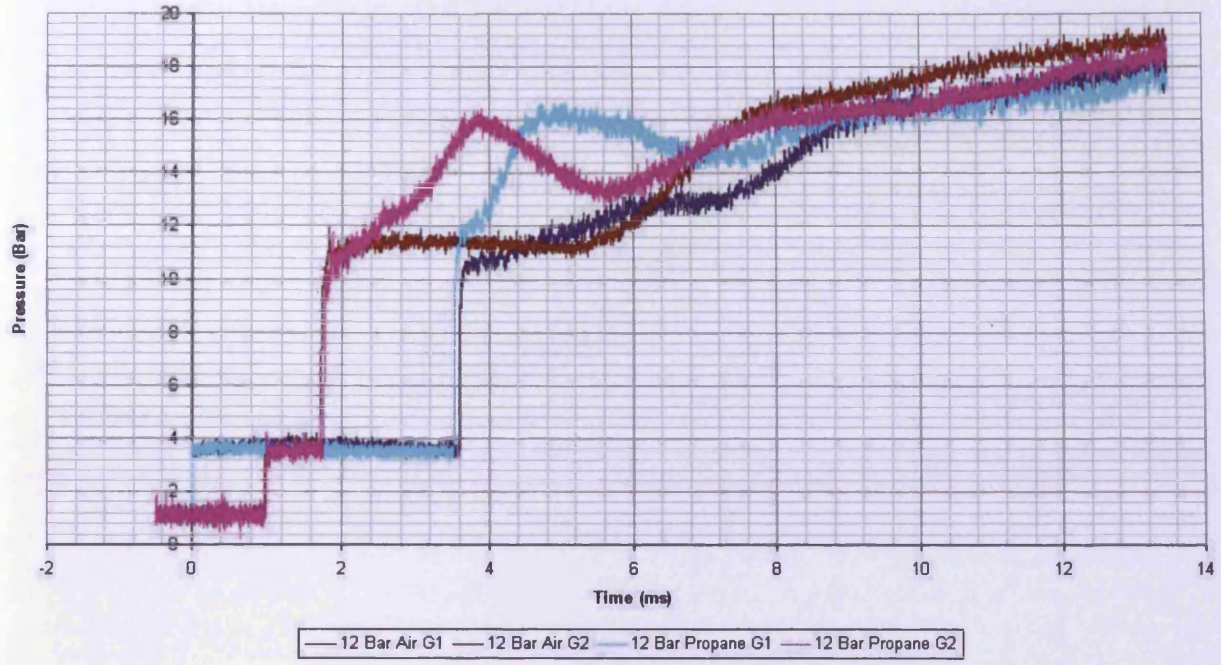

Figure 5.14: Propane Hemispherical Face Results, M=1.83

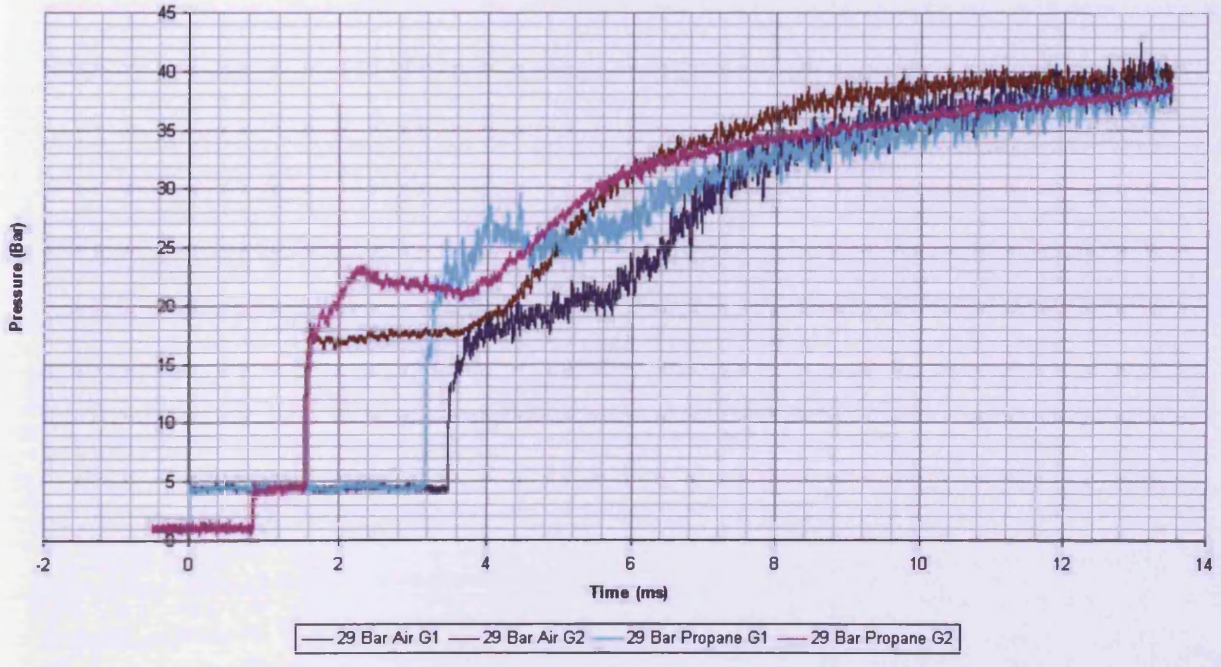

Figure 5.14: Propane Hemispherical Face Results, M=2.00

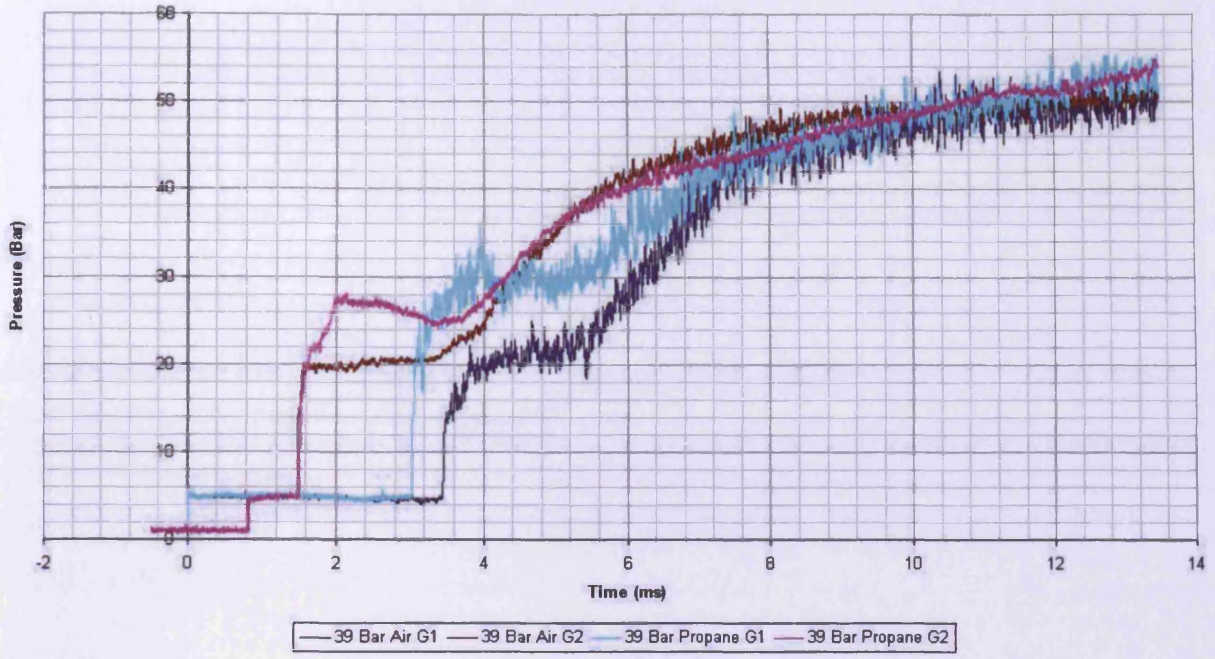

Figure 5.15: Propane Hemispherical Face Results, M=2.08

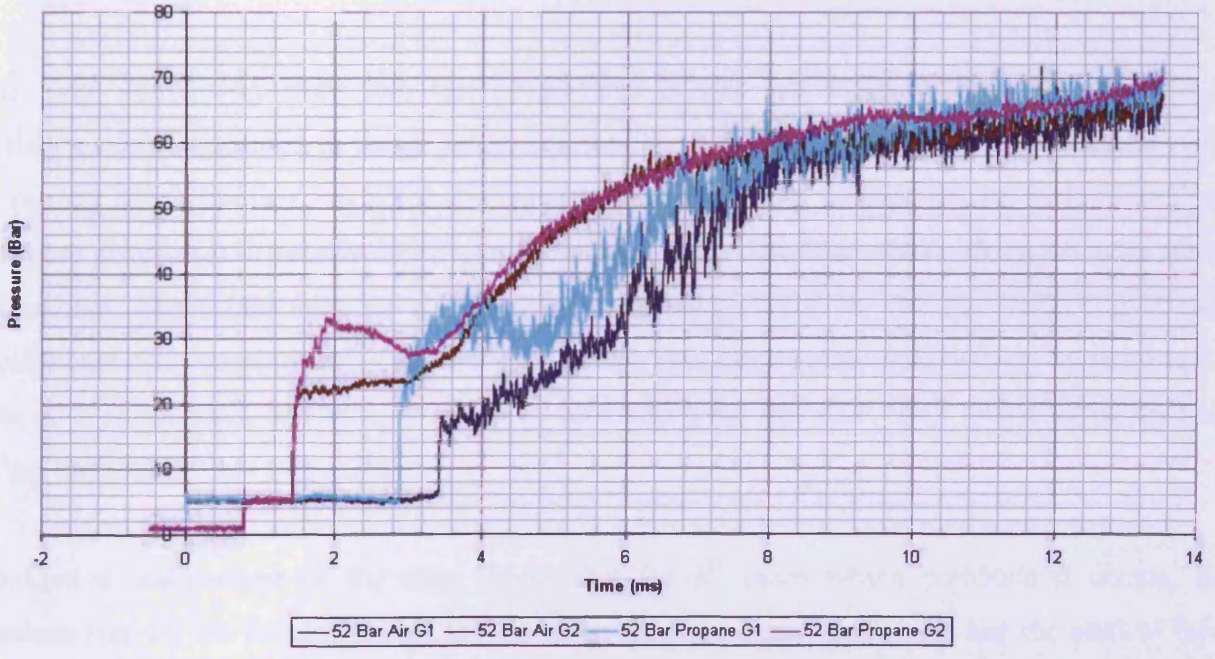

Figure 5.16: Propane Hemispherical Face Results, M=2.16

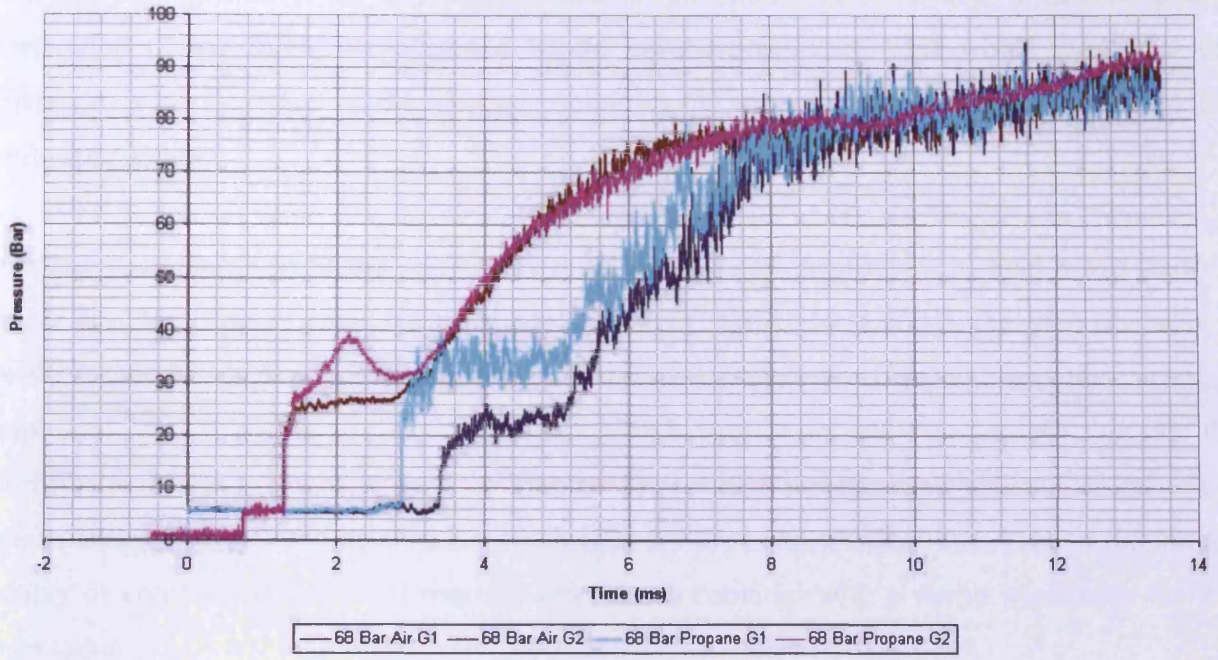

Figure 5.17: Propane Hemispherical Face Results, M=2.23

5.3.4 Propane: Results Discussion

The main conclusion from this test programme is that whilst shock focussing resulted in initiation of deflagrations in many cases, and that these deflagrations became more intense with increasing Mach number, no detonation was achieved utilising propane as the fuel. Apart from the more prominent differences between the shaped faces described above, there are more subtle differences. These can only be observed by comparing results for the two reflecting at each incident shock strength directly against each other. This can be done qualitatively by plotting the data on a single axis, and quantitatively by examining the raw data. This two-pronged analysis forms the basis of this discussion.

Qualitative comparison of the data shows that for all cases where combustion occurs, the pressure rise for the hemispherical face is faster than for the conical face. For the conical face, the rise time further away from the reflecting wall (Gauge1) is less than it is closer to the wall (Gauge2), suggesting that the combustion event is becoming stronger as it travels along the tube. For the hemispherical face, the rise time is greater at Gauge2 for the M=1.70, M=1.83 shock waves, but less for the M=2.0, M=2.08 and M=2.16 shock waves. This suggests that for the weaker shockwaves the combustion event is strengthening with time/ distance along the shock

tube in a similar manner to the conical face, but for the stronger shocks it is weakening slightly. Although an explanation for this phenomenon is not intuitively obviously, it may be due to acceleration of the shock wave caused by the combustion event. This would mean that the difference is in fact due to the change in the shock wave as opposed to a change in the combustion event.

Quantitative comparison of the pressure rises of the faces for each incident shock wave shows a greater rise for Gauge1 than Gauge2. Also apparent is that for Gauge1 the pressure ratio is greater for the hemispherical face than it is for the conical face. For Gauge2, the picture is not so simple. At M=2.0 and M=2.08, the pressure rise is greater for the conical face than for the hemispherical face, whereas at M=2.16 they are almost identical (pressure ratios: Conical = 1.4; Hemispherical = 1.49) and at M=2.23 it is higher for the hemispherical face. Due to the limited number of comparison points, it was not possible to come up with a sound hypothesis for this observation.

The obvious anomalies in the above results are for the conical face at incident shock M=1.70 and M=1.83. The fact the long combustion pressure rise is not present for the hemispherical face suggests that this is an effect of the reflecting geometry as opposed to the incident shock. An explanation for this can be found by considering the growth of the flame during reflection of the shock wave.

As the conical face narrows down to a point the shock focussing is greater than that for the hemispherical face, as demonstrated by the difference in successful initiation at M=1.60. However because of this, the resulting flame is present in only a small proportion of the whole cross section of the shock tube, the flame must grow along the radius of the shock tube as well as along it's length. This would explain the general observation of lower combustion pressure ratio and longer combustion rise time for the conical face. As in Section 5.3.4, the M=1.7 incident shock with the hemispherical face also has a slightly elongated pressure rise with minimal pressure drop-off. This result can also be explained by this hypothesis.

5.4 Hydrogen Test Programme

Table 5.2 shows the experimental test matrix for the stoichiometric hydrogen combustion programme. The test programme for the flat and hemispherical faces were limited due to the reasons given in Section 5.4.1 and 5.4.3. The tests shown in Table 5.2 as repeated were conducted to enhance confidence in the boundary between deflagration and detonation.

Table 5.2: Hydrogen Test Matrix

Driver Pressure	Driver Pressure Ratio	Mach Number	Flat Face	Conical Face	Hemispherical Face
6.5	13	1.60		X (Repeated)	X
9	18	1.70		X (Repeated)	X (Repeated)
22	44	1.94		X	X (Repeated)
29	58	2.00	X	X	
39	78	2.08		X	
52	104	2.16		X	
68	136	2.23	X	X	

5.4.1 Hydrogen: Flat Face

Only two experiments were carried out with this configuration, M=2.00 (Figure 5.18) and M=2.23 (Figure 5.19). The M=2.00 incident shock wave was the first experiment conducted with hydrogen, and so this intermediate strength shock was used to ensure the experimental procedure was suitable. The pressure traces identify a deflagration, but as with the propane test programme, the flat face gave combustion after the arrival of the contact surface. After studying the results of the first experiment, the stronger shock wave was used to see if detonation was possible with the flat face. Again, no detonation occurred and combustion occurred after the arrival of the contact surface, but the deflagration began much earlier than with propane. A pressure rise was seen to begin only 2.6ms after the arrival of the reflected shock at Gauge2 (for propane this was 4.3ms).

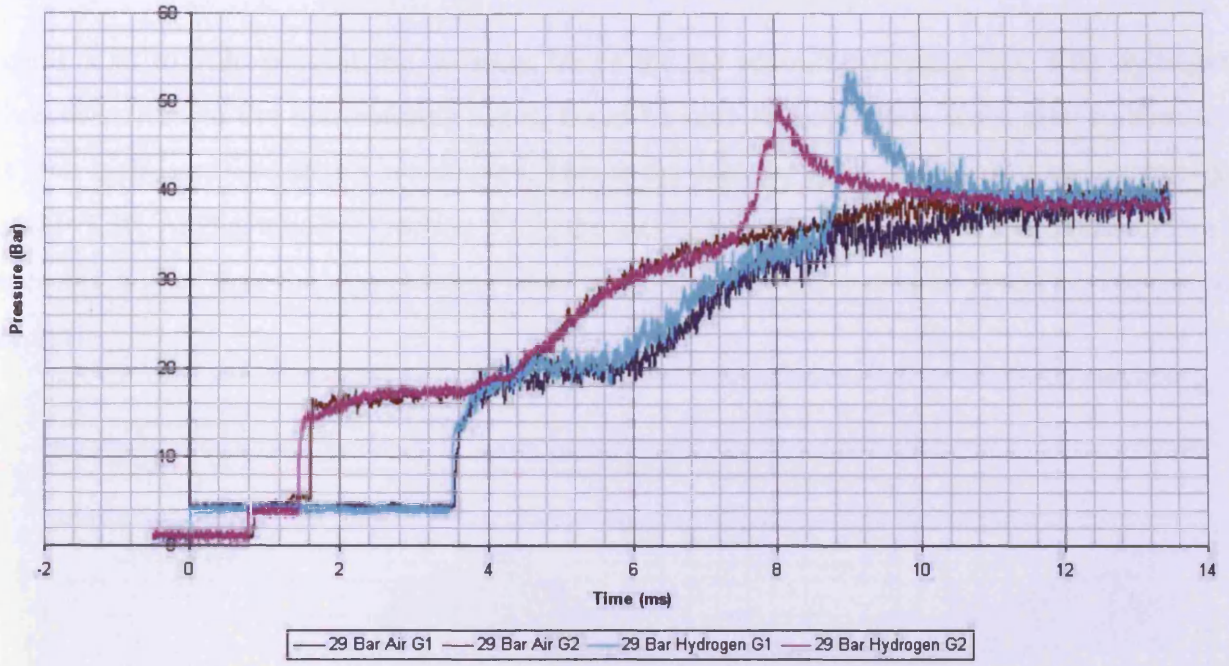

Figure 5.18: Hydrogen Flat Face Results, M=2.00

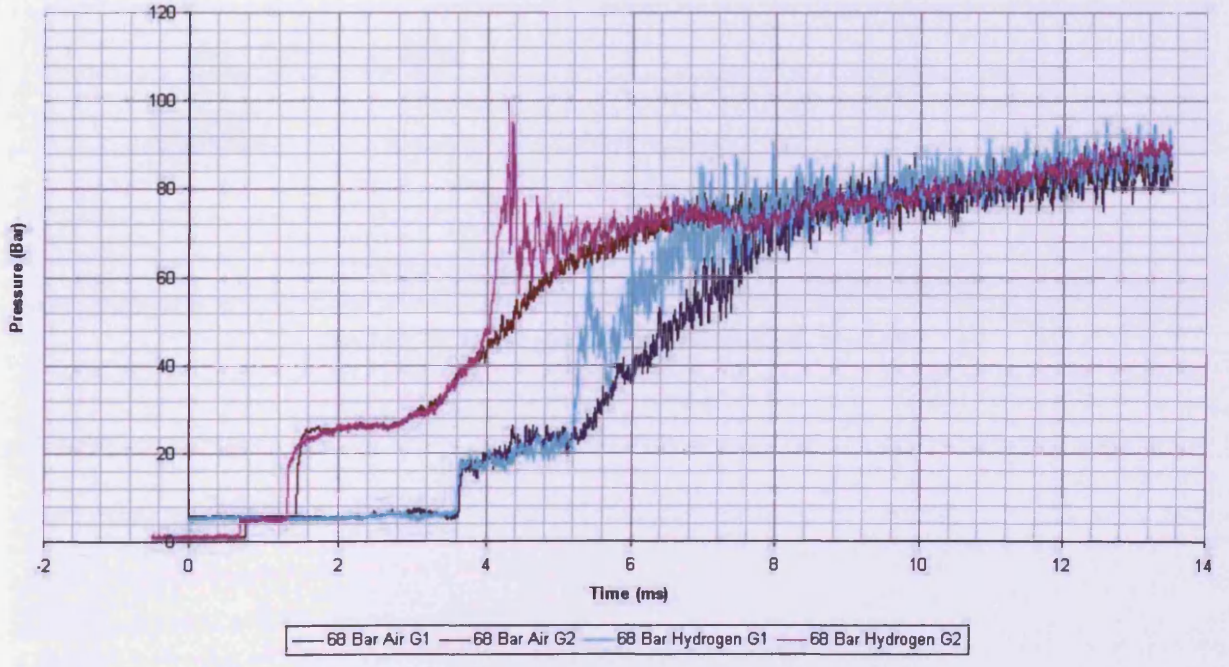

Figure 5.19: Hydrogen Flat Face Results, M=2.23

5.4.2 Hydrogen: Conical Face

Figures 5.20 to 5.26 present the pressure traces for the conical reflecting face with hydrogen. When compared to the non-reacting cases, it can be seen that all of the cases give combustion, but with hydrogen detonation is achieved. This is the case for all of the incident shocks stronger than M=1.70. As discussed in Section 5.2.3, the incident shock speed for the hydrogen mixture is noticeably higher than the non-reacting case, which is due to the increased speed of sound in the mixture.

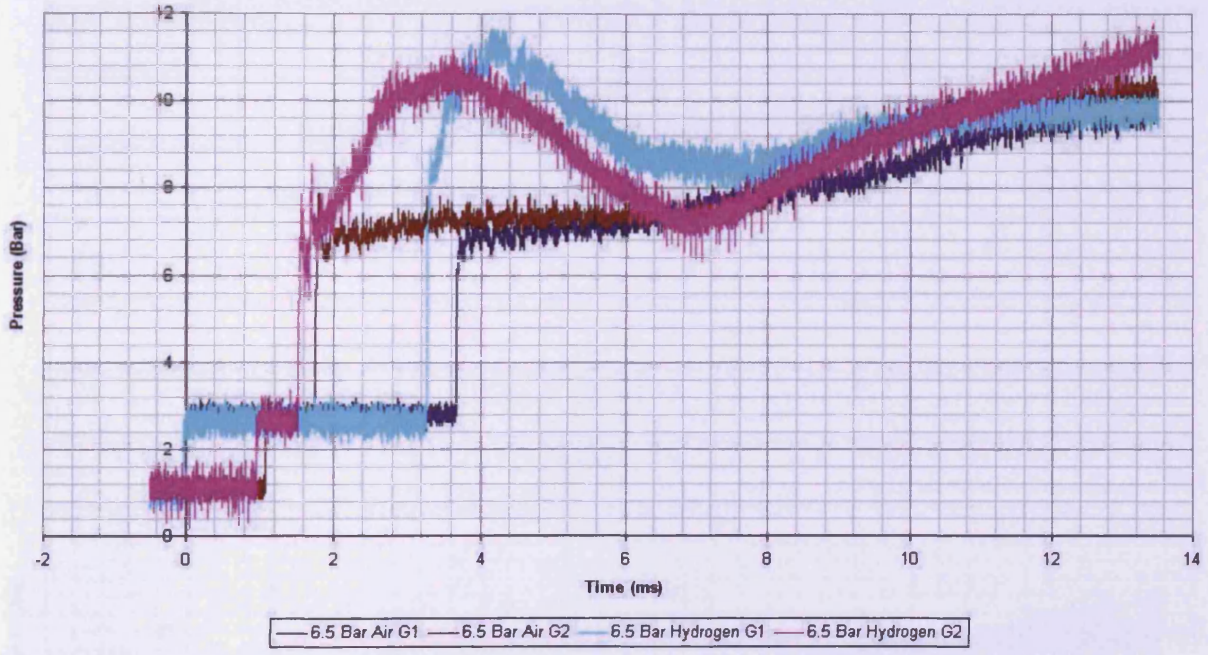

Figure 5.20: Hydrogen Conical Face Results, M=1.60

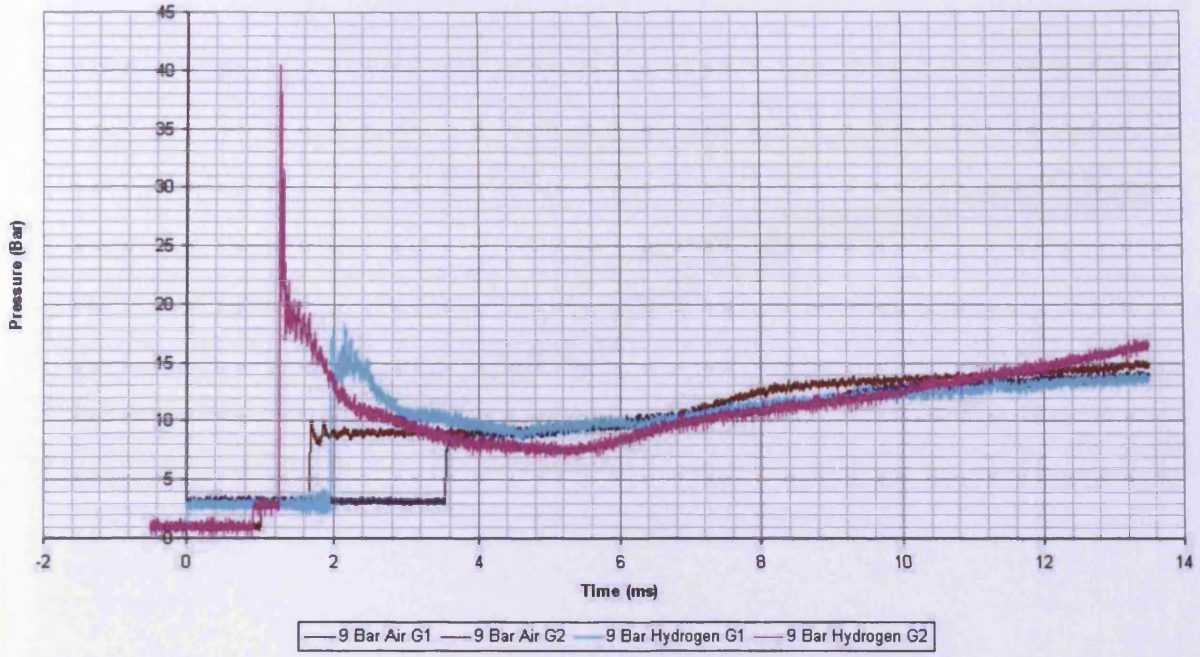

Figure 5.21: Hydrogen Conical Face Results, M=1.70

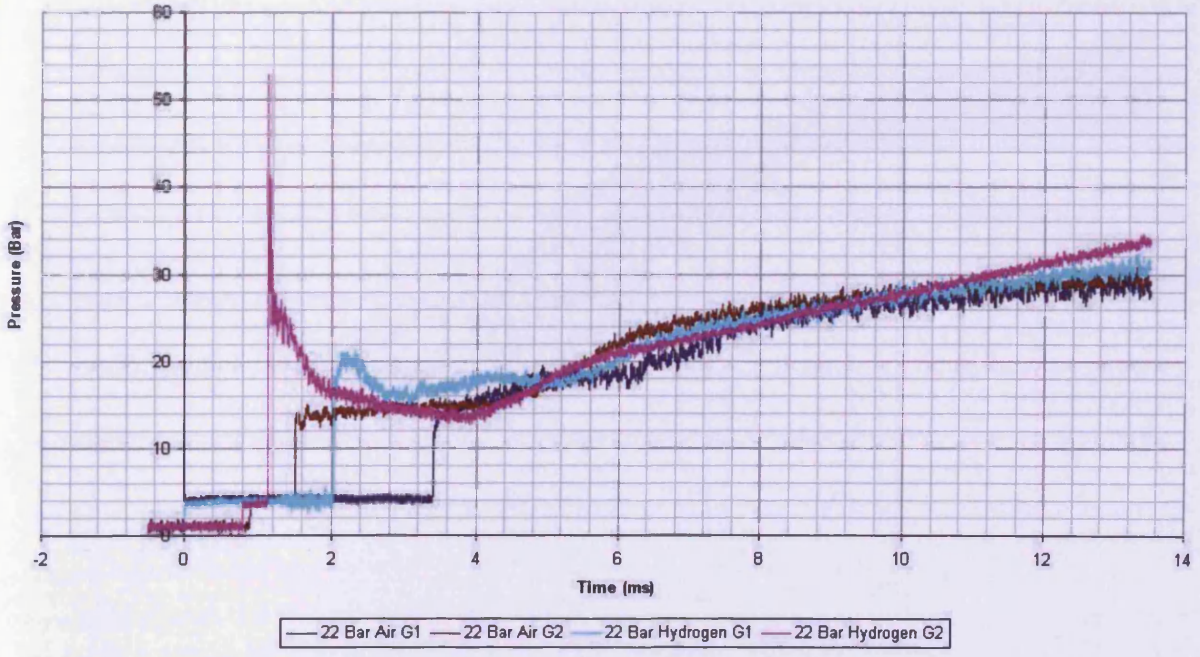

Figure 5.22: Hydrogen Conical Face Results, M=1.94

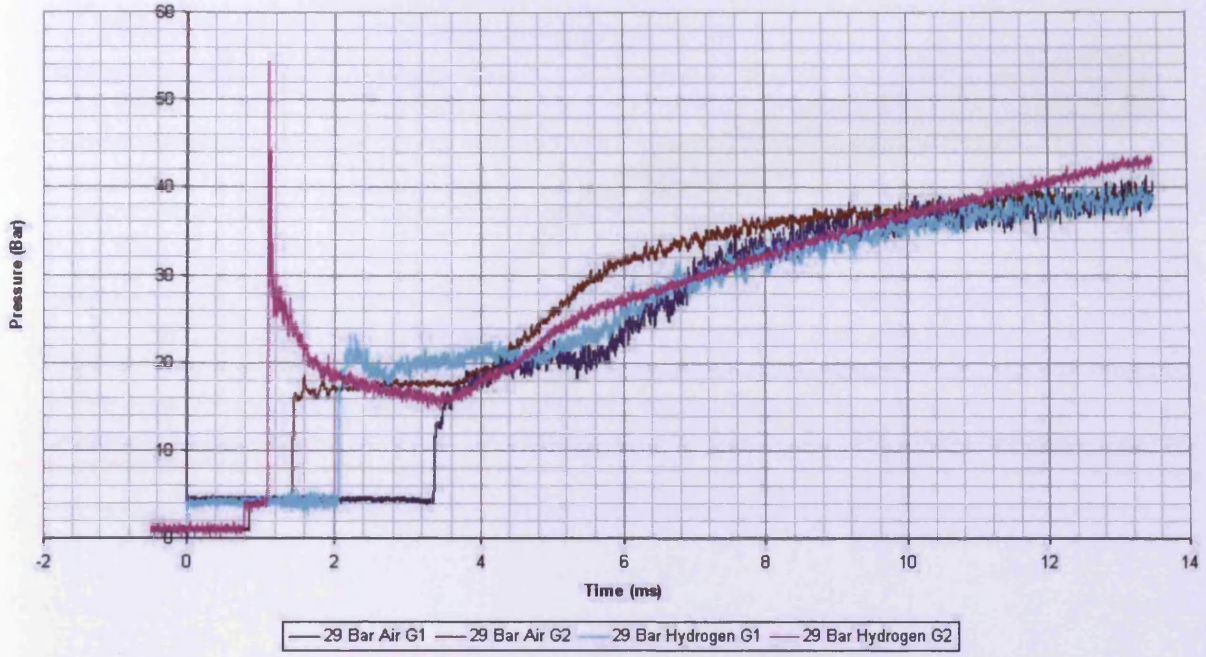

Figure 5.23: Hydrogen Conical Face Results, M=2.00

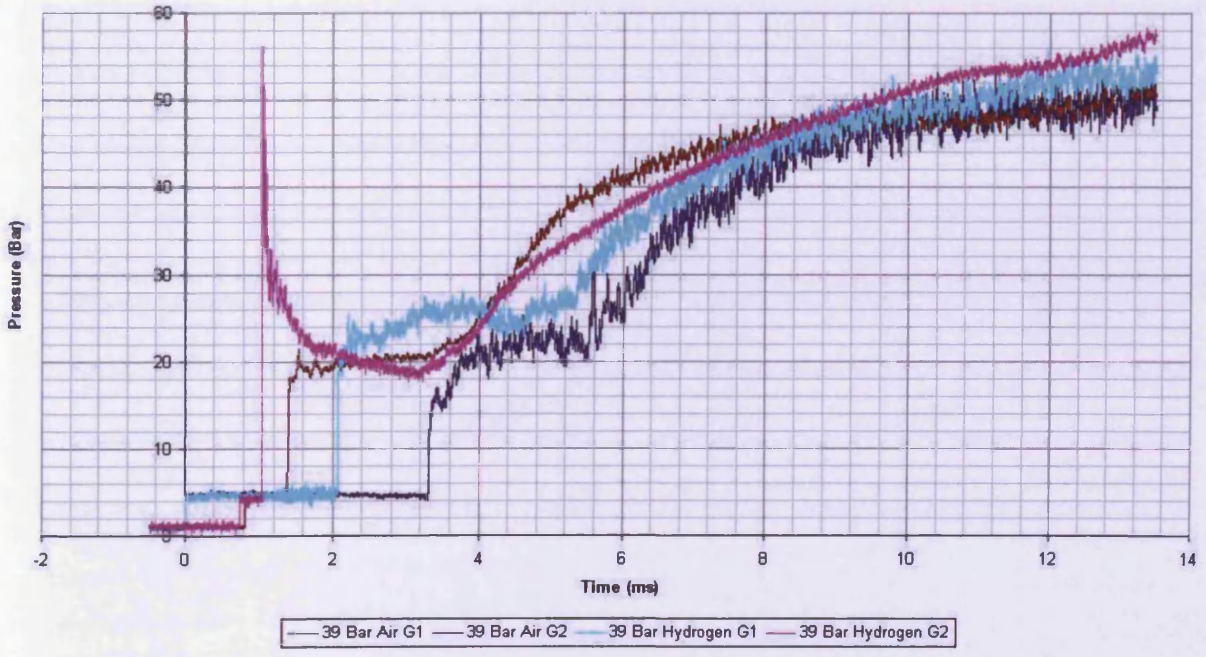

Figure 5.24: Hydrogen Conical Face Results, M=2.08

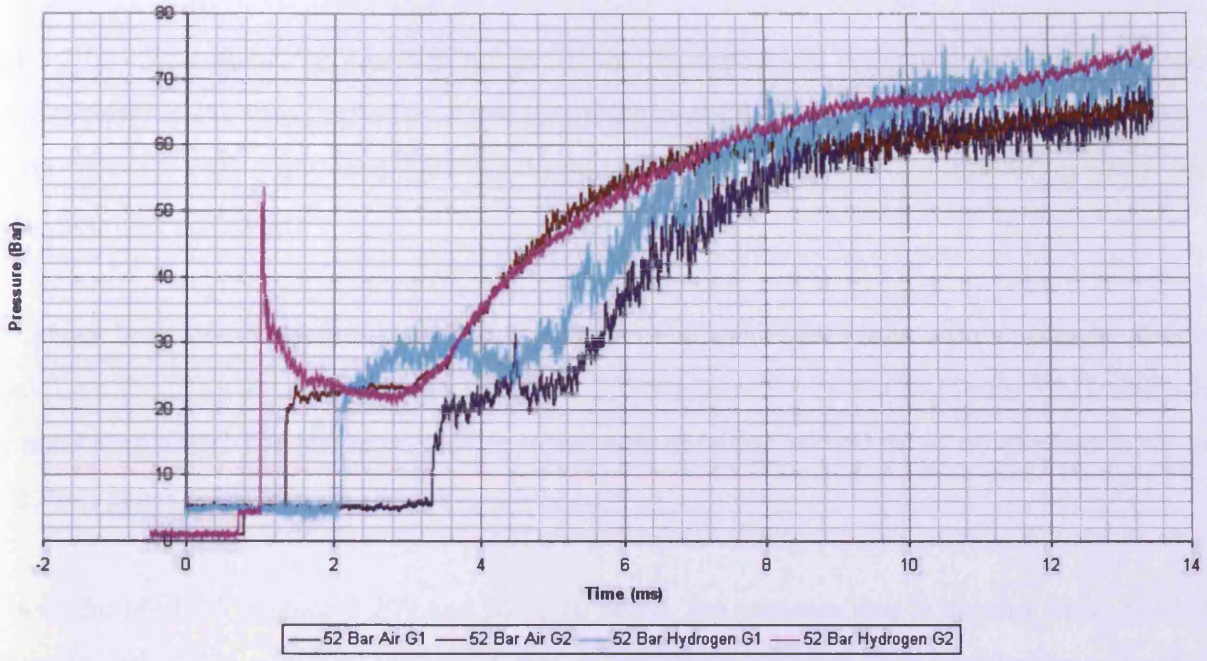

Figure 5.25: Hydrogen Conical Face Results, M=2.16

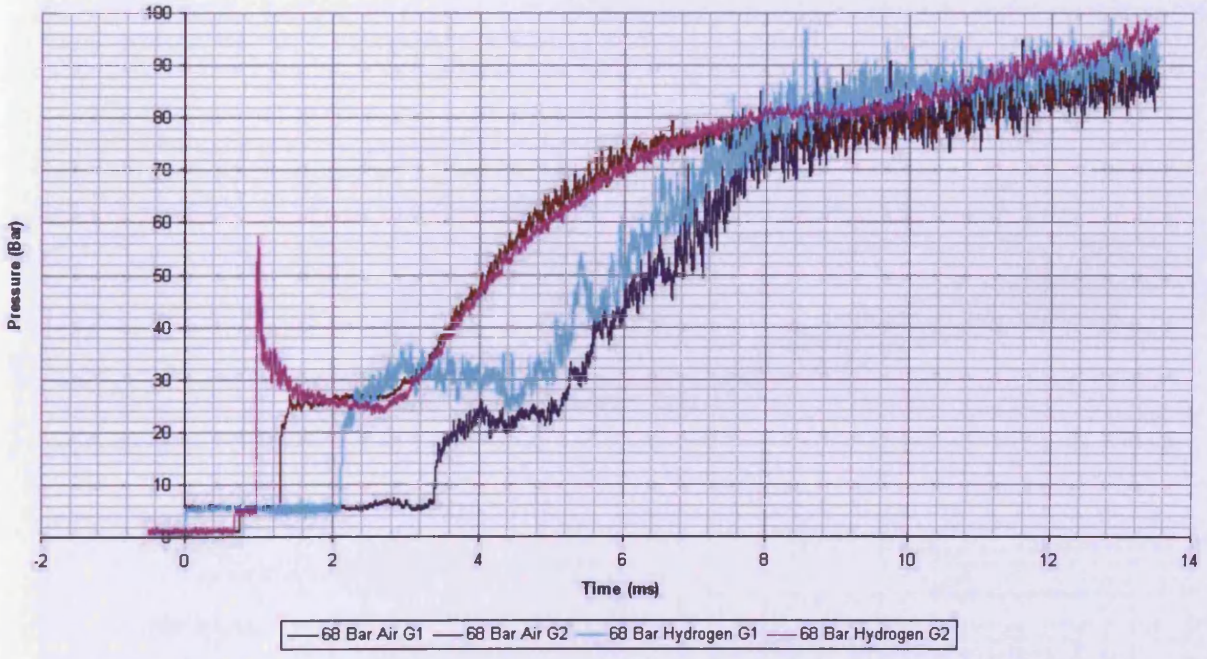

Figure 5.26: Hydrogen Conical Face Results, M=2.23

5.4.3 Hydrogen: Hemispherical Face

Figs 5.27 to 5.29 show the pressure traces for the hemispherical reflecting face with hydrogen. The test programme was limited to a maximum incident shock strength of M=1.94 as the results for the conical reflecting face had not highlighted any additional combustion physics once detonation was achieved.

The lower limit of detonation initiation for the hemispherical face was with a stronger incident shock than the conical face, M=1.94 (Figure 5.29) compared to M=1.60 (Figure 5.21), mirroring the results obtained for propane. Deflagration was obtained for the M=1.60 (Figure 5.27) and M=1.70 (Figure 5.28) incident shocks.

In both the M=1.60 (Figure 5.27) and M=1.70 cases, the pressure rise is quicker away from the reflecting wall. This suggests that the flame is becoming stronger as it travels along the shock tube. The results for the M=1.60 case show pressure oscillations during combustion. As the oscillations are only during the combustion event, this suggests that the oscillations are physical as opposed to being an error on the instrumentation and possibly caused by turbulence.

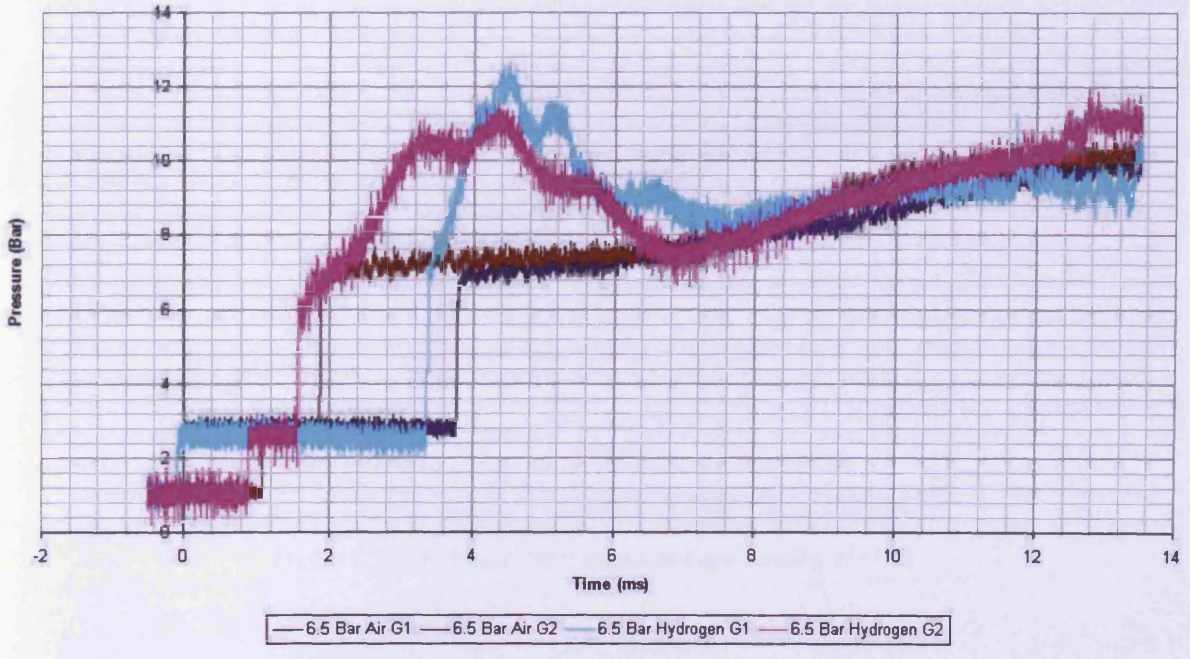

Figure 5.27: Hydrogen Hemispherical Face Results, M=1.60

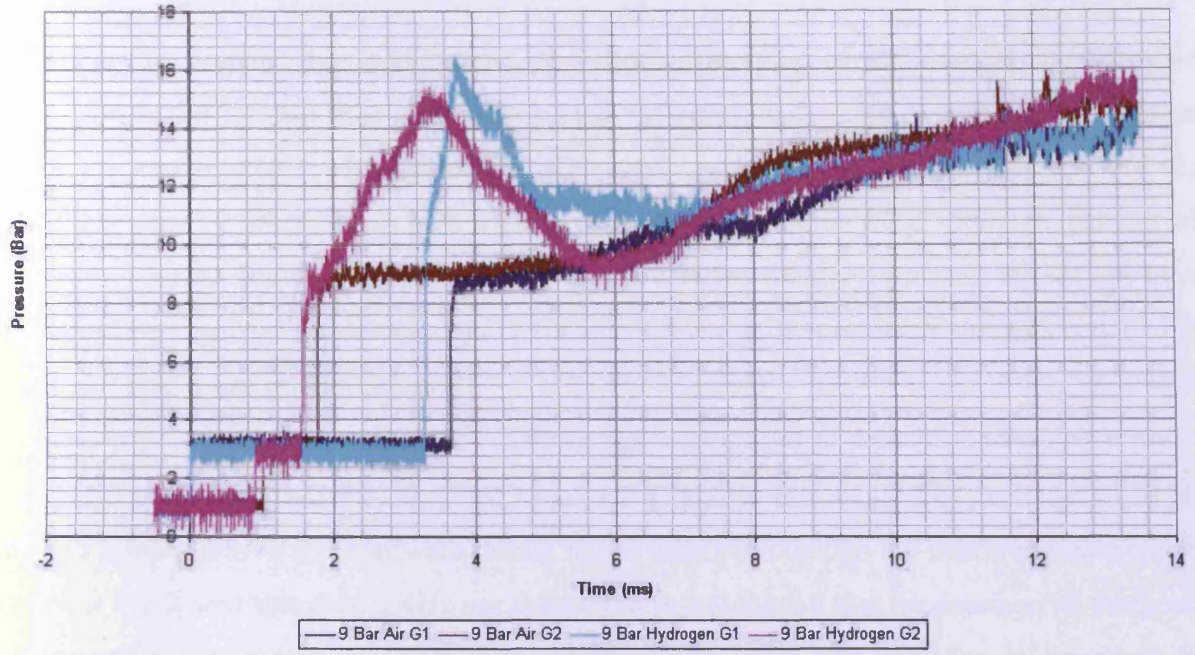

Figure 5.28: Hydrogen Hemispherical Face Results, M=1.70

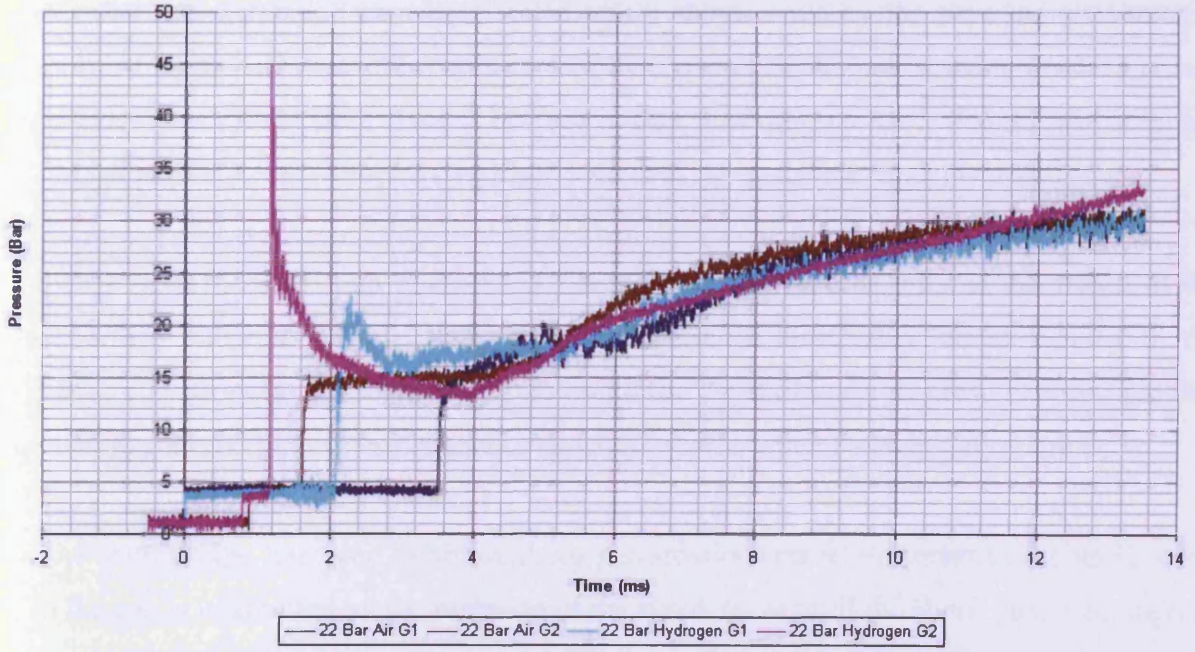

Figure 5.29: Hydrogen Hemispherical Face Results, M=1.94

5.4.4 Hydrogen Results Discussion

Similar to the propane test programme, the shock focussing of the conical face provided combustion during the run-time of the shock tube. However, in the case of hydrogen the pressure records are characteristic of a detonation. The sharp peak in pressure, which drops off very quickly has seen by other researchers when investigating detonation [62]. Although qualitatively the pressure jumps indicate detonation, the pressure ratios obtained (around 10-14) are lower than would be expected for detonation (20 for air, 40 for O_2). It is probable that this is due to the (relatively) low speed of data capture.

As explained in Section 3.4.3, the DAQ was set at a data rate of 2MHz per channel as this appeared a limitation of the hardware during initial tests even though the maximum data capture rate of the DAQ was stated as 5MHz per channel. It is understood that for commercial work with the appropriate equipment available, a minimum data capture rate of 5Mhz is suggested, but 10MHz is preferred [59].

The detonation pressure peak was only recorded on Gauge2. The pressure trace from Gauge1 suggests that the detonation has degenerated into a shock wave by the time the phenomenon reaches it. An explanation for this can be found by considering the non-reacting pressure traces. In these traces, the record from Gauge1 is much noisier than the trace from Gauge2, and at higher shock Mach numbers, the reflected shock pressure does not reach the same level as Gauge2.

It is thought that there are two phenomena causing these differences. First is the arrival of the contact surface, which is responsible for the difference in the reflected pressures recorded by the two pressure transducers. Second, which accounts for the difference in noise between the two transducer signals, is the non-instantaneous shock formation when the diaphragms are burst.

After the shock wave has been established, no perturbations travel upstream to the un-shocked gas, so the gas is unaffected by the presence of the shock wave until the shock passes through it. However, in the first few moments after the diaphragm has burst, the gas flow is subsonic and shock wave has not become established. During this time, perturbations from the release of the high-pressure driver gas travel into the test gas. This causes some gas movement in the driven section, leading to run-up section gas entering the test-section. It is thought that Gauge2 is in the region that contains run-up section gas in the test section, which is why the detonation has failed

by the time it reached the gauge. Although this is happening for the deflagrations in propane, it is thought that some of the effect is mitigated by the expansion of the combustion products, pushing the run-up gas back out past the gauge.

The results for the conical reflecting face can be compared to previous work by Penyazkov et al [63]. As in this study, they find that the presence of a shaped reflecting face enhances combustion initiation. However, the lower limit of detonation initiation for hydrogen with a conical face was found to be with an incident shock wave of M=2.01. This study found that detonation is possible at M=1.70. Although the shock tube diameters are different (76mm for Penyazkov compared to 98mm), this smaller tube diameter should not inhibit detonation initiation.

5.5 Summary

This Chapter has presented results for the reflected shock initiation of stoichiometric propane and hydrogen using three different reflecting faces. Propane was used as it has been shown to have similar detonation characteristics to aviation kerosene vapour, allowing the initiation potential of the reflected shock to be studied without the complications of two-phase mixing or heating required to study kerosene directly. Hydrogen was chosen due to its readiness to detonate and the availability of previous similar studies allowing the benchmarking of the new shock tube.

For propane, combustion has been recorded for all three reflecting faces although no detonation was apparent. For the flat reflecting face, the combustion event appears during a time frame when the exact composition in the fuel mixture is unknown. For the shaped faces, the conical face gives combustion with a weaker incident shock than the hemispherical face, however the combustion events appears stronger for the hemispherical reflecting face when equivalent cases are compared.

For hydrogen, combustion was obtained for the flat reflecting face. When compared to the equivalent propane cases, the combustion event is stronger for hydrogen, which is as expected given the relative reactivity of the two fuels.

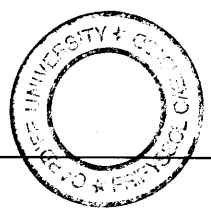

For the conical face detonation results were obtained with hydrogen. A lower limit for the incident shock strength that gave detonation was found. Differences in the detonation results obtained compared to other work have been found, which can be explained as limitations with the instrumentation.

For the hemispherical face detonation results were again obtained with hydrogen. The lower limit for detonation was found to be higher that for the conical face.

Chapter Six

Droplet Breakup in Steady and Pulsed Flows

6.1 Introduction

This Chapter details the work presented at ILASS 2008 [64] to characterise the droplet breakup process in steady and pulsed flows. It will present visual characterisation of the droplet breakup process in steady flows, and data on the nature of the secondary spray. The droplet breakup process is then studied in pulsed flows at conditions relevant to the work conducted in Chapter Seven, unlike previous similar studies which focus on more energetic conditions. This work suggests a relationship between the size of the initial droplets and spray produced, which is then used in Chapter Seven.

6.2 Background

6.2.1 Droplet Formation

In a volume of liquid, there are attractive forces between the molecules in the liquid. A molecule in the centre of a volume of liquid will experience this attractive force from all of its neighbouring molecules, and so all the forces cancel out. However, a molecule on the edge of a volume will experience an uneven force which is directed back towards the liquid leading to a stable volume. This force is known as Surface Tension (σ). When external forces, such as aerodynamic drag or gravity, acting on the volume of the liquid are greater than the surface tension, the volume of liquid (hereafter referred to as a droplet) will breakup.

A simplest example of this fragmentation is caused by gravity. Consider a volume of liquid in a vertical pipette with a droplet formed at the bottom. In this case, the surface tension between the liquid and pipette is overcome by the force of gravity acting on the droplet. When the droplet is small, the surface tension will be strong enough to hold the droplet onto the pipette. At a certain size, the weight of the droplet will be too great and the droplet will fall from the pipette. Equations 6.1 and 6.2 show that for the same liquid, the same orifice size and same gravitational field, each droplet will have the same diameter and mass [65]. This principle is implemented by the droplet generator (Section 6.3.1)

$$m_D = \frac{\pi d_o \sigma}{g} \qquad \text{Equation 6.1}$$

$$D = \left(\frac{6 d_o \sigma}{\rho_L g} \right)^{1/3} \qquad \text{Equation 6.2}$$

6.2.2 Droplet Breakup

Once a droplet is formed, it can itself be broken up into small droplets, known as daughter droplets or secondary spray. The droplet breakup process can be characterised by several non-dimensionless parameters, the most common of which is the Weber Number, We. The Weber number, given in Equation 6.3, relates surface tension and aerodynamic forces. There is a critical We below which droplet breakup will not occur [65], and it has been used in the paper by Pilch and Erdman [66] to distinguish between different droplet breakup regimes (Figure 6.1).

$$\mathrm{We} = \frac{\rho_a \mathrm{v}_{rel} \mathrm{D}}{\sigma} \qquad \text{Equation 6.3}$$

For combustion processes, it is important to have a measure of the ratio of the surface area to the volume of the fluid as greater surface area facilitates combustion. When a droplet breaks-up, the daughter droplets will not be of the same size (as shown experimentally in Sections 6.6 and 6.7). This type of multi-sized spray can be best represented for combustion processes by a hypothetical value known as the Sauter Mean Diameter (SMD). The SMD of a spray is defined as the particle size that has the same surface area/volume ratio as the spray.

Although the droplet breakup process has been well characterised, there is limited work on characterisation of the secondary spray. Although advanced laser techniques such as Phased-Doppler Anemometry (PDA) have been used to characterise more complex phenomenon such as fuel injectors, there appears to be little work on the more fundamental single droplet breakup process.

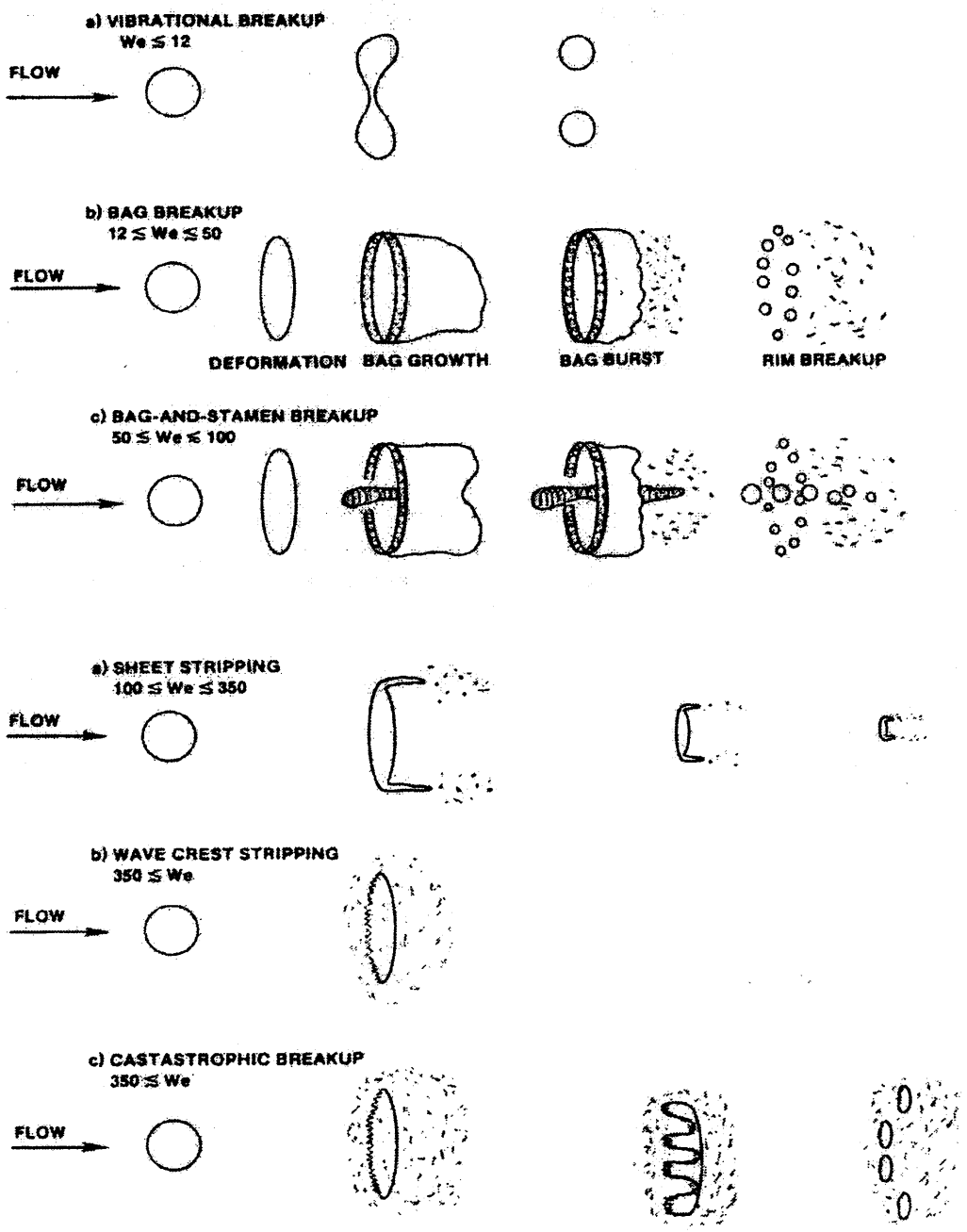

Figure 6.1: Droplet Breakup Processes [66]

Park et al [67] used a PDA based particle sizing system (Phase Doppler Particle Analyser, PDPA) to measure the breakup of diesel droplets in a cross-flow at three Weber numbers. The droplets were produced using a piezoelectric droplet generator and had a diameter of 184μm. In the bag breakup regime (We=68), they found that the secondary spray size was highly position dependent. At higher Weber numbers (We=153, We=383), the results showed that the size of the secondary spray was less size dependent, with the SMD around 20μm.

Joseph et al [60] conducted high speed videography of approximately 2.5mm water and other fluid droplets in a shock tube. The Weber numbers studied were all very high (over 15,000) due to the size of the droplet and the Mach numbers used (M=2-4). The images show that although the breakup is generally catastrophic in nature, there is evidence of bag-type breakup even at these very high Weber numbers.

6.3 Equipment

6.3.1 Droplet and Air Flow Generator Evolution

The experimental rig underwent several revisions over the course of the experimental programme in order to extend its operational range. The first set-up is shown in Figure 6.2. The set-up consists of a reservoir of water connected to a pipette via rubber surgical tube, held on a standard laboratory retort stand. The flow of water was controlled via a thumbscrew.

Figure 6.2: Original Retort Stand Set-up

The airflow was provided by house air at 7 barG, although this could be reduced (thus reducing the air flow velocity) using a gas regulator. The air exited from a solid tube, approximately 30cm

long and 22mm diameter (which can be seen in Figure 6.3). At first, the flow of air from the end of the tube was very weak, however the addition of "flow straighteners" in the form of plastic drinking straws, increased the strength of the airflow dramatically. Through control of the delivery air pressure, the air velocity from the exit of the tube could be varied between 20 and 45 ms^{-1}, measured using a hot-wire anemometer.

Although the use of a reservoir and pipette to produce water droplets appears rudimentary, it was possible to control the flow reasonably well to produce droplets at the required rate. In fact, off-the-shelf droplet generators were appraised during the course of the project, but their performance was no better than the system in use, so were not pursued.

In order to generate pulsed air flows, the equipment shown in Figure 6.3 was used. This consisted of a metal plenum chamber (light blue) with a solenoid valve at the inlet and outlet. The inlet was connected to the house air, and the outlet fed into the same plastic tube used for the constant flow experiments. The plenum was "charged" by opening the solenoid valve between the plenum and the house air supply. Once the plenum had been filled, the valve was closed. To fire the system, the second valve was opened, firing the charge of air. The air pulse could not be characterised using a hot wire anemometer, so was characterised using a Laser Doppler Anemometry (LDA) system (Section 6.5.2).

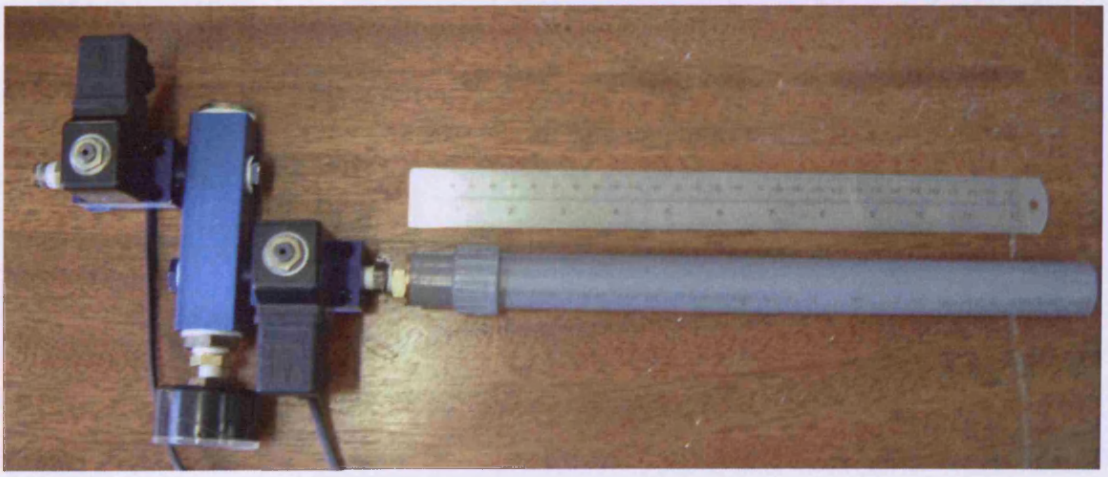

Figure 6.3: Air Pulse Generator

With the pulsed air flow system, the timing of the droplet and air pulse became crucial. At first, this timing was attempted manually, however unsurprisingly this proved to be a virtually impossible task, with less than a 10% success rate in the air pulse "hitting" the droplet successfully. A system that would allow the air pulse to hit the falling droplet consistently and

repeatedly would offer the ability to use a more sophisticated laser-diagnostic technique – such as Phase-Doppler-Anemometry (PDA), allowing detailed spatial and temporal resolution of the secondary spray.

Such a system was developed utilising an infrared droplet counter (Figure 6.4). This registered the droplet when it passed through the sensor and generated a TTL signal pulse. This pulse was used to control the solenoid valve at the outlet of the plenum. The delay before the TTL was generated could be controlled using the associated electronic control system. After implementation of the droplet counter, the success rate of the air pulse hitting the droplet increased to over 90%.

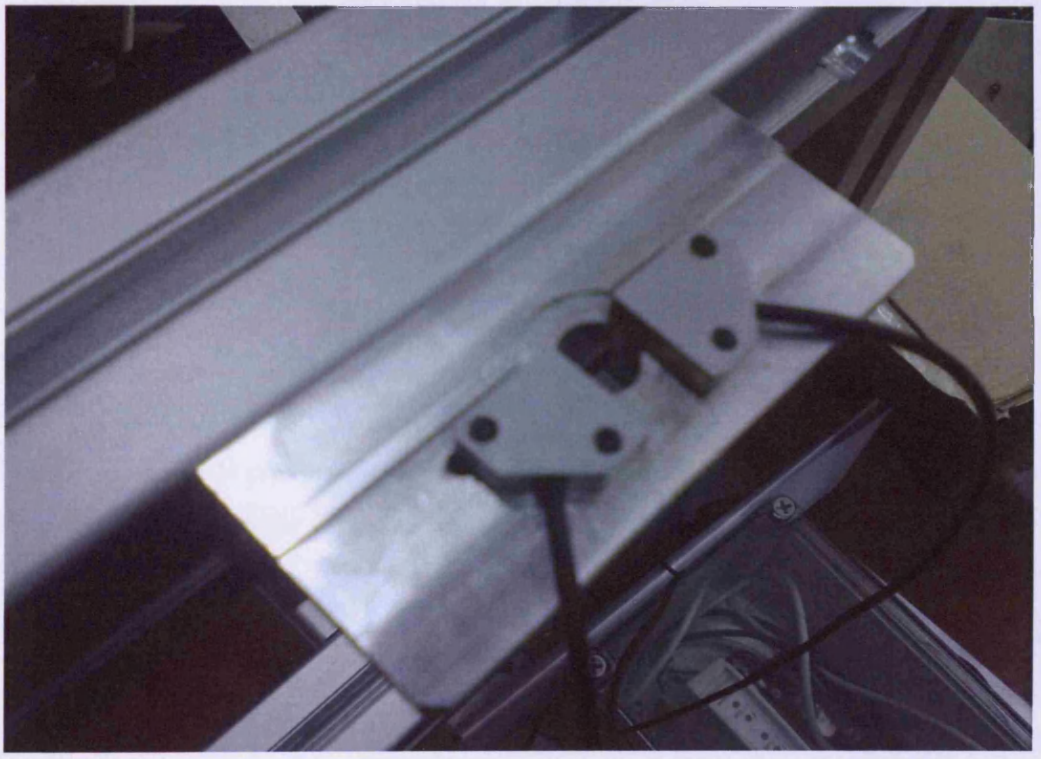

Figure 6.4: Infrared Droplet Counter

The final modification to the rig was to change the laboratory retort stand for a bespoke stand. Although the retort stand functioned adequately, the addition of the droplet counter required much higher precision in the alignment of the pipette, droplet counter and air flow system. The new stand allowed much more precise adjustments in height for example. When attempting to adjust the height using the retort stand, due to the nature of the clamps, there was a need for re-alignment. In addition when tightening the clamping screws, there was the likelihood of an additional slight movement. The presence of a bespoke stand for these droplet breakup

experiments allowed for quicker and easier set-up as all the required components were integrated onto the stand.

Figure 6.5: New bespoke Retort Stand

An image of the stand is given in Figure 6.5. It was made from 2" aluminium Core Bore and Groove System sections. It consisted of a 1m pillar attached to a 250mm by 300mm base (Figure 6.6). The base has 4 adjustable feet to allow levelling of the base in conjunction with the level indicator. In addition, the base has 4 countersunk holes to allow the base to be fixed to the Malvern Spraytec Particle Sizer (Section 6.3.3), which was used for secondary droplet sizing measurements. The pillar had four arms attached to it: the top one with a small circular stand to hold the reservoir of fluid (Figure 6.7a); the second with an adjustable pipette holder (Figure 6.7b); the third with a plate to allow the droplet counter to be mounted correctly (Figure 6.7c), and the fourth with an additional arm mounted at 90° to allow fixing and adjustment of the air flow generator (Figure 6.7d).

Figure 6.6: Stand Base

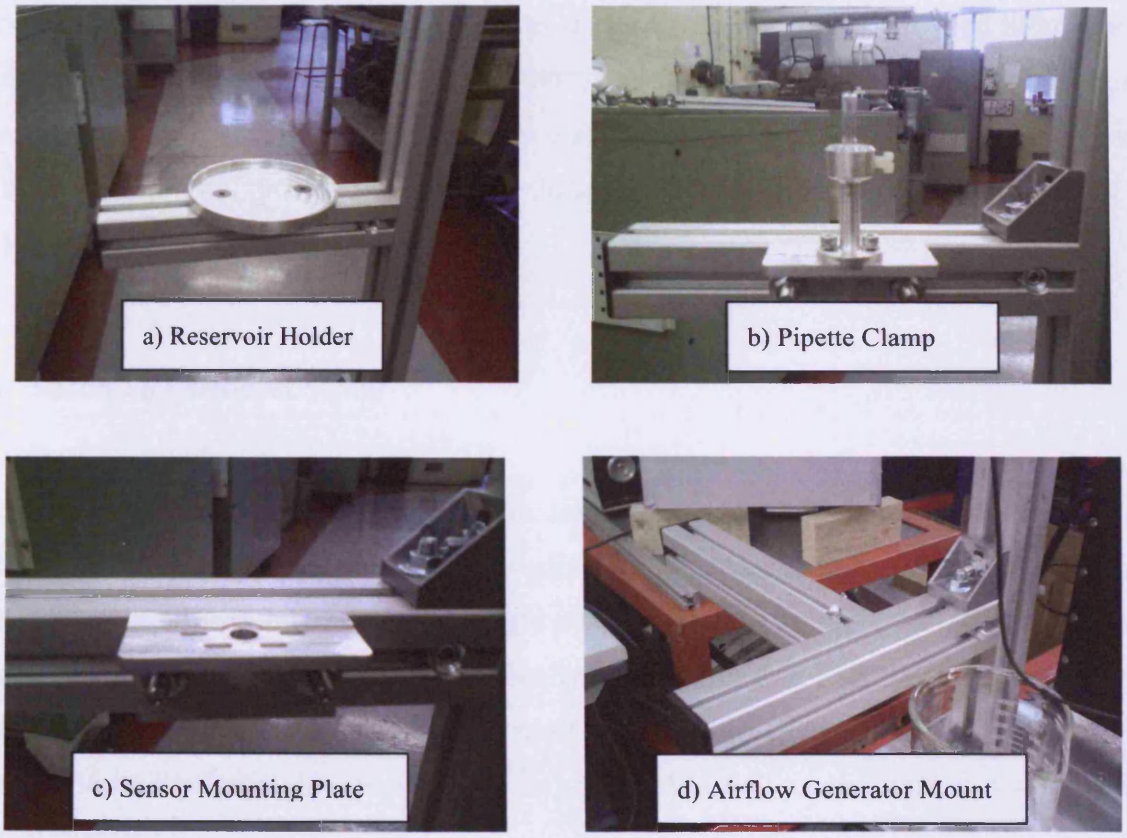

Figure 6.7 Retort Stand Components

6.3.2 High Speed Videography

In order to capture the breakup process, a Photron Fastcam APX RS Mono High Speed Camera was utilised. The camera has a black and white image sensor capable of a maximum frame rate of 250,000 frames per second (fps) and a maximum resolution of 1 megapixel (1,024 x 1,024 pixels), although these are not possible together. The maximum frame rate at 1 megapixel is 3,000 fps, and frame rates up to 10,000 are possible at a resolution of 0.25 megapixels (512 x 512

pixels). All videography was carried out at 3,000 fps in order to take advantage of the full resolution. The results were saved as videos by the camera's software, from which still images could be extracted for presentation.

The shutter speed is also fully adjustable up to a minimum duration of 1/500,000 seconds. Initially, due to lighting constraints, the shutter speed was set to 1/6,000 seconds. However, the improvement of the lighting system (described below) allowed this to be decreased to 1/15,000 seconds, aiding the improvement of picture quality.

At first, in an attempt to eliminate the flicker associated with a.c. mains powered light sources, a d.c. lamp was used. This set-up required relatively long shutter openings, caused blurring of the images captured. An a.c. halogen flood lamp was then used, which was much more powerful than the d.c lamp. This provided much better lighting with no flicker detected, producing some excellent image resolution.

6.3.3 Secondary Droplet Sizing

Measurements of the secondary droplets were conducted using a Malvern Instruments Spraytec Particle Sizer (Figure 6.8). The Spraytec works using a technique called of laser diffraction particle sizing. It utilises the principle that light passing through a droplet will be diffracted, with the angle of diffraction increasing logarithmically with decreasing particle size. The intensity of the light diffracted also decreases with angle scattered. Therefore, small droplets will scatter light at high angles will a low light intensity, and larger droplets will scatter light at shallower angles with higher intensity.

The Spraytec uses a Fourier lens, which focuses light diffracted at the same angle to be focused to the same point on the detector. This allows the Spraytec to measure droplet sizes from 0.1μm to 850μm. The beam width of the Spraytec is 20mm so will only capture a sample of the flow. However as the flow has been seen to be broadly axisymmetric (Figure 6.9) this does not introduce any significant further error into the results.

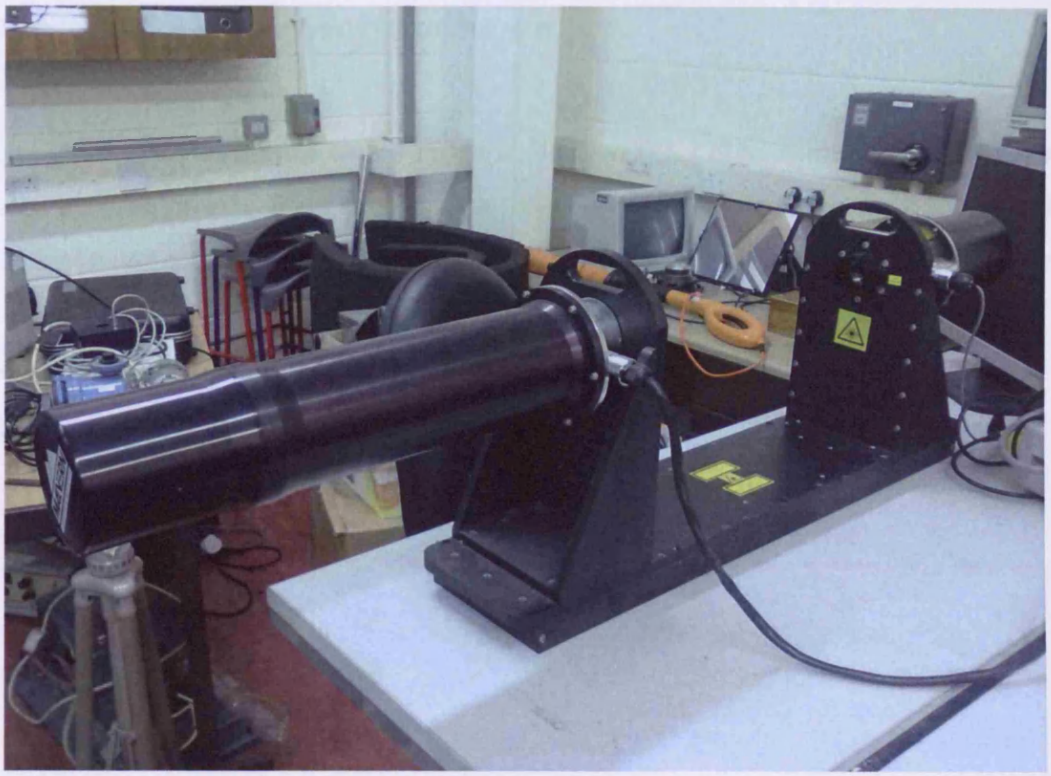

Figure 6.8: Malvern Instruments Spraytec Particle Sizer

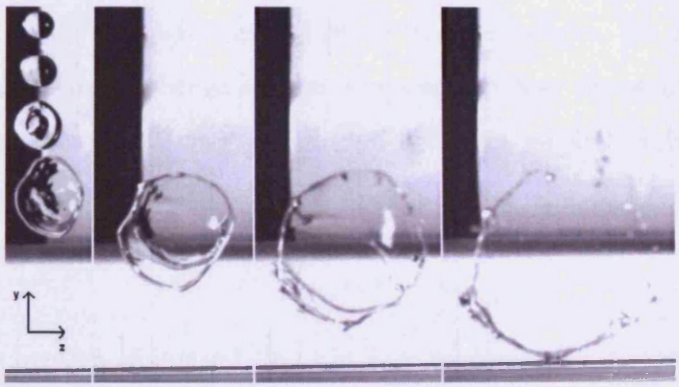

Figure 6.9: Front on visualisation of Bag Breakup

6.4 Experimental Methodology

The experimental procedure can be split into three sections, the first for setting-up of the droplet and gas flow generators, the second for setting-up of the high-speed camera, and the third for setting-up of the Malvern Spraytec.

6.4.1 Droplet and Air Flow Generator Set-Up

The droplet generator was set-up as described in Section 6.3.1. The thumbscrew was loosened to allow water into the pipette from the reservoir. Once droplets began to form and fall from the pipette (into a beaker under the pipette), the thumbscrew was tightened to stop the water flow.

With the original retort stand two additional retort stands were used to hold the air generator. A spirit level was used to ensure that the airflow was straight and level. The air generator and droplets generator were then aligned by allowing a slow stream of droplets to fall, and moving the air generator to the correct position.

6.4.2 High-Speed Camera Set-Up

As discussed in Section 6.3.2, the videography was recorded at 3,000 fps to utilise the maximum resolution of the camera. To ensure that the camera was set up correctly, several steps had to be taken. Firstly, with the camera in position and ready to take images, the lighting conditions that would be used in the experiments were set up. The camera was focussed approximately to the position of the water droplets and spray, and then the appropriate shutter speed was selected which allowed sufficient light into the camera aperture (Section 6.3.2). The camera was then focussed more accurately using the point of a pin.

Once the camera was correctly focussed, the pin was replaced by a metallic engineering ruler. This allowed the spatial size of each pixel to be calculated, so size measurement of the droplets formed by the droplet generator were possible. Although the position of the camera to the droplet generator could be noted, it was necessary to perform this set-up routine every time the camera or rig was moved to retain the quality of the images.

6.4.3 Particle Sizer Set-up

The Spraytec was set-up so that the laser beam was level with the airflow, which was done by spraying water into the airflow. The water was carried into the laser beam by the airflow, where it diffracted the laser light, enabling the beam to be seen.

Two background readings were necessary to calibrate the Spraytec. The first was to assess the electrical noise present in the system, and the second was to find the amount of background light present and ensure correct alignment of the laser and detector. To assess the noise, the detector ring was covered so that no light could enter it, and the noise assessment was begun on the system software. To assess the background light and ensure correct alignment, the detector was uncovered and extra lights in the room (that would not be required during experiments) were switched off. The background light assessment was then begun on the system software. Individual detector readings below 50 and an average below 25 are recommended for optimal operation of the Spraytec.

The Spraytec was run at its maximum data acquisition rate of 2,500Hz. Several triggering methods were available, but the one that proved most reliable was Transmission Triggering, with a transmission level of 90%. Data was gathered from the time of the first signal until no more signals were detected, then presented as accumulated data over the time window of measurement by the Spraytec software.

6.5 Preliminary Results

6.5.1 Droplet Size

The size of the droplets was calculated by pixel counting. Figure 6.10 shows an example of one of the five images used. The droplets were determined to have a diameter of 3.0±0.1mm. Figure 6.11 shows a stream of droplets, at a rate higher than was used in experiments, demonstrating the repeatability of the droplet generator.

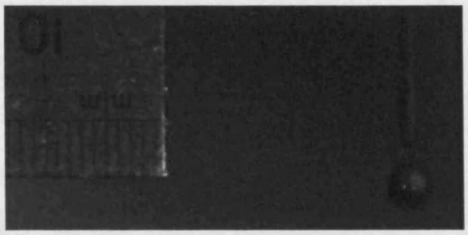

Figure 6.10: Droplet Sizing Example Image

Figure 6.11: Repeatability of Droplet Generator

6.5.2 Pulsed Air Flow Characterisation

As mentioned in Section 6.3.1, the steady airflow was characterised using a hot-wire anemometer. This method was not suitable for the pulsed airflow, so an alternative method, LDA, was used. LDA is a non-intrusive technique which allowed measurement of the velocity of seeding particles introduced into the pulsed flow. The velocity of the system used was a Dantec Flowlight 1D system, operated in backscatter mode, with a laser wavelength of 532nm. Light from a laser is split into two beams, with the frequency of one beam shifted by 40MHz to allow measurement of directionality. The two beams cross to form a control volume, forming an interference pattern. Seeding particles in the flow reflect the light, which is collected by the receiving optics. The frequency of the light can be used to calculate the velocity of the particles.

The airflow was seeded using a nebuliser producing micrometer sized water droplets. The nebuliser was placed at the exit of the pulse generator, and the control volume of the LDA system was aligned using a traverse. Velocity measurements were taken at 10mm intervals from the exit of the pulse generator (hereafter referred to as the z-axis), with the pulse generator fired

25 times for each position. Peak flow velocities were easy to define for z=50mm to z=150mm but between z=10mm and z=40mm the results were not as expected. It is thought that this is due to the LDA system registering large numbers of slow moving droplets which are following ambient air entrained into the flow. Results for these cases could be calculated by using a polynomial extrapolation of the successful results (Figure 6.12). The agreement between the polynomial and the measured data points was good, with $R^2 = 0.9902$. The final velocities are shown in Table 6.1, along with the calculated Weber number for a 3mm water droplet.

Table 6.1: Pulsed Flow Velocities

Z Position (mm)	Velocity (ms^{-1})	Calculated/Measured	Weber number
10	195	Calculated	1,893
20	175	Calculated	1,525
30	160	Calculated	1,275
40	145	Calculated	1,047
50	125	Measured	778
60	120	Measured	717
70	105	Measured	549
80	90	Measured	403
90	80	Measured	319
100	70	Measured	244
110	65	Measured	210
120	50	Measured	124
130	45	Measured	101
140	45	Measured	101
150	40	Measured	80

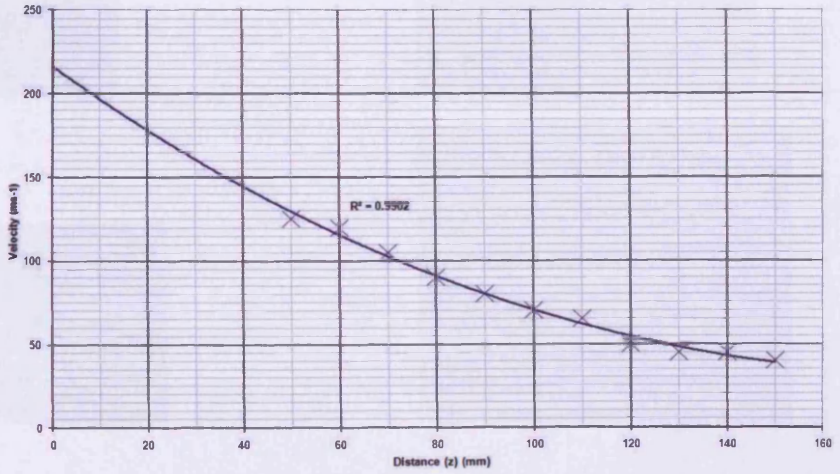

Figure 6.12: LDA Velocity Extrapolation

6.6 Constant Flow Results

Figure 6.12 shows the breakup of a droplet in a constant airflow with We = 20. Each image is approximately 10 frames, or 3.33ms apart (also true for Figures 6.13, 6.15 and 6.17). The images provide an excellent example of bag breakup and show the initial deformation of the droplet, the formation of a disk, the formation and growth of the bag, the bursting of the bag and the final breakup of the bag ring. From the final two images, it can be seen that there are a large number of visible droplets which are not small enough to support a deflagration or detonation.

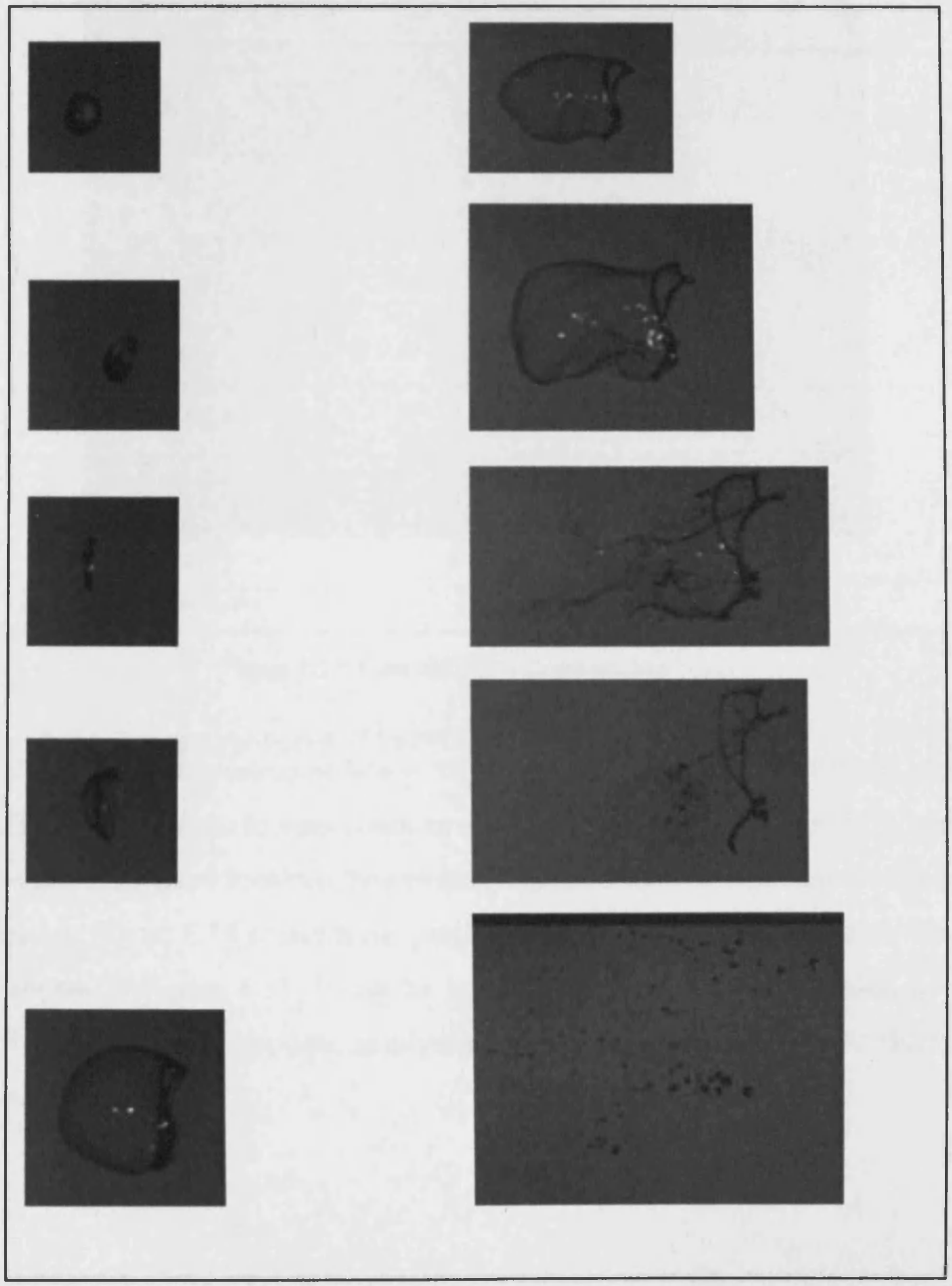

Figure 6.12: Constant Flow Breakup, We = 20

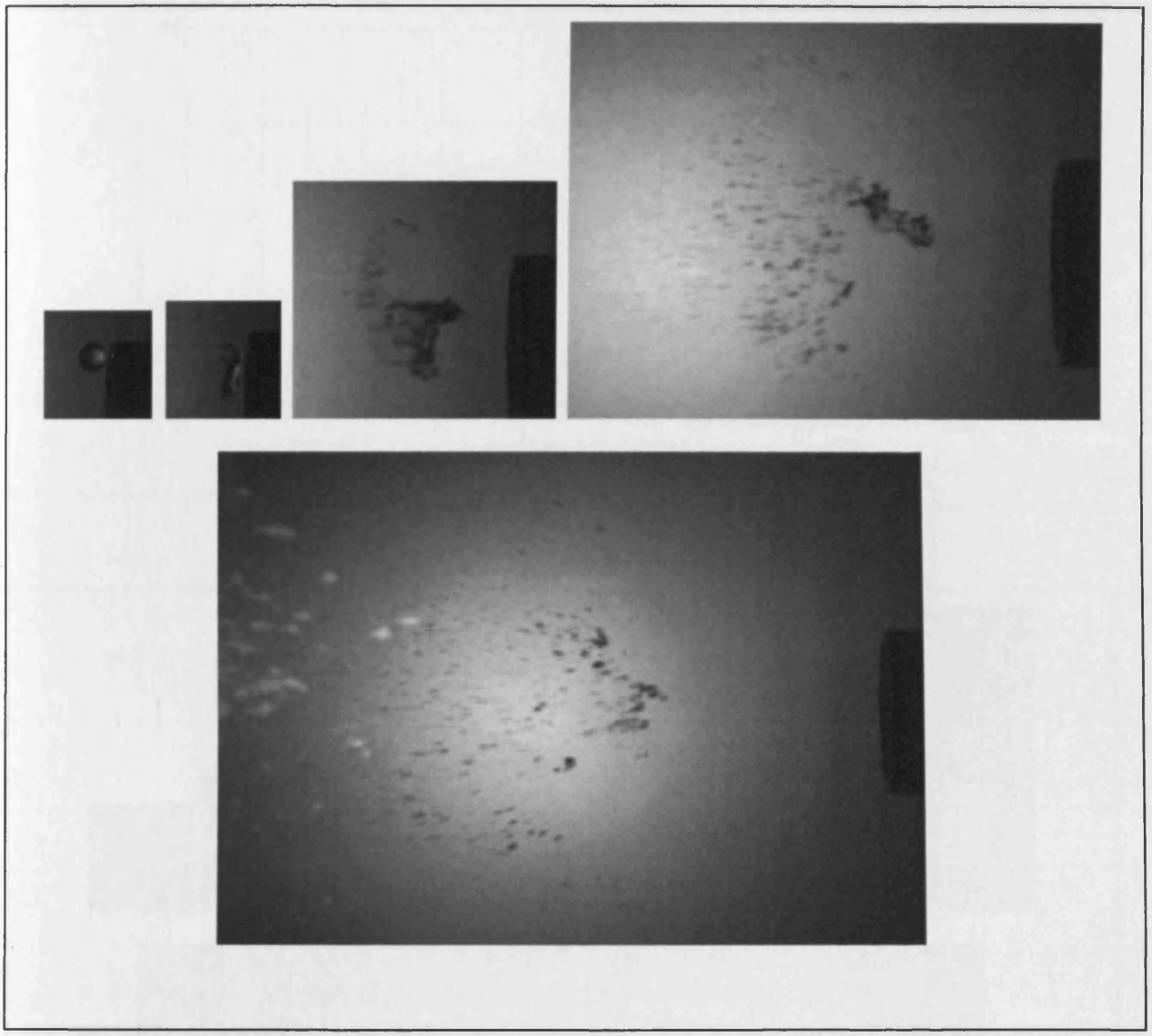

Figure 6.13: Constant Flow Breakup, We = 51

Figure 6.13 shows droplet breakup at We = 51 which is in the bag and stamen breakup regime (Figure 6.1). The clarity of the images is not as sharp as in Figure 6.12 due to the increased speed of the airflow and associated breakup, however it is possible to see the bag breaking and stamen in the third image. Figure 6.14 presents the particle size distribution recorded by the Spraytec for the breakup shown in Figure 6.13. It can be seen that a very small proportion of the expected normal distribution has been capture, implying that the majority of the secondary spray is in droplets greater than 850μm.

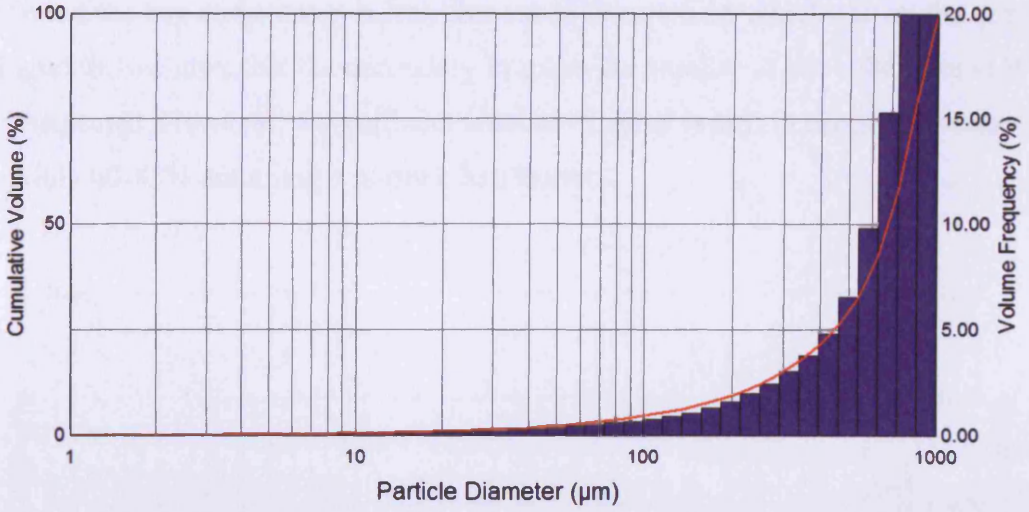

Figure 6.14: Particle Size Distribution. Constant Flow, We = 51

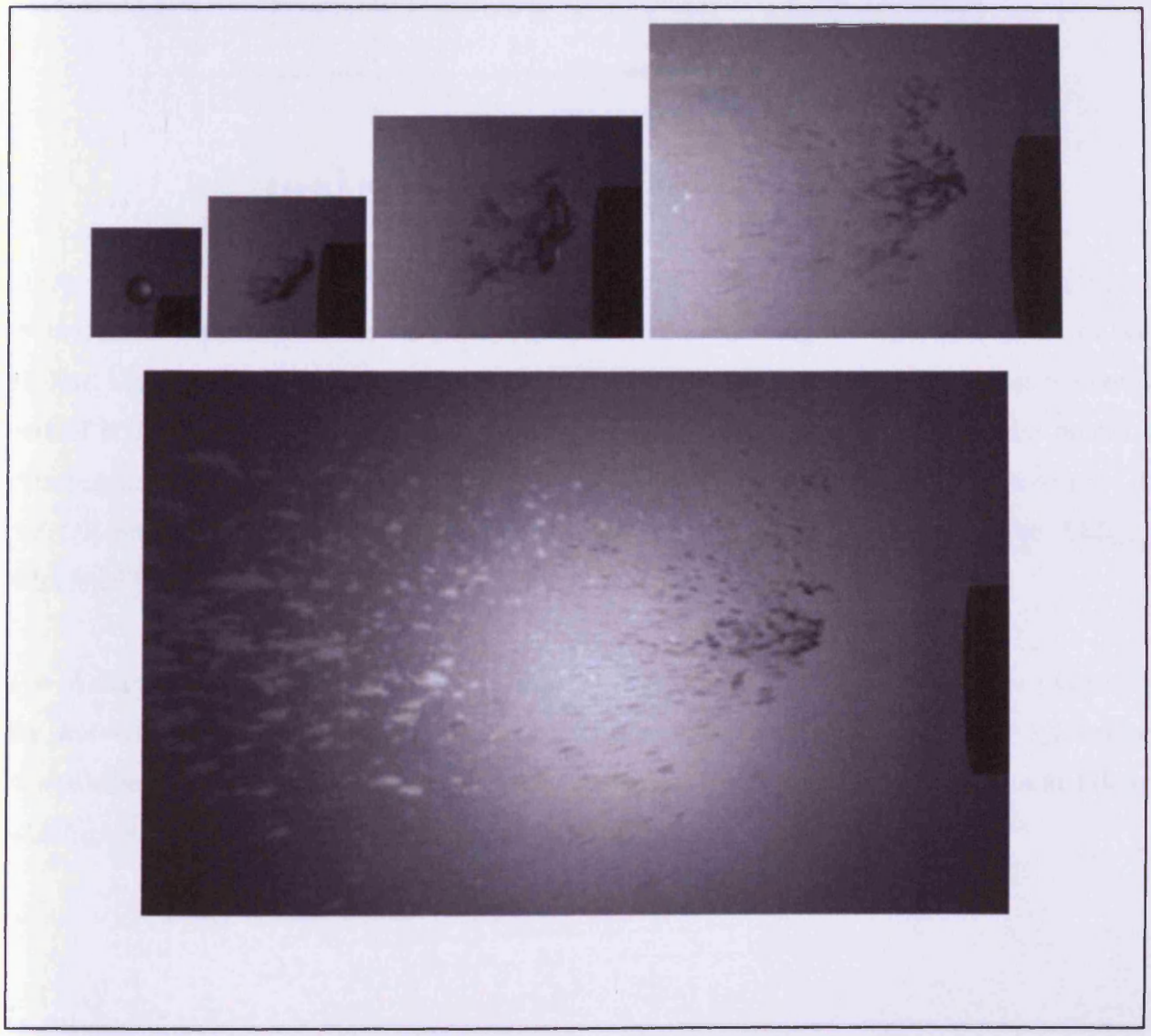

Figure 6.15: Constant Flow Breakup, We = 84

The formation of the bag and stamen is less obvious in Figure 6.15 which shows the breakup for We = 84. Figure 6.16 shows that the secondary droplets are smaller at We = 84 than at We = 51, as would be expected. However, a significant amount of spray is still in droplets greater than 850μm, possibly 40-45% assuming a normal distribution.

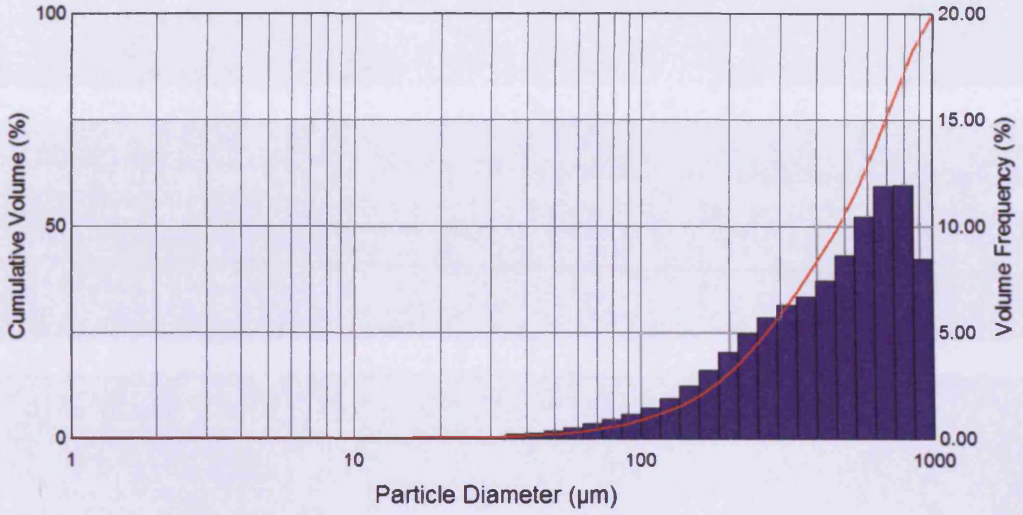

Figure 6.16: Particle Size Distribution. Constant Flow, We = 84

Figure 6.17 shows the breakup for the case of a high Weber number. This was achieved by removing the plastic tube from the airflow generator and replacing it with a short piece of 6mm air-line. From the images it can be seen that the droplet begins to breakup as soon as the bottom part of it enters the air stream. Stripping of the droplet continues until the droplet breaks up catastrophically. Figure 6.18 shows the particle size distribution for this case. It can be seen that the full normal distribution is captured, with the peak around 60-70μm and an SMD, as calculated by the Spraytec software, of 17.2μm.

The Weber number could not be calculated exactly as the air velocity could not be measured – the hot wire anemometer did not have an appropriate range, and the LDA system was unavailable. However the velocity can be estimated using isentropic flow calculations at 170ms^{-1}, which gives an approximate Weber number of 1,200.

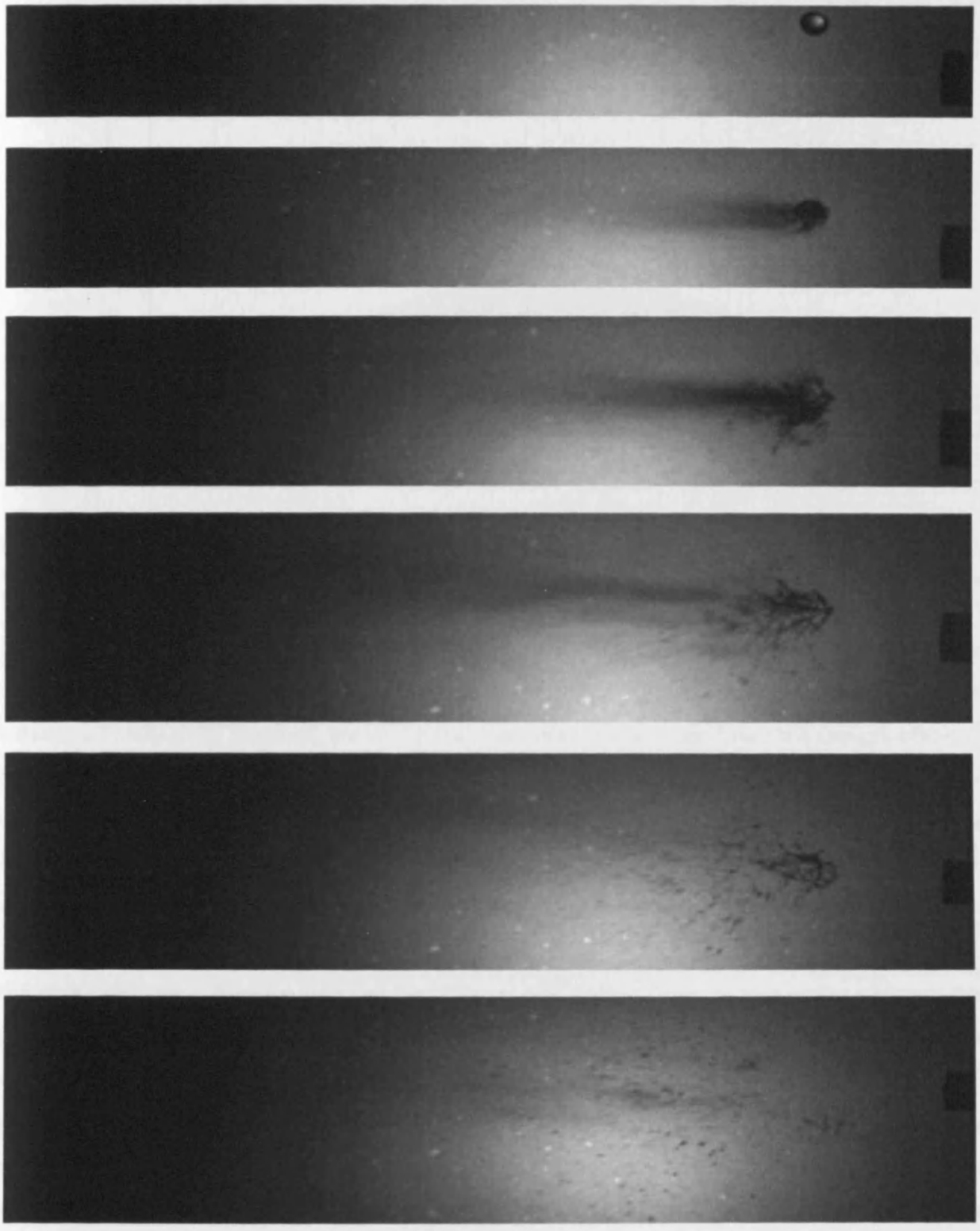

Figure 6.17: Constant Flow Breakup, Unknown We

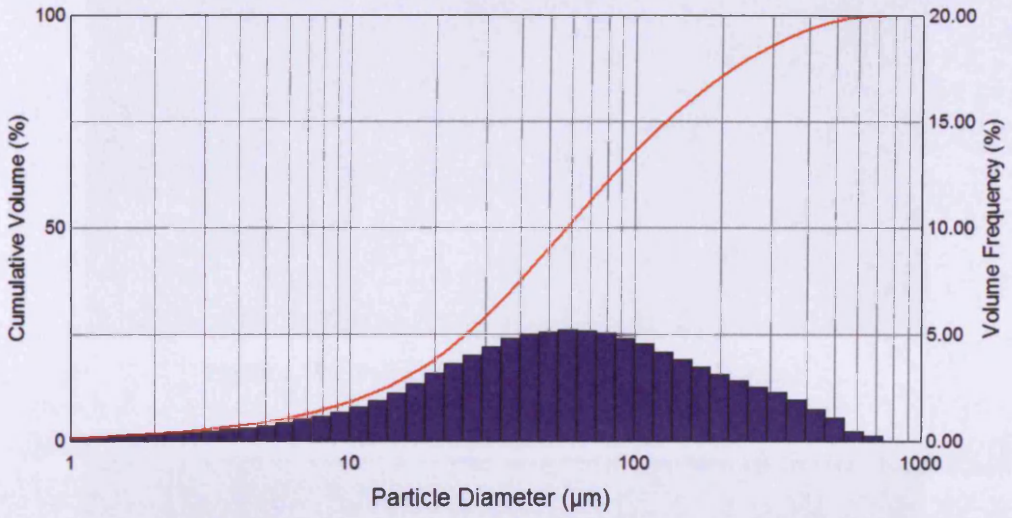

Figure 6.18: Particle Size Distribution. Constant Flow, Unknown We

6.7 Pulsed Flow Results

Videography was recorded for droplets falling into the path of the pulsed air stream between z=10mm and z=80mm away from the pulse generator exit. Although the droplet counter enabled consistent results to be obtained, the set-up was very time-consuming. From the images obtained, it could be seen that the timing was accurate for distances up to 40mm from the pulse generator exit. Beyond this distance, the images suggested breakup more akin to the constant flow cases than the other pulsed flow cases, with the droplet beginning to deform when coming into line with the top of the pulse generator exit, suggesting that the timing was not quite correct.

The major obvious difference between the constant and pulsed flows is that in the constant flow the bottom of the droplet experiences the air flows first, while with the pulsed flow cases the whole diameter of the droplet is subjected to the airflow at the same time. This causes the movement of the water closest to the air generator first and appears to give catastrophic breakup in all cases, which, given the Weber numbers from Section 6.5.2, is consistent with breakup in steady flows (Section 6.2.2). The other major difference is the time scale of breakup, with the droplet being fully broken up within 5-6 frames (1.67-2ms) at z=10mm, compared to 90 frames (30ms) for the bag breakup above.

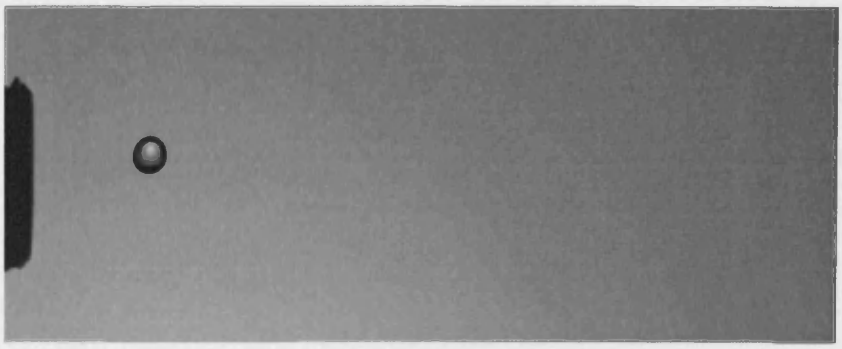

Figure 6.19a: Pulsed Flow Breakup, z=10mm, Frame 1

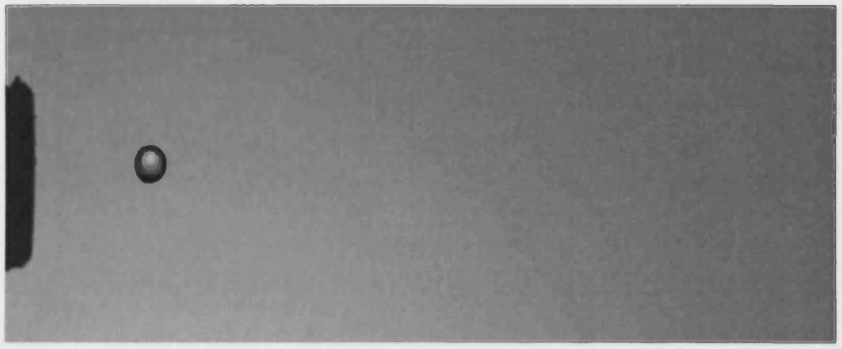

Figure 6.19b: Pulsed Flow Breakup, z=10mm, Frame 2

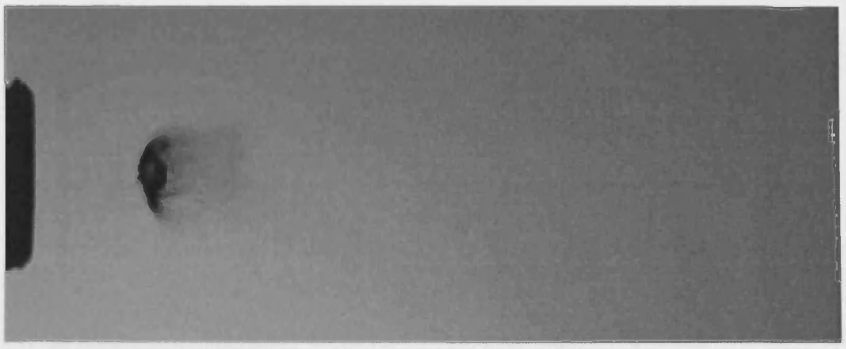

Figure 6.19c: Pulsed Flow Breakup, z=10mm, Frame 3

Figure 6.19d: Pulsed Flow Breakup, z=10mm, Frame 4

Figure 6.19e: Pulsed Flow Breakup, z=10mm, Frame 5

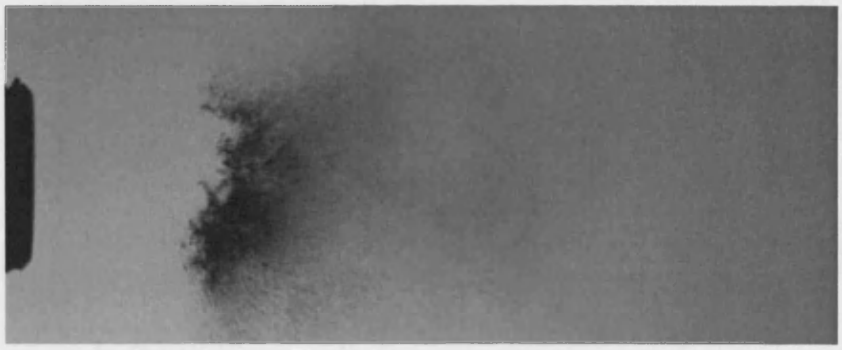

Figure 6.19f: Pulsed Flow Breakup, z=10mm, Frame 6

Figure 6.19g: Pulsed Flow Breakup, z=10mm, Frame 7

Figure 6.19h: Pulsed Flow Breakup, z=10mm, Frame 8

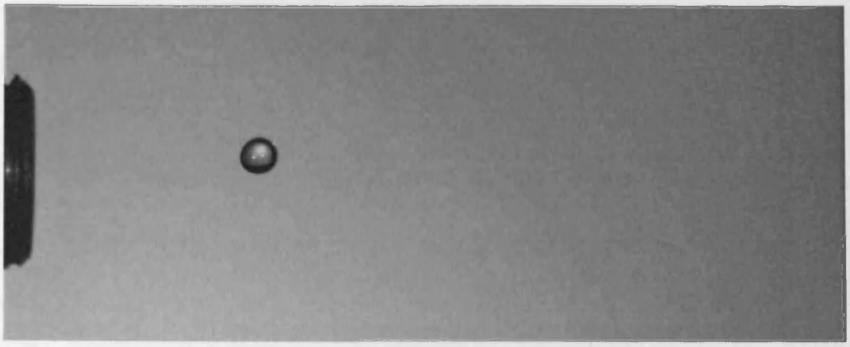

Figure 6.20a: Pulsed Flow Breakup, z=20mm, Frame 1

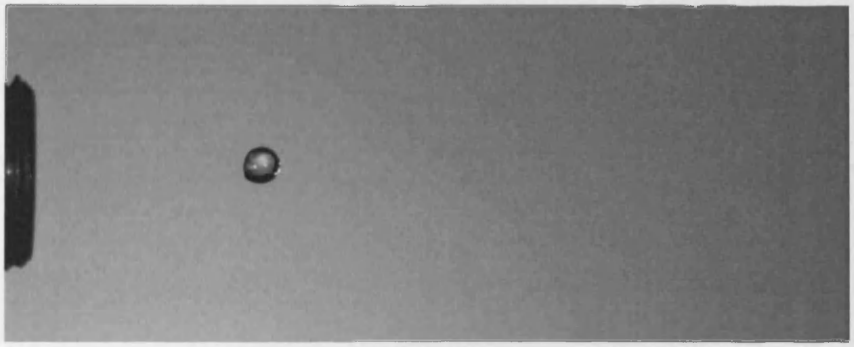

Figure 6.20b: Pulsed Flow Breakup, z=20mm, Frame 2

Figure 6.20c: Pulsed Flow Breakup, z=20mm, Frame 3

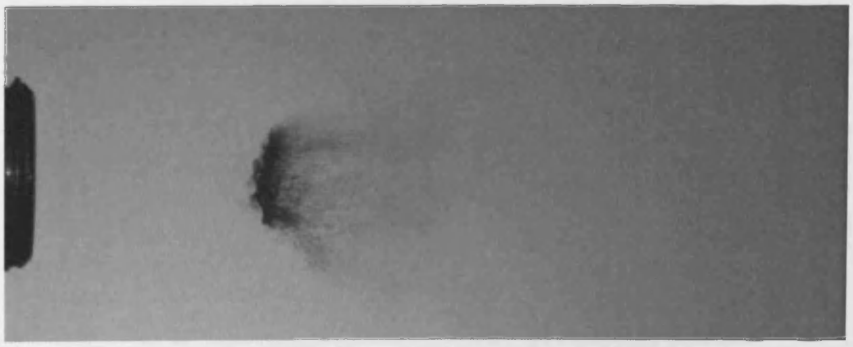

Figure 6.20d: Pulsed Flow Breakup, z=20mm, Frame 4

Figure 6.20e: Pulsed Flow Breakup, z=20mm, Frame 5

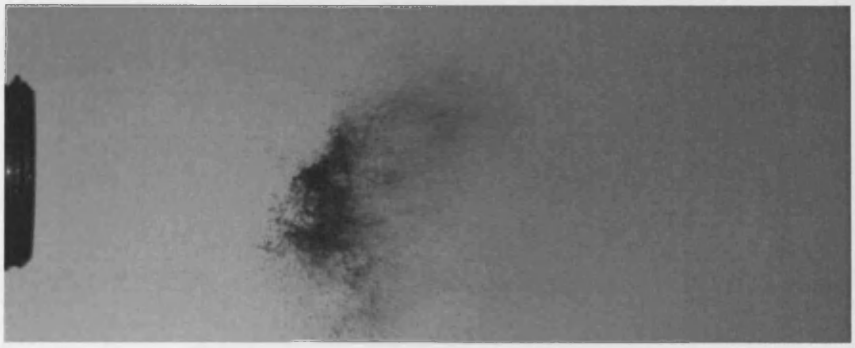

Figure 6.20f: Pulsed Flow Breakup, z=20mm, Frame 6

Figure 6.20g: Pulsed Flow Breakup, z=20mm, Frame 7

Figure 6.20h: Pulsed Flow Breakup, z=20mm, Frame 8

Figure 6.20i: Pulsed Flow Breakup, z=20mm, Frame 9

Figure 6.20j: Pulsed Flow Breakup, z=20mm, Frame 10

As expected, the secondary droplet size can be seen to increase as z increases. At z=10mm, We=1,893, (Figure 6.19a-h), there are very few visible droplets and most of the water appears to be in a fine mist. At z=20mm,We=1,525, (Figure 6.20a-j), again a large proportion of the water appears to be in a fine mist, however there does appear to be some secondary breakup occurring, with the appearance of bag-like structures towards the end of the breakup process. At z=30mm,We=1,275, (Figure 6.21a-l) there are many more visible droplets, and more larger-scale structures can be seen during the breakup process, with what appears to be several occurrences of bag-breakup. At z=40mm, We=1,047 (Figure 6.22a-o), the break-up time has been extended to 4ms and there are visible droplets present at the end of the process, the larges of which can be estimated, by pixel counting, at 0.9-1.0mm.

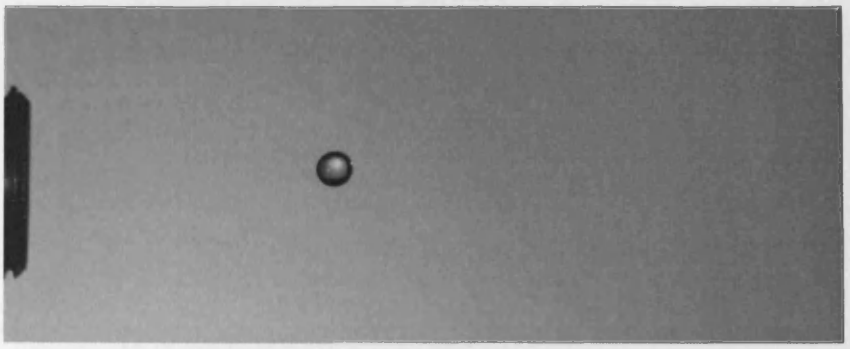

Figure 6.21a: Pulsed Flow Breakup, z=30mm, Frame 1

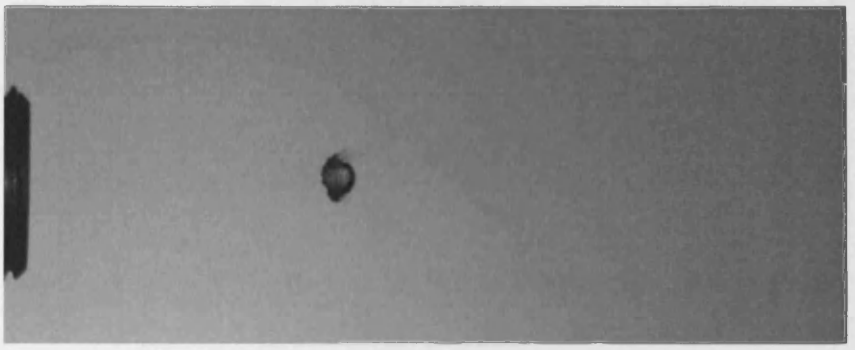

Figure 6.21b: Pulsed Flow Breakup, z=30mm, Frame 2

Figure 6.21c: Pulsed Flow Breakup, z=30mm, Frame 3

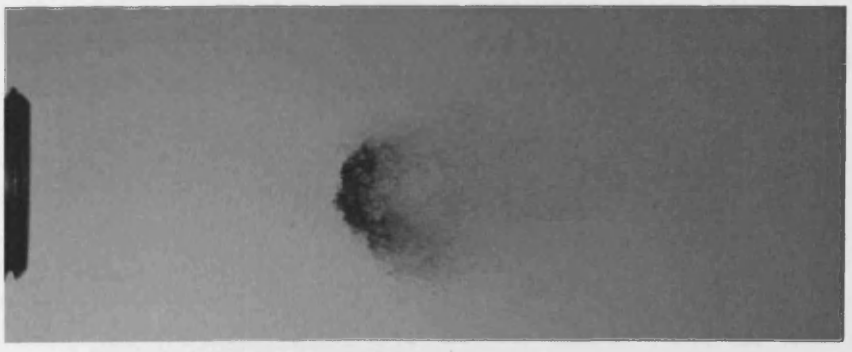

Figure 6.21d: Pulsed Flow Breakup, z=30mm, Frame 4

Figure 6.21e: Pulsed Flow Breakup, z=30mm, Frame 5

Figure 6.21f: Pulsed Flow Breakup, z=30mm, Frame 6

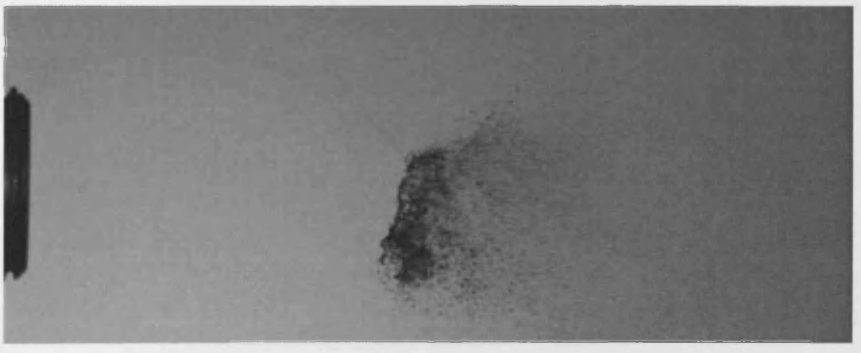

Figure 6.21g: Pulsed Flow Breakup, z=30mm, Frame 7

Figure 6.21h: Pulsed Flow Breakup, z=30mm, Frame 8

Figure 6.21i: Pulsed Flow Breakup, z=30mm, Frame 9

Figure 6.21j: Pulsed Flow Breakup, z=30mm, Frame 10

Figure 6.21k: Pulsed Flow Breakup, z=30mm, Frame 11

Figure 6.21l: Pulsed Flow Breakup, z=30mm, Frame 12

Initial inspection of the breakup at z=50mm (We=778), z=60mm (We=717) z=70mm (We=549) and z=80mm (We=403) appeared to show that the largest droplets formed during breakup were of a similar size. From pixel counting, the size of the largest visible droplets were indeed very similar, and were in the range of 0.9-1.1mm, a third of the diameter or a ninth of the volume of the original droplet. This suggests an upper bound on the largest secondary droplets produced during breakup.

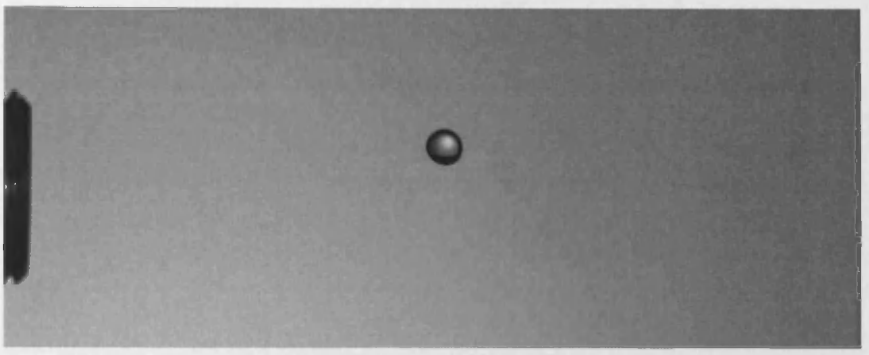

Figure 6.22a: Pulsed Flow Breakup, z=40mm, Frame 1

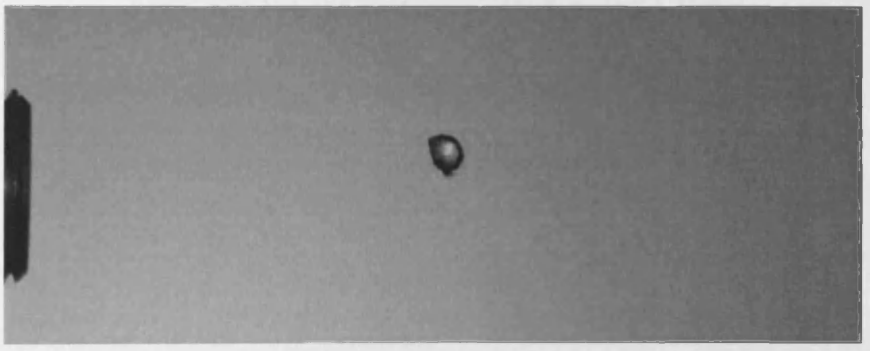

Figure 6.22b: Pulsed Flow Breakup, z=40mm, Frame 2

Figure 6.22c: Pulsed Flow Breakup, z=40mm, Frame 3

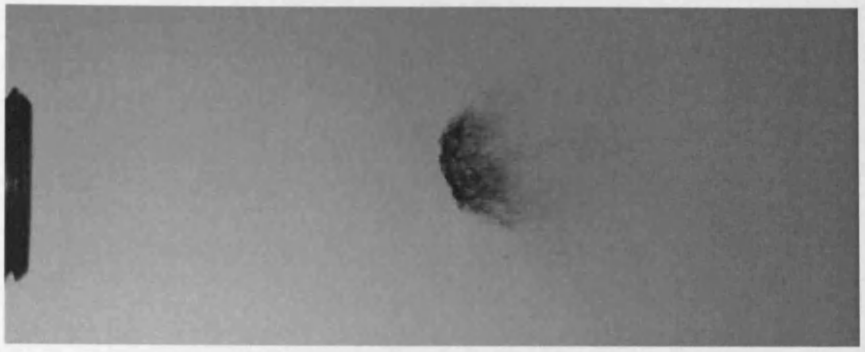

Figure 6.22d: Pulsed Flow Breakup, z=40mm, Frame 4

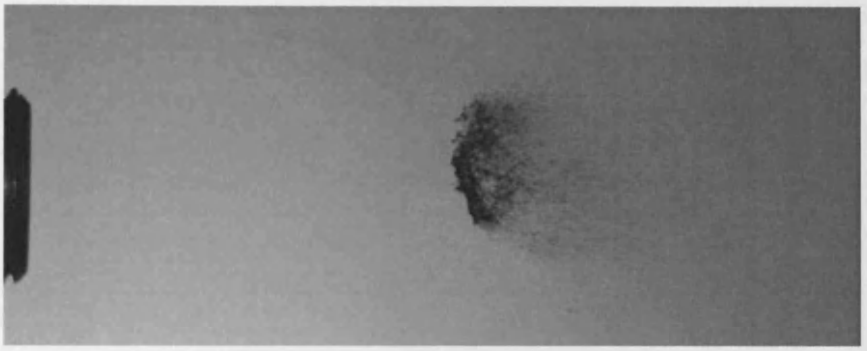

Figure 6.22e: Pulsed Flow Breakup, z=40mm, Frame 5

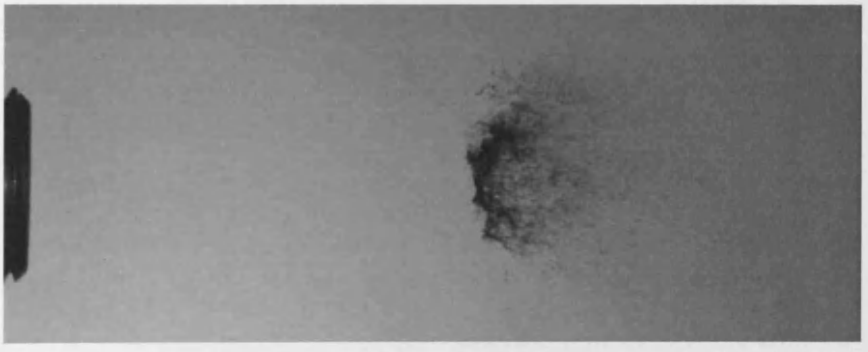

Figure 6.22f: Pulsed Flow Breakup, z=40mm, Frame 6

Figure 6.22g: Pulsed Flow Breakup, z=40mm, Frame 7

Figure 6.22h: Pulsed Flow Breakup, z=40mm, Frame 8

Figure 6.22i: Pulsed Flow Breakup, z=40mm, Frame 9

Figure 6.22j: Pulsed Flow Breakup, z=40mm, Frame 10

Figure 6.22k: Pulsed Flow Breakup, z=40mm, Frame 11

Figure 6.22l: Pulsed Flow Breakup, z=40mm, Frame 12

Figure 6.22m: Pulsed Flow Breakup, z=40mm, Frame 13

Figure 6.22n: Pulsed Flow Breakup, z=40mm, Frame 14

Figure 6.22o: Pulsed Flow Breakup, z=40mm, Frame 15

6.8 Discussion

The constant flow results show that it is possible to produce some very fine sprays suitable for use in combustion from large droplets. The high Weber number case (approx. 1,200) gave a SMD of 17μm from a 3mm droplet, a primary/secondary spray SMD ratio of 176. To form a spray suitable for detonation (SMD of approximately 5μm) using a constant flow with We=1,200, the initial spray SMD needs to be in the region of 880μm.

In some cases, typically for lower Weber numbers, not all the droplets within the distribution were measured. In these cases, it was difficult to make precise correlations, especially for We=51 where very little of the spray had been characterised. For We=84, the SMD of the characterised spray is 283 μm, although as the distribution has been clipped of the larger droplets, it is likely to be substantially higher than this. This value gives primary/secondary spray SMD ratio of 10.6, so to obtain a spray suitable for detonation, an initial SMD of less than 53μm is required.

From the pulsed flow results, the highest Weber number case (We=1,893) resulted in a very fine mist. As no droplet sizing data was available, interpretation of the images suggests that a pulse of this strength will readily create a spray suitable for detonation. For pulses with Weber numbers of 403 – 778, there appears to be an upper limit on the size of the daughter droplets of 1 mm (measured from pixel counting of images). This observation in similar to that of Park et al [67], for constant flows of Weber numbers 153 and 383 where the secondary spray SMD plateaus. For pulses at these Weber numbers therefore, an initial spray of 15μm would lead to detonable secondary spray less than 5 μm. Obtaining primary sprays with SMD of 15μm is achievable with commercial injectors and delivery systems (e.g. automotive direct injection systems).

6.9 Summary

This Chapter has presented results characterising the droplet breakup process in steady and pulsed flows, as presented at ILASS 2008 [64]. The Chapter details the design and evolution of the experimental rig built to undertake this work, and the instrumentation used to characterise the droplet breakup process. The characterisation of the pulsed flow using LDA is shown, and the method used to extrapolate the available data for errant data points is described.

The Chapter then presents imagery of the droplet breakup process and sizing data for the secondary spray. Previously established droplet breakup mechanisms for steady flow are demonstrated with the equipment used for this study. Secondary spray sizing data is present for this steady flow, with the full distribution captured for high Weber numbers, and partial distributions captured for low Weber numbers characteristic of bag breakup due to the large size of the initial droplet. From this data tentative predictions are made for the size of the initial droplets required to produce a spray capable of sustaining detonation propagation in the flows studied.

Chapter Seven

Reflected Shock Ignition in Pulse Detonation Engines

7.1 Introduction

This Chapter utilises all of the knowledge gained in the preceding Chapters to experimentally investigate the initiation of liquid kerosene by reflected shock waves for application to PDEs. It will present successful combustion data for kerosene in the shock tube, and compare to the test programmes for propane and hydrogen. From this comparison, predictions are made on the probability of successful detonation for conditions not attempted. The Chapter concludes with a summary of the knowledge gained and the applicability to PDEs.

7.2 Equipment

The equipment used in this experimental programme is broadly as described in Chapter Four, apart from the addition of the liquid fuel injection system and the modification of the reflecting wall to accommodate the fuel injector, as described in the rest of Section 7.2.

7.2.1 Liquid Fuel Injector

The fuel injector used was a Bosch C2 Pressure Swirl Injector. This injector has been used in numerous studies in within Cardiff School of Engineering, so has been extensively characterised [68-70]. The fuel for the injector (aviation kerosene) was pressurised using two different accumulators, a high-pressure accumulator (maximum fuel pressure 200 bar) and a low-pressure accumulator (maximum fuel pressure 7 bar) via bottled oxygen-free nitrogen. Non-return valves and pressure relief valves were placed at appropriate points in the system to optimise safety. The injector was controlled electronically through a 12V power source and pulse generator. The generator could be customised, with the pulse frequency, duration, and voltage variable. The pulse generator also had several different modes – single (for a single pulse), continuous (for continuous pulses until switched off) and burst (a set number of pulses).

As droplet size is proportional to injector pressure for liquid injectors [70], it was initially decided to operate the injector at a low fuel injector pressure to attempt to create high Weber numbers in the shock tube (calculated in Section 7.3). The 7 bar accumulator gave a much lower fuel injection pressure than is normal, so it was necessary to ensure that the injector would work

with this injection pressure, that the fuel droplets were not so large that they would simply fall to the bottom of the chamber, and to check the spray penetration length (the length of the spray into the chamber). These tests are described in Section 7.3.

7.2.2 Fuel Injector Set-Up

The set-up process was the same for both accumulators. The accumulator was cleaned and dried to remove impurities from previous experiments, filled with fuel to an appropriate level and then connected to the fuel injector. The injector control system was initialised, with care taken to ensure that the pulse generator was set up first before the injector power supply was switch on, otherwise the injector would begin to fire. The accumulator was connected to the nitrogen supply enabling the fuel to be pressurised. It was necessary to remove the air present in the system between the accumulator and injector, which was achieved by operating the injector until it fired consistently.

7.2.3 Reflecting Face

Due to the dimensions of the fuel injector it was not possible to integrate the injector into the reflecting faces that had been used for the non-reacting and gaseous fuel experimental programmes. Therefore to mount the fuel injector, an alternate end flange was modified although only a flat reflecting face was available. The injector was mounted axially along the centre of the shock tube, with the injector tip flush with the reflecting wall.

7.3 Injector Characterisation Experiments

From previous work [70] it was known that the optimal injection time for the injector used was 5ms – up to this injection time the mass injected varied linearly with injection time, and after this the injected mass remained constant. As this worked had been carried out at higher injection pressures (40-70bar) and with a different fluid (water), it was necessary to measure the amount of fuel delivered for the conditions used in this study. To accomplish this, fuel was injected 5,000 times into a bottle, and the weight of the injected fuel was calculated using a high-precision scale. This procedure was repeated a further two times giving a total of 15,000 fuel injections.

This method gave a mass of 5.35±0.02 mg/injection over the 15,000 injections. Similar tests carried out with an injection time of 10ms gave a mass of 4.95mg/injection, appearing to confirm the previous results of Crayford [70].

To ensure that the injector would function at low injector pressures as described in Section 7.1.1, three high speed videography experiments was undertaken using the Photron Fastcam APX RS Mono High Speed Camera described in Section 6.3.2. The injector was mounted in a 4" Perspex tube with an acrylic end flange in the same manner as described in Section 7.1.1 for mounting in the shock tube. The camera was operated at 3,000 fps and full 1 megapixel resolution. Several halogen floodlamps were used to backlight the experimental set-up. In this set-up, the injector protruded slightly from the acrylic flange, which allowed the camera to be focussed on the injector.

The first experiment concentrated on ensuring the injector was operational with the low injector pressure, so the camera was concentrated on the near-injector region. The images confirmed that the injector sprayed fuel (which had also been seen during set-up of the injector), and that the fuel penetrated the combustion chamber and did not simply "plate out" underneath the injector.

The second experiment involved looking at the penetration of the spray. From the first experiment, an estimate could be made as to how far the spray was travelling on the chamber. A ruler was clamped in around this estimated position using retort stands. The camera was then repositioned and refocused so that images of the estimated position were taken. The images suggested that some larger droplets travelled as far as 500mm from the injector, but that the bulk of the spray was contained within 350-400mm of the injector.

An estimate of the injector SMD was made using Equation 7.1 [65]. The value for constant A was calculated using data gathered for this injector for water sprays at injector pressures of 40-60 bar [70]. An average value for the constant A was estimated as 1.94 for this injector. Using the calculated injector orifice size of 0.5mm [68] gave an SMD of 52μm, which appears to be low given the images recorded above. It is possible that this is due to the very low injector pressure used compared to those used for calculating the value of constant A. This estimated SMD gives Weber numbers in the shock tube ranging from 350 (M=1.60) to 740 (M=2.23).

$$SMD = A\sigma^{0.25}\mu_L^{0.25}\rho_L^{0.125}d_0^{0.5}\rho_A^{-0.25}\Delta P_L^{-0.375} \qquad \text{Equation 7.1}$$

7.4 Shock Tube Methodology

The initial methodology followed for these experiments was as described in Section 4.2 with the fuel injected before Step 5. To provide enough fuel for a stoichiometric fuel-air mix in half of the test section (due to the penetration of the injector spray) 30 injections of 5ms were needed, which were conducted at a rate of 10Hz. The procedure continued at Step 5 after the injections were completed. In addition to cleaning residual pieces of diaphragm from the shock tube after the experiments, some absorbent material was used to dry the shock tube of any residual fuel. During the course of the experimental programme the methodology changed as a result of the experiments. These changes are detailed as appropriate in Section 7.5.

7.5 Shock Tube Results

7.5.1 Low Pressure Fuel Injection

Tests were carried out at a fuel injection pressure of 7 bar with incident shock waves of strength M=1.83 (We=431), M=2.00 (We=575) and M=2.08 (We=631) but no combustion results were obtained. The same experiments were then carried out for an increased number of fuel injections and with a variation in the experimental timing to test for rainout, but again no combustion was recorded for either modification.

7.5.2 High Pressure Fuel Injection

As no combustion was achieved with the low-pressure fuel injection pressure, an attempt was made with higher fuel injection pressures. Although this reduced the shock tube Weber number, it increased the residence time of the fuel within the shock tube. The high pressure accumulator described in Section 7.2.1 was set to give a fuel injection pressure of 60 bar as this pressure has been shown to provide the optimal spray characteristics for this injector [70]. Using Equation 7.1, an estimated SMD of 22μm was obtained which is close to the required injector SMD stated in Section 6.8 of 15μm. This leads to estimated Weber numbers in the shock tube ranging from 150 (M=1.60) to 313 (M=2.23). When operated with the methodology described in Section 7.4,

i.e. with the shock tube firing after injection had finished, no combustion results were obtained. However, when the timing was altered so that the shock tube was fired while the injector was operating, successful combustion pressure traces were recorded.

Successful combustion was achieved in the shock tube for kerosene at M=2.00 as shown in Figure 7.1. The pressure trace shows that combustion was achieved in the liquid kerosene/air mixture at an incident shock strength that can be compared to the equivalent results obtained for propane (Figure 7.2) and hydrogen (Figure 7.3). Such a comparison suggests that the kerosene-air mixture undergoes combustion more readily than propane and slightly less readily than hydrogen.

The pressure traces of Gauge2 show that the pressure for kerosene is lower than that for air from approximately 4ms (apart from the combustion region at approximately 9ms). Considering the discussion in Section 5.2.2, it is thought that this is caused by heating and evaporation of the kerosene droplets, which slightly reduces the temperature in the shock tube.

Comparing the kerosene combustion to hydrogen, the time between the reflected shock passing Gauge2 and combustion being registered at Gauge2 was 7.0ms for kerosene and 6.5ms for kerosene, with the combustion pressure ratio 1.11 compared to 1.41 for hydrogen.

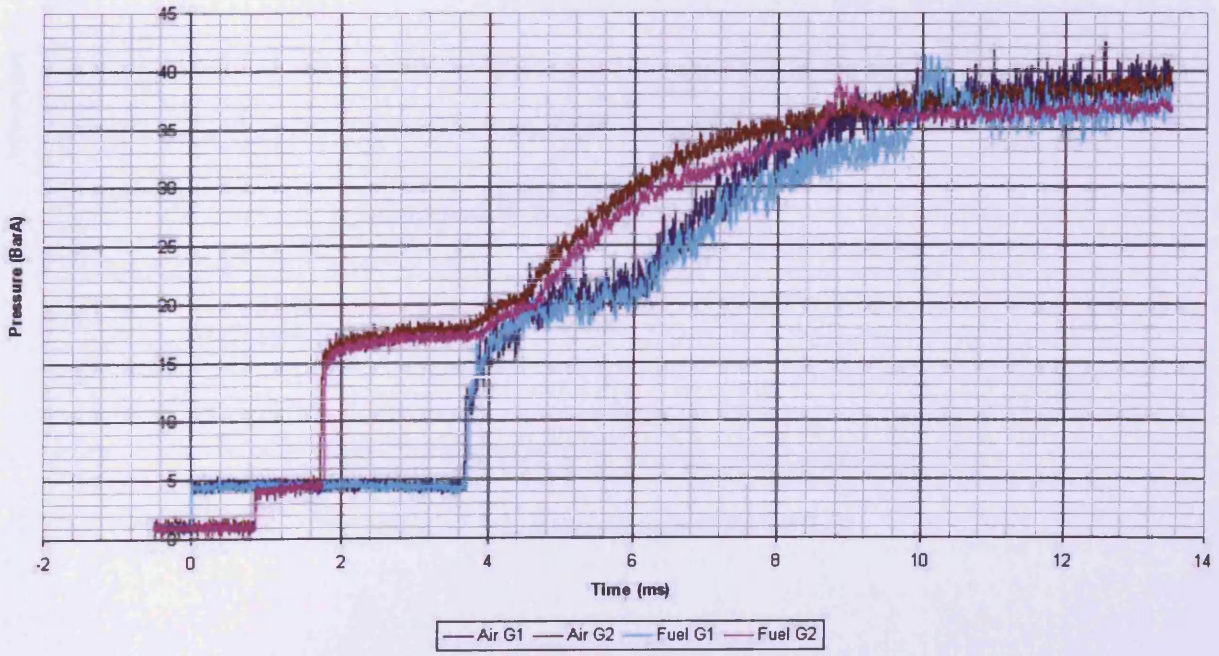

Figure 7.1: Kerosene Combustion, M=2.00

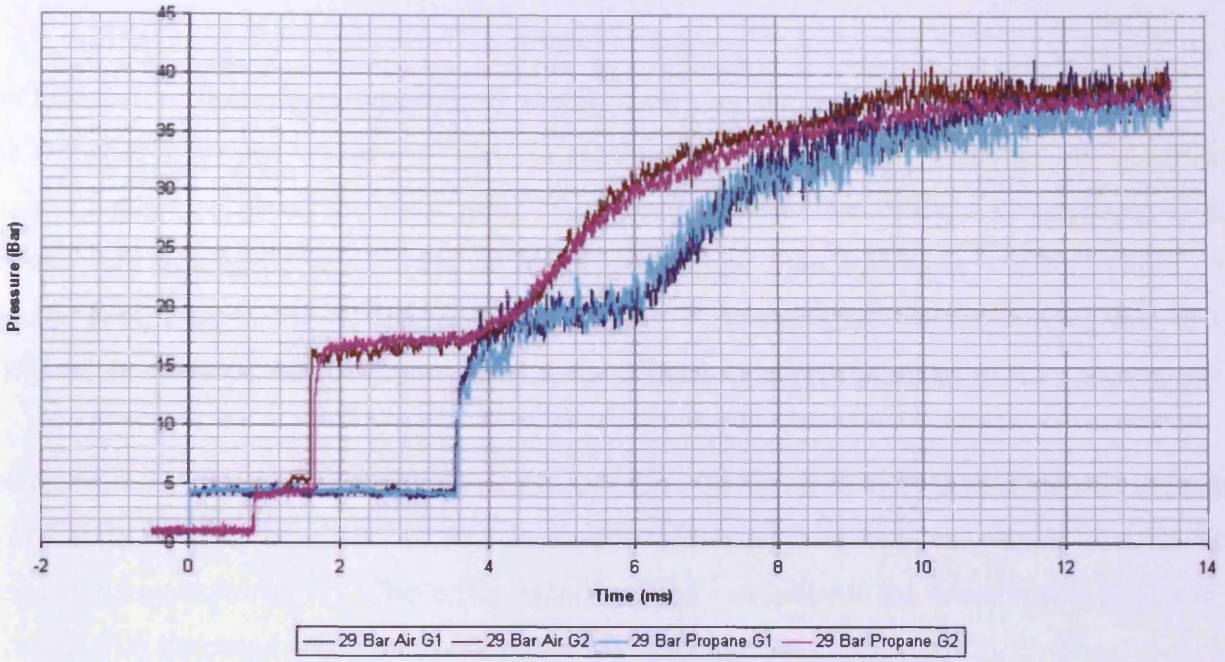

Figure 7.2: Propane Combustion, M=2.00

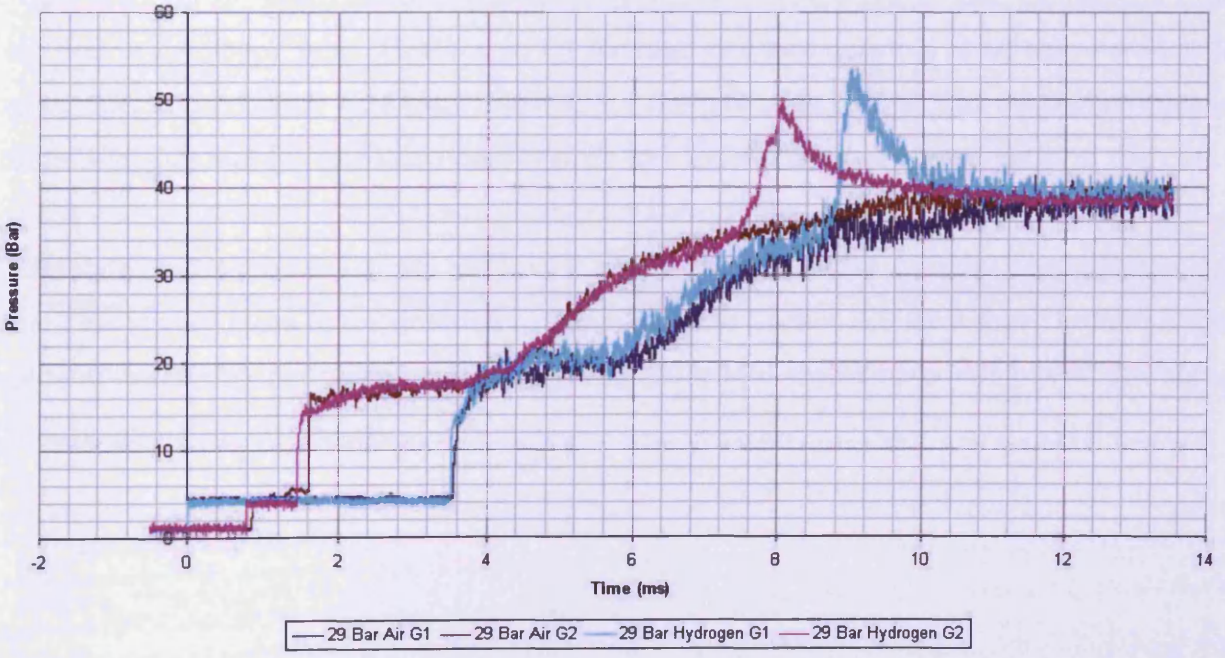

Figure 7.3: Hydrogen Combustion, M=2.00

7.6 Discussion of Liquid Fuel Combustion

The fact that kerosene combusted more readily than propane initially appears counter intuitive. The fact that hydrogen was more prone to combustion than propane in this set of experiments was not a surprise given the propensity of hydrogen to detonate. What was surprising is that propane will autoignite at a lower ambient temperature than hydrogen – 450°C (723K) for propane compared to 560°C (833K) for hydrogen. This indicated that the burning rate or the ignition delay time of the fuel contributed to the difference in results seen.

The autoignition temperature of kerosene is substantially lower than both propane and hydrogen at 210°C. It has also been shown that the ignition delay time of kerosene vapour reduces with increasing temperature [71]. These two facts are likely to indicate the reasons why combustion occurred with kerosene when it did not occur with propane.

Timing issues have been shown to be an important factor with shock reflected initiation of liquid fuels. The fact that combustion occurred if the shock tube was fired during injection suggest that the time scale for the experiment as described in Section 7.4 was longer than the residence time of the fuel in the shock tube. This is true for the high-pressure injection at 60 bar as well as the original injection pressure of 6 bar. Considering the reduction in SMD of the higher injection pressure suggests that the residence time is more important than the Weber number in this case.

As calculated in Section 7.5.2, the SMD of the high injection pressure spray was approximately 22μm. This is very close to the criterion of 15μm given in Section 6.8 for a shock to form a spray capable of sustaining detonation suggesting that detonation would be possible with this set up, after some minor modifications.

7.7 Application to Pulse Detonation Engines

The aim of this thesis, as defined in Section 1.3.1, is "to investigate problems preventing implementation of a Liquid-Fuelled Pulse Detonation Engine (PDE) into a practical Aircraft". This Section presents a summary of the work conducted in this thesis, and how this work is directly applicable to fulfilling the aim of this thesis.

The literature review has highlighted relative dearth of knowledge of liquid fuelled detonations when compared to gaseous fuelled detonations The two main methods of initiating detonations have been presented – Direct and DDT. The application of these methods to PDEs has been discussed, and some novel designs presented. The Chapter has also highlighted the difficulty involved with generating a liquid fuel-air mixture that is able to support detonations due to droplet size and mixing. Droplets in the sub-5 micron range are required – something that is not readily achievable with current fuel injector technology. Mixing considerations have been shown to be important as detonation propagation has been shown to be very dependent on fuel concentration. The Chapter ends by presenting some PDE engine designs, focussing on those that utilise shocks for initiation purposes. This method then forms the basis for the rest of the study.

Investigation of single droplet breakup in pulsed flows was conducted to gain an understanding of the breakup process and quantify the relationship between initial droplet size and secondary spray SMD. High-speed videography has show that for a range of lower Weber numbers similar to those experienced in the shock tube in Chapter Seven, a maximum secondary droplet size appears. This relationship suggests that a spray with droplet sizes in the region of 15μm will produce a secondary spray suitable for detonation propagation in the shock tube, a criterion that is achievable with current injector and fuel delivery technology.

Combustion was achieved with a flat reflecting face for liquid kerosene at an incident Mach number M=2.00 with a spray SMD of approximately 22μm. The importance of fuel residence time in the shock tube has been highlighted as being potentially more important than the SMD and Weber number in this case. Comparing the results to those obtained for hydrogen suggests that with a shaped reflecting face, detonation in kerosene is possible in the shock tube.

Chapter Eight

Numerical Simulations of a PDE Fuel-Air Mixing Valve

8.1 Introduction

This Chapter presents the results of numerical simulations of an industrial prototype pulse detonation engine. The results of the industrial partner's numerical simulations into a proposed liquid-fuel/air mixing valve are presented and reviewed, and modifications to the simulation are proposed. These modifications are then used in a new simulation programme, which further builds on the previously presented single-phase, single-gas work by introducing a gaseous fuel to clarify the mixing processes occurring. Finally recommendations are made to improve the design of the mixing valve.

8.2 Background

The PDE test bed was donated to Cardiff University by an industrial partner. As part of the development work undertaken by the company, the main reasons behind the unsuccessful operation of the first version of the rig were identified as poor atomisation of the liquid fuel droplets and poor mixing of the fuel and air. A parametric CFD study was undertaken by the company to improve the design of the fuel-air inlet valve, a summary of the report produced is presented and reviewed in this Section [72].

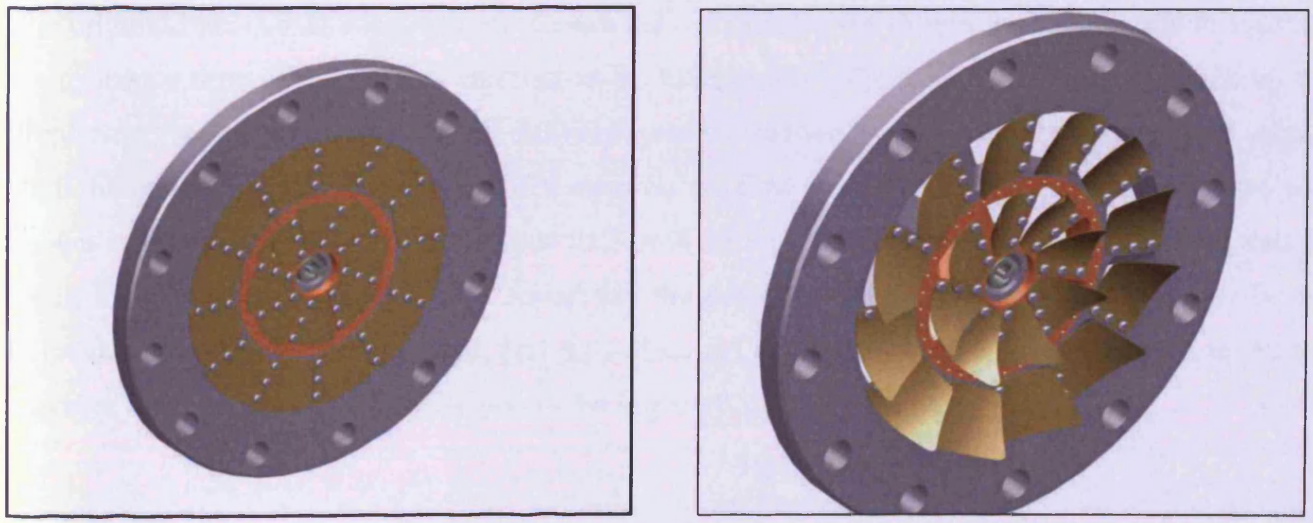

Figure 8.1: Original Industrial Air valve

The original valve, as shown in Figure 8.1, consisted of two concentric rings of eight openings, each with a reed valve. The reeds were designed to open and allow air into the detonation chamber when the upstream pressure was higher than the chamber pressure (most of the engine cycle). When the

chamber pressure was higher than the upstream pressure (during detonation) the reeds would close. The subsequent parametric study investigated 8 different valve configurations and several different reed opening angles and made predictions on how each would mix the fuel and air. However, the simulations were run with air only and the mixing predictions were made by studying the flow structure of the air.

8.2.1 PDE Test Rig

The PDE rig was designed as part of a study by to investigate the feasibility of using PDEs in non-re-usable vehicles such as missiles and reconnaissance drones. It included detailed investigation into the possible flight envelope and mission profile that could be achieved.

The rig was designed to be small and portable so that it could be moved to suitable sites for testing and avoid expensive safety issues such as noise and fire suppression. It was designed to run on a liquid aviation fuel (JP-10), and consisted of 2 tubes each capable of running at 50 Hz providing a total frequency of 100 Hz. Air flow into the tube would be controlled by the flexible reed valves already described. The rig was designed so that the engine timing was controlled by the ignition system, removing the need for complicated control systems and expensive control valves.

The original Fuel-Air-Mixing system (Figure 8.1) relied on swirl to mix the fuel/air and to increase the residence time of the fuel-air mixture in the tube, and aerodynamic shear forces to break-up the droplets. As stated previously, the air delivery system consisted of two sets of concentric reed valves. Both the inner set and outer set imparted swirl on the flow in the same direction – so the valve was known as a co-swirl valve. The fuel was delivered through 0.5mm orifices between the two sets of reeds. Their own experimental work found that the shear forces present in the flow was insufficient to break up the liquid fuel droplets, and they observed that most of the liquid fuel ended up on the chamber wall, which is most likely due to the imparted swirl.

8.2.2 Original Model

In order to improve the design, the company undertook a parametric CFD study of different configurations to try to improve the mixing. The different configurations that were tested are shown

in Table 8.1. Each reed could either be clamped radially (imparting swirl), or circumferentially on the top or bottom. This is demonstrated by Figure 8.2, which shows Configuration 6 from Table 8.1.

Table 8.1: Industrial Partner's Clamping Configurations

Configuration Number	Inner Reed Clamping	Outer Reed Clamping	
1	Radially	Radially	Co-Swirl
2	Radially	Radially	Counter-Swirl
3	Circumferentially Top	Circumferentially Top	
4	Circumferentially Bottom	Circumferentially Bottom	
5	Radially	Circumferentially Bottom	
6	Radially	Circumferentially Top	
7	Circumferentially Bottom	Radially	
8	Circumferentially Top	Radially	

Figure 8.2: New Air Valve Design, Configuration 6

Additionally, different reed valve opening angles were studied to investigate the affect that this would have. The final test matrix is shown in Table 8.2.

The calculations were carried out using the CFX v11 CFD software. The inlet mass flow rate was $0.3 kgs^{-1}$, and an air inlet temperature of 35°C. The model was run with air modelled as an ideal gas, and the Shear Stress Transport (SST) Turbulence model was used.

The model was set up as a $^{1}/_{8}^{th}$ (45°) sector with periodic boundary conditions to reduce the number of computational cells required. The flow upstream of the valve was modelled for 3 tube diameters

and simplified to a straight pipe. Downstream, the domain was 12 tube diameters. This was consistent with the PDE tube length of 1.2m.

Table 8.2: Industrial Partner's Reed Opening Angles

Valve Configuration	Reed Opening Angles
Radially Clamped – Co-Swirl	5°, 10°. 15°
Radially Clamped – Counter-Swirl	5°, 10°. 15°
Circumferentially Clamped Top	5°, 10°. 15°
Circumferentially Clamped Bottom	5°, 10°. 15°
Inner Radially Clamped Outer Circumferentially Clamped Bottom	5°
Inner Radially Clamped Outer Circumferentially Clamped Top	5°
Inner Circumferentially Clamped Bottom Outer Radially Clamped	5°
Inner Circumferentially Clamped Top Outer Radially Clamped	5°

The simulations were initially run as steady state calculations as it was assumed that the flow would not be time dependent. However, poor convergence implied that the flow was in fact time-dependent, and subsequent transient calculations appeared to support this. During the calculations, the outlet diameter was reduced by 38%. This was due to the fact that a central recirculation zone was found which was producing reversed flow at the exit.

8.2.3 Company's Results

The results of these simulations were provided in a report in PDF format [72]. Unfortunately, some of the results images were missing in the supplied version and it was not possible to obtain the originals, therefore, the results section here is a summary of the discussion section of the report.

Co-Swirl

The results show that there is a strong radial velocity outwards just downstream of the valve which is responsible for carrying the fuel out to the walls and explains the results seen in the experimental study. As the reed opening angle is increased, the radial velocities are more concentrated closer to the valve. Also, increasing the reed opening angle causes the region of high positive velocity to be increased. The low and reversed flow region in the centre extends further downstream, and the swirling flow is more prominent.

Counter-Swirl

The counter-swirl configuration results in a much larger re-circulation zone than in the co-swirl case. There are significant positive axial velocities just downstream of the valve and around the recirculation zone. There is a strong radial velocity close to the valve, however the swirl tends to cancel itself out and the bulk flow downstream has a much lower level of swirl. This would suggest that the fuel could be pulled back into the centre of the tube. However due to the high axial velocities, there is a risk that the fuel would bypass the detonation region.

The reed opening angle has a complex relationship with the flow characteristics. The recirculation zone at 5° extends further downstream than 10°, however the zone extends again for 15° opening angle.

Circumferentially Clamped (Top/Bottom)

When both sets of reeds are clamped on the top, the flow, as would be expected, is concentrated through the centre of the tube, giving jet-flow. When the reeds are clamped on the bottom, forcing the flow out towards the wall. A recirculation zone is formed, which is approximately 1 tube diameter long, and the flow becomes fairly uniform after this point.

In discussing the circumferentially clamped configurations, it is suggested that a hybrid clamping configuration may be optimal. These configurations are now presented.

Inner Radially Clamped Outer Circumferentially Clamped Top

This produces a well-defined recirculation zone. There is a strong degree of swirl at the centre, which reduces towards the walls. A decent amount of mixing occurs, and radial velocities suggest that the fuel will be carried towards the centre of the tube. The overall flow is fairly uniform 2 tube diameters downstream of the valve.

Inner Radially Clamped Outer Circumferentially Clamped Bottom

This produces a large recirculation zone and high axial velocities close to the wall. There is a risk that this configuration would give poor mixing as the fuel would be transported with the bulk flow close to the wall, and bypass the detonation region.

Inner Circumferentially Clamped Top Outer Radially Clamped

This configuration results in the bulk of the flow passing through the centre of the tube with high velocity. This is similar to the Circumferentially Clamped Top flow, so is considered unviable.

Inner Circumferentially Clamped Bottom Outer Radially Clamped

This arrangement gives a flow very similar to the Co-Swirl configuration, with a small central re-circulation zone and the fuel is likely to be transported to the walls.

8.2.4 Discussion

The preceding information has all been summarised from information provided by the industrial partner [72]. Analysis of the report by the author of this thesis suggests that the simulations conducted give a good starting point to further investigation, however several areas for concern were identified.

The first of these concerns is the mass flow rate.

The report states that flow metering gives a mass flow rate of 0.3 kgs^{-1}, however previous communication with the industrial partner specified the mass flow rate as 0.5kgs^{-1} for the rig [51]. It's possible that during experiments, the mass flow rate was reduced to try to achieve detonation,

however there is no way of confirming this. Therefore, it was decided to maintain the original mass flow rate of $0.5kgs^{-1}$ for these simulations.

The second main area for concern is the reed opening angles. The results of the Co-Swirl case suggest that the velocities downstream of the valve increase with increasing reed opening angle. However, Equation 8.1 for mass flow rate shows that for the velocity to increase either the mass flow rate needs to increase or the flow area or density need to decrease. As the flow area (through the reeds) is increasing, and there is no obvious reason for an increase in temperature (to decrease the density), this suggests that the mass flow rate is increasing. This is further discussed in Sections 8.3.1 and 8.3.2.

$$\dot{m} = \rho \, a \, V \qquad \text{Equation 8.1}$$

Another concern is that the numerical simulation is judged to be converged when the residuals drop to a pre-determined level. The solution is actually converged when the residuals reach a steady level. This can take a large number of iterations, and it is likely that there will be an oscillation in the values of the residuals. In most calculations, it is more appropriate to calculate until the changes in the flow property of interest are negligible. Such properties can be forces, i.e. lift, drag and moment, or mass flow rates at the inlet and outlet, etc.

8.3 New Model Creation and Meshing

This, and subsequent sections, describe the work undertaken by the author of this thesis to improve the quality of simulations compared to the work described in Section 8.2.

The software chosen to run the new simulations was Ansys FLUENT. This was due to the fact that it was available in the University, and that the author had prior experience of running FLUENT. This series of simulations was undertaken to understand the optimum air inlet valve configuration that would give appropriate mixing, and allow detonations to form. These simulations new introduced propane fuel to enable better predictions of mixing. In order for this to happen, it is important that the large scale fluid dynamic structures are resolved with sufficient accuracy and that the mixing of the fuel and air can be seen.

The main valve was created in the dedicated CAD package SolidEdge. The company provided technical drawings of the valve, and the model was initially set up faithfully using these drawings. The actual valve, a photograph of which is shown in Figure 8.2, contains many features which can cause added difficulties when trying to generate a mesh for use in FLUENT such as chamfered edges and the very small reed thicknesses. It was decided to remove these chamfered edges to ease mesh creation, and the reed thicknesses were set to a nominal 2mm.

The other main feature of the design that would have caused difficulties in meshing was the curved upper and lower edges of the reeds. When the reed is rotated about one of these edges, there would have been either a gap where fluid could flow through which would have had to been sealed, or the reed would have jutted out into the valve, disrupting the airflow through it. It was also found that these curved edges caused difficulties when meshing as highly skewed elements, or elements with negative volumes were formed. The curved edges in the valve and reeds were therefore changed to straight edges. This change caused a reduction in the flow through the valve of 7.5%. It was thought that this would have a minimal affect on the flow, as the areas were still much larger than the calculated reed opening areas.

8.3.1 Flow Choking

The industrial partner's parametric CFD study used arbitrary reed opening angles of 5°, 10° and 15°, which were then modified to 2° and 5° on the basis on Finite Element Analysis The opening area that these angles gave was calculated to obtain an estimate of the flow velocity through the reeds. However, when the opening areas for the 2° and 5° openings was calculated, it was found that the values would lead to the flow being choked – i.e. the reed opening areas were restricting the mass flow through the valve. It was therefore decided to calculate all the reed opening areas for this work to keep the flow through the valve at a consistent value for all the configurations.

8.3.2 Reed Opening Calculations

Due to the shape of the reeds, clamping the reeds in the different positions identified in Table 8.1 gives different openings for the air to flow through. These different areas will lead to different air velocities though the valve, so the flow regimes for the different configurations cannot be compared on a like-for-like basis. To allow like-for-like comparisons, it was decided to keep the exit area from

the reeds constant, which would give a constant airflow velocity through the valves. The opening angles were kept the same for the inner and outer valves to reduce the number of possible combinations.

The valve geometry was created in the SolidEdge CAD package, and then transferred over to GAMBIT. The reeds were then rotated about the appropriate edge in GAMBIT by the desired angle. Three faces were created in GAMBIT which corresponded to the openings, and the area of these faces was found using the SUMMARISE FACE option in GAMBIT. These were then combined to form the different configurations as described in Table 6.1. The total areas were then compared to the flow throat area, and the Mach number expected through the openings obtained using Isentropic Flow Tables. Table 8.3 gives the final opening angles chosen for each configuration.

Table 8.3: New Reed Opening Angles

Configuration	Reed Opening Angle (°)
Radially Clamped Inner & Outer	11
Circumferentially Clamped Inner & Outer	13
Radially Clamped Inner Circumferentially Clamped Bottom Outer	18
Radially Clamped Inner Circumferentially Clamped Top Outer	20
Circumferentially Clamped Bottom Inner Radially Clamped Outer	9

8.4 Mesh Creation

As with all CFD simulations creating an appropriate mesh is vital in obtaining a valid solution but is also one of the most time consuming aspects of the work. It is important to have sufficient cells to resolve the flow features, however for practical reasons, the cell count should also be as low as possible. For this project, the available hardware limited the cell count to 1.2 million cells. Assuming the same volume as used by the industrial partner (full section not $1/8^{th}$ sector), this gives an average cell volume of 11.8 mm^3. Although this may sound reasonable, the cell size in the region of most interest (just downstream of the valve) is unlikely to resolve the flow with sufficient accuracy given the complex geometry. Also, such a fine mesh is not required upstream of the valve, where the flow

will be along the main flow axis with relatively little deviation. Therefore, the cell size will need to be varied across the model, depending on the resolution required.

8.4.1 Periodic Mesh

It was not possible to obtain a converged solution using 45° sectors, or indeed using 90° or 180° sectors. This is due to the fact that the fluid flow is not periodic in the region downstream of the valve, but is actually highly complex, three dimensional and time-dependent as described in Section 8.7. This was only discovered once the full geometry was modelled.

8.4.2 Full Geometry Mesh

The mesh chosen for the geometry was an unstructured tetrahedral mesh. An unstructured mesh was chosen as the flow was expected to be highly complex and three-dimensional with a high degree of swirl. It was therefore not possible to align the mesh with the flow – a major benefit of using a structured mesh. Tetrahedral cells were used as the geometry was mainly cylindrical and because the mesh would be complex near the valve meaning a hexahedral mesh would not be suitable.

As already discussed, it was not appropriate to keep the same mesh density throughout the geometry. The geometry was split into sections so that different cell sizes could be used in the different regions. The regions are presented in Table 8.4. The flow inlet was at x= -300 mm, with the outlet at x=1200 mm, and the main body of the valve between x=0 and x=10.

To check for grid dependency, the co-swirl simulation was repeated with approximately double the cell count (around 2,000,000) on an alternate machine that was temporarily available. Graphs were produced which compared the velocity magnitude, x component and z component of velocity at the central axis and on lines at 10mm, 20mm, 30mm, 40mm and 50mm from the central axis for the two simulations. It was seen that the simulations followed the same pattern for the velocities, except that the re-circulation zone was slightly stronger and longer with more cells. The velocities differed near the wall due to the influence of the boundary layer. Finally, the denser mesh resolved smaller recirculation zones where the velocity oscillated around the value provided by the coarser mesh. However, as the main flow features of interest to this work were the same, the coarser mesh was used with a degree of confidence.

Table 8.4: Mesh Regions

Region No	Region Start	Region End	Mesh Size	Mesh Count (Average)	Region Volume (mm^3)	Average Cell Volume (mm^3)
1	-300	-55	8	29,678	2,252,736	75.9
2	-55	-5	4	13,335	459,742	34.5
3	-5	5	2	70,734	65,552	0.927
4	5	20	1	686,048	109,570	0.160
5	20	70	2	211,492	459,742	2.17
6	70	120	4	13,407	459,742	34.3
7	120	210	8	131,384	10,022,380	76.3
TOTAL	**-300**	**1210**		**1,156,077**	**13,829,464**	**12.0**

8.5 FLUENT

FLUENT is a general purpose CFD code that has many options facilitating modelling of a wide range of flow problems. It requires a pre-generated grid (or mesh) where each of the cells is treated as a control volume, and the relevant flow equations are applied to the cell. For this problem, the equations used are: conservation of mass; conservation of energy; the Navier-Stokes equations for momentum; a turbulence model, and a species transport equation.

The equations for conservation of mass, momentum and energy have a general form which can be applied in a compressible, 3D viscous flow, although they can be simplified for incompressible flows, 1D or 2D flows or inviscid flows (the latter are known as the Euler Equations). The general equations, along with their derivation can be found in Anderson [52], while the specific versions as applied in FLUENT can be found in the FLUENT User Manual [73].

Application of the full conservation equations to 3D complex geometries with turbulence would require computational resources that are currently unavailable and are likely to be unavailable for a significant amount of time. Therefore, to calculate turbulence, a model is used which generally falls into one of two categories – Reynolds-Averaged Navier-Stokes (RANS) or Large Eddy Simulation (LES).

In RANS, the solution variables (e.g. x-velocity) in the Navier-Stokes equations are averaged out (over time or space) so that they are composed of a mean and fluctuating value. This leads to Reynolds Stresses in the (averaged) Navier-Stokes equations which need to be modelled. The different models for the Reynolds stresses are discussed in Section 8.4.2. In LES, a filter is applied so that any turbulent eddies larger than the filter size (which is usually the same as the cell size) are calculated explicitly, with those below the filter size modelled. Although potentially better suited to this application where the large scale structures are of interest, the computational cost of LES is prohibitively high and was therefore not used.

Mixing in FLUENT is modelled by calculating the local species mass fraction using a convection-diffusion equation.

8.5.1 Fluent Options

After running initial test simulations, the following options were used for the main test programme:

Solver – Pressure Based. The pressure based solver was used as it allowed for the use of combustion and multiphase models. Although outside the scope of this study, future simulation of combustion and/or liquid would enhance the results of this study. Use of the pressure based solver will also allow for easy comparisons of future simulations with this study.

Time Dependency – Transient Solver. During the initial test simulations, confirming the findings reported by the industrial partner, the steady state solver would not converge. Therefore, the transient solver was used.

Evaluation of Gradients and Derivatives – Least Squares Cell Based. There are three options for the calculating the Gradients and Derivatives – Green-Gauss Cell based, Green-Guass Node based and Least Squares Cell based. On unstructured meshes, the Least Squares method has comparable accuracy to the Green-Guass Node based, but is less computationally expensive, and is much superior to the Green-Gauss Cell based method [73].

Pressure–Velocity Coupling – PISO. The PISO algorithm with "Neighbor" Correction is recommended for all transient calculations [73].

Discretization Scheme – Second Order. For flows where the flow is not aligned with the mesh, i.e. rotating flows, turbulent flows or unstructured tetrahedral meshes, second order discretization is recommended.

Pressure Interpolation Scheme – PRESTO! The PRESTO! scheme is recommended for flows with high swirl numbers and high-speed rotating flows [73].

Turbulence Models – RNG k-ε Model / RSM Model. Both the RNG (Re-Normalisation Group theory) k-ε model and RSM (Reynolds Stress Model) are RANS models. The RNG k-ε model is a two-equation model, whereas the RSM is a seven-equation model when applied in three dimensions. The standard k-ε model is widely used in many engineering applications. The RNG k-ε model is a derivation of the k-ε model which is more suitable for highly strained flows and swirling flows [73]. The RSM accounts for directionality in its averaging technique, so is more suited for complex flows where the area of interest comes form this directionality, such as highly swirling flows. Section 8.5.2 provides further details on the turbulence models used in each of the cases.

Table 8.5: Boundary Conditions

Boundary	Variable	Value
Operating Pressure		0 Pa
Inlet	Mass Flow Rate	0.5 kgs^{-1}
	Gauge Pressure	107000 Pa
	Turbulent Intensity	10%
	Turbulent Length Scale	0.00756
	Temperature	300 K
Outlet	Gauge Pressure	101325 Pa
	Turbulent Intensity	10%
	Turbulent Length Scale	0.00756
	Temperature	300 K

Boundary Conditions – Mass Flow Inlet, Pressure Outlet. The Mass Flow Inlet boundary condition allows the specification of the mass flow at the boundary. This is ideal for this problem as the mass flows are already known. The Pressure Outlet boundary condition allows the static pressure at the boundary to be set. Again, this is ideal for this model as it is known that the PDE vents to atmosphere. The boundary conditions used are detailed in Table 8.5.

8.5.2 Turbulence Modelling

Initially all the geometries were attempted with the RNG k-ε Model. This worked for the geometries where the inner and outer reeds were clamped in a similar manner – i.e. the Co-Swirl, Counter-Swirl and Circumferentially Clamped Bottom cases, but not for the hybrid cases. It is believed that the RNG k-ε model is unable to resolve the shear stress caused by the differently clamped reeds, hence the need for the RSM model. The first three geometries were initially computed using the RNG k-ε model, and then repeats were conducted using the RSM model for the non-mixing case. The different results produced by the two models are discussed as appropriate in Section 8.7.

8.6 Fuel

Initially, all the geometries were run without fuel to gain an idea of the flow structure produced by the valve. Once these had been obtained, propane gas was added at a rate that would give a stoichiometric fuel-air-mixture. From the first simulation that included fuel it was obvious that the velocity of the fuel was much higher than the velocity of the air that it was injected into, and that this destroyed the flow generated by the valve. As the PDE was designed for operation with liquid fuel, the mass flow rate of fuel was high when using gaseous fuel due to the Air-Fuel-Ratio (AFR) and relative energy densities of the two fuels.

As the objective of study was to look at the effectiveness of the valve at mixing the fuel and air, the absolute ratio of fuel to air is not vital. Therefore, the mass flow rate of the fuel was halved to reduce the velocity of the fuel, bringing it much closer to the bulk velocity of the air. The boundary conditions used for the Fuel Inlet are given in Table 8.6.

Table 8.6: Fuel Inlet Boundary Conditions

Case	Variable	Value
Full Fuel	Mass Flow Rate	0.0323 kgs^{-1}
	Gauge Pressure	0 Pa
	Turbulent Intensity	10%
	Turbulent Length Scale	0.00084
	Temperature	300 K
Half Fuel	Mass Flow Rate	0.0166 kgs^{-1}
	Gauge Pressure	0 Pa
	Turbulent Intensity	10%
	Turbulent Length Scale	0.00084
	Temperature	300K

8.7 Results

8.7.1 Co-Swirl

This model is the one closest to the original valve design. The industrial partner's simulations found that there was a strong radial velocity present, which was said to be responsible for carrying the fuel to the chamber walls.

This study found that the valve configuration, as expected from the geometry, resulted in a large degree of swirl throughout the chamber. The fluid pathlines in Figure 8.3 show that there is a region of re-circulating flow that extends to approximately 350-400mm downstream of the valve. When the pathlines are coloured by residence time, the flow in this region is seen to have a very long residence time, 65ms compared to around 30ms residence time for the bulk of the flow in the chamber.

From velocity contour plots, the velocity magnitude in the central region is much lower than in the bulk of the flow. This can of course be attributed to the swirl induced by the valve. The velocity magnitude in this region is between $10ms^{-1}$ – $40ms^{-1}$, while the velocity in the main flow region is above 80 ms^{-1}.

The x-velocity (down the length of the tube) plot in Figure 8.4 shows that the recirculation zone extends to just over 500mm downstream of the valve – longer than is shown by the pathlines. In the central region of the flow, there appears to be a stagnant region where the x-velocities are lower than in the main recirculation zone – 0 ms^{-1} – 5ms^{-1} compared to 15ms^{-1} – 20ms^{-1}.

At the exit of the tube there is a negative velocity in the central region, i.e. there is flow into the tube from the outside. It is believed that this is caused by the swirling nature of the flow at the exit.

At full mass flow rate (Figure 8.5), the fuel exits the valve at a velocity of around 180 ms^{-1} into the "stagnant zone". This does not destroy the zone completely, but it appears that the fuel is transported to the border between the swirling and non-swirling flow in the boundary layer. Stoichiometric concentrations are not achieved until 1,000mm from the valve where the flow meets the suction zone at the exit of the tube.

At half fuel mass flow rate, mixing is much better than for the full fuel case. Figure 6.6a shows that at 350mm downstream of the valve, the fuel and air is mixed to within 10% of the "stoichiometric" target (for the half fuel mass flow rate cases, "stoichiometric" mixture is at φ=0.5, so at 350 mm downstream of the valve in this case, the mixture is $0.45 \leq \varphi \leq 0.55$). Figure 8.6b shows that at 600mm downstream of the valve, the mixture is within 5% of the target ($0.475 \leq \varphi \leq 0.525$). Although this is much better than the full fuel case, it should be remembered that mixing to within 5% of the target occurs at six tube diameters downstream of the valve, and to within 10% three and a half tube diameters downstream of the valve. Considering the tube is only twelve tube diameters long, this is not considered to be a suitable solution.

The RSM version of the Co-Swirl geometry produced an interesting result when compared to the RNG k-ε model. From X-Velocity contour plots (Figure 8.7), it can be seen that the re-circulation zone extends the whole way down the chamber, connecting with the exit recirculation zone seen on the RNG k-ε model.

The RSM Model suggests better mixing for the Co-Swirl case than the RNG k-ε model. At half fuel mass flow rate, the case is mixed to within 10% at 300mm downstream of the valve (Figure 8.8a), and to within 5% at 400mm (Figure 8.8b), although the central region appears richer and the outer region leaner, with a step change defining the border between the two.

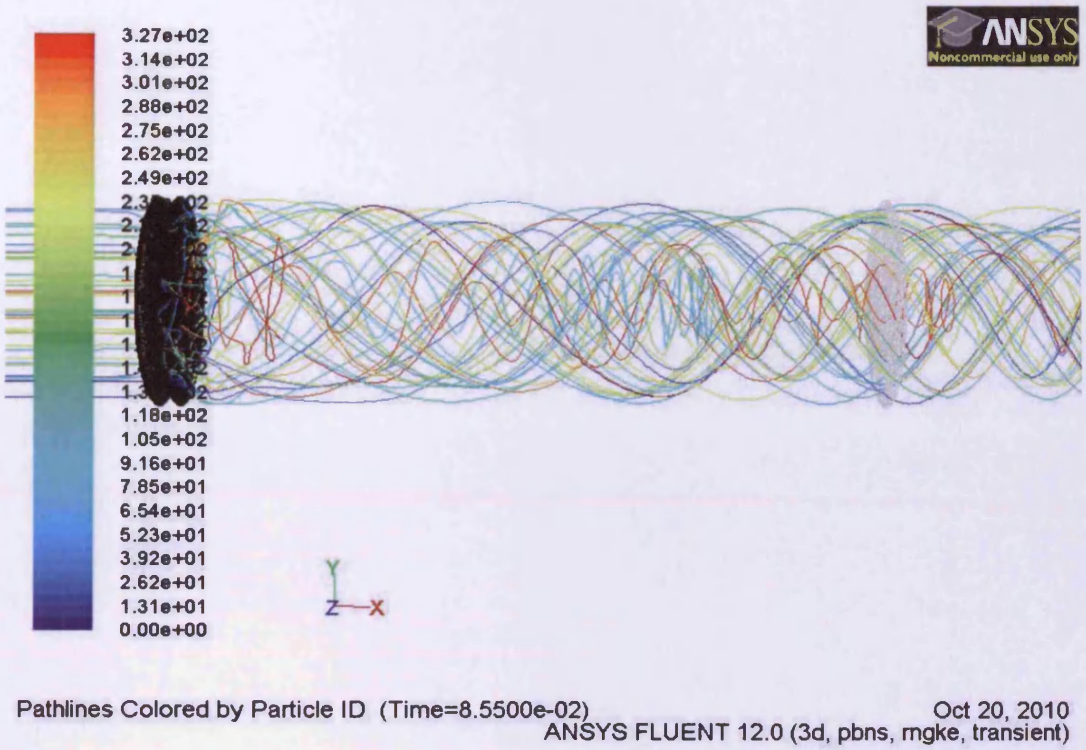

Figure 8.3: Co-Swirl Pathlines

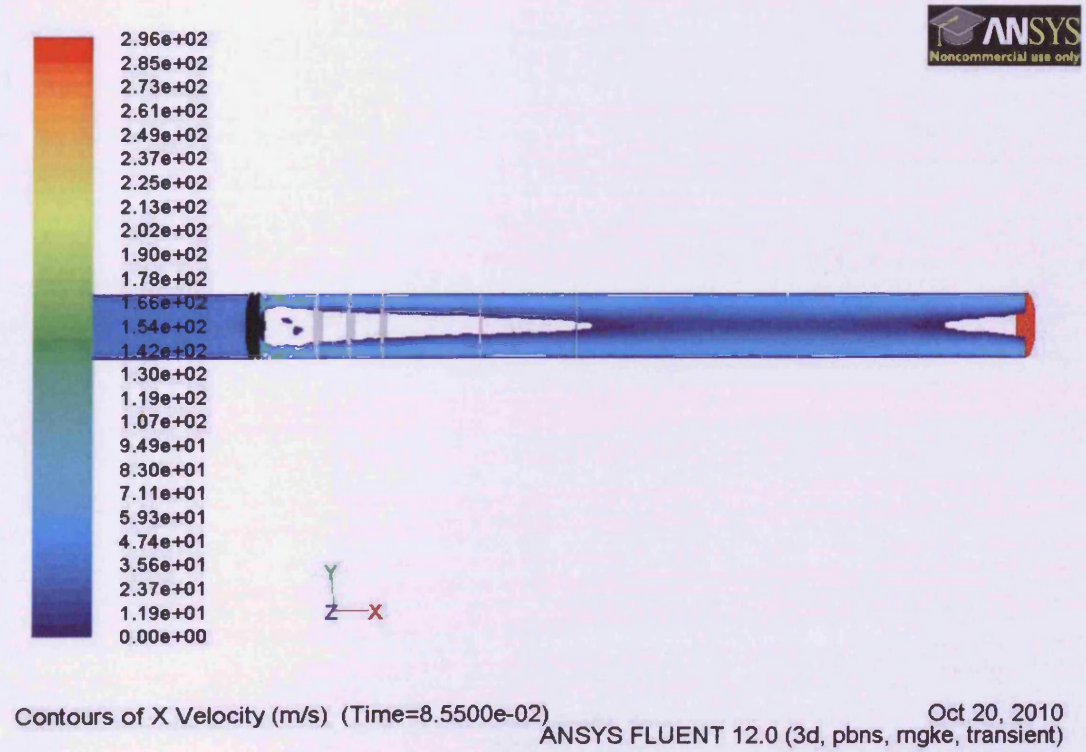

Figure 8.4: Co-Swirl Positive X Velocity Plot

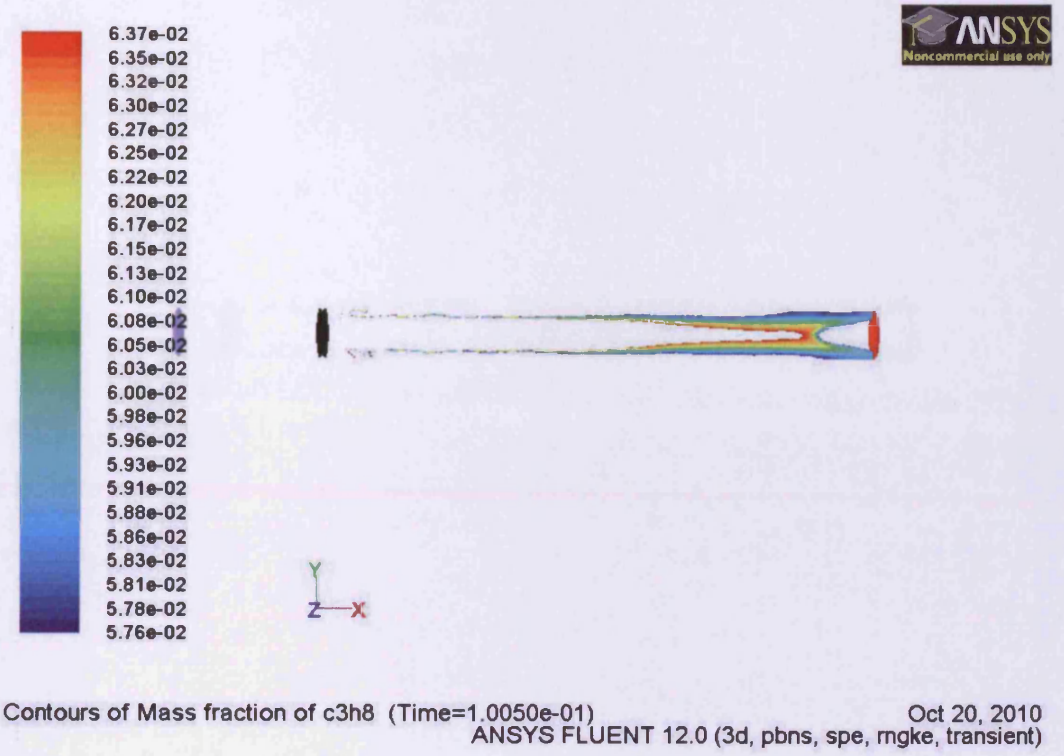

Figure 8.5: Co-Swirl Mixing at Full Mass Flow Rate

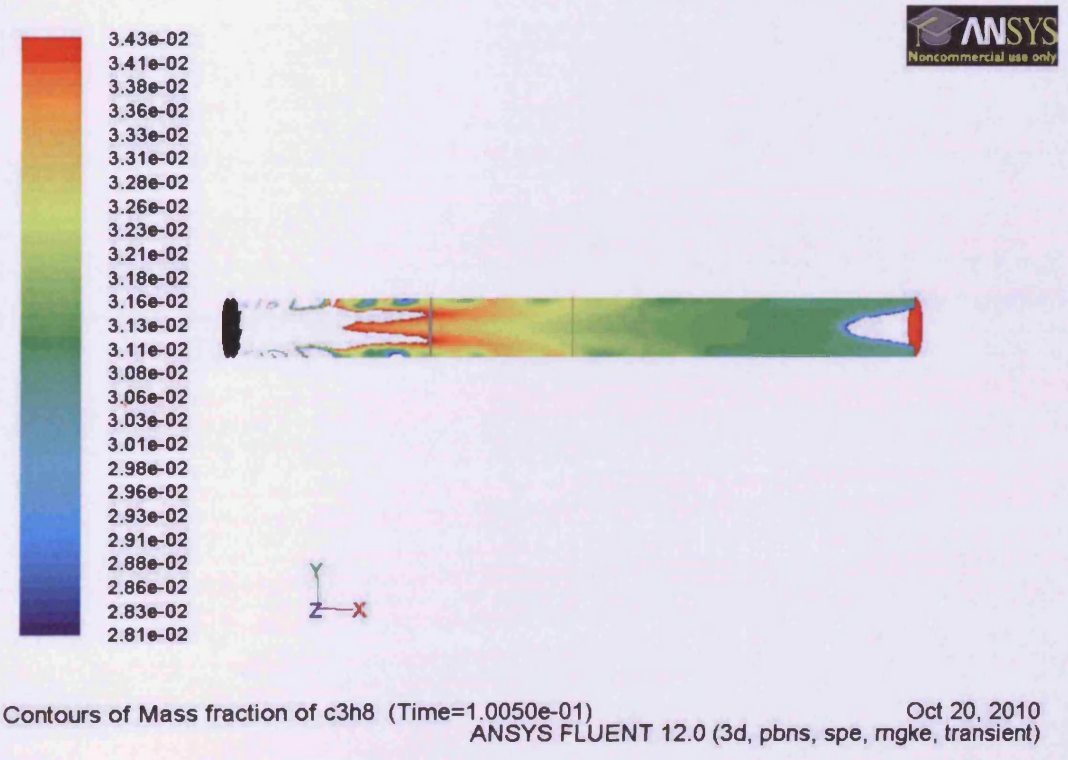

Figure 8.6a: Co-Swirl Mixing at Half Mass Flow Rate to 10% of target

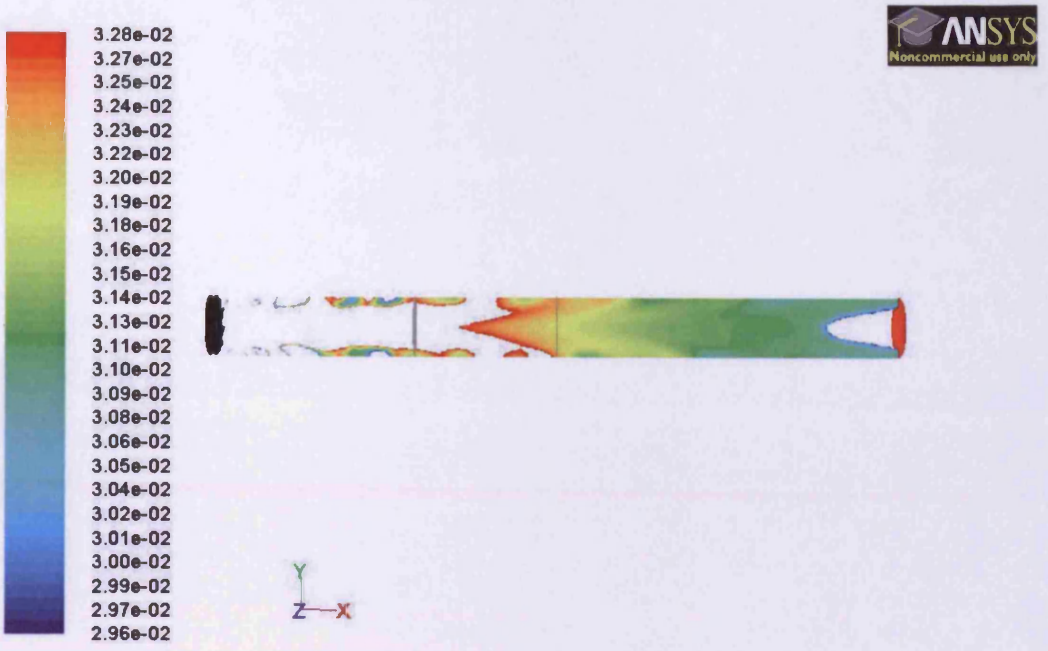

Figure 8.6b: Co-Swirl Mixing at Half Mass Flow Rate to 5% of target

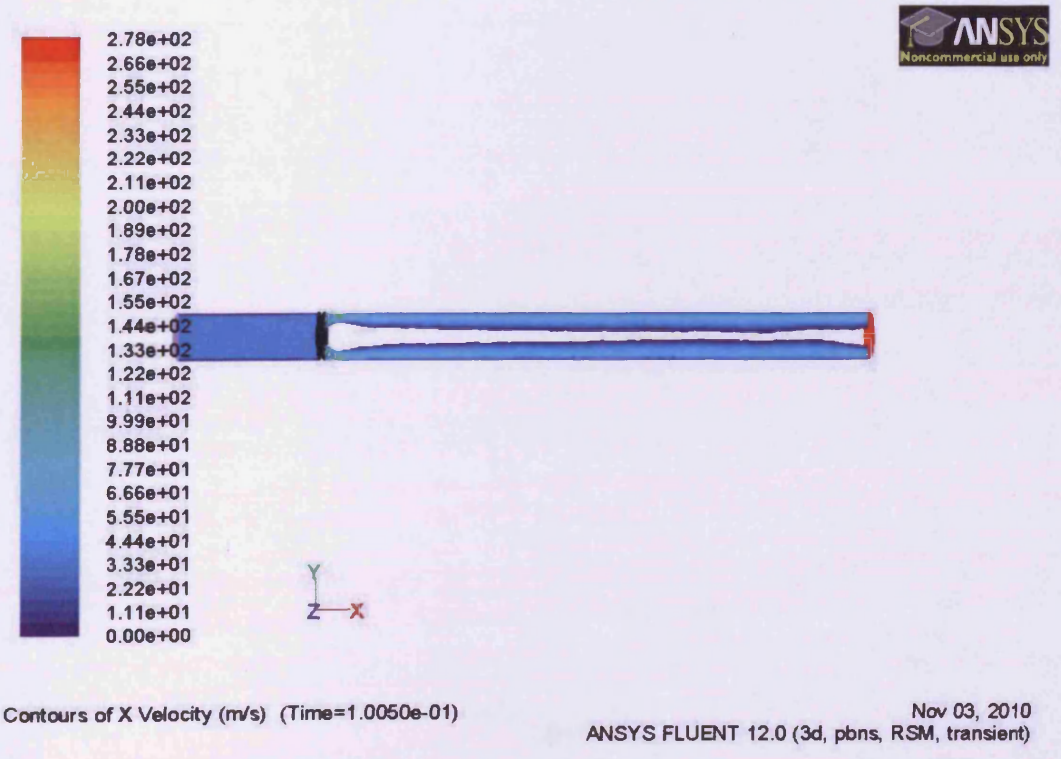

Figure 8.7: Co-Swirl Positive X Velocity Plot for RSM Model

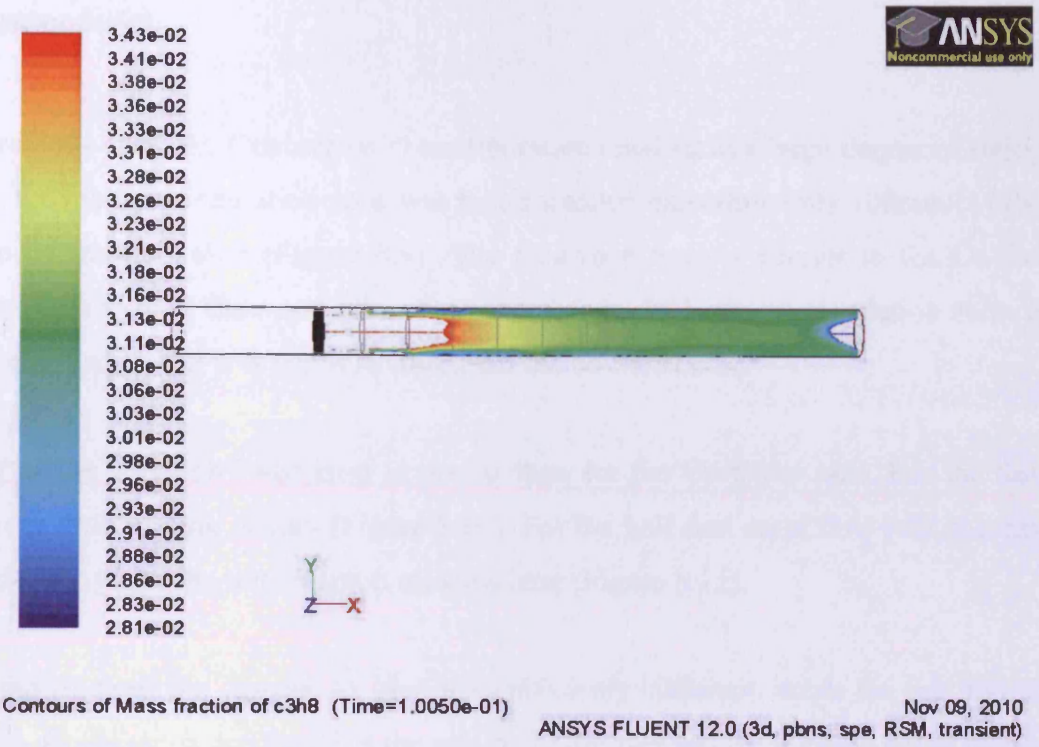

Figure 8.8a: Co-Swirl Mixing at Half Mass Flow Rate to 10% of target for RSM Model

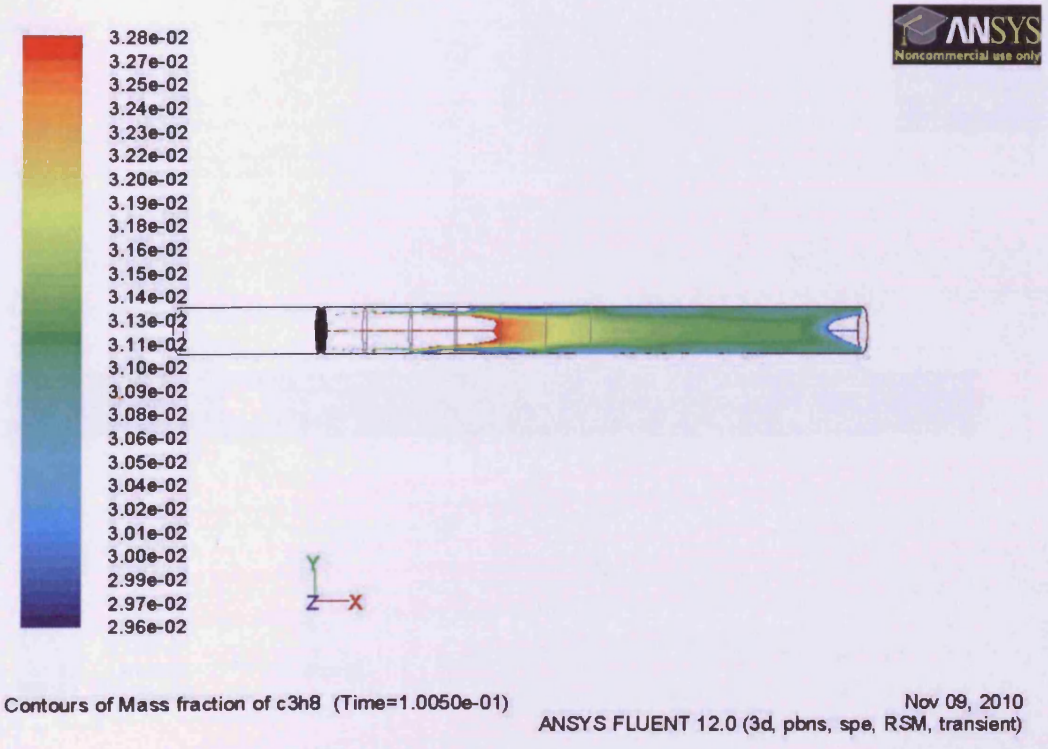

Figure 8.8b: Co-Swirl Mixing at Half Mass Flow Rate to 5% of target for RSM Model

8.7.2 Counter Swirl

As in the previous case, the Counter swirl configuration resulted in a large degree of swirl. However, in this case, the main re-circulation zone was much smaller, extending only 100mm (1 tube diameter) downstream of the air valve (Figure 8.9). The residence time is similar to the Co-Swirl case at around 35ms for the bulk flow and 65ms for particles caught in the re-circulation zone. At the exit, there is a suction zone, but it is much smaller than the co-Swirl case.

The mixing in the Counter-Swirl case is poorer than for the Co-Swirl case. For the full fuel mass flow rate, very little mixing occurs (Figure 8.10). For the half fuel mass flow rate, the central region remains fuel-rich, while the outer region remains lean (Figure 8.11).

The RSM model does not appear to give a significantly different result for the non-mixing case (Figure 8.12). However, it predicts that the mixing of the fuel and air is much better than in the RNG k-ε model, with the mixture being to within 10% of the target across the cross section at 800mm downstream of the valve (Figure 8.13).

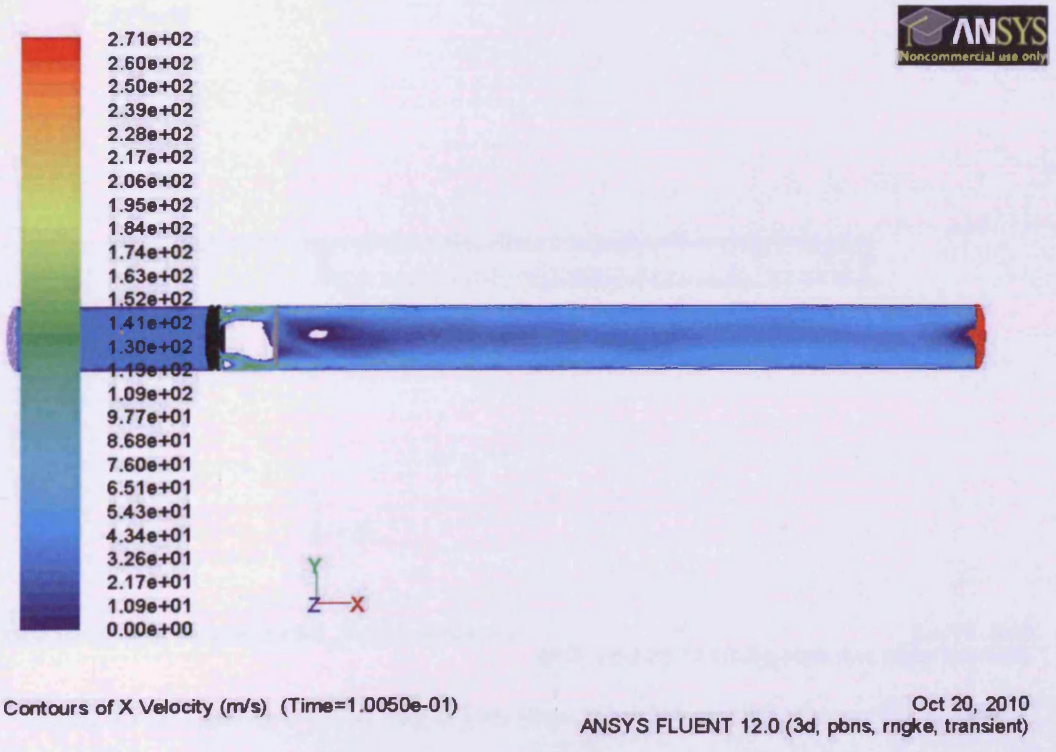

Figure 8.9: Counter-Swirl Positive X Velocity Plot

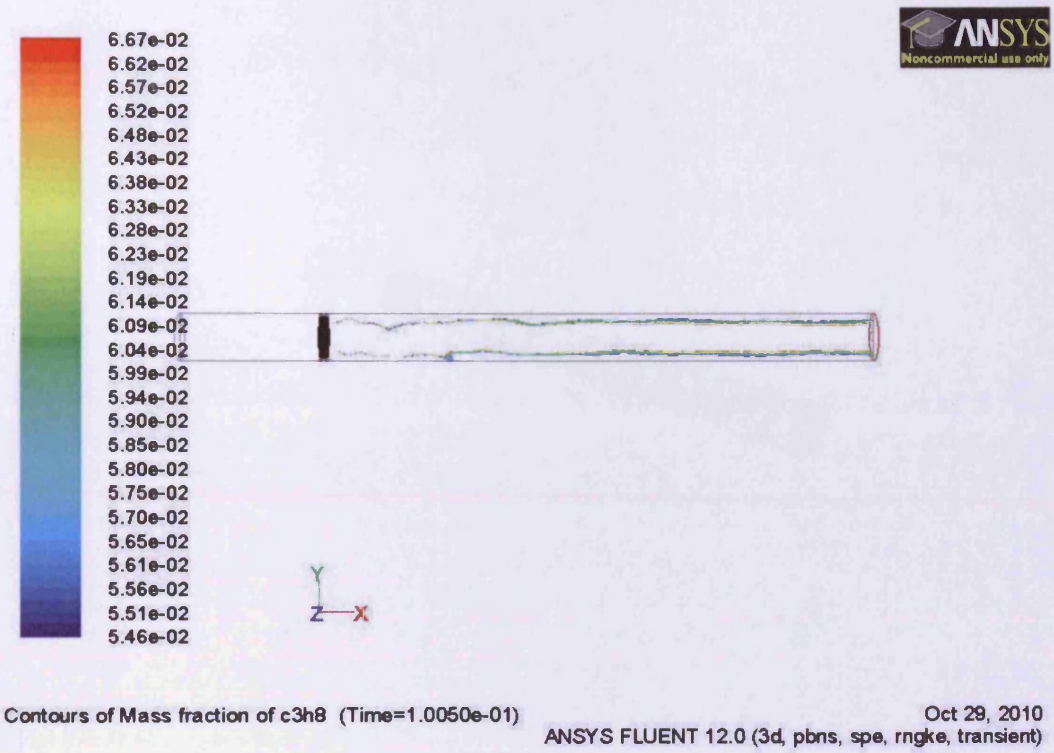

Figure 8.10: Counter Swirl Mixing at Full Mass Flow Rate to 10% of target

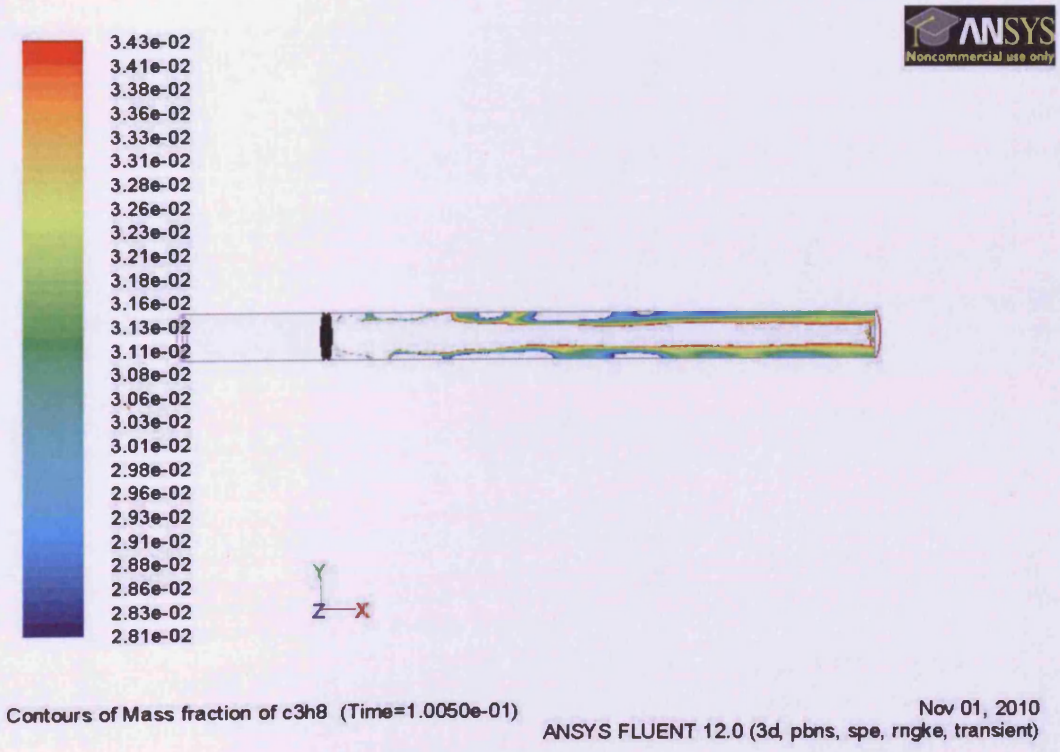

Figure 8.11a: Counter Swirl Mixing at Half Mass Flow Rate to 10% of target (front view)

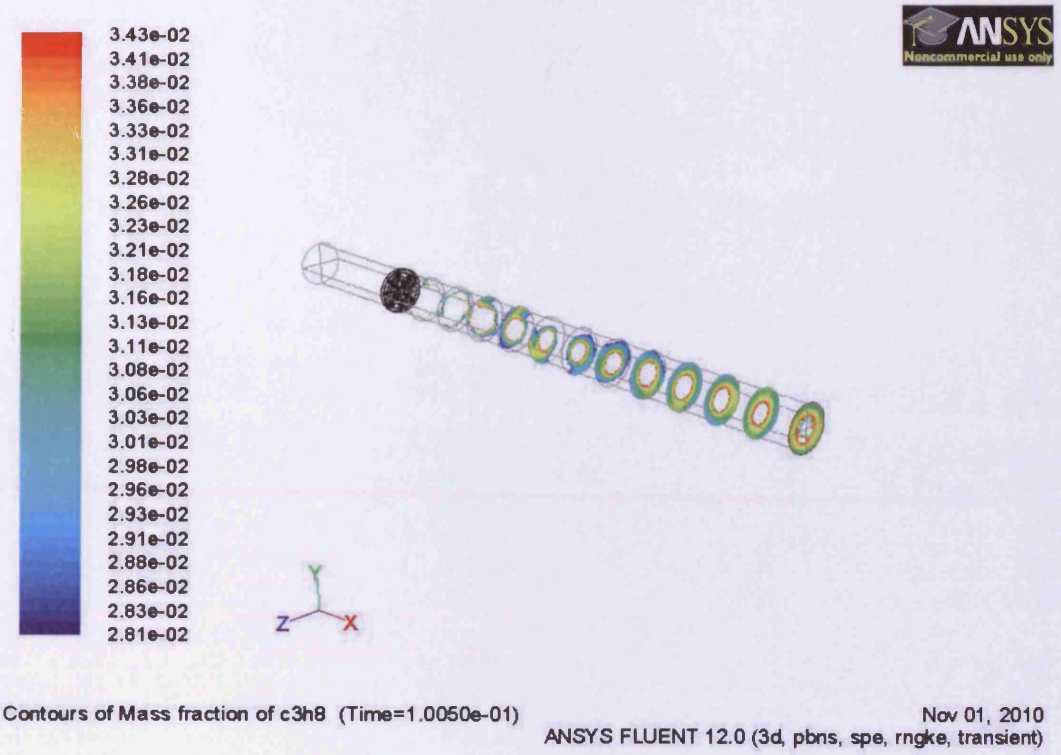

Figure 8.11b: Counter Swirl Mixing at Half Mass Flow Rate to 10% of target (cross sectional views)

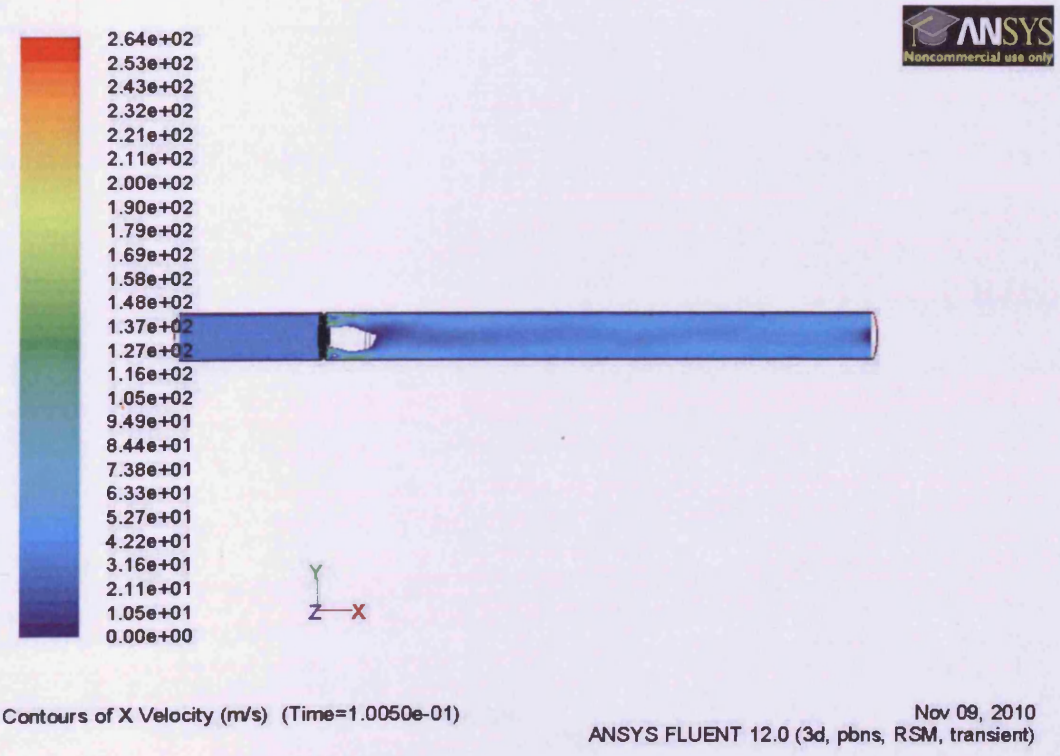

Figure 8.12: Counter-Swirl Positive X Velocity Plot RSM Model

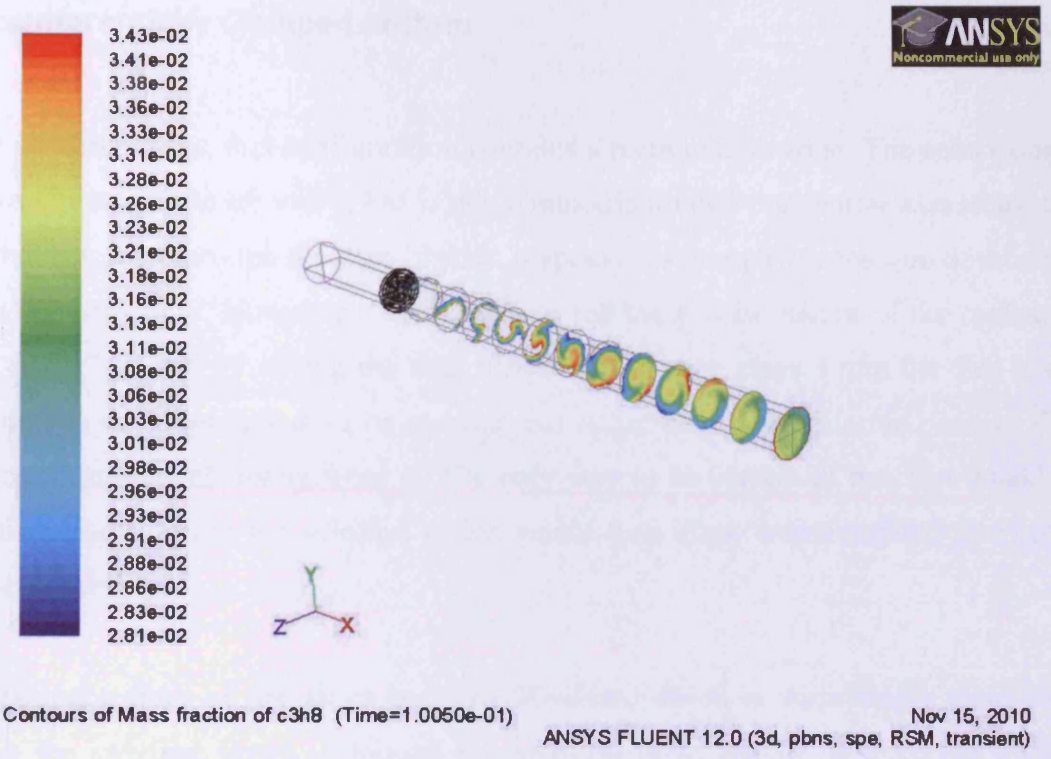

Figure 8.13a: Counter Swirl Mixing at Half Mass Flow Rate RSM Model to 10% of target (cross sectional views)

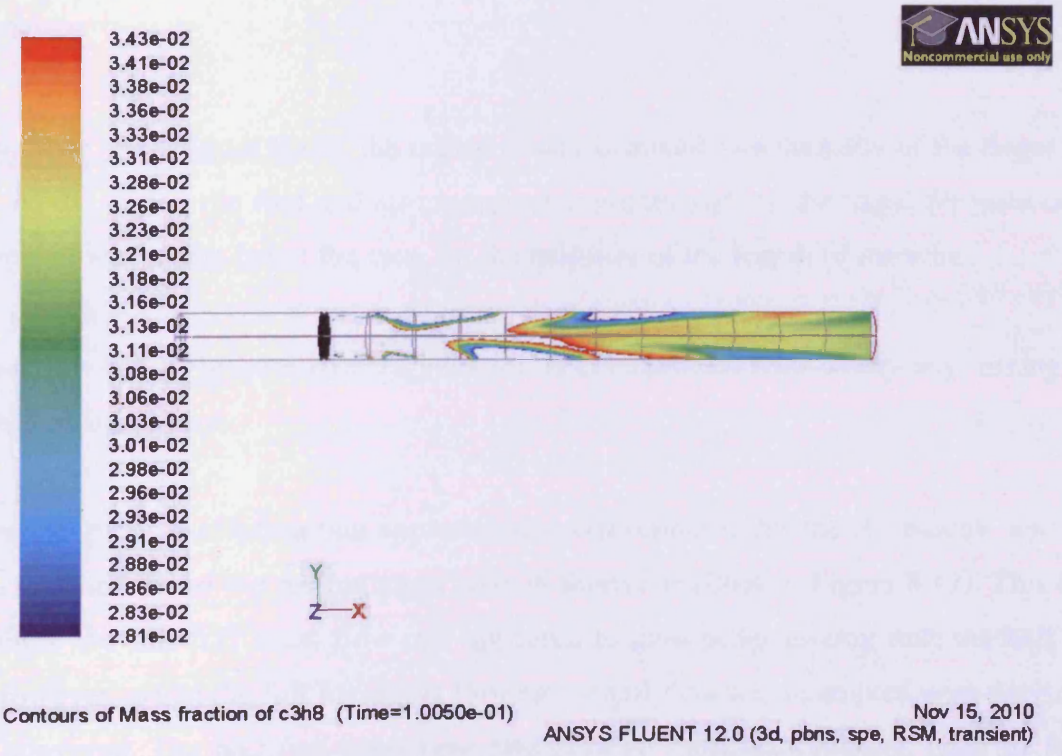

Figure 8.13b: Counter Swirl Mixing at Half Mass Flow Rate RSM Model to 10% of target (front view)

8.7.3 Circumferentially Clamped Bottom

As with the swirling cases, this configuration contains a recirculation zone. The zone extends around 250mm downstream of the air valve, but is not symmetric around the central axis (Figure 8.14). By looking at the data files through the time history, it appears as though the position of the recirculation zone is moving with time. However it is difficult to tell the precise nature of the movement due to the "strobe effect" caused by saving the data files every 10 time steps. From the data available, the recirculation zone does not appear to be moving, but rather there is a preferred position for the zone with occasional movements away from it. The only way to be certain of this fact would be to save data more frequently during the solution which would then allow more detailed study of the exact nature of the instability.

The bulk residence time of the air is between 30-40ms, which is surprisingly close to the times exhibited by the swirling flows. Although the swirling flows would be expected to have longer residence times, it must be remembered that the flow is being driven by a constant mass flow rate, so the time taken for a particle to move from one end of the domain to the other will be relatively steady.

At full mass flow rate (Figure 8.15), the region which is mixed to within 5% of the target mixture is very small. At the outlet, the fuel and air are mixed to within 10% of the target for most of the cross sectional area, however this is not the case for the majority of the length of the tube.

At half mass flow rate (Figure 8.16), the situation is even poorer, with hardly any mixing occurring between the fuel and the air.

The RSM model gives a solution that appears more axisymmetric for the X-velocity, and compared to the RNG k-ε model and the recirculation zone is shorter at 200mm (Figure 8.17). This case is the only one where the full fuel mass flow rate appeared to give better mixing than the half fuel mass flow rate. However, when the full fuel mass flow rate simulation was attempted with the RSM model it failed to converge. The half fuel mass flow rate gave no significant mixing, with the fuel stream deflected downwards by the recirculation zone (Figure 8.18).

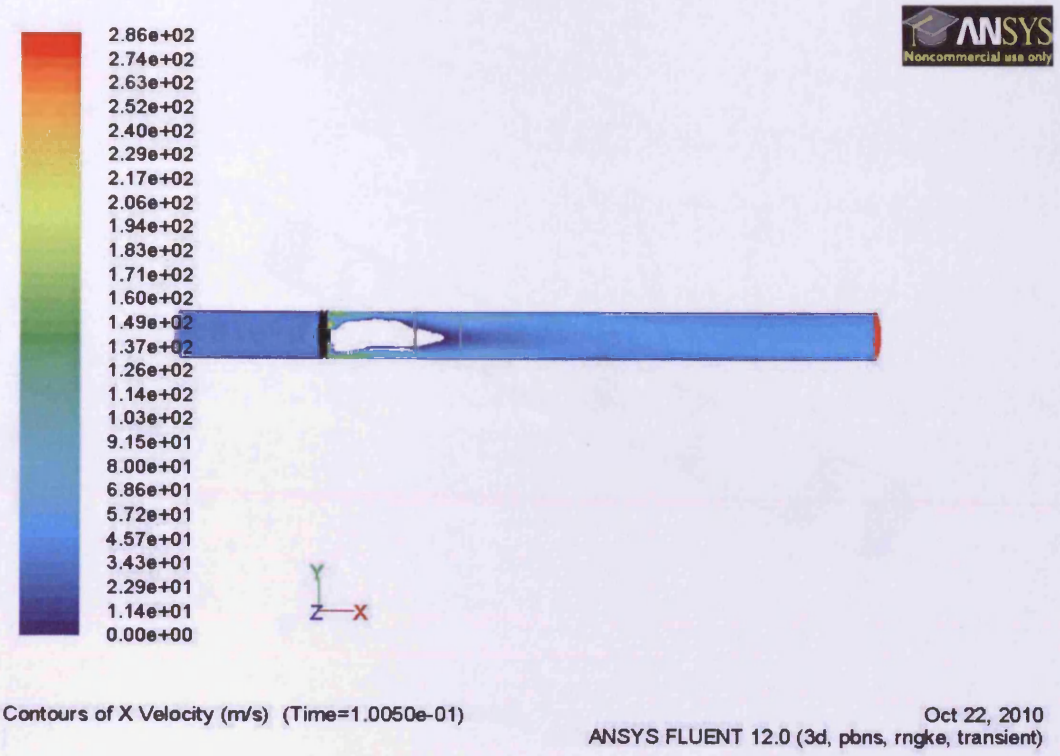

Figure 8.14a: Circumferentially Clamped Bottom No Fuel Positive X velocity (front view)

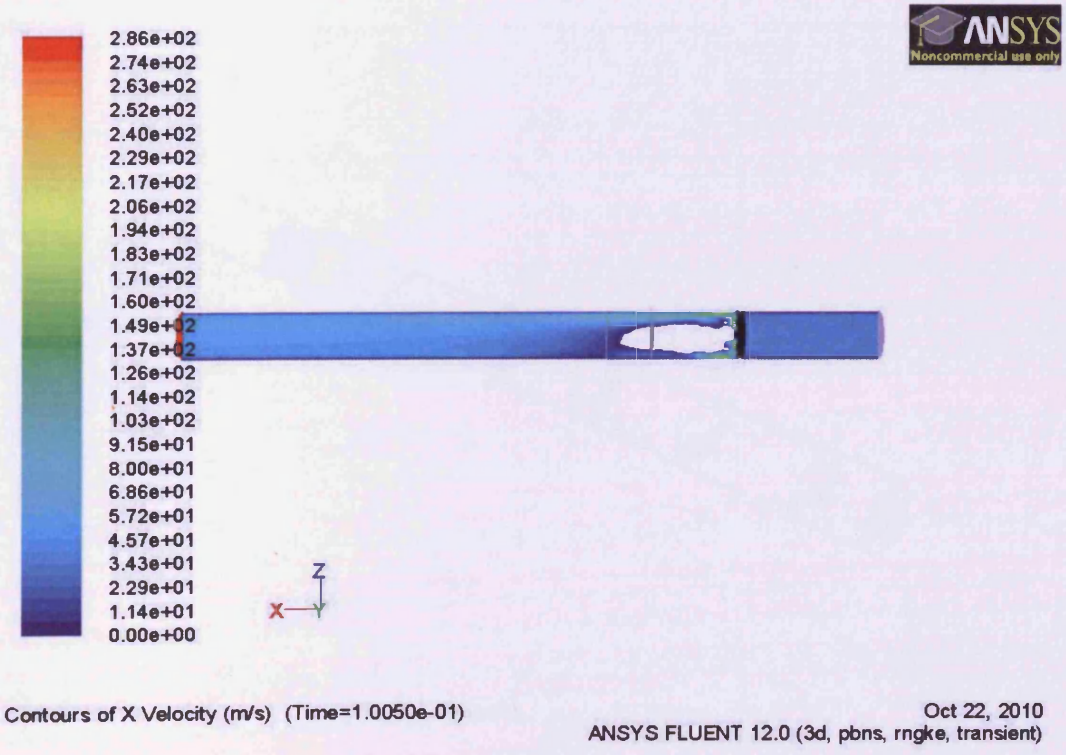

Figure 8.14b: Circumferentially Clamped Bottom No Fuel Positive X velocity (top view)

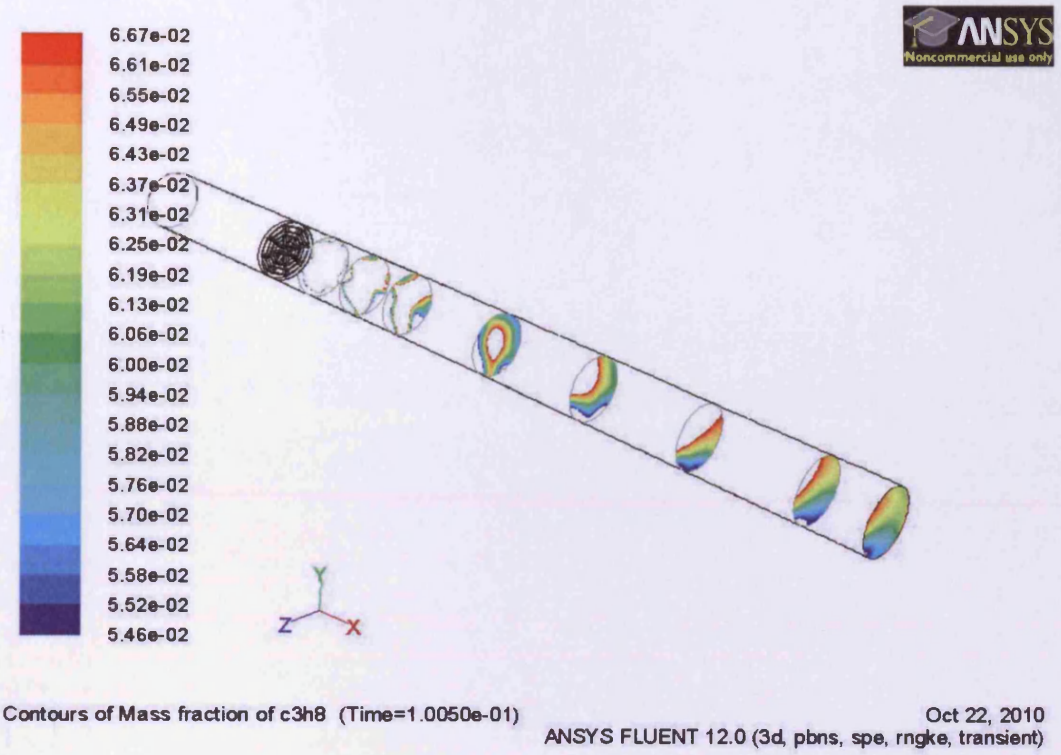

Figure 8.15a: Circumferentially Clamped Bottom Mixing at Full Mass Flow Rate to 10% of target

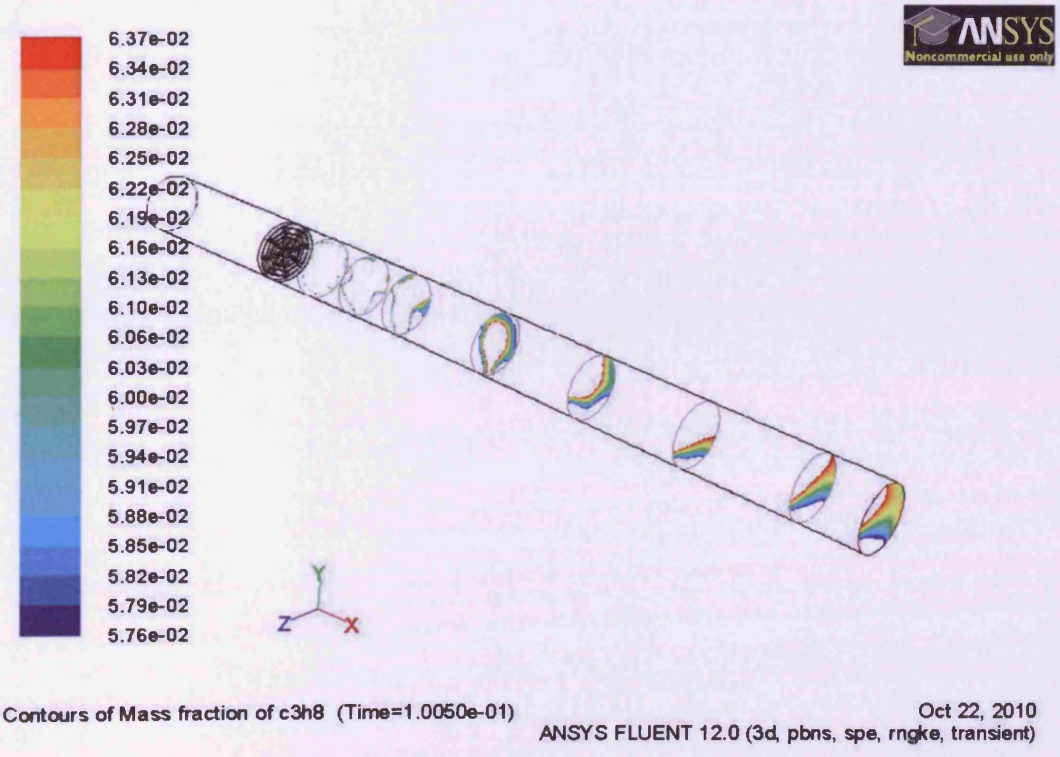

Figure 8.15b: Circumferentially Clamped Bottom Mixing at Full Mass Flow Rate to 5% of target

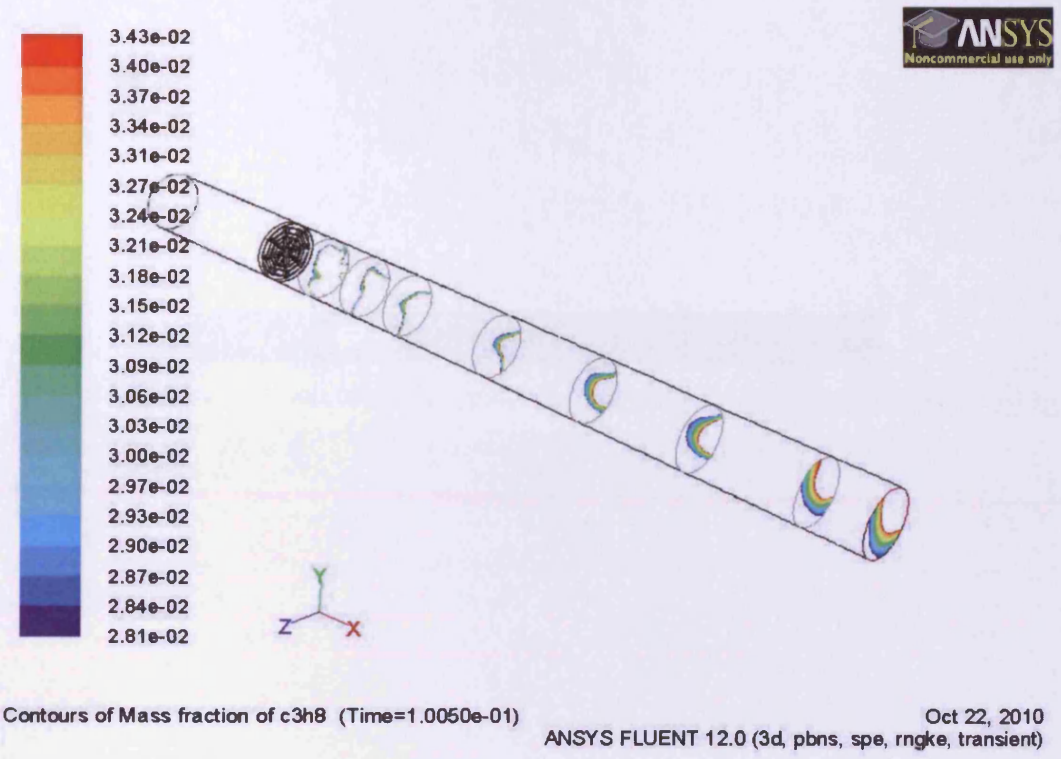

Figure 8.16a: Circumferentially Clamped Bottom Mixing at Half Mass Flow Rate to 10% of target

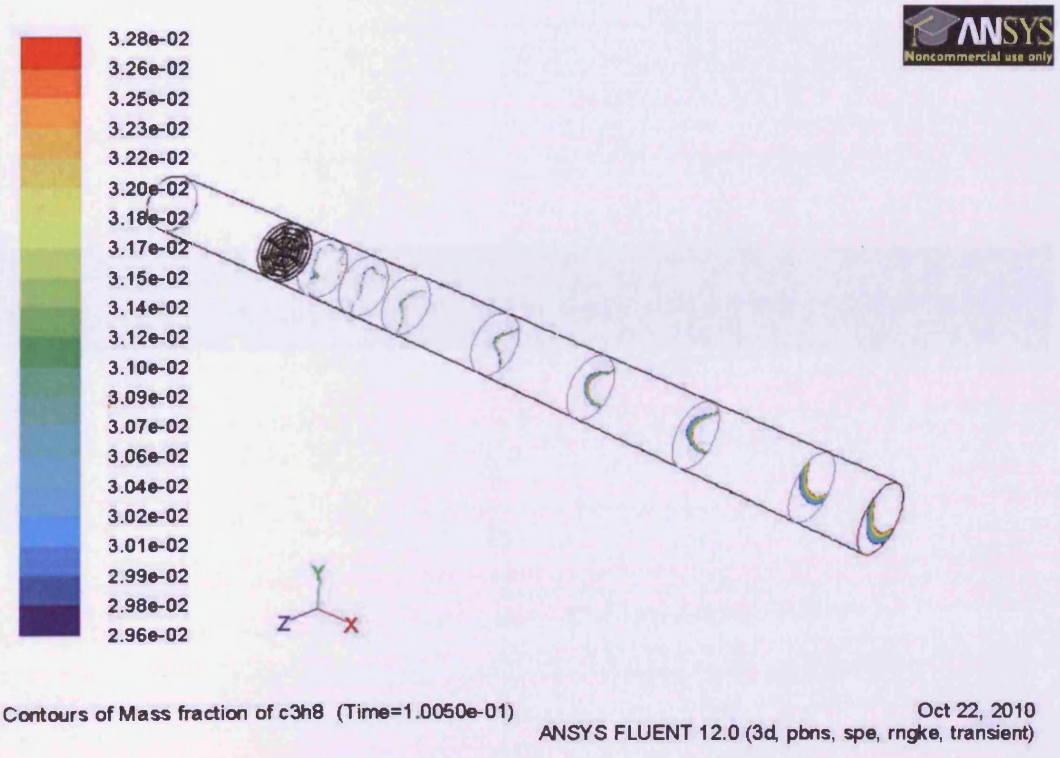

Figure 8.16b: Circumferentially Clamped Bottom Mixing at Half Mass Flow Rate to 5% of target

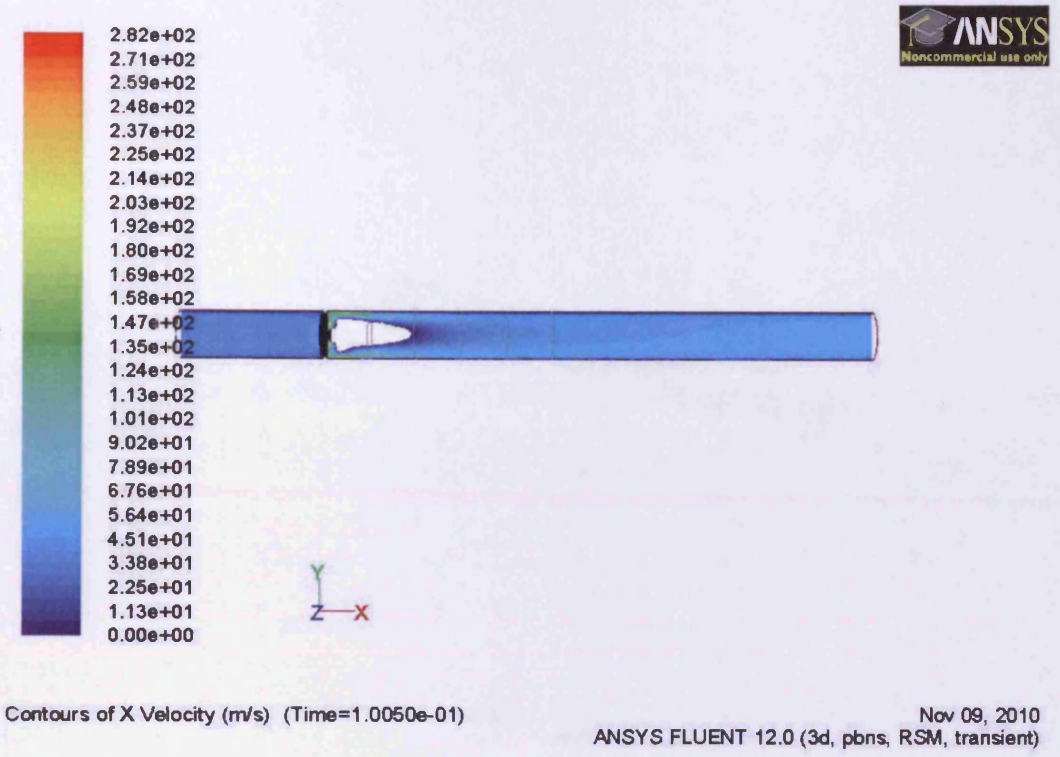

Figure 8.17: Circumferentially Clamped Bottom No Fuel Positive X velocity RSM Model

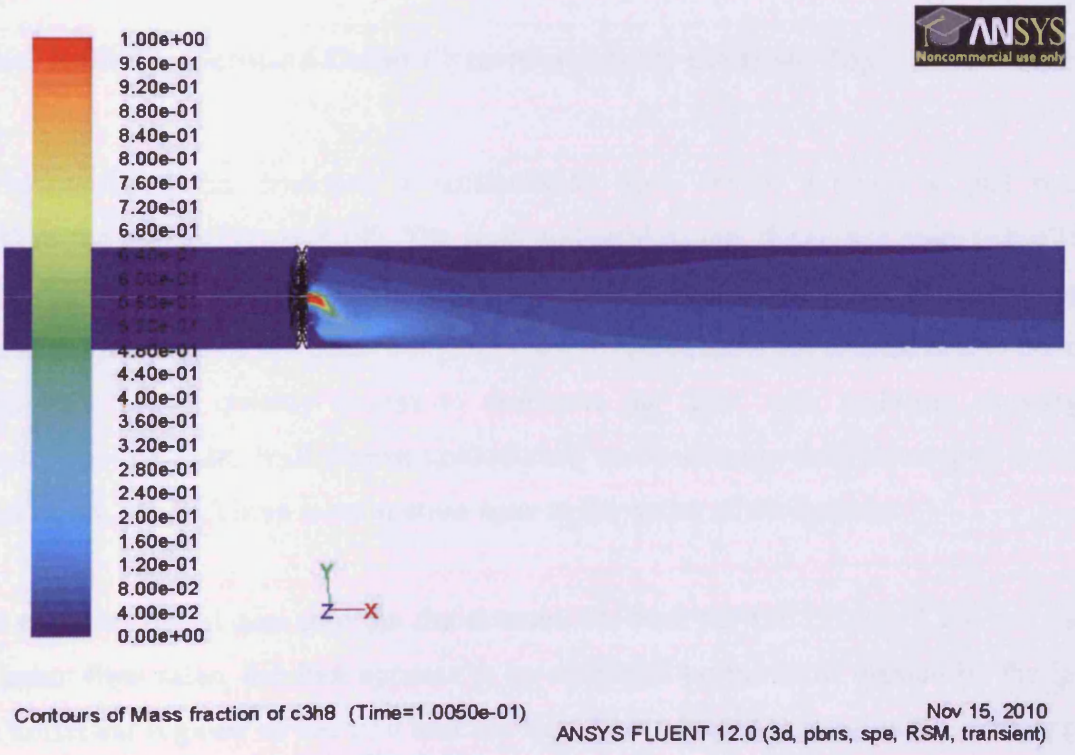

Figure 8.18a: Circumferentially Clamped Bottom Mixing at Half Mass Flow Rate RSM Model (full concentration field)

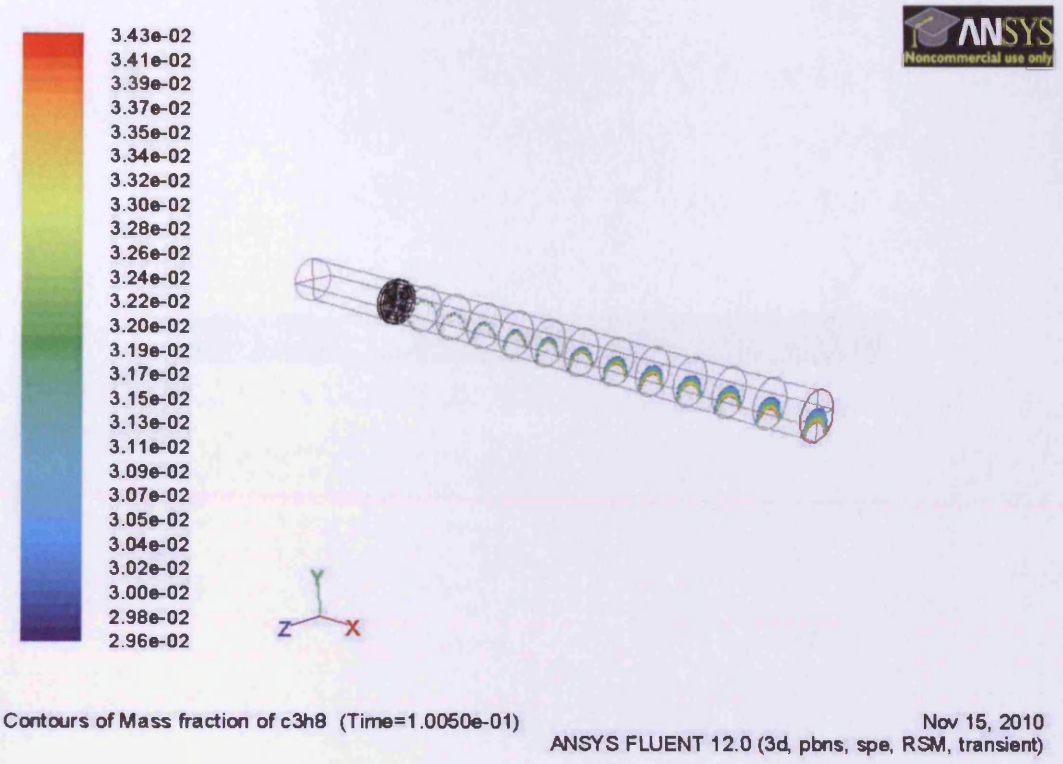

Figure 8.18b: Circumferentially Clamped Bottom Mixing at Half Mass Flow Rate RSM Model to 10% of target

8.7.4 Inner Radially Clamped Outer Circumferentially Clamped Top

This hybrid configuration produces a recirculation zone which extends to just over 200mm downstream of the valve (Figure 8.19). The zone is shaped so that the widest point is but 50mm from the valve unlike the fully swirling flows where it is at the valve, Additional small recirculation zones are present at the junction of the outer wall and the valve, and these are created due to the outer reeds pointing inwards. Swirl quickly begins to dominate the flow, with pathlines showing swirling behaviour close to the outer wall almost immediately and becoming fully developed around 300mm downstream of the valve. There is no suction zone at the outlet of the domain.

Looking at cross sectional cuts through the domain, for both the full (Figure 8.20) and half (Figure 8.21) fuel mass flow rates, the fuel appears to be entrained by the swirl created by the inner reeds. This leads to helical regions of too rich and too lean flow which become smaller further away from the valve. As in previous cases, the mixing appears better for the half fuel mass flow compared to the full fuel mass flow.

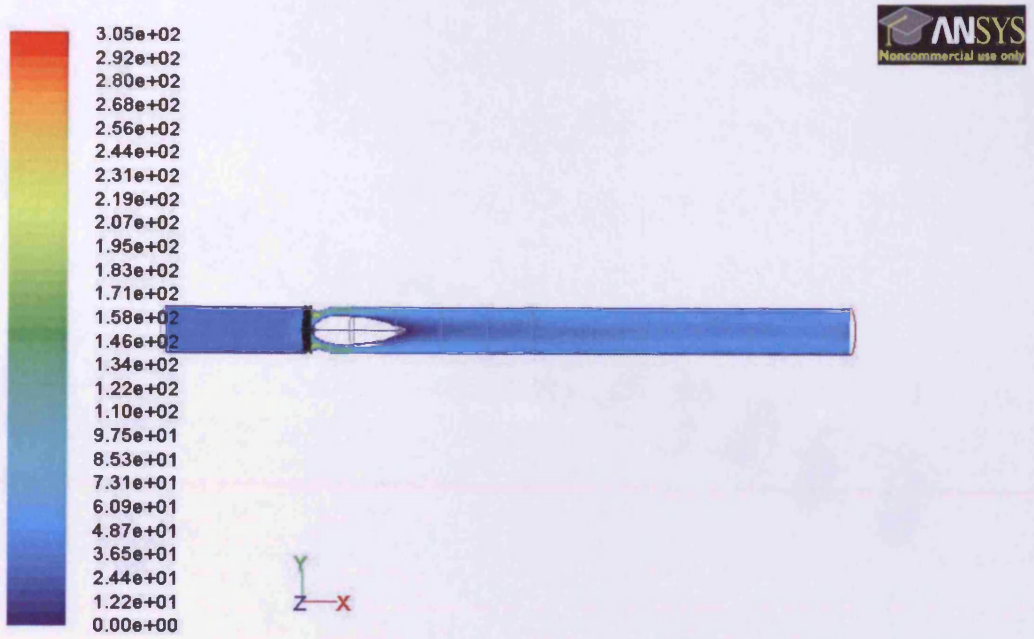

Figure 8.19: Inner Radially Clamped Outer Circumferentially Clamped Top Positive X Velocity Plot

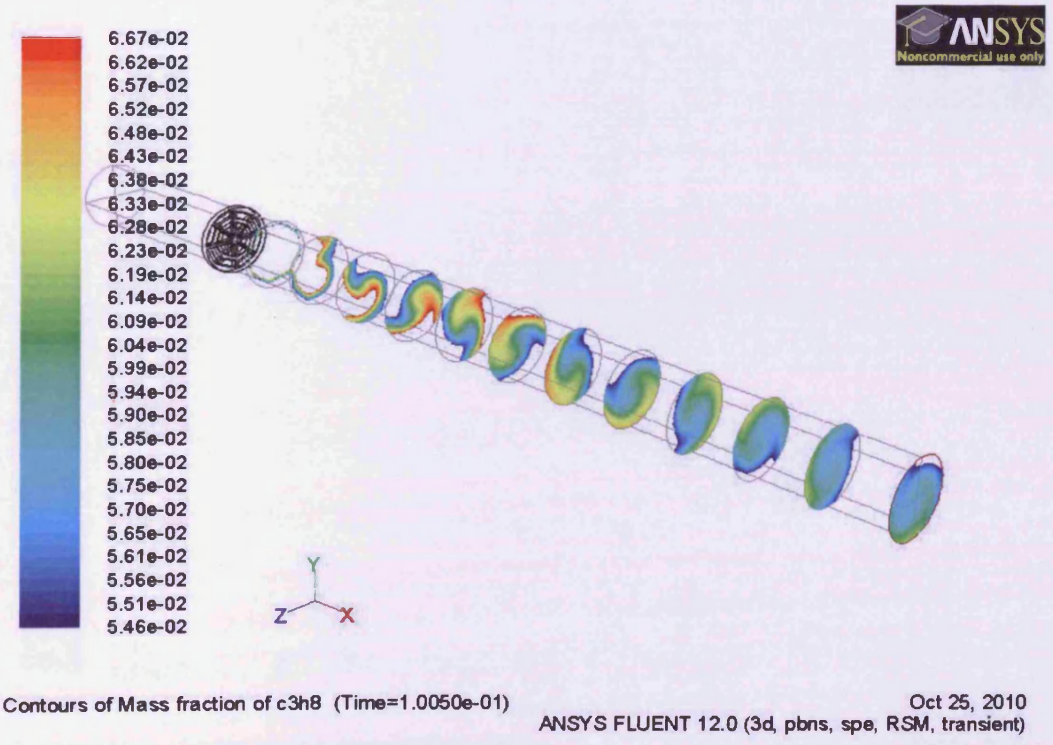

Figure 8.20a: Inner Radially Clamped Outer Circumferentially Clamped Top Mixing at Full Mass Flow Rate to 10% of target

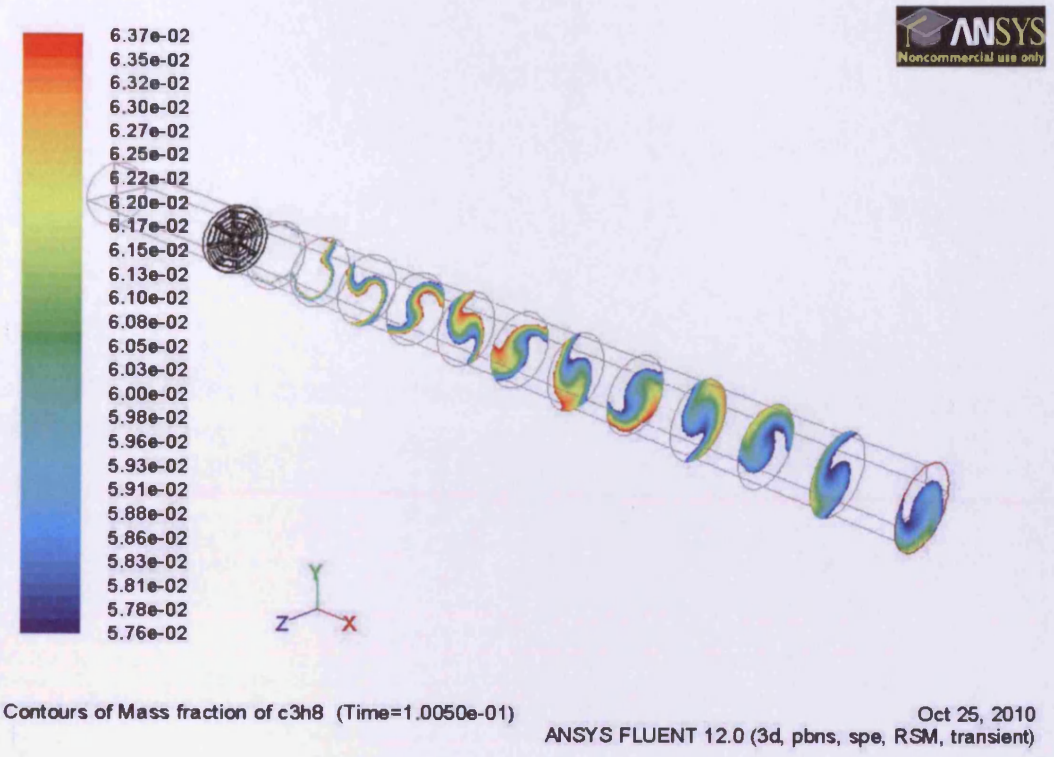

Figure 8.20b: Inner Radially Clamped Outer Circumferentially Clamped Top Mixing at Full Mass Flow Rate to 5% of target

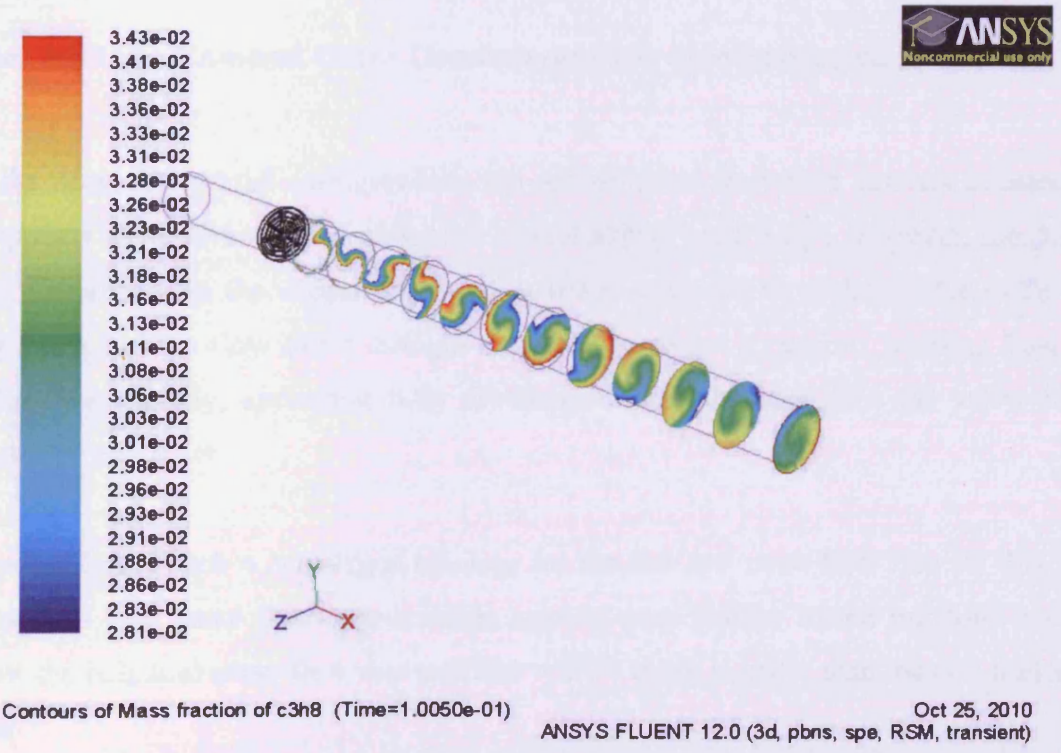

Figure 8.21a: Inner Radially Clamped Outer Circumferentially Clamped Top Mixing at Half Mass Flow Rate to 10% of target

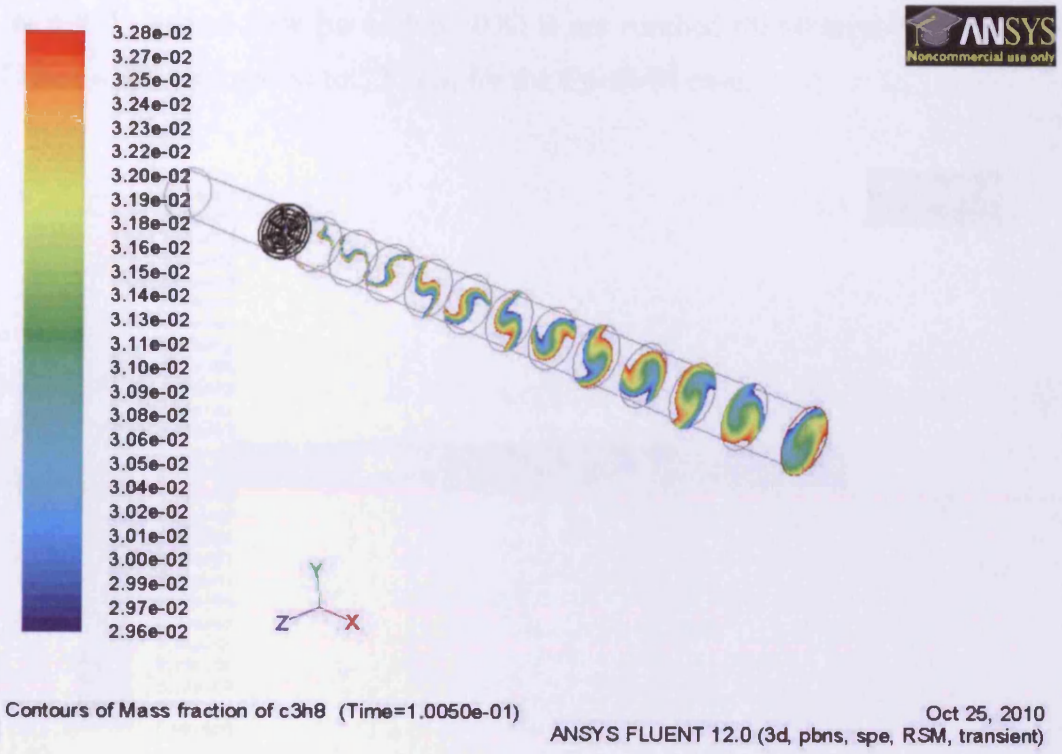

Figure 8.21b: Inner Radially Clamped Outer Circumferentially Clamped Top Mixing at Half Mass Flow Rate to 5% of target

8.7.5 Inner Radially Clamped Outer Circumferentially Clamped Bottom

Similar to the previous hybrid configuration, the recirculation zone here extends 200mm from the valve and appears to be symmetrical about the central axis (Figure 8.22). However, the shape of the zone is very different with the widest point about 30mm downstream, probably due to the influence of the outer reeds and the flow of air through the outer openings. As before, swirling flow begins to dominate the flow quickly, appearing fully developed around 300mm from the valve. No suction zone is created at the outlet.

It was not possible to reach a converged solution for the full fuel mass flow rate for this geometry. However the half fuel mass flow rate solution appears very similar to the previous case, so it is assumed that the half fuel mass flow rate solution will be more suitable than the full fuel mass flow rate solution.

Clamping the outer reed at the bottom (this case) appears to give slightly better mixing as the mix is within 5% of the target at the outlet of the domain (Figure 8.24), when compared to clamping the outer reed at the top (previous case). However the mixing doesn't appear to be as good as in the co-

swirl case, as a fully mixed flow (to within 10%) is not reached till 600mm-700mm downstream of the valve (Figure 8.23), compared to 350mm for the Co-Swirl case.

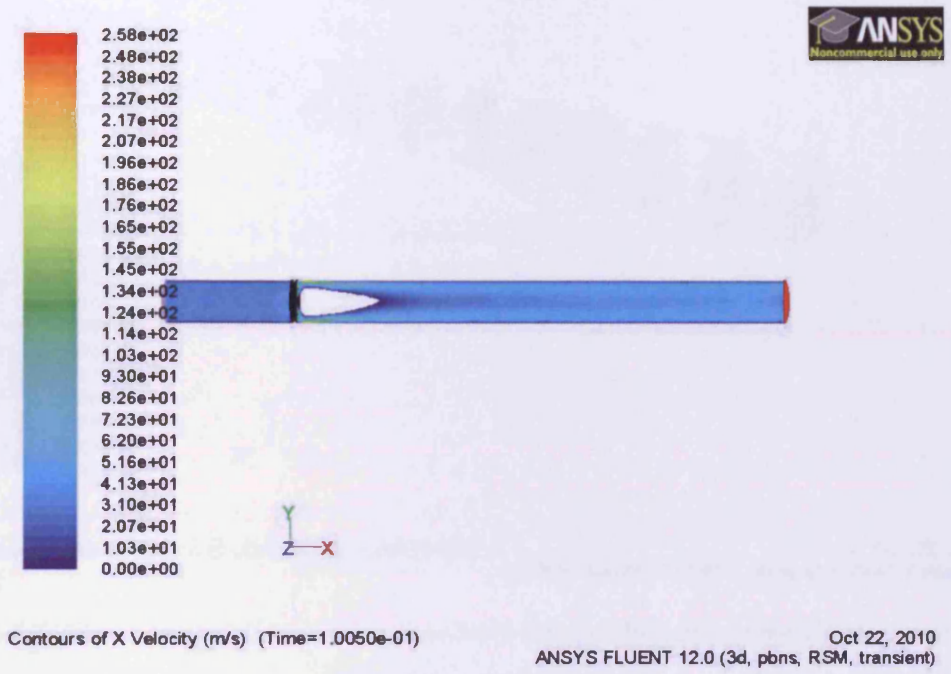

Figure 8.22: Inner Radially Clamped Outer Circumferentially Clamped Bottom Positive X Velocity Plot

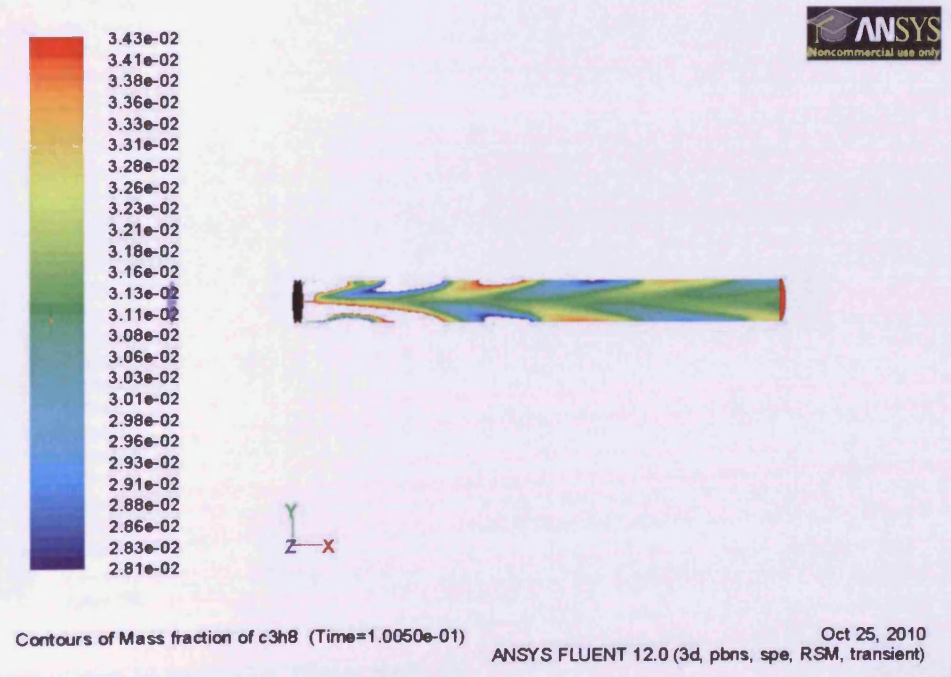

Figure 8.23a: Inner Radially Clamped Outer Circumferentially Clamped Bottom Mixing at Half Mass Flow Rate to 10% of target (front view)

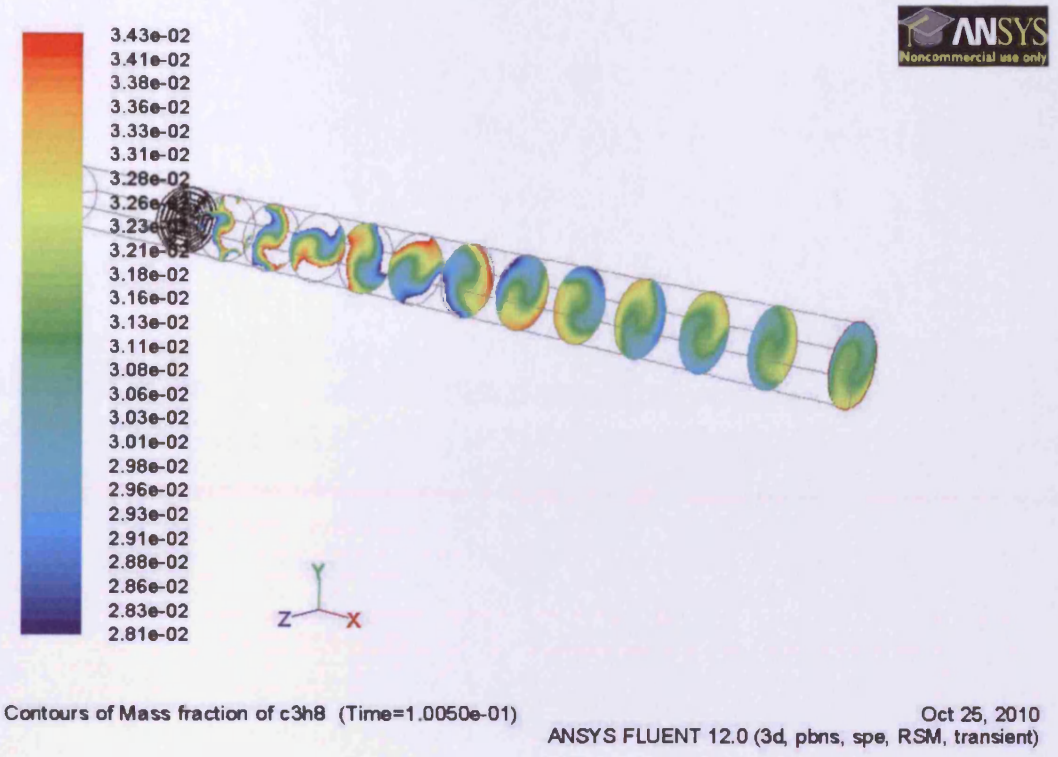

Figure 8.23b: Inner Radially Clamped Outer Circumferentially Clamped Bottom Mixing at Half Mass Flow Rate to 10% of target (cross sectional views)

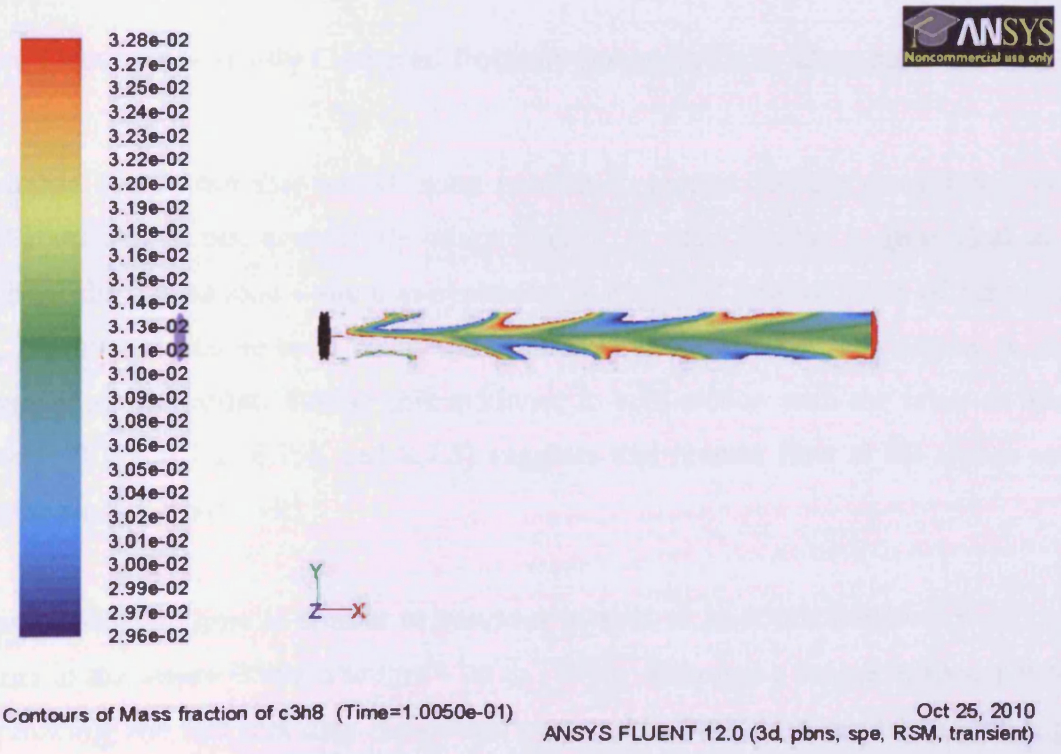

Figure 8.24a: Inner Radially Clamped Outer Circumferentially Clamped Bottom Mixing at Half Mass Flow Rate to 5% of target (front view)

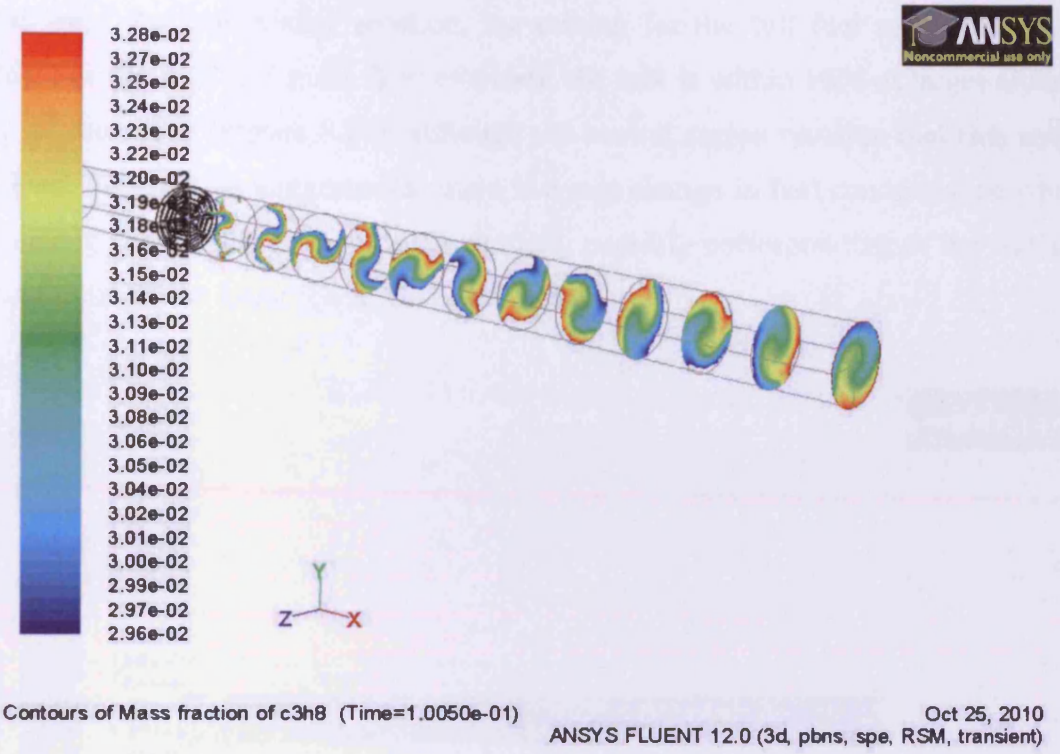

Figure 8.24b: Inner Radially Clamped Outer Circumferentially Clamped Bottom Mixing at Half Mass Flow Rate to 5% of target (cross sectional views)

8.7.6 Inner Circumferentially Clamped Bottom Outer Radially Clamped

The recirculation zone from this model again extends to around 200mm downstream of the valve (Figure 8.25). Although not completely axisymmetric, it does display a great deal of rotational symmetry about the centre axis – the non-symmetry is hidden if contour plots of the whole domain are viewed, however it can be seen when taking surface slices through the domain. A reverse flow region is present at the outlet. Taking this evidence in conjunction with the other swirling/ hybrid flows (Sections 8.7.1, 8.7.2, 8.7.4, and 8.7.5) suggests that reverse flow at the exit is only created when the outer reeds impart swirl.

The bulk flow residence time is similar to previous models at 30-35ms, however it appears that the residence time in the centre is much longer – up to 100ms. Although a longer residence time can be a positive for mixing, the fact that only the central portion has the longer residence time suggests that there is little mixing between the central region and bulk flow. This implies that fuel mixing for this geometry will be poor.

As predicted from the non-mixing solution, the mixing for the full fuel mass flow case is poor (Figure 6.26). For the half fuel mass flow rate case, the mix is within 10% of target around 575mm downstream of the valve (Figure 8.27), although the central region remains fuel rich and the outer region fuel lean. Figure 8.28 suggests that there is a step change in fuel concentration when moving from the centre to the circumference of the domain, possibly corresponding to the border between the air passing through the inner reeds and outer reeds.

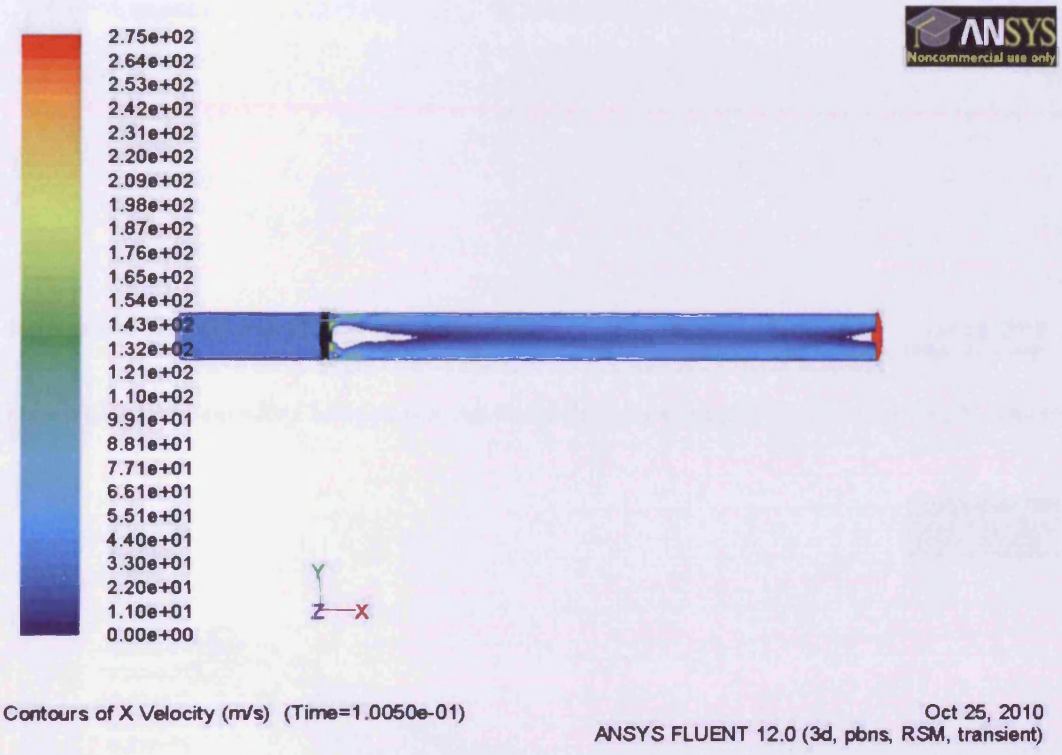

Figure 8.25a: Inner Circumferentially Clamped Bottom Outer Radially Clamped No Fuel Positive X velocity (front view)

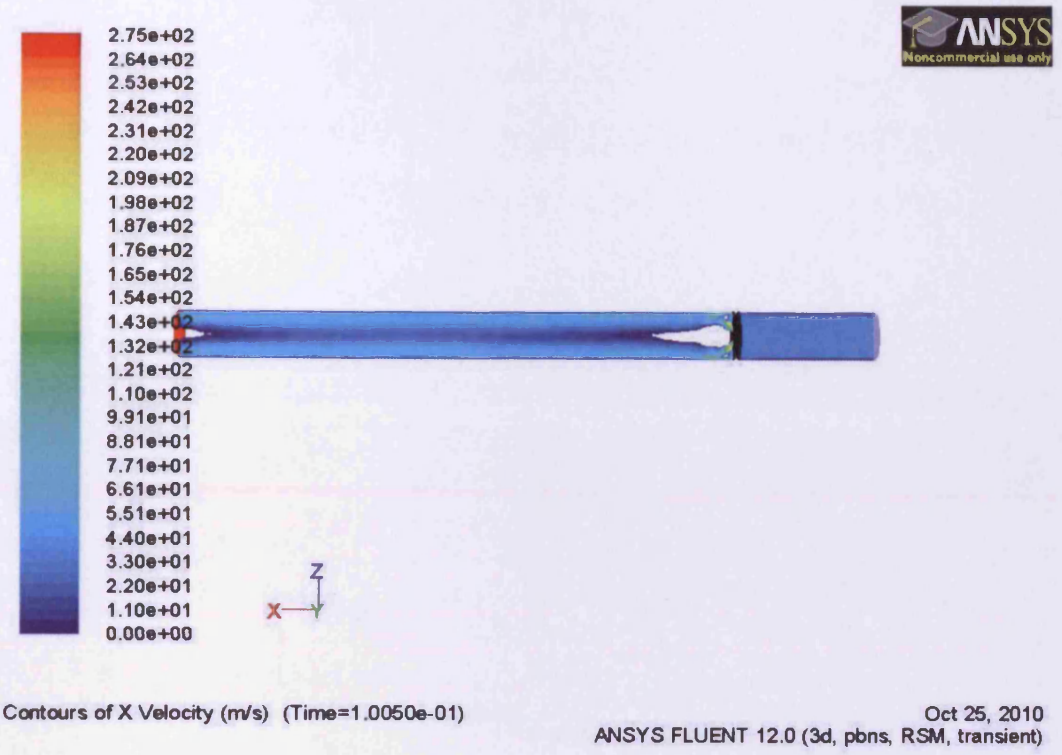

Figure 8.25b: Inner Circumferentially Clamped Bottom Outer Radially Clamped No Fuel Positive X velocity (top view)

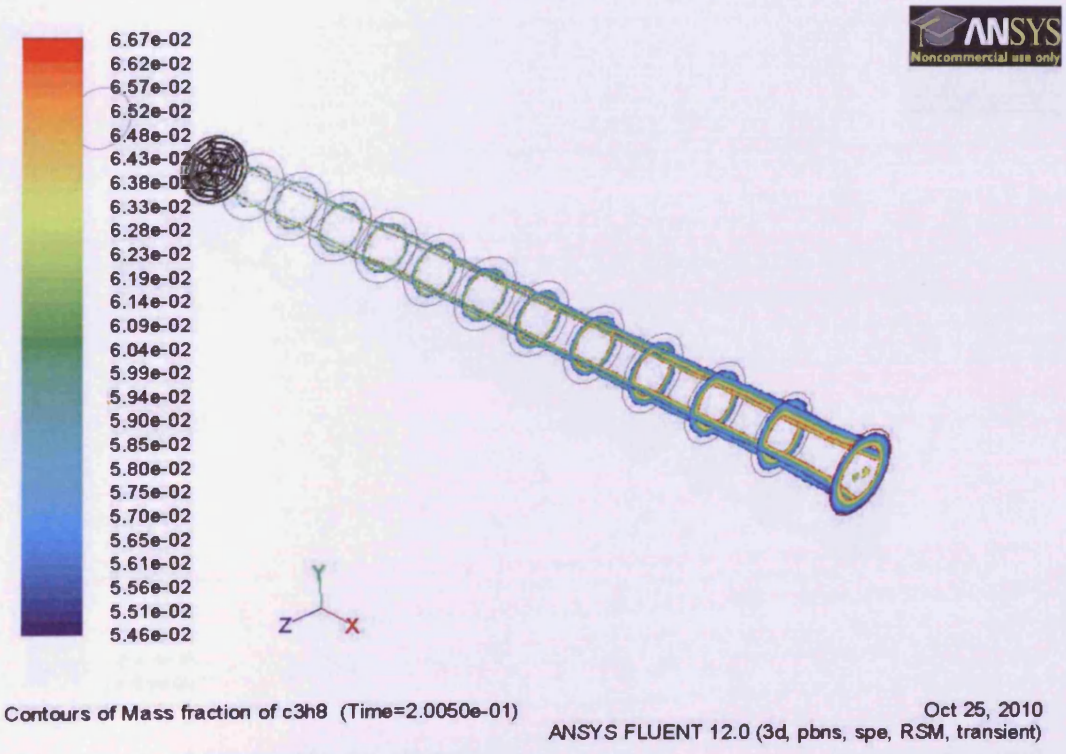

Figure 8.26: Inner Circumferentially Clamped Bottom Outer Radially Clamped Mixing at Full Mass Flow Rate

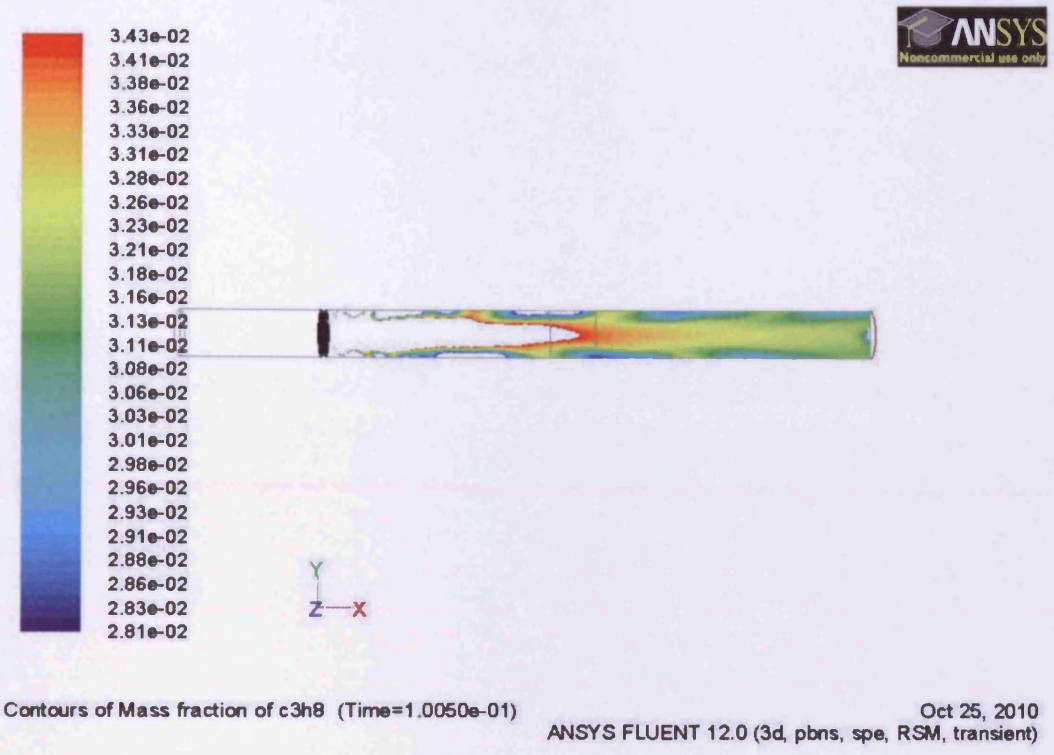

Figure 8.27a: Inner Circumferentially Clamped Bottom Outer Radially Clamped Mixing at Half Mass Flow Rate to 10% of target (front view)

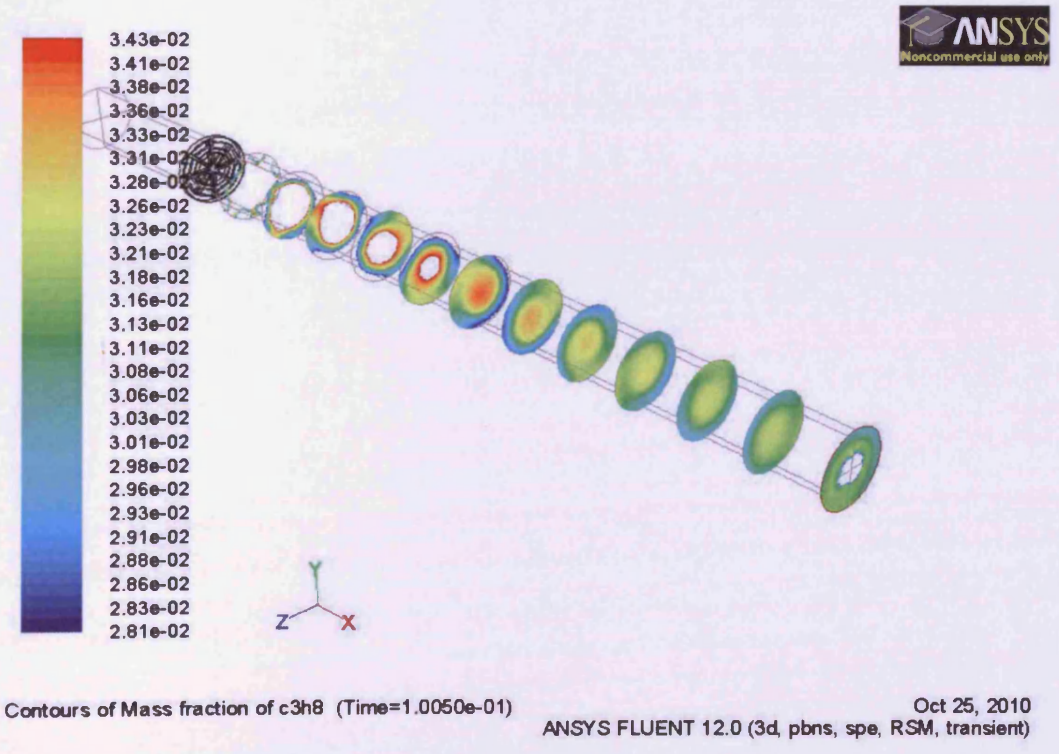

Figure 8.27b: Inner Circumferentially Clamped Bottom Outer Radially Clamped Mixing at Half Mass Flow Rate to 10% of target (cross sectional views)

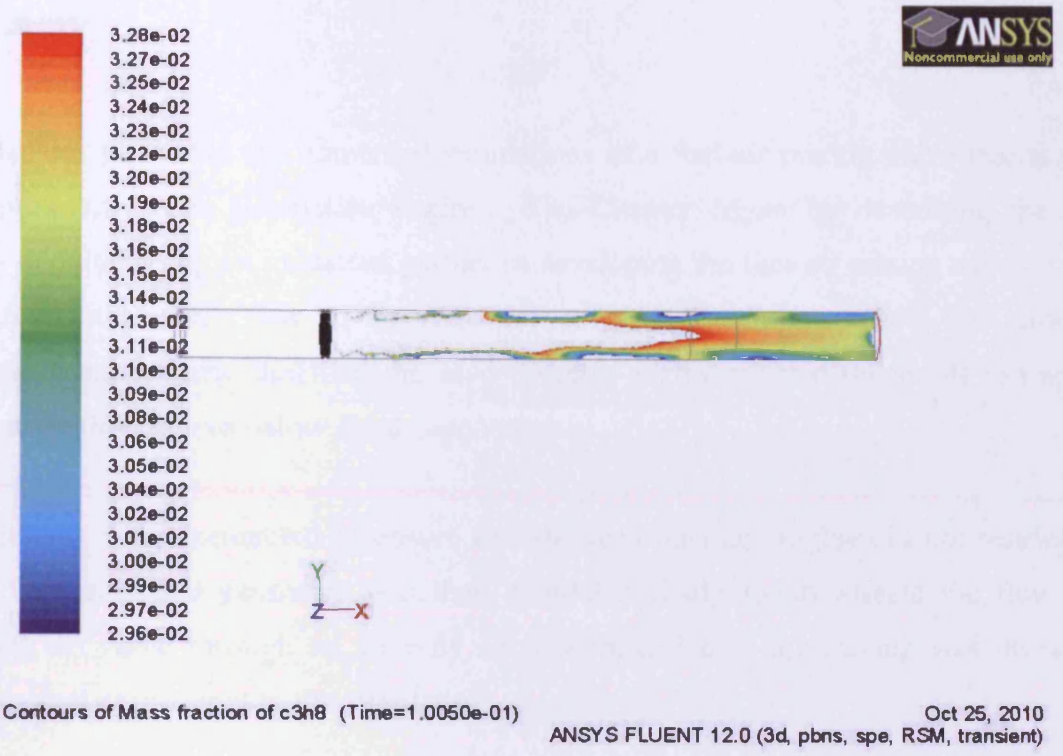

Figure 8.28a: Inner Circumferentially Clamped Bottom Outer Radially Clamped Mixing at Half Mass Flow Rate to 5% of target (front view)

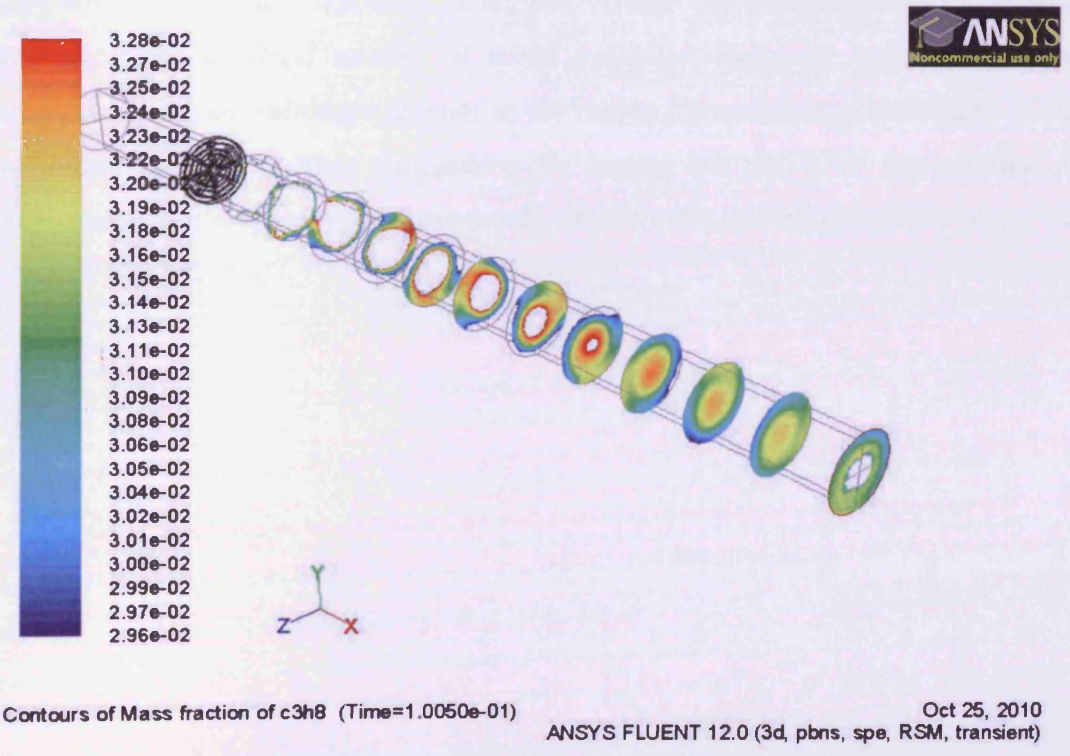

Figure 8.28b: Inner Circumferentially Clamped Bottom Outer Radially Clamped Mixing at Half Mass Flow Rate to 5% of target (cross sectional views)

8.8 Summary

This Chapter has presented the numerical simulations of a fuel-air mixing valve that is part of an industrial prototype pulse detonation engine. The Chapter began by describing the numerical simulations undertaken by an industrial partner in developing the fuel-air mixing valve. A review of this work found that there was an inconsistency between the air mass flow rate simulated and reported during experiment, and that the reed opening angles selected on the design appeared to restrict the mass flow rate to below the design value.

New calculations were conducted to ensure that the reed opening angles did not restrict the mass flow rate. This modified geometry was then simulated firstly to investigate the flow structures generated by the valve through an air only simulation, and then the mixing was investigated by introducing a fuel component to the simulation.

Propane fuel was chosen as, from the research presented in Chapter Two, the majority of any liquid fuel used in a pulsed detonation engine must be in vapour form. The results of this analysis showed that the Co-swirl and Inner Radially Clamped Outer Circumferentially Clamped Bottom configurations provided the best mixing of those available. However, mixing was achieved far downstream of the valve, i.e. mixing was poor in the region immediately downstream of the valve. It has been recommended that further simulations be carried out that alter the position of the fuel injector, as it is the author's opinion that this would improve the mixing capability of the valve.

Chapter Nine

Conclusions and Future Work

9.1 Conclusions

A thorough review of current detonation literature and PDE design has been has been undertaken. This has shown that the criterion for successful propagation of detonations in liquid fuels has been established, and that this is beyond commercial fuel injector and delivery systems. The two main methods of detonation initiation in PDEs have also been discussed with their limits highlighted. This has led to the proposal of using reflected shocks to prepare the fuel-air mixture so that it is able to support detonation propagation and to initiate the detonation.

A shock tube facility has been designed and built to conduct experimental studies into the initiation of detonations by reflected shocks. The shock tube has been designed to operate with both liquid and gaseous fuels – the latter through the design of a bespoke slide valve to separate reactive and non-reactive gases in the shock tube. Reliable firing of the shock tube has been achieved through the use of a double-diaphragm firing mechanism.

The shock tube has been commissioned and shown to produce excellent repeatability for non-reacting shock propagation. The non-ideal processes present in the shock tube have been quantified and empirical relationships have been developed. These relationships aid future use of the shock tube by easing experimental design and have allowed the development of a Matlab model.

Gaseous combustion experiments have been conducted in the shock tube using stoichiometric propane and stoichiometric hydrogen. Stoichiometric propane was used for its similarity to kerosene vapour for detonation propagation and hydrogen for its propensity to detonate. The experimental programme has shown that propane detonation was not possible with the conditions tested but hydrogen detonation was achieved. The reflecting face had a dramatic affect on combustion initiation with the conical reflecting face initiating combustion (both detonation and deflagration) for weaker incident shock waves than the hemispherical face. However for deflagration, the hemispherical face appeared to give stronger combustion than the conical face for the same incident shock wave.

The fuel-air mixing in a prototype PDE has been investigated using numerical simulations. Several variations of a fuel-air mixing valve with axial fuel injection were investigated. The results showed that the best mixing was given by the Co-swirl and Inner Radially Clamped Outer

Circumferentially Clamped Bottom configurations. Although, the required mixing was achieved within the length of the detonation chamber, the target mix was not formed until a significant distance downstream of the valve, leaving a significant region close to the valve with an undesirable mixture.

An experimental study of droplet breakup in steady and pulsed flows has been conducted to study the ability of shock waves to produce liquid fuel-air mixtures suitable for detonation propagation. The study, conducted using high-speed videography and laser diagnostic techniques, has confirmed previously published droplet breakup mechanisms in steady flow, and has quantified the secondary spray formed by the breakup process. Droplet breakup studies in pulsed flows, relevant to the rest of the work in this thesis, have been preformed and recorded using high speed videography. The results show catastrophic breakup, consistent with previous observations for steady flow. Relationships have been suggested that would allow the use of current injector and fuel delivery technology for liquid fuelled pulse detonation engines using reflected shock initiation.

Detonation initiation for liquid kerosene using reflected shocks with a flat reflecting face has been attempted. When compared to the results of gaseous fuels from earlier in this study, the results suggest that detonation initiation is possible for liquid kerosene with the use of a shaped reflecting face which would provide a new liquid fuel preparation/ initiation technique for PDEs.

9.2 Future Work

Although the shock tube performed well, some minor modifications would allow more detailed results to be obtained:

- The length of the test section should be increased. This would enable the first pressure transducer to be placed further away from the mixture/air interface, improving the results gained from this transducer.
- The number of pressure transducers used should be increased. Although two transducers were sufficient to record the pressure and velocity of the shock and combustion waves, additional transducers would allow more detailed analysis of the phenomena as they moved such as the potential acceleration of the shock and combustion waves.

- The timing and control system of the shock tube can be improved. All control was conducted manually which lead to long "delay" times and the potential for errors. An automated control process would speed up firing of the shock tube and eliminate the potential for errors in the firing process.
- Further work is required to improve the liquid fuel injection system. The injector was only able to inject fuel into half of the length of the test section. An alternative method is required to increase the length of the fuel-air mix, thus improving the quality of the results.

The numerical simulations were successful in modelling the fuel-air mixing valve. However validation work is required to enable confidence in the results. The following simulation work would build on the work already undertaken:

- Positioning of the fuel injector(s) on the circumference as opposed to axially may enable faster mixing. This hypothesis needs to be simulated.
- The introduction of a liquid fuel into the simulation as opposed to a gaseous fuel would allow simulation of droplet movements in this highly complex flow.

Investigation into droplet breakup physics has allowed some correlations to be suggested. The following work would enable more detailed correlations to be formed:

- An improvement of the air generator should be considered which would form an air stream with a greater surface area. This would help with the timing issues experienced with the pulsed flows.
- The pressure of the air generator can be increased. This would allow a larger range of conditions to be studied, providing the potential for correlations predicting the size of the secondary spray from the Weber number and initial droplet size.
- The use of a more sophisticated laser diagnostic technique should be investigated. The use of the droplet counter has enabled automation of the droplet breakup rig, and this could be used to employ a technique such as PDA to allow temporal and spatial resolution of the secondary spray.

References

1. Century of Flight. *Airlines and Airliners.* [cited 2011 Jan]; Available from: http://www.century-of-flight.net/Aviation%20history/coming%20of%20age/De%20Havilland%20Comet.htm
2. Airports Council International World. *ACI's World Airport Traffic Report for 2009* 2010 [cited 2011 Jan]; Available from: http://www.airports.org/cda/aci_common/display/main/aci_content07_c.jsp?zn=aci&cp=1-5-54_666_2__.
3. Rolls-Royce plc. *Trent 900 Specification Brochure.* 2009 [cited 2011 Jan]; Available from: http://www.rolls-royce.com/Images/brochure_Trent900_tcm92-11346.pdf.
4. Aerodynamics Research Centre Department of Mechanical and Aerospace Engineering University of Texas at Arlington. *Pulsed Detonation Engines.* 2010 [cited 2010 Dec]; Available from: http://arc.uta.edu/research/pde.htm.
5. U.S. Department of Transportation Federal Aviation Administration Flight Standards Service. *Chapter 13 'Transition to Tailwheel Airplanes for' from Airplane Flying Handbook.* 2004 [cited 2007 Jan]; Available from: http://www.faa.gov/library/manuals/aircraft/airplane_handbook/media/faa-h-8083-3a-6of7.pdf.
6. Pratt & Whitney. *Commercial Products Description for JT9D.* [cited 2011 Jan]; Available from: http://www.pw.utc.com/Products/Commercial/JT9D.
7. Jane's Information Group. *General Electric GE90-115B (United States), Aero-engines - Turbofan.* 2009 [cited 2011 Jan]; Available from: http://www.janes.com/articles/Janes-Aero-Engines/General-Electric-GE90-115B-United-States.html.
8. UK Patent Number GB1069217.
9. UK Patent Number GB1213551.
10. Jim Kelly posting on Popular Science. *After Combustion: Detonation!* 2003 [cited 2011 Jan]; Available from: http://www.popsci.com/military-aviation-space/article/2003-08/after-combustion-detonation.
11. Schauer, F., *Presentation of Current Research work at AFRL.* 2009: Port Talbot.
12. Kailasanath, K., *Review of Propulsion Applications of Detonation Waves.* AIAA Journal, 2000. **38(9)**: p. 1698-1708.
13. Larine Barr posted on the official web site of the U.S. Air Force. *Pulsed detonation engine flies into history.* 2008 [cited 2011 Jan]; Available from: http://www.af.mil/news/story.asp?id=123099095.
14. Dora Musielak posted on American Institute of Aeronautics and Astronautics. *PDE Operational Cycle* 2010 [cited 2011 Jan]; Available from: https://info.aiaa.org/tac/PEG/HSABPTC/Image%20Library/Forms/DispForm.aspx?ID=10&Source=https%3A%2F%2Finfo%2Eaiaa%2Eorg%2Ftac%2FPEG%2FHSABPTC%2FImage%2520Library%2FForms%2FAllItems%2Easpx&RootFolder=%2Ftac%2FPEG%2FHSABPTC%2FImage%20Library.
15. Lockheed Martin Corporation. *SR-71 Blackbird.* 2011 [cited 2011 Jan]; Available from: http://www.lockheedmartin.com/aboutus/history/SR71Blackbird.html.
16. Lu, F.K., J.M. Meyers, and D.R. Wilson, *Experimental Study of a Pulse Detonation Rocket with Shchelkin Spiral*, in *24th International Symposium on Shock Waves.* 2004: Beijing.
17. Glassman, I., *Combustion.* 1996, San Diego: Academic Press.
18. Chapman, D.L., *On the rate of explosion in gasses.* Philosophical Magazine, 1899. **47**: p. 90-104.

19. Jouget, J.C.E., *On the propagation of chemical reactions in gases.* Journal de Mathématiques Pures et Appliquées, 1905. **1**: p. 347-425.
20. Fickett, W. and W.C. Davis, *Detonation: Theory and Experiment.* 2000: Dover Publications.
21. Zel'dovich, *On the theory of propagation of detonations in gaseous systems.* Journal of Experimentals and Theoretical Physics, 1940. **10**: p. 542-568.
22. von Neumann, J., *Theory of Detonation Waves.* 1942, Office of Scientific Research and Development, USA: Aberdeen Proving Ground, Maryland.
23. Döring, W., *Über den Detonationsvorgang in Gasen.* Annaleen der Physik, 1943. **435**(6-7): p. 421-436.
24. Edwards, D.H., G.O. Thomas, and M.A. Nettleton, *The Diffraction of a Planar Detonation wave at an Abrupt Area Change.* Journal of Fluid Mechanics, 1979. **95(1)**: p. 79-96.
25. Saretto, S.R., et al., *Studies of Detonation Transition in a Gradual Area Expansion for Multi-Cycle PDE Applications.* Proceedings of the Combustion Institute, 2005. **30**: p. 2809-2816.
26. Khasainov, B., et al., *Detonation Diffraction from Circular tubes to Cones.* Shock Waves, 2005. **14(3)**: p. 187-192.
27. Nettleton, M.A., *Gaseous Detonations: Their Nature, Effects and Control.* 1987, London: Butterworths.
28. Dabora, E.K. and L.P. Weinberger, *Present Status of Detonations in Two-Phase Systems.* Acta Astronautica, 1974. **1(3-4)**: p. 361-374.
29. Dabora, E.K., K.W. Ragland, and J.A. Nicholls, *Drop-size effects in spray detonations*, in *Symposium (international) on combustion.* 1969: University of Poitiers.
30. Cramer, F.B., *The onset of detonation in a droplet combustion field*, in *Proceedings of the Combustion Institute.* 1963: Cornell University, USA.
31. Kailasanath, K., *Liquid Fuelled Detonations in Tubes.* Journal of Propulsion and Power, 2006. **22(6)**: p. 1261-1268.
32. Borisov, A.A., et al., *The Reaction Zone of Two-Phase Detonations.* Astronautica Acta, 1970. **15**(5): p. 411-417.
33. Bowen, J.R., et al., *Hetrogeneous detonation supported by fuel fogs or films.* Proceedings of the Combustion Institute, 1971. **13**: p. 1131-1139.
34. Bull, D.C., M.A. McLeod, and G.A. Mizner, *Detonation of Unconfined Fuel Aerosols.* Progress in Astronautics and Aeronautics, 1981. **75**: p. 48-60.
35. Brophy, C.M., et al., *Detonation of a JP-10 aerosol for pulse detonation engine applications.* High Speed Deflagration and Detonation: Fundamentals and Control, ed. G.D. Roy, et al. 2001, Moscow: ELEX-KM Publisher.
36. Austin, J.M. and J.E. Shepherd, *Detonations in Hydrocarbon Fuel Blends.* Combustion and Flame, 2002. **132**: p. 73-90.
37. Ciccarelli, G. and J. Card, *Detonation in Mixtures of JP-10 Vapour and Air.* AIAA Journal, 2006. **44(2)**: p. 362-267.
38. Beltman, W.M., E.N. Burcsu, and L. Zuhal, *The Structural Response of Cylindrical Shells to Internal Shock Loading.* Journal of Pressure Vessel Technology, 1999. **121**: p. 315-322.
39. Fan, W., et al., *Experimental Investigation on Two-Phase Pulse Detonation Engine.* Combustion and Flame, 2003. **133**: p. 441-450.
40. Rocourt, X., et al., *Detonability of simple and representative components of pyrolysis products of kerosene: Pulsed detonation engine application.* Shock Waves, 2005. **14(4)**: p. 283-291.
41. Rocourt, X., et al., *Thermal degradation of two liquid fuels and detonation tests for pulse detonation engine studies.* Shock Waves, 2007. **16(3)**: p. 233-245.

42. Roy, G.D., et al., *Pulse Detonation Propulsion: Challenges, Current Status, and Future Perspective.* Progress in Energy and Combustion Science, 2004. **20**: p. 545-672.
43. Cooper, M., et al., *Direct Experimental Impulse Measurements for Detonation and Deflagrations.* Journal of Propulsion and Power, 2002. **18(5)**: p. 1033-1041.
44. Frolov, S.M., *"Liquid-fuelled, air-breathing pulse detonation engine demonstrator: Operation principles and performance".* Journal of Propulsion and Power, 2006. **22(6)**: p. 1162-1169.
45. Li, C. and K. Kailasanath, *Detonation Initiation by Annular-Jet-Induced Imploding Shocks.* Journal of Propulsion and Power, 2005. **21(1)**: p. 183-186.
46. Jackson, S.I. and J.E. Shepherd, *Toroidal Imploding Detonation Wave Initiator for Pulse Detonation Engines.* AIAA Journal, 2007. **45(1)**: p. 257-270.
47. Japanese Patent JP2005315250.
48. United States Patent US2006123201.
49. Koznetsov, M.S. *Detonation Propagation, Decay, and Reinitiation in Nonuniform Gaseous Mixtures.* in *International Symposium on Combustion.* 1998. Boulder, Colorado.
50. Ishii, K. and M. Kojima, *Behavior of detonation propagation in mixtures with concentration gradients.* Shock Waves, 2007. **17(1-2)**: p. 421-429.
51. Hurley, C., *Discussion of QinetiQ PDE Prototype*, A.K. Majithia. 2008: UK.
52. Anderson, J.D., *Modern Compressable Flow: With Historical Perspective.* 2001, London: McGraw Hill.
53. Gaydon, A.G. and I.R. Hurle, *The Shock Tube in High-Temperature Chemical Physics.* 1963, London: Chapman and Hall
54. Kinney, G.F. and K.J. Graham, *Explosive Shocks in Air.* 1985, Berlin: Springer.
55. Ciccarelli, G. and B. De Witt, *Detonation initiation by shock reflection from an orifice plate.* Shock Waves, 2006. **15(3-4)**: p. 259-265.
56. Dean, A.J., et al., *Autoignition of Surrogate Fuels at Elevated Temperatures and Pressures.* Proceedings of the Combustion Institute, 2007. **31**: p. 2481-2488.
57. Cadman, P., G.O. Thomas, and P.B. Butler, *The Auto-Ignition of Propane at Intermediate Temperatures and High Pressures.* Physical Chemistry Chemical Physics, 2000. **2**(23): p. 5411-5419.
58. Schildberg, H., *Determination of the composition ranges in which Propene/O2/N2 and Methane/O2/N2 transit from deflagration to detonation in vessels of 20l and 2500l*, in *UKELG 41st Meeting.* 2008: Shell Technlogy Centre, Thornton, UK.
59. Oakley, G., *Private Correspondence.* 2008.
60. Joseph, D.D., J. Belanger, and G.S. Beavers, *Breakup of a liquid drop suddenly exposed to a high-speed airstream.* International Journal of Multiphase Flow, 1999. **25**: p. 1263-1303.
61. National Instruments. *NI LabVIEW Technical Resources: Getting Started, Support, and Downloads.* 2009 [cited 2009 March]; Available from: http://www.ni.com/labview/technical-resources/.
62. Thomas, G.O. and R.L. Williams, *Detonation Interaction with Wedges and Bends.* Shock Waves, 2002. **11**: p. 481-492.
63. Penyazkoz, O.G., K.L. Sevruk, and K. Allhusan. *Auto-ignition of Hydrogen-Air Mixture at Nonuniform Flow and Boundary Condition.* in *European Combustion Meeting.* 2009. Vienna, Austria.
64. Majithia, A.K., et al., *Droplet breakup quantification and processes in constant and pulsed air flows*, in *22nd ILASS-Europe.* 2008: Lake Como, Italy.
65. Lefebvre, A., H, *Atomization and Sprays.* 1989, Indiana: Hemisphere Publishing Corporation.

66. Pilch, M. and C.A. Erdman, *Use of Breakup Time Data and Velocity History Data to Predict the Maximum Size of Stable Fragments for Acceleration-Induced Breakup of a Liquid Drop.* International Journal of Multiphase Flow, 1987. **13**: p. 741-757.
67. Park, S.W., S. Kim, and C. Lee, S, *Breakup and atomization characteristics of mono-dispersed diesel droplets in a cross flow air steam.* International Journal of Multiphase Flow, 2006. **32**: p. 807-822.
68. Kay, P.J., *Characterising thermofluid spray dynamics for energy-efficient automotive engines*, in *Engineering*. 2006, PhD Thesis, Cardiff University.
69. Morris, D., *Temperal charactarisation of various g-di fuel injector concepts*, in *School of Engineering*. 2003, PhD Thesis, Cardiff Univeristy.
70. Crayford, A.P., *Supression of methane-air explosions with water in the form of 'fine' mists*, in *Engineering*. 2004, PhD Thesis, Cardiff University.
71. Vasu, S.S., D.F. Davidson, and R.K. Hanson, *Jet fuel ignition delay times: Shock tube experiments over wide conditions and surrogate model predictions.* Combustion and Flame, 2008. **152**: p. 125-143.
72. Emmerson, P.R., J.P. Wood, and S.L. Mistry, *Design and Analysis of an Air Valve for a Pulse Detonation Engine.* 2008, Industrial Partner's Report: UK.
73. Ansys Ltd., *FLUENT 6 User Manual.* 2006.